Computational Investigation of the Role of Ion Channels Remodelling Associated with Age Development in the Cardiac Pacemaker Cells

A thesis submitted to

The University of Manchester

for the degree of Doctor of Philosophy

in the Faculty of Sciences and Engineering

2019

Azzah Mohammed Alghmdi

SCHOOL OF NATURAL SCIENCE

Department of Physics and Astronomy

Contents

This thesis contains 51,722 words.

List of Tables

List of Figures

Abstract

University of Manchester

Azzah Alghamdi

Degree Programme: Doctor of Philosophy

Thesis Title: Computational Investigation of the Role of Ion Channel Remodelling Associated with Age Development in the Cardiac Pacemaker Cells

The sinoatrial node (SAN) is the primary cardiac pacemaker, which generates spontaneous action potentials (APs) and regulates the rhythms of the heart. The function of the SAN declines with age development, and this results in marked differences in the morphology and characteristics of APs and affects the pacemaking activities, consequently increases the incidence of sinus node dysfunction (SND) in older adults. These changes may be attributable to different sets of ion-channel interactions at different ages. The mechanism underlying the pathogenesis for cardiac pacemaker dysfunctions associated with ageing remain uncertain. In this project, using a computer modelling approach, we investigated the role of age-related remodelling of ion channels on pacemaking activites of the SAN at single-cell and tissue level. The research explained in this thesis utilised electrophysiological data from experiments in different species at the ion-channel level to develop novel mathematical models of neonatal, aged and diabetic conditions. A mathematical model of neonatal rabbit SAN cells was developed by modifying the current densities and/or kinetics of ion channels (I_{Na}, $I_{Ca,L}$, I_f, I_{NaCa}, I_{Kr} and I_{Ks}) in a SAN adult-cell model. At single cell level, simulation results showed that the ion channels altered during maturation play a functional role in slowing down the pacemaking APs. At the tissue level, these integral effects increase the activation time across the intact SAN-atrium, leading to decreased AP conduction velocity and heart rate. Moreover, vagal nerve activity elucidated a high sensitivity of neonatal SAN cells to acetylcholine. The effect of ACh amplified in neonates, under high concentration, leading to possible sinus arrest or conduction exit. Similarly, the ionic mechanisms underlying SND associated with ageing were assessed. A mathematical model of adult rat SAN cells was modified to investigate two case studies of cardiac pacemaker dysfunction, identified experimentally, which arose from different pathways of electrical remodelling in ion channels (I_f, I_{CaL}, I_{NaCa}) and Ca^{2+} handling proteins proteins (RyR2, and SERCA2a) in the ageing rat heart. Our results suggest that the integral action of all remodelled ion channels and Ca^{2+} handling can be accounted for producing bradycardic effects as manifested by heart rate reduction, the remodelled $I_{Ca,L}$, either via a gain or loss of function, contributes primarily to ageing-related bradycardia. Therefore, ageing-related bradycardia can be linked to different remodelling “pathways”. A one-dimensional string model of SAN-atrium was constructed, through incorporating the regional heterogeneity of SAN tissue, and coupled to atrial tissue. The new model was utilised to simulate the spontaneous activity and AP conduction across the SAN-atrium under normal conditions and SND associated with ion channel deficiency in diabetes. The model successfully produced similar

propagation and conduction activities to experimental observations in normal SAN.The functional alternation of ion channel; $I_{Ca,L}$, $I_{Ca,T}$, I_f and I_{NaCa} in diabetic rat closely resemble those observed in experimental SND. Finally, a mathematical model of mouse SAN cells was utilised to investigate the effect of changes in abundance of hyperpolarisation-activated cyclic nucleotide-gated channel (HCN) on the APs and pacemaker rate, during over-expression of gene target TBX18, which is used to enhance pacemaker function in a rat subsidiary atrial pacemaker (SAP), a model of sick sinus syndrome (SSS). Simulation results showed that the changes of the HCN abundance could explain the observed changes in beating rate. This suggests that TBX18 may have the potential to restore pacemaker function in human SSS.

The Author

Azzah Mohammed Alghamdi completed a Master of Physics (MCS) degree at King Abdulaziz University (KAU), School of Physics and Astronomy, Saudi Arabia in 2009. In September 2014, she joined the Biological Physics group in the School of Physics & Astronomy at the University of Manchester to begin work on her Doctor of Philosophy degree, under the supervision of Professor Henggui Zhang. This thesis represents her first major research project.

Declaration

No portion of the work referred to in this thesis has been submitted in support of an application for another degree or qualification of this or any other university or other institute of learning.

Copyright

The following four notes on copyright and the ownership of intellectual property rights must be included as written below:

i. The author of this thesis (including any appendices and/or schedules to this thesis) owns certain copyright or related rights in it (the "Copyright") and s/he has given The University of Manchester certain rights to use such Copyright, including for administrative purposes.

ii. Copies of this thesis, either in full or in extracts and whether in hard or electronic copy, may be made only in accordance with the Copyright, Designs and Patents Act 1988 (as amended) and regulations issued under it or, where appropriate, in accordance with licensing agreements which the University has from time to time. This page must form part of any such copies made.

iii. The ownership of certain Copyright, patents, designs, trademarks and other intellectual property (the "Intellectual Property") and any reproductions of copyright works in the thesis, for example graphs and tables ("Reproductions"), which may be described in this thesis, may not be owned by the author and may be owned by third parties. Such Intellectual Property and Reproductions cannot and must not be made available for use without the prior written permission of the owner(s) of the relevant Intellectual Property and/or Reproductions.

iv. Further information on the conditions under which disclosure, publication and commercialisation of this thesis, the Copyright and any Intellectual Property and/or Reproductions described in it may take place is available in the University IP Policy (see http://documents.manchester.ac.uk/DocuInfo.aspx?DocID=2442 0), in any relevant Thesis restriction declarations deposited in the University Library, The University Library's regulations (see http://www.library.manchester.ac.uk/about/regulations/) and in The University's policy on Presentation of Theses3.

Acknowledgements

Thanks and appreciation are to be given firstly to Allah, who has provided me with the strength, health, family support and courage to complete this work.

I would like to express my deepest gratitude to my supervisor, Prof. Henggui Zhang, for his expertise, advice, help, patience and understanding throughout my Ph.D. study. This thesis would not have been possible without his continuous support and encouragement.

I extremely grateful to my beloved parenets: my dearest father, Mohammed and my my dearest mother, Salehah, words cannot express the feelings I have for them for their constant unconditional support and for their daily prayers, you deserve more than mere thanks words. It is just because of you I am who I am today. Thank you from the bottom of my heart for the love, kindness, encouragement that you both have provided to me along the way. “You are... God’s special gift to me”. Mother these last words for you “you will always stay in my heart, non-never forgotten, until we meet again ”..

I am grateful to my amazing small family including my husband: Abdullah, my son,Thamer and my daughters, Reema, Lara, and Jouri, who shared with me every moment in this journey, this dream would not have materialised without thier endless love, support and patience. “Thank you all, very much, you mean the world to me”.

I am also very grateful to my wonderful siblings, who have provided me with moral and emotional support during my life. I am blessed to have you in my life.

I am also indebted to the King Abduaziz University, Jeddah University, and Saudi Cultural Bureau for providing me with the opportunity to undertake this study; their encouragement and support has been invaluable.

It is a pleasure to show my special thanks to all those people in Biophysical Group for their friendship and assistance.

Supporting Work

- Alghamdi AM, Testrow CP, Whittaker DG, Zhang H. The Mechanism Underlying Heart Rate and Pacemaking Activity Decline in Developing Sinoatrial Node of the Rabbit Heart. Computing in Cardiology.2018. (Conference proceedings).
  Available from: http://www.cinc.org/archives/2018/pdf/CinC2018-224.pdf

- Choudhury M, Black N, Alghamdi A, Souza A D', Wang R, Yanni J, et al. TBX18 overexpression enhances pacemaker function in a rat subsidiary atrial pacemaker model of sick sinus syndrome. The Journal of Physiology.2018; 596:6141–55.
  Available from:
  https://www.ncbi.nlm.nih.gov/pmc/articles/PMC6292813/pdf/TJP-596-6141.

- Algamdi . A. M. Zhang. H. Cardiac pacemaker dysfunction arising from different pathways of electrical remodelling in the ageing rat. The Physiological Society. In: Proc Physiol Soc 43, PC014 [Internet]. Aberdeen; 2019. Available from: https://www.physoc.org/communications/cardiovascular-respiratory-and-autonomic-control-crac/ Proceedings of the Physiological Society, 2019, Proc Physiol Soc, 43.(Conference proceedings).

Chapter One - Introduction

1.1. The heart

The heart is an exceptional organ which beats up to 100,000 times a day as it pumps nearly 800 litres of blood through the body.[1] Blood circulation guarantees oxygen supply and transportation of nutrients and hormones, and it ensures the excretion of metabolic waste from the millions of cells throughout the body.[1] The significance of continuous blood circulation is underscored by the entire dependence of the lives of mammals on the non-stop second-to-second beating of the heart, which performs two to three billion heartbeats across the average lifespan in humans.[2] Consequently, any disease of this organ can lead to dangerous consequences.[2,3]

Pathological alterations to heart function, such as those caused by ischaemic heart disease and an array of other heart conditions such as cardiac arrhythmia, angina, congenital heart disease, heart attack, cardiomyopathy and heart failure, can be fatal.[4] The heart is one of several bodily organs whose functions deteriorate with age, thus, the heart diseases are the second leading causes of death throughout England and Wales from 2015 to 2017**.** Ischaemic heart disease accounted for 10.9% of total deaths registered in 2017.[5] Owing to the rise in the ageing population, the trend is predicted to put the National Health Service under significant strain as demand for treatment increases with the growing numbers of age-related cardiovascular diseases.[5] The immense economic and health pressure relevant to cardiac arrhythmias and cardiovascular disease, as well as the high monetary and treatment costs, create functional disabilities and low quality of life linked with the aftermath of the disease. There is an urgent demand for a better understanding of the underlying mechanisms associated with pathologies of the heart.

There has been remarkable progress regarding the understanding of the pathological mechanisms of heart disease, in addition to the development of new strategies for managing the condition. Yet current treatments for heart disease are primarily restricted to the fitting of artificial pacemakers, using drugs, coronary angioplasty, heart transplantation, and coronary bypass surgery. These treatments have reduced the number

of fatalities related to heart disease. However, heart disease cannot be fundamentally cured by relying on these treatments. To completely cure heart disease, the underlying pathological mechanisms of the various forms of the disease required to be fully understood.

In the past few decades, remarkable efforts have been made to develop experimental methods and protocols that can be applied in a bid to undrestand the complexities that underlie the function of healthy and diseased hearts. These techniques have facilitated cardiac investigations including; a deep understanding of the functions and structures of heart-related proteins [6,7]; uncovering subcellular mechanisms and activities; revealing cellular membrane potentials [8]; and non-intrusively imaging the whole heart activities of the heart *in vivo.*[9,10] The experimental techniques and animal models have significantly advanced knowledge of the heart under various conditions. However, limited resources and ethical concerns mean that performance of human-tissue experiments has proved to be a challenge. The limitations are compounded by the lack of data and understanding of the human heart, particularly under normal conditions, due to an overwhelming fraction of human data have been gathered from studies on diseased hearts. Consequently, numerous experiments on animal organs have been conducted to examine the mechanisms and functions of the heart, as well as to explore avenues for new therapies. These animal models include dogs, sheep, guinea pigs, rabbits, rats and mice, gina pigs, rabbits, and rats.[9-15] Additionally, ion-channel expression measurements in non-cardiac cells has been a useful tool to uncover the function of single-ion channels under healthy or diseased conditions.[16,17]

Beyond the basic medical and biological mechanisms, the heart is both a mechanical pump and an electrical conductor. This mix of functions require an interdisciplinary approach to address the disease. A combination of mathematics and physics, for instance, ‘computer modelling’ is complement approach to the experimental biology and clinical observations can aid the global attempt to understand the complexities that surround the pathology of cardiac diseases.[18]

1.2 Uses of cardiac models

Development of computational models has been fundamental to gaining a better quantitative and qualitative understanding of the structure and functions of healthy and diseased hearts. [19] Over the last 50 years, computational models of cardiac activities have increasingly been utilised to enhance cardiac physiology studies. [20] These

models are considered to form a powerful research tool to understand all aspects of cardiac function and have paved the way for a multi-scale integrative approach through which experiments inform construction and validation of models. Such models can then be applied to examine and test hypotheses, which are currently challenging to examine experimentally.[21] Cardiac-model building is based mainly on numerous observations and data obtained from experimental and clinical studies that are employed first to develop and validate the computational models, while the computational models are performed to examine the experimental hypothesis and to predict a theory. Hence they provide valuable resources and targets for further research.[22]

Noble *et al* [23] developed the first biophysically computational model of cardiac myocytes. This work was based on the pioneering model drawn up by Hodgkin and Huxley.[24] The work of Noble and colleagues has since inspired various experimental- and computational-modelling studies that have been conducted and combined in an iterative manner; numerous observations and resources obtained from the experimental and clinical studies have been employed to develop and validate the computational models. Cardiac models have become more complex. The present generation of cardiac models incorporates biophysical descriptions of detailed multicellular ion-channel currents and formulations of intracellular-calcium dynamics.[14, 25-27] These mathematical models of whole-cell function can be integrated into anatomically comprehensive heart geometries that show intricate microstructure which has been obtained through use of techniques such as diffusion tensor imaging to study behaviour at tissue level.[28-30] These models have informed various cardiac models that have been used in numerous applications such as testing hypotheses from experiments, preclinical drug safety testing, predicting and providing valuable resources and targets for experimental studies, and examination of key mechanisms that underlie the origin and maintenance of arrhythmias in the heart.[22, 31, 32]

Computational models of the cardiac system offer numerous advantages over conventional experimental methods that are employed in biomedical research. The first advantage is that modelling is easy to control: the entire process that is of interest can be monitored. For instance, a researcher can alter conditions quickly through application of a pure single-channel block, fixing a single variable such as intracellular calcium concentration, and the alteration of the size of myocytes or tissue, all of which would be difficult to execute experimentally. Second, modelling is interlinked with data recording, which leads to seamless collection of data for every aspect and process of a study during

modelling. For example, obtaining the gating variables of ion channels in adjacent cells at the tissue level can be executed easily, in contrast with the difficulties of simultaneous recording of two variables during an experimental study.[33] Third, modelling reduces demand on time and resources compared with conventional experiments. Modelling only uses computers, which are becoming more powerful and less costly. Also, simulations of a similar nature can be replicated without external instructions, whereas experiments have numerous practical limitations. Fourth, modelling can be performed without samples, which is a significant advantage over experimental studies, which can be challenged by the limited availability of samples, a concern that is typical among human-related experiments. Additionally, the non-intrusive nature of modelling implies it is not subject to similar ethical demands as cardiac physiology tests involving animals.

However there are disadvantages associated with computational models. Given that the cardiovascular system is structurally and functionally complex and is characterised by a non-linear biological system, computational modelling of this system is an oversimplification, and can only represent part of the heart's complexity. Consequently, cardiac models and their intrinsic assumptions must be subjected to rigorous experiments to design comprehensive models that capture predictive power and mechanistic insights.[20] Moreover, a model's functional capabilities must be characterised adequately to highlight the scope of its applicability.[34] Therefore, cardiac models are instrumental, especially when integrated closely with experimental and clinical results.[35] Despite these drawbacks, computational modelling makes a valuable contribution to the current multidisciplinary research efforts to grasp the extent of the heart's complexity.

1.3 Project motivation

The advancement of health-care technology has been shown to extend the average lifespan and lead to a greater improvements in the mean age at death, hence, increasing elderly population.[36] For example, the current number of people aged 65 years and above in the UK is nearly 12 million (11,989,322) people, around 18.2% of the UK population compared with 15.9% in 2007.[5] By 2030 the number of people aged 65 years and over is projected to grow to one in five people and become 21.8% of the UK population.[5] Fifty years later, it is anticipated there will be an additional 8.6 million people of age 65 years and above, a further population roughly equivalent to the size of London.[5]

Ageing itself is not a disease. However, it represents a life-long process of accumulation of damage and pathology, which means that ageing is a leading predisposing factor for cardiac disease. The emergence of cardiovascular disease changes the cardiac function. [37,38] It particularly affects age-related susceptibility to irregular heartbeats, or an arrhythmia, which is likened to a change in functionality of the heart. For example, sinus nodes dysfunction (SND) or sick sinus syndrome (SSS) is a prevalent cardiac arrhythmia that is associated with ageing sinoatrial nodes (SAN), the heart's primary pacemaker. SND has been shown to be a major precursor of sinus arrest, sinus bradycardia, SAN exit block, slow SAN-atrium conduction, or alternating periods of bradycardia and tachyarrhythmia. It has also been linked with atrial fibrillation (AF), heart failure, and sudden cardiac death (SCD). Therefore, the existence of SND informs the implantation of an artificial pacemaker. In the UK, this condition accounts for 27% of all pacemaker implants (40,000 artificial pacemaker implantations every year).[38] SSS prevalence occurs across all ages, but old age is a major predisposing factor.[36] Some studies have associated SND with cell senescence and fibrosis. However, recent electrical modelling studies have suggested that noteworthy electrical changes in the function and expression of ion channels and other cellular elements may result in slowing down of heart rate during age development.[38-40] Significant age-related differences have been observed in characteristics and morphology of action potentials (AP) between neonatal, adult, and elderly SAN cells. These may resulted from differences in ion-channel interactions between them. Nevertheless, matters that underlie the pathogenesis of ageing are not clear and need to be understood fully. In order to investigate these alterations during ageing, the electrophysiology of a healthy mature heart may need to be investigated first. Observed differences can have important implications for the diagnosis and treatment of cardiac rhythm disorders in the immature, adult, and aged individual.

The current study aims to investigate the role of age-associated alterations of ion-channels and calcium (Ca^{2+}) handling proteins on the pacemaking activity of the SAN. This will provide new insights in the field of cardiovascular ageing. This investigation is addressed through use of biophysically-detailed computational models of SAN cells for different animal models. The main purpose of using different species of animals for the SAN models employed in this thesis is to validate the results from the models based on the experimental measurements. In addition, the following goals are determined in different chapters of the thesis:

I. To determine the mechanisms that underlie the slowing of pacemaking APs and heart rate with age development in two different periods of age. This is described in detail in the following section;

II. To develop a novel 1D biophysically mathematical model of a rat SAN-atrium that can be used to simulate the electrical activity of rat SAN in healthy and diseased conditions;

III. To examine whether changes in the abundance of hyperpolarisation-activated cyclic nucleotide-gated channels (HCN) are responsible for recorded changes in beating rates. This is informed by the fact that 'biopacemaking' uses gene therapy to overexpress pacemaking activity through manipulation of gene expression. This strategy offers a potential for the restoration of pacemaking function in SSS without use of electronic pacemakers.

1.4 Thesis organisation

This section provides a detailed description of the chapters in this thesis that follow this introductory **Chapter One**.

Chapter Two discusses the theoretical background of the structures and functions of the heart and cardiac-cells, and the electrophysiology of a cell membrane, including the ion-channel movement at single-cell level to the resultant APs. A literature review of published studies of SAN modelling of cardiac pacemaker cells is included. The chapter also highlights some heart diseases that are associated with the dysfunction of the SAN.

Chapter Three contains a discussion of physical laws and principles that relate to biophysically detailed mathematical models involved in simulating the cardiac cells and tissues.

Chapter Four explains the development of a new computational single-cell model of neonatal rabbit SAN cells based on available experimental data obtained from neonatal SA node cells [40,41] A multi-cellular, two-dimensional model of the intact SAN-atrium [32] is updated to address the functional impact of remodelled ion channels during maturation at the tissue level on pacemaking electrical activities and their conduction. Further investigation of the effect of a neurotransmitter, acetylcholine, on the pacemaking activities in neonatal cells as compared with those in the adult. The newly developed model of neonate rabbit SAN reproduced in both single cells and at tissue

level are validated by comparison of the simulated results with the experimental observations on the behaviour of the heartbeat in neonatal rabbit.

In **Chapter Five**, the mathematical model of electrical AP of rat sinoatrial myocytes [42] is used to determine whether age-induced changes identified in ion-channel currents are sufficient to account for the observed age-induced sinus bradycardia that is represented by the reduction in heart rate (HR) observed in rats. The simulation study investigates the role of age-related remodelling, in particular of ion-channel currents, in the spontaneous activity of the SA node, and how various changes have a direct influence on the waveform of APs and pacemaking activities. These include the cycle length (CL), action potential duration (APD_{50}), peak amplitude (PA), maximal upstroke velocity (dV/dt_{max}) and maximal diastolic potential (MDP).

Chapter Six describes the development of one dimentional mode of SAN-atrium tissue, this was done through updating of the model that was described in Chapter Five with taking into account the investigation of the propagation of the AP at the tissue level

. To this end, the regional variations of the rat SA node are considered on the basis of available ratio data from Zhang *et al.* [40] Additionally, a 1D model of the rat heart is developed, with a particular focus on structural heterogeneity. The individual cellular models used to build the 1D model in this chapter are: central and peripheral SAN; and an atrial model which was developed by Majumder *et al.* [16] Simulations are carried out to investigate the behaviour of the AP propagation and activation and conduction sequence and timing. The new model is used to investigate a case study of the effect of structural remodelling of the ionic-channel current in STZ-diabetic rat SAN.

In Chapter Seven, the presented work in this chapter was published in *J Physiol (2018),*[43] this paper mainly relies on an experimental study about describing the use of bradycardic rat subsidiary atrial pacemaker tissue (SAP) to evaluate the effect of alternative gene targets on pacemaking rate and heart-rate stability as well as the restoration of isoprenaline response. These targets included the Na^+/Ca^{2+} exchanger NCX1, and the transcription factors TBX3 and TBX18 known to be involved in SAN embryonic development. The experimental studies *In vitro* have been done by M.C. and G.M.M.; the qPCR measurements were obtained by A.D., H.D., J.Y. and M.C. Moreover, the computer-modelling part of this paper was based on incorporating three different isoform-specific HCN channel electrophysiology into mouse SAN by W. R, I used this mouse SAN model to simulate the effect of the changes in HCN abundance

that measured in mRNA on the APs and pacemaker rate in SAP condition, and when gene therapy targeting TBX18 is used to restore slow pacemaking in SSS.[43] This work is based on the assumption that the mRNA level is representative of the expression levels of functional channel protein at the cell membrane. The method does not aim to generate definitive biophysically detailed AP models; rather, it offers a form of bioinformatics to investigate the possible impacts of changes in transcript levels.

In **Chapter Eight**, the major findings of the study are discussed, with a view to summarising the unique nature of simulation findings derived in this thesis. Limitations and successes of the study are highlighted, as well as possible future work.

References

1. Martini F, Ober WC. Fundamentals of Anatomy and Physiology. Pearson Benjamin Cummings; 2006. p. 12

2. World Health Organization. World Heart Day. WHO [Internet]. 2018 [cited 2019 Jun 17]; Available from: https://www.who.int/cardiovascular_diseases/world-heart-day/en/

3. Huikuri H. Sudden Death Due to Cardiac Arrhythmias. N Engl J Med [Internet]. 2002 Mar 21 [cited 2019 Jun 18]; 346(12):946–7. Available from: http://www.nejm.org/doi/abs/10.1056/NEJM200203213461218

4. Bhatnagar P, Wickramasinghe K, Wilkins E, Townsend N. Trends in the epidemiology of cardiovascular disease in the UK. Heart,[cited 2019 Jul 27]; Available from: http://dx.doi.org/10.1136/heartjnl-2016-309573

5. Patel V. Deaths registered in England and Wales 2017. Office for national statistics. 2018.

6. Shinagawa Y, Satoh H, Noma A. The sustained inward current and inward rectifier K+ current in pacemaker cells dissociated from rat sinoatrial node. J Physiol [Internet]. 2000;523 Pt 3:593–605. Available from: http://www.pubmedcentral.nih.gov/articlerender.fcgi?artid=2269831&tool=pmcentrez&rendertype=abstract
7. Yan Z, Bai X-C, Yan C, Wu J, Li Z, Xie T, *et al.* Structure of the rabbit ryanodine receptor RyR1 at near-atomic resolution. Nature [Internet]. 2014 [cited 2019 Jul 27];517. Available from: https://www.nature.com/articles/nature14063.pdf

8. Voigt N, Heijman J, Wang Q, Chiang DY, Li N, Karck M, *et al.* Cellular and molecular mechanisms of atrial arrhythmogenesis in patients with paroxysmal atrial fibrillation. Circulation. 2014 Jan 14;129(2):145–56.
9. Csepe TA, Zhao J, Hansen BJ, Li N, Sul L V, Lim P, *et al.* Human sinoatrial

node structure: 3D microanatomy of sinoatrial conduction pathways. Prog Biophys Mol Biol. 2016 ;120(1–3):164–78. Available from: http://www.ncbi.nlm.nih.gov/pubmed/2674320

10. Butters TD. Development of a virtual 3D sheep atria for the study of clinical atrial fibrillation. 2012.

11. Artman M, Ichikawa H, Avkiran M, Coetzee WA. Na+/Ca2+ exchange current density in cardiac myocytes from rabbits and guinea pigs during postnatal development. Am J Physiol [Internet]. 1995 Apr [cited 2018 Feb 21];268(4 Pt 2):H1714-22. Available from: http://www.ncbi.nlm.nih.gov/pubmed/7733375

12. Satoh H. Sino-Atrial Nodal Cells of Mammalian Hearts: Ionic Currents and Gene Expression of Pacemaker Ionic Channels. J Smooth Muscle Res [Internet]. 2003 [cited 2018 Jul 4];39(5):175–93. Available from: https://www.jstage.jst.go.jp/article/jsmr/39/5/39_5_175/_pdf/-char/en

13. Severi S, Fantini M, Charawi LA, Difrancesco D. An updated computational model of rabbit sinoatrial action potential to investigate the mechanisms of heart rate modulation. J Physiol. 2012;59018:4483–99.

Satoh H. Sino-Atrial Nodal Cells of Mammalian Hearts: Ionic Currents and Gene Expression of Pacemaker Ionic Channels. J Smooth Muscle Res [Internet]. 2003 [cited 2018 Jul 4];39(5):175–93. Available from: https://www.jstage.jst.go.jp/article/jsmr/39/5/39_5_175/_pdf/-char/en

14. Majumder R, Jangsangthong W, Feola I, Ypey DL, Pijnappels DA, Panfilov A V. A Mathematical Model of Neonatal Rat Atrial Monolayers with Constitutively Active Acetylcholine-Mediated K + Current. PLoS Comput Biol [Internet]. 2016 [cited 2018 Oct 31];12(6). Available from: https://journals.plos.org/ploscompbiol/article/file?id=10.1371/journal.pcbi.1004946&type=printable

Severi S, Fantini M, Charawi LA, Difrancesco D. An updated computational model of rabbit sinoatrial action potential to investigate the mechanisms of heart rate modulation. J Physiol. 2012;59018:4483–99.

15. Kharche S, Yu J, Lei M, Zhang H. A mathematical model of action potentials of mouse sinoatrial node cells with molecular bases. Am J Physiol Circ Physiol. 2011;301(3):H945–63.

16. Olson TM, Alekseev AE, Liu XK, Park S, Zingman L V, Bienengraeber M, *et al.* Kv1.5 channelopathy due to KCNA5 loss-of-function mutation causes human atrial fibrillation. Hum Mol Genet [Internet]. 2006 [cited 2019 Jul 27];Vol. 15(No. 14). Available from: https://academic.oup.com/hmg/article-abstract/15/14/2185/2355893

17. Makita N, Horie M, Nakamura T, Ai T, Sasaki K, Yokoi H, *et al.* Drug-Induced Long-QT Syndrome Associated With a Subclinical SCN5A Mutation. Circulation. 2002;(106):1269-1274. [cited 2019 Jul 27]; Available from: http://www.circulationaha.org

18. Clayton RH, Bernus O, Cherry EM, Dierckx H, Fenton FH, Mirabella L. Models of cardiac tissue electrophysiology: Progress, challenges and open questions. Prog Biophys Mol Biol [Internet]. 2011 Jan [cited 2019 Jul 27];104(1–3):22–48. Available from: https://linkinghub.elsevier.com/retrieve/pii/S0079610710000362

19. Winslow RL, Trayanova N, Geman D, Miller MI. Computational medicine: translating models to clinical care. Sci Transl Med [Internet]. 2012 Oct 31 [cited 2019 Jun 18];4(158):158rv11. Available from: http://www.ncbi.nlm.nih.gov/pubmed/23115356

20. Clayton RH, Bernus O, Cherry EM, Dierckx H, Fenton FH, Mirabella L, *et al.* Models of cardiac tissue electrophysiology: progress, challenges and open questions. Prog Biophys Mol Biol [Internet]. 2010 [cited 2019 Jun 18]; Available from: http://bioinformatics.bio.uu.nl/pdf/Clayton.pbmb10-0.pdf

21. Clayton RH, Panfilov AV. A guide to modelling cardiac electrical activity in anatomically detailed ventricles. Prog Biophys Mol Biol [Internet]. 2008 [cited 2018 Aug 13];96:19–43. Available from: www.elsevier.com/locate/pbiomolbio

22. Quinn TA, Kohl P. Combining wet and dry research: experience with model development for cardiac mechano-electric structure-function studies. [cited 2019 Jun 18]; Available from: https://www.ncbi.nlm.nih.gov/pmc/articles/PMC3583260/pdf/cvt003.pdf

23. Noble D. A modification of the Hodgkin--Huxley equations applicable to Purkinje fibre action and pace-maker potentials. J Physiol [Internet]. 1962 Feb [cited 2019 May 3];160(2):317–52. Available from: http://www.ncbi.nlm.nih.gov/pubmed/14480151

24. Hodgkin AL, Huxley AF. A quantitative description of membrane current and its application to conduction and excitation in nerve. J Physiol I [Internet]. [cited 2017 Jul 25];7:500–44. Available from: https://www.ncbi.nlm.nih.gov/pmc/articles/PMC1392413/pdf/jphysiol01442-0106.pdf

25. Colman MA, Aslanidi O V, Kharche S, Boyett MR, Garratt C, Hancox JC, *et al.* Pro-arrhythmogenic effects of atrial fibrillation-induced electrical remodelling: insights from the three-dimensional virtual human atria. Authors J Physiol [Internet]. 2013 [cited 2019 Jun 18];591:4249–72. Available from: https://www.ncbi.nlm.nih.gov/pmc/articles/PMC3779115/pdf/tjp0591-4249.pdf

26. Butters TD, Aslanidi O V., Inada S, Boyett MR, Hancox JC, Lei M , *et al.* Mechanistic links between Na+ channel (SCN5A) mutations and impaired cardiac pacemaking in sick sinus syndrome. Circ Res. 2010;107(1):126–37. 27. Grandi E, Pasqualini FS, Bers DM. A novel computational model of the human ventricular action potential and Ca transient. [cited 2019 Jun 18]; Available from: https://www.ncbi.nlm.nih.gov/pmc/articles/PMC2813400/pdf/nihms153606.pdf

27. Li P, Lines GT, Maleckar MM, Tveito A. Mathematical models of cardiac

pacemaking function. Front Phys [Internet]. 2013 Oct 30 [cited 2019 Aug 1];1:20. Available from: http://journal.frontiersin.org/article/10.3389/fphy.2013.00020/abstract

28. Benson AP, Bernus O, Dierckx H, Gilbert SH, Greenwood JP, Holden A V, *et al.* Construction and validation of anisotropic and orthotropic ventricular geometries for quantitative predictive cardiac electrophysiology. Interface Focus [Internet]. 2011 [cited 2019 Jun 18];1:101–16. Available from: https://www.ncbi.nlm.nih.gov/pmc/articles/PMC3262240/pdf/rsfs20100005.pdf

29. Aslanidi O V, Nikolaidou T, Zhao J, Smaill BH, Gilbert SH, Holden AV, *et al.* Application of micro-computed tomography with iodine staining to cardiac imaging, Europe PMC Funders Group. [cited 2019 Jun 18]; Available from: https://www.ncbi.nlm.nih.gov/pmc/articles/PMC3493467/pdf/ukmss-49413.pdf

30. Stephenson RS, Atkinson A, Kottas P, Perde F, Jafarzadeh F, Bateman M, *et al.* High resolution 3-dimensional imaging of the human cardiac conduction system from microanatomy to mathematical modeling. Sci Rep [Internet]. 2017 Dec 3 [cited 2019 Jun 18];7(1):7188. Available from: http://www.nature.com/articles/s41598-017-07694-8

31. Callaghan NI, Hadipour-Lakmehsari S, Lee S-H, Gramolini AO, Simmons CA. Modeling cardiac complexity: advancements in myocardial models and analytical techniques for physiological investigation and therapeutic development *in vitro*. APL Bioeng [Internet]. 2019 Mar [cited 2019 Jun 18];3(1):011501. Available from: http://www.ncbi.nlm.nih.gov/pubmed/31069331

32. Bai X, Wang K, Yuan Y, Li Q, Dobrzynski H, Boyett MR, *et al.* simulation study Mechanism underlying impaired cardiac pacemaking rhythm during ischemia : A simulation study. 2017;093934.

33. Salama G, Hwang S-M. Simultaneous optical mapping of intracellular free calcium and action potentials from Langendorff perfused hearts. Curr Protoc Cytom. 2009 July ; 0 12: Unit–12.17 [cited 2019 Jun 18]; Available from: http://www.dalsa.com/markets/ccd_vs_cmos.asp

34. Cooper J, Mirams GR, Niederer SA. High-throughput functional curation of cellular electrophysiology models. Progress in Biophysics and Molecular Biology. 2011.(107)11-20

35. Aslanidi O V, Colman MA, Stott J, Dobrzynski H, Boyett MR, Holden AV, *et al.* 3D virtual human atria: a computational platform for studying clinical atrial fibrillation Europe PMC Funders Group. Prog Biophys Mol Biol [Internet]. 2011 [cited 2019 Jun 18];107(1):156–68. Available from: https://www.ncbi.nlm.nih.gov/pmc/articles/PMC3211061/pdf/ukmss-37019.pdf

36. National Iinstitute for Cardiovascular Outcomes Research. Cardiac rhythm management (arrhythmia audit) [Internet]. [cited 2019 Jul 27]. Available from: https://www.nicor.org.uk/national-cardiac-audit-programme/cardiac-rhythm-management-arrhythmia-audit/

37. Lakatta EG, Sollott SJ. Perspectives on mammalian cardiovascular aging: humans to molecules. Comp Biochem Physiol Part A Mol Integr Physiol [Internet]. 2002 Aug 1 [cited 2019 Jul 28];132(4):699–721. Available from: https://www.sciencedirect.com/science/article/pii/S1095643302001241?via%3Dihub

38. Choudhury M, Boyett MR, Morris GM. Biology of the Sinus Node and its Disease. Arrhythmia & Electrophysiology Review 2015; 4(1):28–34 [Internet]. [cited 2019 Mar 12]. Available from: www.AERjournal.com

39. Csepe TA, Kalyanasundaram A, Hansen BJ, Zhao J, Fedorov V V, Thomsen MB. Fibrosis: a structural modulator of sinoatrial node physiology and dysfunction. Frontiers in Physiology. 2015.(6);37 [cited 2019 Jul 27]; Available from: www.frontiersin.org

40. Allah EA, Tellez JO, Yanni J, Nelson T, Monfredi O, Boyett MR, *et al.* Changes in the expression of ion channels, connexins and Ca2+-handling proteins in the sino-atrial node during postnatal development. Exp Physiol. 2011;96(4):426–38.

41. Zhang H, Holden A V, Kodama I, Honjo H, Lei M, Varghese T, Boyett AMR. Mathematical models of action potentials in the periphery and center of the rabbit sinoatrial node. Am J Physiol Hear Circ Physiol. 2000;279: H397–H421

42. Tao T, Paterson DJ, Smith NP. A model of cellular cardiac-neural coupling that captures the sympathetic control of sinoatrial node excitability in normotensive and hypertensive rats. Biophys J [Internet]. 2011;101(3):594–602. Available from: http://dx.doi.org/10.1016/j.bpj.2011.05.069

43. Choudhury M, Black N, Alghamdi A, D'Souza A, Wang R, Yanni J, *et al.* The Journal of Physiology TBX18 overexpression enhances pacemaker function in a rat subsidiary atrial pacemaker model of sick sinus syndrome. Authors J Physiol [Internet]. 2018 [cited 2019 Mar 22];596:6141–55. Available from: https://www.ncbi.nlm.nih.gov/pmc/articles/PMC6292813/pdf/TJP-596-6141.pdf

Chapter Two - Physiological Background and Literature

In this chapter the background knowledge that forms the basis of the thesis is introduced. First, the anatomy and function of the heart in the circulatory system is described. The description focuses on the sinoatrial node, its physiological functions, anatomy, and role in the cardiac conduction system. In the second section, cardiac electrical activity is demonstrated. A description is offered of the cardiac action potential. The explanation distinguishes between cell types, and focuses on the pacemaking activity and on the relationship between action potential traits, the heart and the electrocardiogram. Then, a chronological review is offered of development of the mathematical representation of sinoatrial node (SAN) cells. Emphasis is placed on the various model studies and the cardiac disease and arrhythmias related to the SAN.

2.1 The heart and circulatory system

The heart is the first organ to develop during the early stages of pregnancy in animals [1], and it continues beating until death. The main function of this hollow organ is to pump blood around the body.[2] The heart plays a vital role in the circulatory system of the human body, working as a synchronised pump in two different pathological systems through a network of vessels, as shown in Figure 2.1. The first path drives blood around the right side of the heart (the pulmonary circuit), and this leads to the transfer of deoxygenated blood through the pulmonary artery and to the exchange of carbon dioxide gas through the lungs. The second path of the double pump serves the left side of the heart (the systemic circuit), supplying oxygen-rich blood from the heart to other parts of the body. The circulatory system also includes: the arterial structure, which is composed of a network of blood vessels that supply oxygen-rich blood from the heart to the body; and the venous system, which is a complex system of blood vessels and veins that drains blood into the right atrium of the heart. Capillaries are the smallest blood vessels. These form the crucial link between the venous and the arterial systems in the heart's external structure. They are made of very thin walls that enable nutrients and oxygen to be supplied to various surrounding cells.

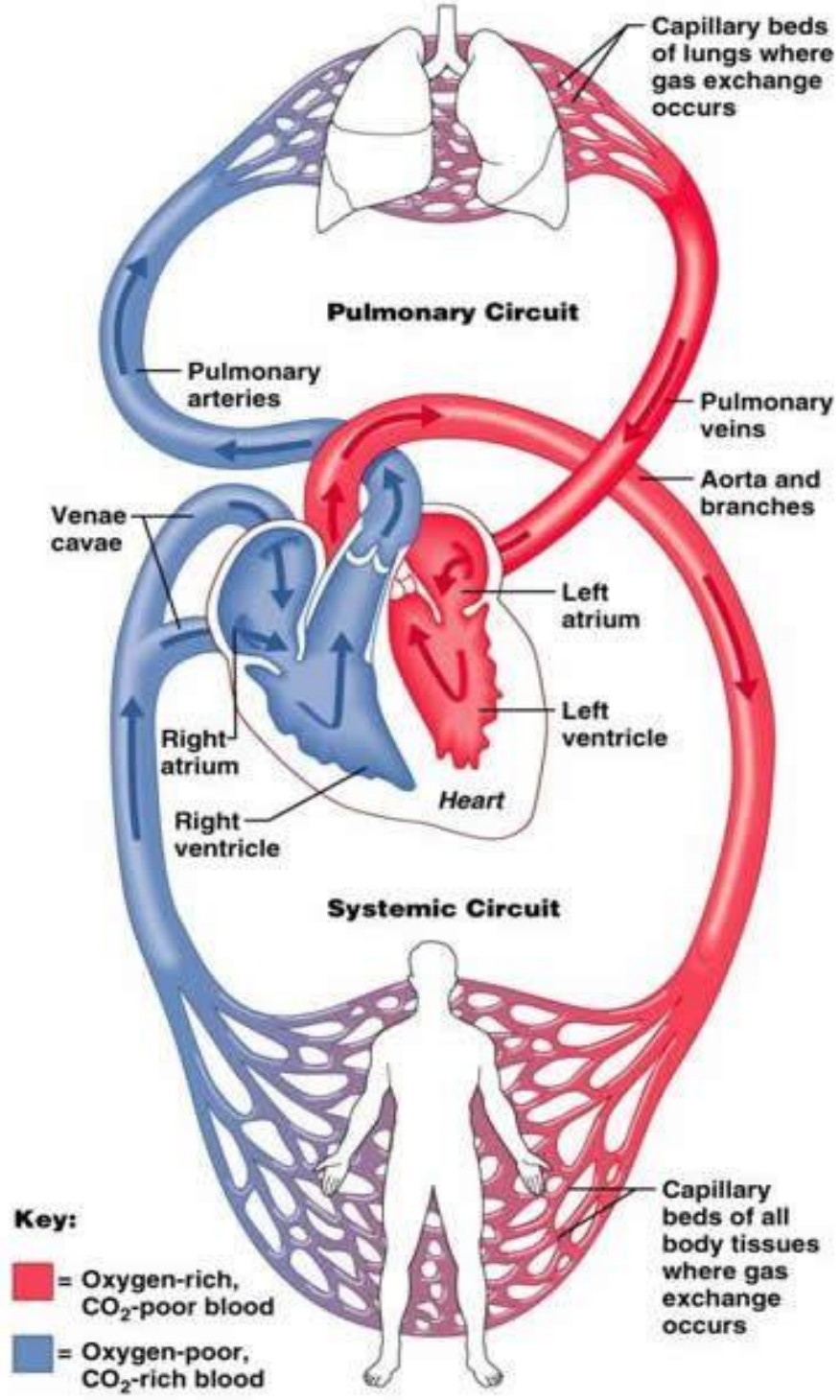

Figure 2.1. A representation of the circulatory system and blood circulation within the human heart. Arrows indicate direction of blood flow. The diagram shows the pulmonary circuit (blue colour), and the systemic circuit (red colour).[3]

2.1.1 The anatomy of the heart

In humans, the heart is located in the centre of the chest, between the lungs, posterior to the sternum and lying to the right side in the body. The heart consists of four chambers, with one upper and one lower chamber on each side. The upper chambers are known as the atria, while the lower chambers are referred to as the ventricles (Figure 2.2)**.** The blood enters the heart via the atrium and is directed into the respective ventricle located on the same side, from where it is pumped out to either the lungs or the body. The two atria are separated by the inter-atrial septum (AS), and the two ventricles are separated by the inter-ventricular septum (IVS). There is a layer of connective tissue that separates the walls of the chambers of the heart, and therefore, provides electrical insulation between them; this connective tissue is formed from substantial amounts of fat. Both atria and ventricles are connected through valves; the tricuspid valve (right), and the mitral valve (left).[4] The right ventricle is also connected to the pulmonary artery, which connects to the lungs through the pulmonary valve; the left ventricle also contains another valve called the aortic valve, which carries the blood from lungs to heart after gas exchange has occurred. These valves contain extensions of the fatty connective tissue and prevent the blood in the ventricles from flowing back into the atria. The function of each heart chamber is determined, in effect, by its size and the thickness of the components. For example, the atria are formed by thin, small walls, which are appropriate for their required function; they pump blood into the ventricles at relatively low pressure. By contrast, the ventricle walls are thick, because greater pressure is required to pump blood into and around the circulatory system.[5] This complex system is responsible for the circulation of the blood, which transports nutrients, oxygen, hormones and metabolic waste from or to cells all over the body, and helps to maintain body temperature and ionic homeostasis, and helps the body to fight disease.

2.1.2 Blood flow through the heart

A schematic representation of the anatomy of the heart is shown in Figure 2.2. The deoxygenated blood is collected from the body within the right atrium via the superior and inferior vena cava (SVC and IVC, respectively); these are the two primary veins that collect blood from all systemic veins. The blood is then pumped into the right ventricle via the tricuspid valve. This is followed by the closure of the tricuspid valve due to the ventricle contraction, which prevents blood from flowing back into the atrium. During contraction of the right ventricle, the pulmonary valve opens to allow blood flow into

the pulmonary artery, which then also shuts to prevent re-entry of the blood into the ventricle. The blood is finally forced into the lungs through the pulmonary system, which enables the gas exchange to and from the blood (carbon dioxide removal and oxygen absorption). From here, the oxygen-rich blood is driven from the lungs through the pulmonary vein into the left atrium, and then into the left ventricle through the mitral valve in the same manner as that which has been explained for the right side. The blood is then pumped into the aorta through the aortic valve. The aorta is considered to be the largest and primary artery of the body; from the left ventricle, it splits into small arteries and capillaries that deliver oxygenated blood throughout the body, after which this entire cycle repeats. It is worth noting that the heart itself is supplied with oxygen-rich blood via capillaries in its walls, as its structure and function prevents direct oxygen absorption from the blood within its chambers. The time during which the heart undergoes contraction is known as the systolic period. Following the systolic period, the heart needs some time to relax and refills with blood to repeat the cycle.[4] This relaxation period is called the diastolic period.

2.1.3 Cell types in the heart

The heart contains different cell types: the endothelial; fibroblast; smooth muscle; cardiac myocytes. Cardiac fibroblasts make up the majority of heart cells, and are responsible for the synthesis of the extracellular matrix and collagen.[6] Smooth-muscle cells are found in the coronary arteries, as well as in the inflow and outflow vasculature. The cardiac myocytes include pacemaker cells (referred to as ‘auto-rhythmic cells’) and the non-pacemaker cells (known as ‘working myocardium’).[6, 7] These various types of cells serve different purposes in support of the structural, biochemical and electrophysiological-mechanical characteristics of the heart.

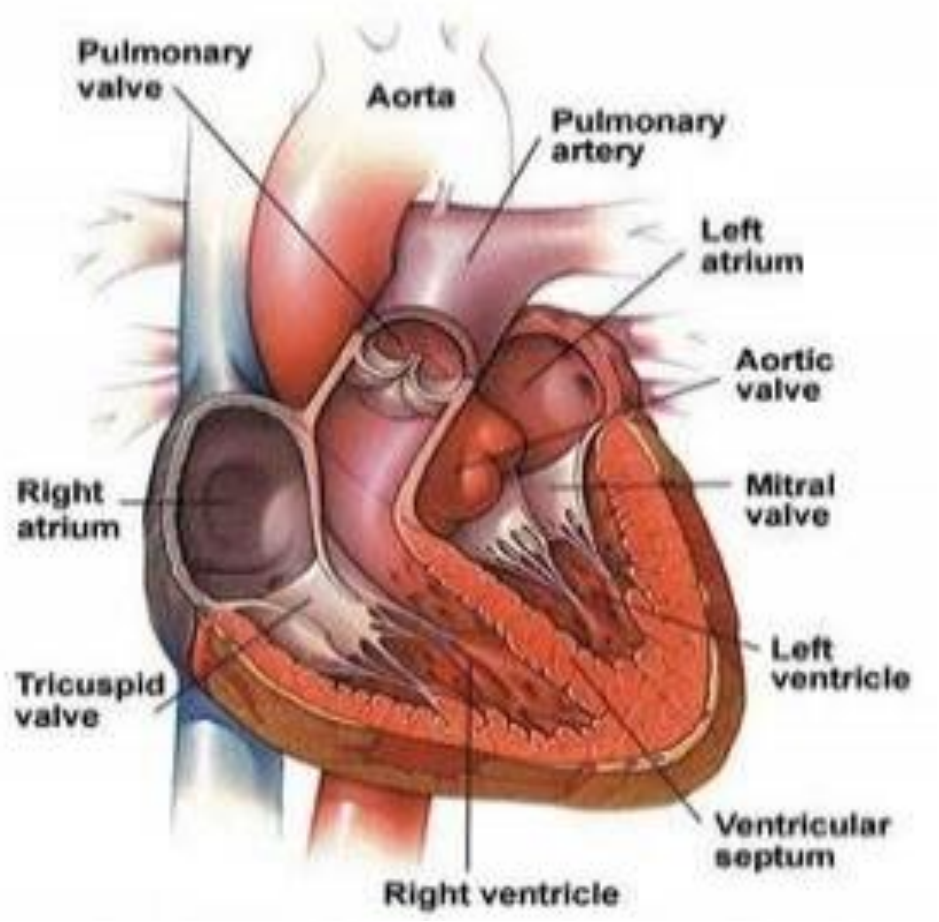

Figure 2.2. Illustration of the anatomical composition of the heart, indicating the structure of the heart and the direction of blood flow within each chamber.[8]

As mentioned, there are two types of cardiac myocytes, which are categorised according to their ability to initiate and generate the AP: auto-rhythmic cells, or 'pacemakers', which include the SAN, atrioventricular node (AVN), and a vast network of fibres that spreads across the ventricles called the Purkinje fibre network (PF), and which spontaneously initiate and conduct 'oscillatory' APs [2]; and contractile cells, which are found in the atrial and ventricular myocardium and can be defined as 'non-pacemaking cells'. These do not initiate their own action potentials but are electrically excited when they receive a stimulus from autorhythmic cells, and thus generate an electrical AP when the membrane potential reaches a certain threshold value. They then propagate electrical waves and produce contractions. Cardiac myocytes in the atria and ventricles are the main constituent of the muscular walls of the myocardium, each of which has a contractile capability similar to that of the skeletal muscle and contribute to the contraction of the heart. The size and shape of cardiac myocytes vary according to the region of the heart under consideration; they are typically ~ 100μm in length with a

radius of 15–20μm, and can be described as essentially cylindrical in shape.[9, 10] Adjacent cells connect with each other both electrically and mechanically. Finally, the pacemaker cells are specialised cardiomyocytes that are excitable and capable of spontaneous generation of electrical excitation impulses. They constitute the cardiac conduction system (CCS), in which these cells are less contractile than those of the working atrial and ventricular myocardium,[9] because they are designed for the rapid conduction of electrical impulses rather than the contraction of the heart. These cells are typically smaller than cells of the working myocardium. For example, central cells of the human and dog SAN cells are approximately 25–30μm in length and 5-10μm in diameter.[10] These small primary pacemaker cells are responsible for the initiation and regulation of cardiac rhythm.[11] All pacemaker tissues exhibit certain cellular characteristics that distinguish them from non-pacemaking cardiac myocytes. For instance, pacemaking cells are lack of T-tubular system [12] and various ion channels of pacemaking cells share similar tissue-specific expression levels.[13] Therefore, it is possible that they share similar basic pacemaking mechanisms.[13] The electrical-excitation wave path that starts from SAN and spreads through the CCS is introduced in the following section.

2.1.4 The cardiac conduction system (CCS)

Two centuries ago, Galvani and Volta demonstrated the relationship between spontaneous heart contractions and electrical phenomena.[14] These events result in normal cardiac contraction, and any slight change in these activities may lead to severe cardiac rhythm disorders. The central nervous system controls several activities of the heart, such as frequency of contractions and contraction force, but the heart's primary functionalities do not rely on its intervention. A denervated and transplanted heart can function optimally and adapt itself to new circumstances through independent initiation of heart beats and their rhythmicity. This ability has been attributed to some intrinsic features of cardiac tissue such as its automaticity.[14] The electrical signal coordinates the heart's mechanical activity through a network of special myocytes known as the cardiac conduction system (CCS).

The CCS comprises: the SAN, Bachmann's bundle, the AVN, the bundle of His or the atrioventricular bundle, the left and right bundle branches, and the Purkinje fibre network (PF).[15] The main function of the CCS is to initiate and propagate electrical excitation throughout the rest of the heart and consequently coordinate heart contraction,

which enables the heart to drive the circulatory system.[16] The timing and strength of the contraction in the CCS is affected by abnormal conditions such as genetic mutations, ischaemia, heart failure and hypertension, and this affects the pacemaking activities of the entire cardiac output.[17]

Figure 2.3 shows the pathway taken by electrical excitation waves that propagate in the heart. The SAN's cells are autonomous oscillators that comprise a group of specialised pacemaker cells that are located at the top of the right atrium, near to the junction with the superior vena cava. Under normal conditions, the SAN generates spontaneous electrical impulses, which travel from cell to cell through the pacemaker net via gap junctions and conduction fibres – a process that takes about 40ms – to the atrial cardiac cells, where they stimulate the atria to contract. The propagation of the electrical impulses from the right atrium to the left atrium is primarily through a fast conduction pathway known as the 'Bachman bundle', which leads from the crista terminalis. This pathway enables almost synchronous contraction of the right and left atria, even though cardiac electrical activity starts in the right atrium. Then, the excitatory wave passes to the AVN, a specialised conducting tissue that is located at the junction between the atria and ventricles, and indeed couples the atrium and ventricle. The AVN functions as a secondary pacemaker for the heart and acts as the main pacemaker when there is a failure of the SAN, or its action is somehow otherwise blocked. Under normal conditions, the conduction of electrical excitation in the AVN is slower than that in the SAN; the electrical impulse takes at least 100ms to reach the AVN. This delay at the AVN is crucial as it enables the atria to move blood into the ventricles before they receive the signal to contract.[18] Then, the electrical wave passes through the bundle of His, which is located at the crest of the interventricular septum and splits into two branches (the right and left bundle branches).[19] Both branches play an important role in achievement of a synchronous activation of both the left and right ventricles.[20] This is followed by movement of the excitation impulses from the two branches of the bundle of His to the network of fibres called the 'Purkinje fibres,' which spread through tree-like branching into the right and left bundle branches across the interior of the ventricles, ending on the ventricles' endocardial surfaces. At this point the action potentials activate the ventricular muscles and spread outward through the ventricular walls to the epicardial surfaces. The time required for the excitation wave to travel through the ventricles is 30ms, which enables both ventricles to contract at the same time and the blood to be injected into both the pulmonary and systemic circulatory pathways.

To summarise the CCS pathway, the electrical excitation wave of the heart is fired from the SAN, and then rapidly spreads along the crista terminalis (CT) to the right atrium. Then, the Bachmann's bundle stimulates contraction of the left atrium. Excitation impulses are generated within the slow pathways of the AVN, through which the electrical signals then pass, via the His-Purkinje system, to the ventricles. The sophisticated nature of the CCS helps the four chambers of the heart to contract regularly with a predefined temporal sequence.[19] The electrical impulse of cardiac myocytes within the CCS is conducted spontainouly. However, they have the ability to serve as subsidiary pacemakers, for instance if the SAN fails to generate spontaneous rhythmic APs, and they can act as functional pacemakers though with slower pacemaking rates than the usual system.[21] The electrical excitation rates of APs in different types of human cardiac network components is summarised in Table 2.1.

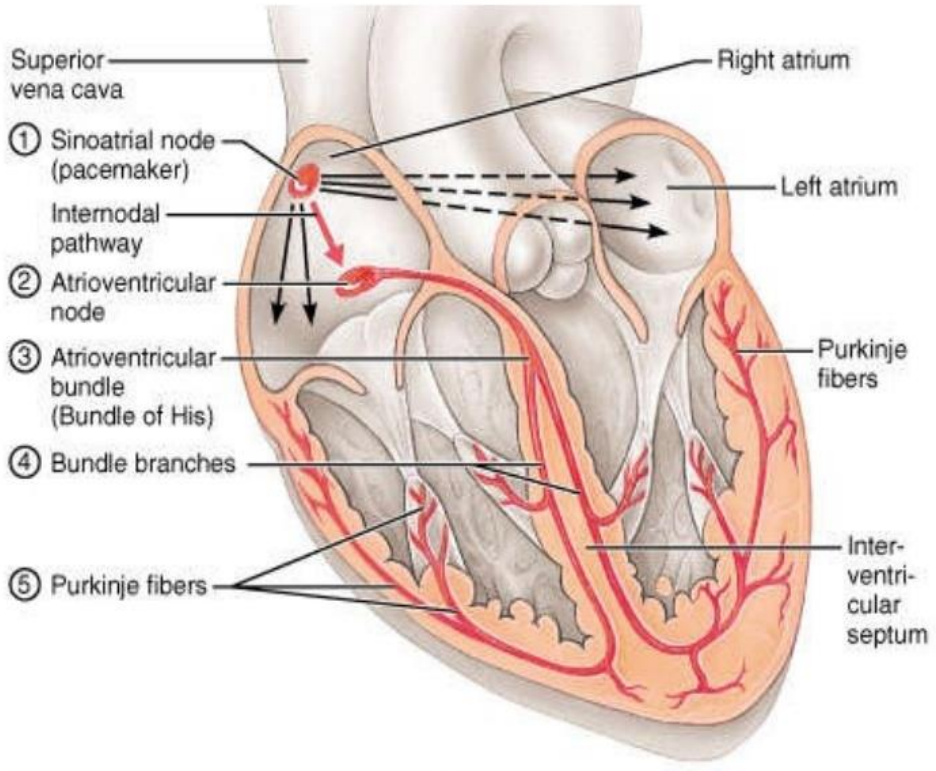

Figure 2.3. The conduction pathway for electrical signals along the pacemaking cells.[22]

Table 2.1. Average rates of human action potentials in autorhythmic tissues of the cardiac system.[23] The SAN is the heart's engine, and drives the heart rate at approximately 70-80 beats per minute (bpm). If the SAN were to break down, the AVN would drive the heart rate at 40-60bpm, and if the latter were to stop functioning, the Purkinje fibres would take over driving ventricular tissues at around 30bpm.

Tissue type	Pacemaking rate (bpm)
SAN	70-80
AVN	40-60
Purkinje fibres	20-40
Total heart rate (in humans)	60-100

2.1.5 Detailed anatomy and function of the sinoatrial node

As described earlier, the SAN, which is found in the right atrium, serves as the primary site for the formation of a normal heartbeat (sinus rhythm). Flack and Keith discovered more than a century ago the presence of SAN tissue. This is now known to be a vast, heterogeneous complex adjacent to the crista terminalis. SAN tissue is bounded by the superior and inferior venae cava in the vertical direction, and by the interatrial septum and the crista terminal node (a thick bundle of atrial muscle) in the horizontal direction (Figure 2.4). It is characterised by distinct regions defined by unique electrophysiological and structural attributes.[10] The main body of this tissue is crescent-shaped, as shown in Figure 2.4A. It is partitioned into two sections; the larger part is in the upper section of the right atrium and named 'head', and the thinner, smaller part is positioned in the inferior right section and extends below the head and known as a'tail'.[24] In large animals, such as humans, the node is functionally isolated with the exception of exit pathways, which facilitate communication between the SAN and atrial tissue. The insulation is guaranteed by a connective tissue, which protects the pacemaker's automaticity in SAN against the suppersive effect that can resulted from electrical interaction between the SAN cells and the atrial myocardium.[25]

Pacemaker cells in the sinus node region vary by size and electrophysiological properties. They can be categorised into three different groups: (1) elongated-spindle-shaped cells, which are composed of a slightly striated cell body with one or more nuclei and are of length up to 80μm[15]; (2) spindle cells, which are predominantly mono nucleated, of a similar shape to the elongated-spindle cells, but shorter in length (up to

40µm); and (3) spider cells, which are irregularly shaped with blunt ends. The distribution of cell types is not clearly understood, but experiments have demonstrated that none of the three cell types are located exclusively in a specific SAN area. In the case of the rabbit SAN, a uniform distribution of all three pacemaker-cell types has been noted in the central area. Figure 2.4B illustrates a schematic representation of the three cell types. Additionally, an illustration of an atrial cell is represented. The crista terminalis region is composed of atrial cells alongside spindle cells. The septal region of the SAN is composed of atrial cells and a nearly uniform number of the other three cell types combined between them.[24]

The SAN tissue is anatomically and functionally inhomogeneous.[25] The central region of the SAN is composed of a relatively small number of cells that are poorly organised and this area is surrounded by a large amount of hyperpolarised atrial muscle [26], whilst the peripheral region of the SAN is characterised by larger cells with a well-organised structure of the constituent myofilaments.[27]

Within the SAN tissue itself, there are several electrophysiological differences between the SAN cells at the centre and those at its periphery. The APs of the central SAN are longer and exhibit a lower upstroke velocity than the length and upstroke velocities of the peripheral APs. Additionally, the arrangement and morphology of cells changes gradually from centre to periphery.[28, 29] Another key feature of distinct differences between each of these regions of the SAN, the cells can differ by cell capacitance, which is lower in the central cells than in the peripheral cells. Conduction velocities of the centre and periphery tissue also differ considerably. For example, in mice the conduction velocity of the central SAN is around 4cm/s, but has been found to be about 49cm/s in the periphery. These features may help gradually to match SAN activity with the right atrium and promote an antegrade direction of conduction.[10] The first site of activation is called ‘the leading pacemaker site’, which is responsible for initiation of the action potential. This leading pacemaker site is normally referred to as the central area of the SAN. [28] The AP propagates from this region through the peripheral area of the SAN, then to the atrial muscle that is around the crista terminalis.[30] While the principal function of the peripheral cells of the SAN is to forward the AP from the centre (leading pacemaker site) to the atrial cells, the periphery can present some pacemaker activity.[31, 32]

Heart rate changes can therefore be mediated by a shift in the leading pacemaker rather than by a single pacemaker site. For instance, the leading pacemaker site can shift from the central position toward the SAN periphery during sympathetic stimulation, and thus increase the heart rate. This modification may also lead to bradycardia in the SAN through a caudal shift in the primary pacemaker.[30]

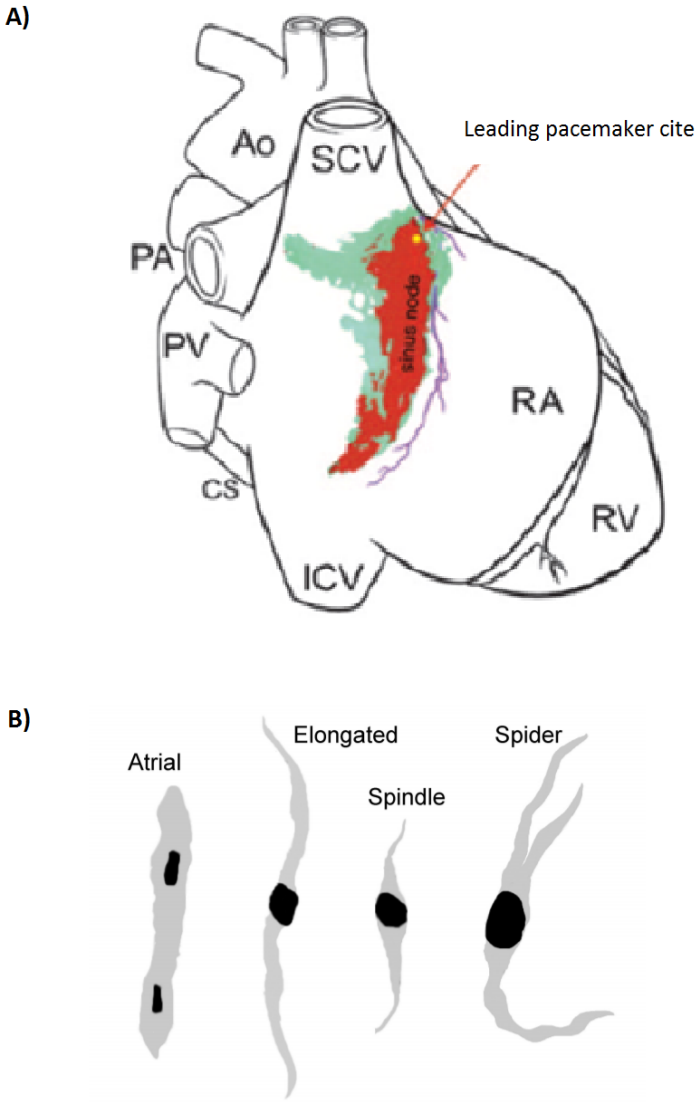

Figure 2.4: (A) A schematic diagram that illustrates the SAN location and the range of central (red) and peripheral (green) sinus node tissue.[31] (B) Graphic illustration of cells located in the SAN region. Left to right: atrial cells; large elongated spindle-shaped cells; spindle cells, which resemble the elongated spindle-shaped cells but with short length; and irregular spider-shaped cells.[24]

2.2 Electrophysiology of cardiac cells

2.2.1 The structures of cell membranes and the membrane potential

The microscopic structure of the electrically active components of a mammalian heart needs to be understood in order to understand the sequence of macroscopic details of cardiac electrical excitation. The cell membrane, or sarcolemma, is formed from a thin phospholipid with a bilayer structure that consists of different proteins with a hydrophilic head and tail and separate intracellular and extracellular spaces (Figure 2.5).[9] The lipid bilayer structure of cell membranes plays a crucial role in controlling the movement of different polar solutes, such as proteins, nucleic acids, and amino acids, through their transmembrane. The difference in charge between the intracellular and extracellular spaces results in a variation of charge around the membrane potential. This difference is defined as the transmembrane potential (V_m), which is determined by the net flow between the internal and external potentials:

$$V_m = u_i - u_e$$

where u_i is the intracellular potential and u_e is the extracellular potential.

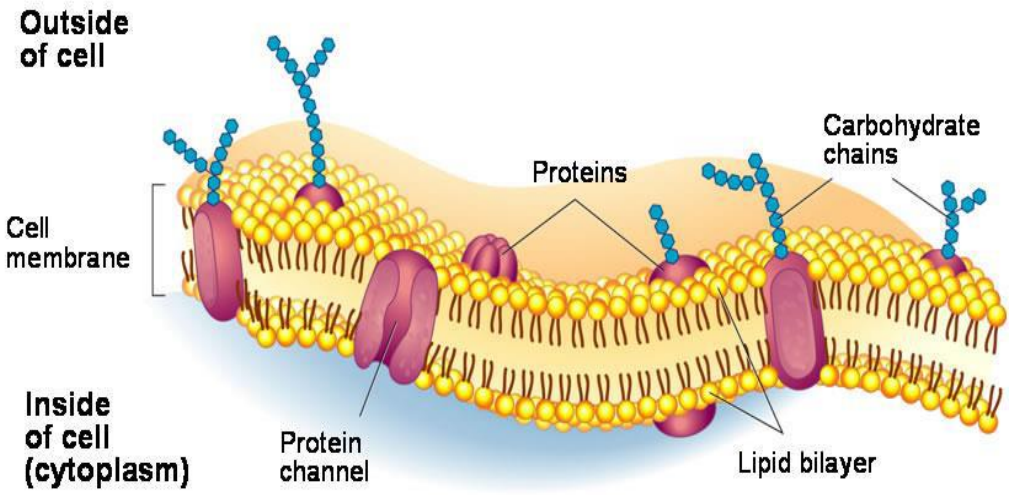

Figure 2.5. Schematic diagram illustrating the fundamental structure of cell membranes, which consist of a lipid bilayer with a width of 4-10nm.

The embedded protein molecular structures, which lie across the cell membrane, form the ionic gated channels, ion pumps and ion exchangers.[18] They are composed of tunnels with gates that regulate the flow of ions across the membrane of the cardiac cells.

Complex interactions of ionic mechanisms with the fluids in the extracellular and intracellular spaces produce the action potentials of auto-rhythmic cells, which spread across the heart and produce heart contractions. Ion channels are either voltage-gated response dependent, which means they change in response to changes in membrane potential, or ligand-gated dependent, whereby they change in response to the binding of chemical messengers such as cyclic adenosine monophosphate (cAMP).

The basic properties of ion-channel gates are selectivity and permeability. They enable certain ions to flow through the channels and distribute heterogeneously across the cell membrane, e.g., sodium (Na^+), potassium (K^+), and calcium (Ca^{2+}) ions, and to a lesser extent chloride (Cl^-) ions, along their concentration gradients through a sequence of open, closed or inactive gates regardless of the type of ion channel.[33] This process creates differences in membrane potentials, commonly referred to as action potentials (APs).[18] The idealised diagram (Figure 2.6) represents an example of the movement of sodium ions through a voltage-gated Na^+ channel through three states. The first state (Figure 2.6A) represents the resting membrane potential when the channel is closed; the second configuration (Figure 2.6B) shows the open state (activation) of the sodium channel and an influx of Na^+ ions follows during electrical excitation. After channel activation, which causes the upstroke of the action potential, the ion channel configuration changes to its third state, in which the channel no longer responds to electrical stimuli, the gate becomes inactive and no longer responds to electrical excitation (Figure 2.6C).

Voltage-gated ion channels are characterised in relation to the cardiac AP as passive transport. In contrast, ion pumps are representative of active transport, in which energy is required in the form of adenosine triphosphate(ATP) to transfer ions against the electrochemical gradient regardless of the intra- and extracellular concentrations.[34] Ion exchangers are molecular structures that cannot be classified as either active or passive; they are co-transporters, and use the potential energy of single ions flowing into a cell with their electrochemical gradient to move other types of ion out of the cell. Ionic pumps and exchangers play crucial roles to avoid ion accumulation or depletion in the intracellular space, therefore maintaining the cyclic ability of a cell to be excited repeatedly.

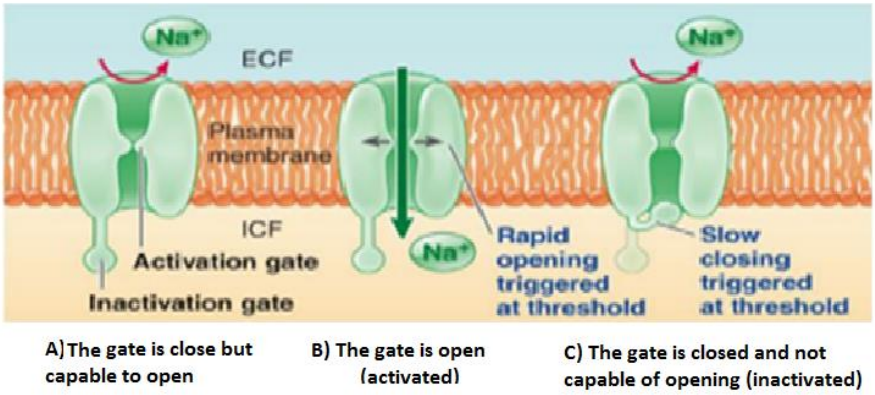

Figure 2.6. An idealised diagram of a voltage-gated Na+ ion channel in which the ion concentration flows across the cell. (A)The state of the ion channel is closed at the resting potential. (B)The channel adopts the open state when electrically stimulated and allows an influx of Na+ ions. (C) The activated state of the ion channel is followed by brief inactivation.[35]

2.2.2 The sarcolemmal ion channel, exchanger and pump in cardiomyocytes

The main ion channels, exchangers and pumps that are involved in AP initiation of cardiac myocytes are the sodium (Na^+), calcium (Ca^{2+}), and potassium channels (K^+). An influx of positive ions from the extracellular surface into the cell membrane, such as Na^+ and Ca^{2+}, acts to raise the transmembrane potential charge (depolarisation) to more positive values. This is known as an inward current. An efflux of positive ions, such as K^+ ions, from the intracellular to extracellular region, can lower the membrane potential (repolarise) to more negative values and is defined as an outward current. Each type of these ion channels exhibits common properties and kinetics, and carries an associated current. The membrane contains many types of ionic-gated channels, ionic pumps and ionic exchangers that regulate the flow of ions across the membrane of the cardiac cells. Therefore, it is clear that the complex interactions of various ionic mechanisms produce the action potential of cardiac cells. The structure of ion channels is defined by gene sequences that are formed of complex proteins with unique folded sequences of amino acids. Particular ion-channel proteins can be present in different isoforms that are responsible for the same current.[36] For example, the hyperpolarisation-activated cyclic nucleotide–gated (HCN) channels are defined by four genes (HCN1, HCN2, HCN3, and HCN4), which are widely expressed throughout the heart and nervous

system. Additionally, there is a link between messenger ribonucleic acids, (mRNA) and the coding of the ion channel and, accordingly, mRNA levels can be used to represent the expression of the ion channel. [33] Table 2.2 outlines the primary currents involved in cardiomyocytes.

Table 2.2. A summary of the primary ion-channel currents in SAN cells, their common names and ion permeabilities.

yIon symbol	Name	Permeability	Type
I_{Na}	Fast sodium current	Na^+	Ion channel
I_f	Hyperpolarising activated funny current	Na^+/ K^+	Ion channel
$I_{Ca,L}$	Long-lasting-type calcium current	Ca^{2+}	Ion channel
$I_{Ca,T}$	Transient-type calcium current	Ca^{2+}	Ion channel
I_{to}	Transient potassium current	K^+	Ion channel
I_{Kr}	Rapid rectifying potassium current	K^+	Ion channel
I_{Ks}	Slow rectifying potassium current	K^+	Ion channel
$I_{K,ACh}$	Acetylcholine activated funny current	K^+	Ion channel
I_{Cap}	Calcium pump	Ca^{2+}	Ionic pump
I_{Nak}	Sodium potassium pump	Na^+/ K^+	Ionic pump
I_{NaCa}	Sodium-calcium exchanger current	Na^+/ Ca^{2+}	Ion exchanger

2.2.3 The action potentials of cardiac cells

The AP is defined as a rapid rise and fall in the transmembrane potential of myocytes, which is resulted from current flow through ion channels, exchangers, and pumps.[27] When myocytes are in their excited state, various ions such as Na^+, K^+, Ca^{2+}, and Cl^- can begin to be transported to or from the cell membrane. The APs of cardiac cells show various configurations in different cell types, this variation is attributed to the spatial heterogeneity of channel expression, thus, there are different morphology and electrical characteristics of APs in the different region of the heart.[27] The following model shows the typical AP of ventricular myocyte (non-pacemaking cardiomyocytes).[33] From Figure 2.7, AP has five different phases, can be identified as:

Phase 0: This is known as the upstroke phase or (depolarisation phase). It occurs when an AP is triggered in pacemaker cell or an adjacent cardiomyocyte which stimuluses the potential of the ventricle cell to rise above -90 mV. Fast Na^+ channels start to activate and rapid influx of Na^+ ions transmitted by the rapid sodium current enter the cell, raising the membrane potential even further. The large Na^+ current depolarises the membrane potential to 0mV and momentarily slightly above 0mV. This is referred to as overshoot, during which the AP approaches the reversal potential for Na^+, and the Na^+ current begins to decrease after reaching a peak and eventually inactivates. Another type of ion channel is also activates during Phase 0; this is the long-lasting Ca^{2+} L-type channel, which opens when the membrane potential is higher than -40mV and triggers a tiny but steady influx of Ca^{2+} ions.

Upon completion of depolarisation, the cell starts to repolarise, or revert to its initial resting state. The cell cannot depolarise again until repolarisation has occurred. Phases 1-3 are the repolarisation phases and coincide with the period during which the cell is refractory and cannot respond to a new stimulus.

Phase 1: This phase is characterised by a brief repolarisation of the AP (early repolarisation phase). During this phase, the Na^+ ions are inactivated. The I_{Na} current declines and a swift momentary outward current I_{to} is triggered, which causes a brief efflux of K^+ ions.[37]

Phase 2: Also known as the 'plateau phase' in ventricular myocytes. This represents the longest phase during creation of APs. This phase is characterised by equilibrium between inward and outward currents. Long –lasting Ca^{2+} channels remain open through which there is a small constant inward flow of Ca^{2+} ions through the cell membrane, while different types of K^+ outward currents flow. During this phase, both inward and outward currents are electrically balanced to ensure that the membrane potential is maintained slightly below 0mV throughout the plateau phase.[37]

Phase 3: The rapid repolarisation phase (also known as the late repolarisation phase) of the AP is characterised by the inactivation of I_{CaL} channels and increased activation of rapid delayed rectifier potassium channels I_{Kr} in addition to the inward rectifier potassium current $I_{K1.}$ This results in increased efflux of K^+ currents and leads to a more negative voltage of the AP. Therefore, during this phase the repolarisation serves to restore the membrane potential to its resting value.

Phase 4: The lack of electrical alterations in 'non-pacemaking cells' which characterise this phase is known as resting membrane potential (RMP). This phase is distinguished by a negative potential. The typical resting potential in ventricle cells is -90 mV. Full repolarisation is achieved as the I_{Kr} and I_{Ks} deactivate, which causes the membrane potential to go into a resting mode. Additionally, it has been shown that the resting potential is to a significant extent influenced by I_{K1}, the sodium-calcium exchanger current, I_{NaCa}, and background currents, all of which facilitate the stability of the diastolic membrane potential.[37]

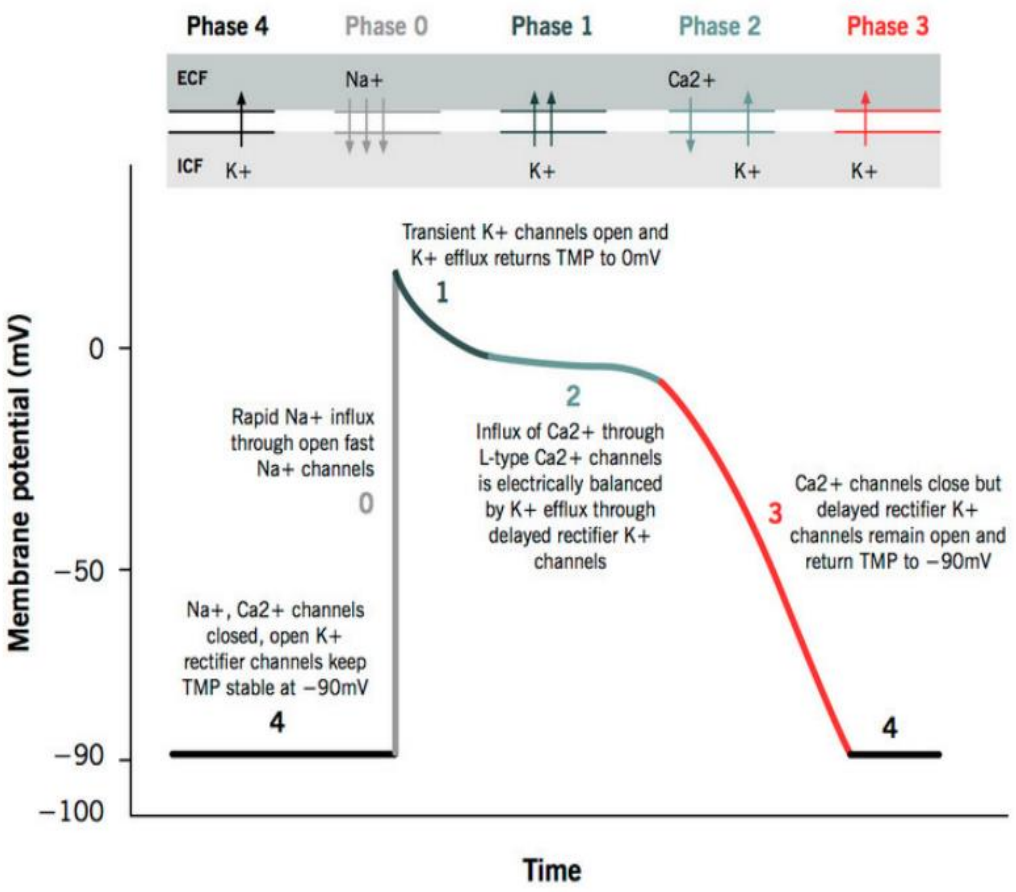

Figure 2.7. A summary of the contribution of ion channels in different phases of the action potential of non-pacemaking ventricular cardiac cells.[33]

2.2.4 The intracellular Ca^{2+} handling

The intracellular Ca^{2+} cycle is responsible for the contraction of cardiac myocytes. Figure 2.8 illustrates the features and basic steps of the calcium cycle inside the cell and more detailed components of the cell including the sarcoplasmic reticulum (SR),

ryanodine receptors (RyR), the L-type Ca^{2+} channel ($I_{Ca,L}$), the intracellular Ca^{2+} transients (Cai), Ca^{2+} pump (I_{NaK}), and the $Na^{+/}Ca^{2+}$ exchanger channels (I_{NaCa}). The SR is a smooth endoplasmic reticulum found in myocytes, with a similar membrane structure to cell membrane. It consists of many Ca^{2+}, exchanger, and pump channels, which work systematically together to store a large quantity of Ca^{2+} ions. The RyR typically located in the SR in close proximity to L-type Ca^{2+} channels. The main function of RyR is to release Ca^{2+} ions from the SR.[38]

During a cardiac AP, L-type Ca^{2+} channels open (activation process) and Ca^{2+} ions enter the cell membrane. Cell membrane depolarisation increases both the Ca^{2+} influx into the cell and the Ca^{2+} concentration around the cell membrane,[38] since the RyR channels depend on the intracellular calcium concentration rather than the membrane potential. This elevation of Ca^{2+} concentration around the cells induces the sarcoplasmic reticulum (SR) to release more Ca^{2+} ions into the intracellular space in a process known as calcium-induced-calcium-release (CICR).The CICR process accompanies the AP and produces changes in the intracellular Ca^{2+} concentration. These altered concentrations are known as the intracellular Ca^{2+} transients (Cai). These Cai bind with myofilament proteins, causing the cell to contract.[39] Ca^{2+} ions are then restored from their binding sites on the contractile proteins by the SR Ca^{2+} -ATPase (SERCA), and pumped back into the SR. Finally, the remaining Ca^{2+} ions within the SR can be extruded out of the cell and restored to the diastolic level through the Na^{+}/Ca^{2+} exchanger (NCX), and the sarcolemmal ATP-dependent Ca^{2+} pump components (I_{CaP}) located in the cell membrane.

As discussed, the movement of ions through the sarcolemmal ion channels during the AP not only changes the membrane potential, but also affects the concentrations of K^{+}, Na^{+}, and Ca^{2+} in the intracellular space. It is known that the contraction of cardiac myocytes is mediated by Ca^{2+} signalling in the cardiac and skeletal muscle myocytes. The regulation of Ca^{2+} ions inside the cell is governed by a series of sub-cellular structures as shown in Figure 2.8. [40,41]

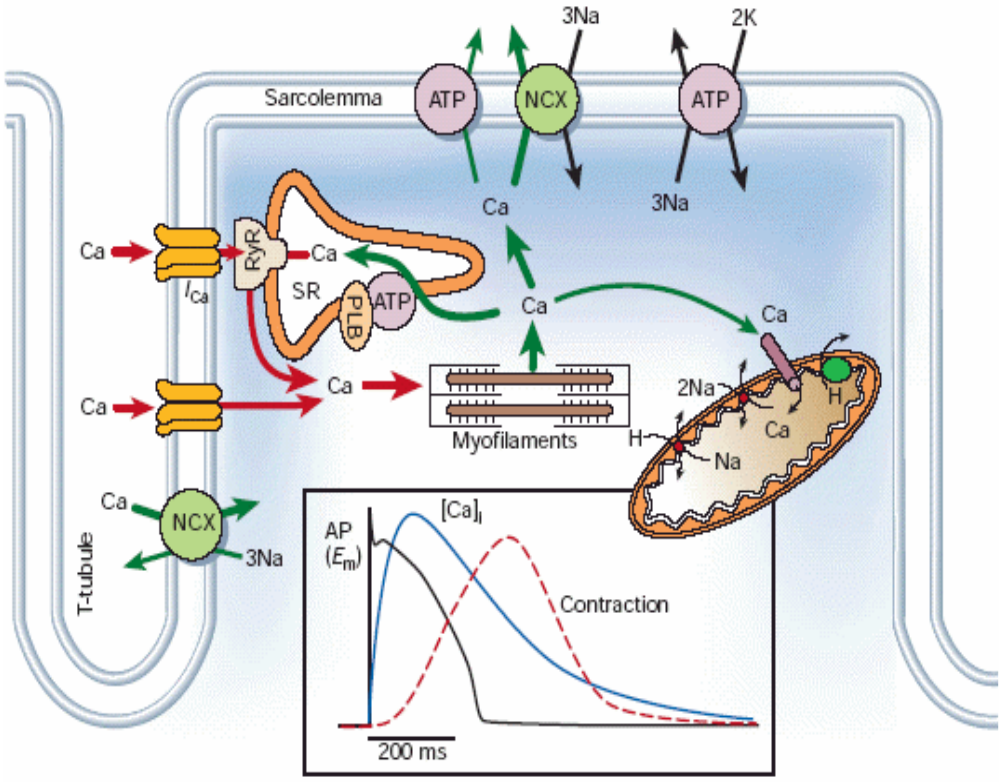

Figure 2.8. Idealised schematic of the intracellular Ca2+ cycle in ventricle cells. A summary of the Ca2+ process can be given as: Ca2+ ions enter the cell membrane during the action potential (AP) as inward Ca2+ current ICaL through calcium channels. This is followed by Ca2+ release from the sarcoplasmic reticulum (SR) through ryanodine receptors (RyR). The Ca2+ ions then bind with the myofilament, which triggers cell contraction. The SR Ca2+-ATPase restores the Ca2+ concentration in the SR, and Ca2+ is extruded from the cell by the ATPase and Na+/Ca2+ exchanger (NCX) located in the cell membrane. The diastolic Ca2+ levels, the Ca2+ transients and contraction associated with the AP are restored. Image taken from[41].

2.2.5 Action potential of the SAN cells

The cells in the SAN generate markedly different AP morphologies to those of the working myocardium. The APs of SAN has a slow diastolic deplarisation phase, the diastolic depolarisation occurs between -60 mV and -40 mV, all these diffrences can be described in four distinct phases:

Phase 0: characterised by a small upstroke velocity compared with the ventricle cells (rapid depolarisation followed by slower repolarisation). [33] The APs of the SAN show

a slow diastolic depolarisation rate due to a gradual depolarisation driven primarily by I_{CaL} and I_{CaT} rather than I_{Na}, which is small (or absent) in nodal cells.[42]

The early repolarisation of the AP (Phase 1 in the working myocardium) is absent in the AP of the SAN due to the absence of the I_{Na}, which means there is no I_{Na} inactivation process that normally produces this phase.

Phases 2 and 3 of the SAN AP follow the same mechanisms as in the working myocardium.

Phase 4 of the AP in the SAN is known as the 'diastolic depolarisation phase', (DD) of the membrane potential, or 'the pacemaker potential'. This phase is derived by the funny current (pacemaker current), I_f,. In addition, Phase 4 of the AP in the SAN is less stable than in Phase 4 of the ventricular AP [43] due to the small presence (or absence) of I_{K1} in nodal cells.

In order to generate the spontaneous AP of the SAN, it is important for cell membranes to depolarise beyond their threshold potential (around -40 mV) during the diastole of Phase4 [44,45]. The rate of propagation in the SAN is slow compared with that of ventricle cells. Figure 2.9 illustrates a comparison of the cardiac action potential in ventricle and SAN. The different pahses of APs in SAN are shown in Figure 2.9.

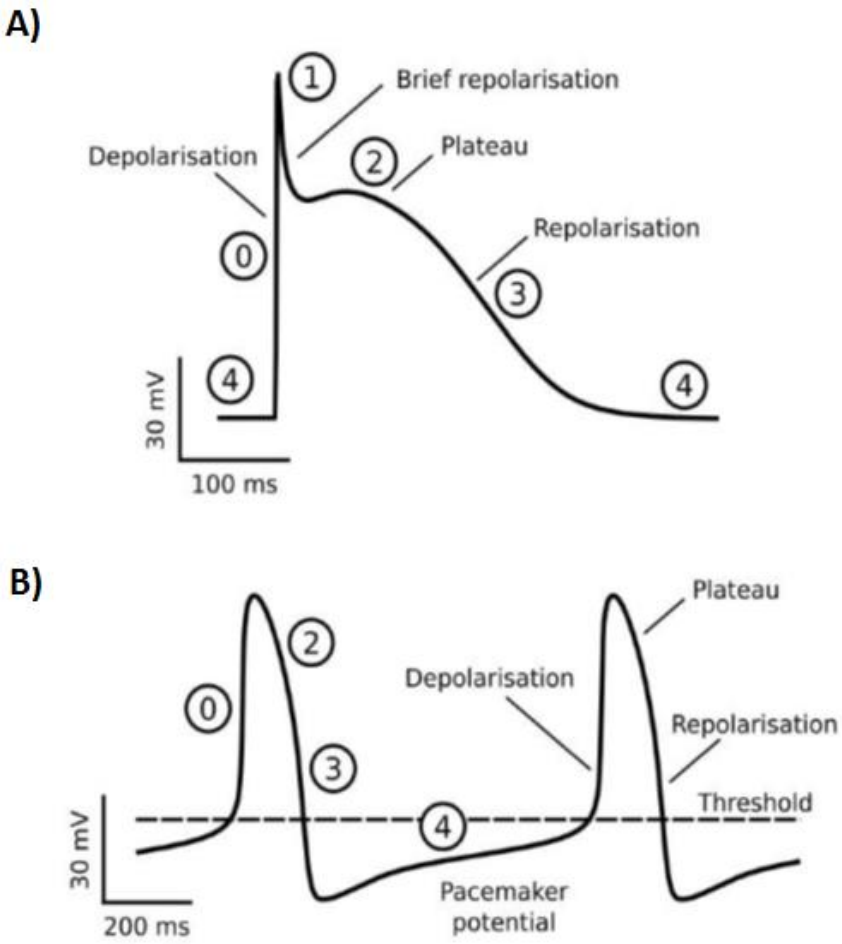

Figure 2.9. schematic diagram illustrating the different phases of the AP in (A) the ventricle and (B) the SAN.[23]

2.2.6 The characteristics of the action potential

There are a number of standard parameters that define AP characteristics, which are used in order to quantify the electrical activity of the AP within cardiac cells, as described below. Quantitative differences in AP characteristics are beneficial to the comparison of the electrical activity of APs between species, regions, and disease states of cardiac cells within a consistent framework, as described below.[36] The measurements of the features are shown in Figure 2.10.

These standard parameters are:

- The maximum diastolic potential (MDP): the most negative point of

transmembrane potential that can be reached at Phase 4 of the action potential of the SAN. This is called the resting membrane potential (RMP) in working myocardium cells (atrial and ventricles). It also refers to the equilibrium potential in cases when there is no net change in membrane potential as a result of ionic currents.

- The maximum upstroke velocity, dV/dt_{max}: this is simply the most positive rate of change of voltage with time during Phase 0 through the evolution of an AP. It is also defined as the maximum rate of change of upstroke velocity (MUV).
- Peak amplitude (PA): also known as overshoot (OS) this is defined as the maximum voltage attained by the membrane potential during the AP time course.
- The cycle length (CL): a measurement of the time interval between two consecutive peak amplitudes in the APs of pacemaker myocytes.
- The action potential amplitude (APA): is equal to the sum of the absolute values of the MDP and PA(OS).
- The action potential duration (APD): refers to the time interval between the MUVs at a specific percentage of total repolarisation of the APs (for example, at 50% (APD_{50}), or at 90% (APD_{90}). APD_{90} is the duration between the MDP and the consequent 90% popularisation of membrane voltage.
- The take-off potential (TOP): this is at an AP slope rate with the line joining the MDP and APO, as shown in Figure 2.10.
- Diastolic depolarisation rate (DDR): this is the rate of membrane potential depolarisation during diastolic phase 4 of the AP. It can be measured by calculating the ratio of y and x of the slope of the line segment between the MDP and the take-off potential as seen in Figure 2.10B.

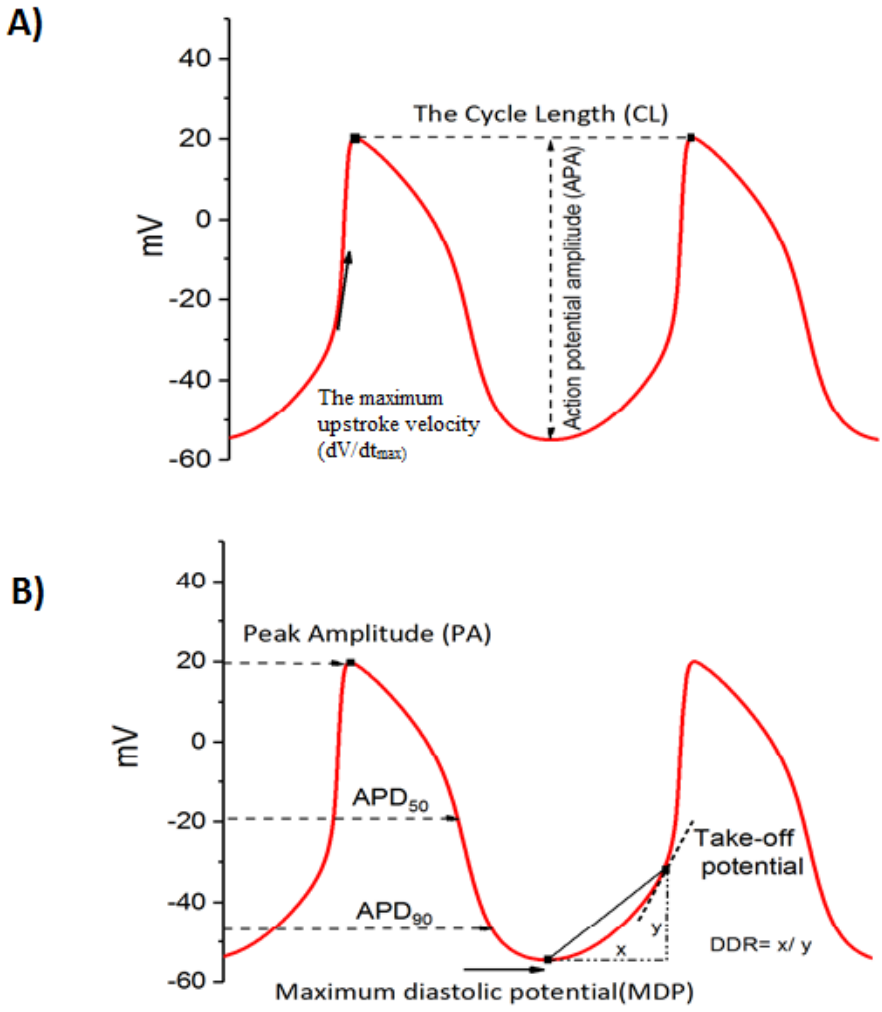

Figure 2.10. The action potential characteristics of pacemaker cells. (A) the action potential amplitude (APA), the cycle length (CL), the maximum upstroke velocity, dV/dt_{max}. (B) The maximum diastolic potential (MDP), peak amplitude (PA), the action potential duration (APD), the take-off potential (TOP), diastolic depolarisation rate (DDR).

2.2.7 The electrocardiogram (ECG)

The electrical changes of the heartbeat can be recorded at the surface of the body, through using the electrocardiography record (ECG), which considered as an extremely important tool in the field of clinical cardiology. Interpretation the waveform in the electrocardiogram (ECG) helps to diagnoses and treats the cardiac electrophysiological disorders and arrhythmias. As illustrated in Figure 2.11, a typical ECG waveform consists of distinct phases, which represent different electrical activities of various regions of the heart:

First, the SAN fires electrical signals that spread from cell to cell throughout the gab junctions to the right atrium and then the left atrium and stimulate them to depolarise. This impulse spreads at high speed (0.8-1.0m/s), and therefore the atrial depolarisation is represented by a P-wave in the ECG. It is notable that no deflections that correspond with activity of the SAN are visible on ECG waveforms.[46]

Second, the P-wave is followed by the PR segment. This corresponds with the time delay of the AVN, which is located in the inferior portion of the atrial septum. It has been noted that there is a 0.1-0.2ms time delay as the signal passes from the SAN to the AVN. This delay provides a chance for the atria to receive a sufficient amount of blood before the signal moves to the ventricles.[47] The atrial repolarisation and both ventricles depolarisation manifest as a QRS complex (the most prominent feature of the ECG), during which the impulse moves fast from the AVN to the bundle of His, then reaches a peak of 5m/s in the Purkinje fibre network. The electrical excitation of the Purkinje network stimulates both ventricles to contract. Finally, the subsequent T-wave deflection refers to the ventricular repolarisation.

When the action potential of the pacemaker cells is not conducted properly through the heart, the cardiac output (ECG) can be affected as contraction strength and timing can be impaired. Consequently, characteristic features of the ECG play a prominent role in the clinical diagnosis of heart disorders and measurements of responses to pharmacological therapies. For example, the recorded ECG shows the PR interval, which corresponds with the time interval between the beginning of the P-wave and the onset of the QRS complex. This therefore indicates the total conduction time within the AVN, which should show a duration of around 120-200ms in a normal human ECG. Any prolongation of this period indicates some form of AVN dysfunction. The total time of occurrence of the QRS complex corresponds with ventricular activation, and should be approximately 60-100ms in duration. Thus, this conduction time and origin can provide information about possible conduction defects/arrhythmia in the heart. The duration of the ST segment [48], which reflects the period between ventricular depolarisation and repolarisation, should be approximately 5-150ms. Thus, analysis of the QRS complex gives information about the intra-ventricular conduction time and the origin of possible conduction defects/arrhythmia. The QT interval represents the complete electrical depolarisation and repolarisation of the ventricles (typically ranging from 360ms to 440ms). Finally, the QT interval, manifested by the period between QRS and the end of the T wave, indicates the complete time required for the depolarisation

and repolarisation of the ventricles. Any recorded prolongation or abbreviation of these intervals, such as long QT or short QT syndromes, may indicate ventricle arrhythmia with a high risk of sudden cardiac death.[49]

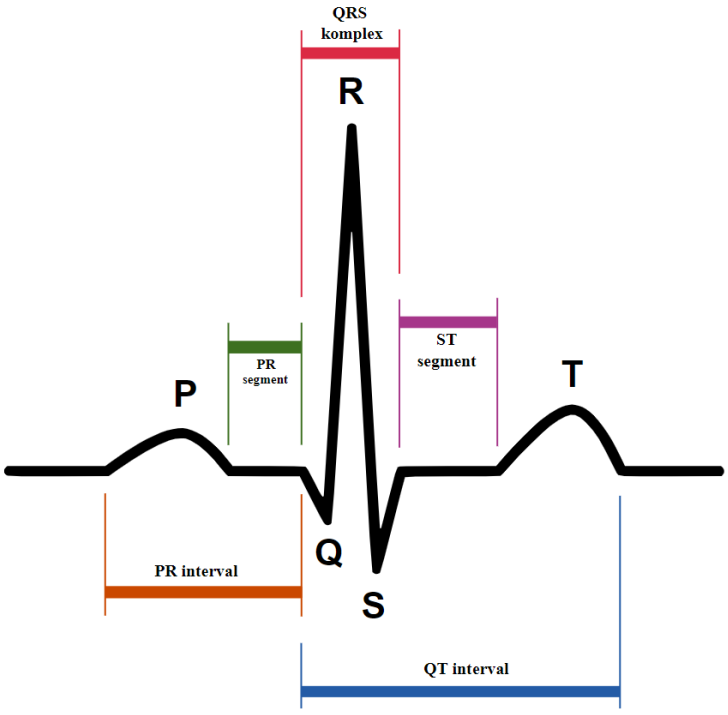

Figure 2.11. Features of a typical human ECG trace. This record represents the conduction system of the heart throughout the electrical excitation waves which are propagated from the pacemaking cells.[29] The PR interval corresponds to conduction through the AVN. The QRS complex represents the duration of ventricular depolarisation. The ST segment shows the isoelectric period between ventricular depolarisation and repolarisation. The QT interval corresponds with the time required for the electrical depolarisation and repolarisation of the ventricles.

2.3 A review of the development of pacemaker cell models

The SAN, a collection of complex pacemaking cells located in the right atrium of the heart, produces electrical waves that spread through the atria and the cardiac conduction system to the ventricles. These waves cause the cardiac muscle to contract to pump the body's blood. In spite of the significant importance of this primary pacemaker, the mechanism has yet to be fully comprehended, and ionic mechanisms that underlie pacemaking are presently the subject of a heated debate. Since the 1960s, several models of cardiac pacemaking cells have been constructed, which are based on various experimental data sets and hypotheses. A recent publication recorded 21 mathematical

models of pacemaking cells that covered nine models for Purkinje cells, 11 for SAN models and one for the AVN cell model.[13,50] All mathematical representations of cardiac cellular electrophysiology are inspired, to some extent, by the electrophysiological study of Huxley and Hodgkin in the giant squid axon [51], which identified the ionic mechanisms that underlie the neuronal action potentials.

Drawing on their findings, the cellular AP can be described as momentary, active alteration in the transmembrane electrical potential (the difference between extracellular and intracellular electrical potentials) of an excitable membrane. This alteration occurs when the membrane is stimulated. This section of the thesis explains the chronological development of mathematical representations of pacemaker cells as summarise in Figure 2.12. State-of-the-art cardiac pacemaker modelling is critically assessed, with a particular focus on prevailing hypotheses, their differences and limitations.

The first cell model to represent cardiac pacemaker cells (Purkinje cell), AP and its atomicity was established by Noble in 1962.[52] Drawing on Hodgkin-Huxley formalism, Noble mapped out a long-lasting depolarisation stage of Purkinje fibre AP with newly known ion channels based on new experimental results. Additionally, the model included a chloride current as a leak current. Noble's work suggested that, with some modifications, the Hodgkin-Huxley formulation could be employed in models of cardiac cells. The drawback of this model is the lack of several key ion currents. For instance, the sodium current, in the Noble model, is the only inward-flowing current mediated by Na^+ ions required for membrane depolarisation. Calcium currents are not included. I_{K1} is considered as an inward rectifier K^+ current that causes the repolarisation of the transmembrane potential to its resting state, and the outward current I_{K2} is represented as a K^+-mediated pacemaker current. It was suggested that, during diastolic depolarisation (DD), the outward I_{K2} steadily declined and the inward sodium current, I_{Na}, was was responsible for spontaneous APs. The membrane would be repolarised following the stimulation of AP through the outward I_{K2} current, and so on. This repeated activity was an oscillator referred to as the 'membrane oscillator' as it referred to the sequences in the transmembrane potential, or it was called simply the M-clock (membrane 'clock').

In 1975, McAllister, Noble and Tsien introduced an updated model of a cardiac Purkinje cell, inspired by newly discovered experimental findings.[53] Their model, which they called the 'MNT model', reformulated the pacemaker current I_{K2}. Until the 1970s, the

I_{K2} 'decay' hypothesis had informed the modelling of cardiac pacemaking mechanisms. It was supported by a range of experimental and theoretical studies, such as findings which suggested that the regulation of I_{K2} could accelerate the pacing rate induced uner sympathetic stimulation.[53]

In 1979, Brown *et al.*[54] discovered a novel current and its role in the generation and acceleration of SAN pacemaking processes. It became known as the 'funny' current (I_f), for several reasons: one, it is a mixed Na^+-K^+ current; second; it activates upon hyperpolarisation, or negative deflection from the resting membrane potential (depolarisation causes most voltage-gated channels to activate); third, it is characterised by very low kinetics. These three unique attributes are appropriate for I_f to play the role of pacemaker current; however, funny current has different attributes from those of I_{K2}. I_{K2} is an outward current and its activation is triggered during depolarisation, whereas I_f is an inward current triggered by activation following hyperpolarisation. Thus, the discovery of the new current I_f in SAN cells prompted a series of experimental and modelling studies with aim to radically reinterpret of I_{K2}.[13] It was established that, while I_{K2} had a reversal potential near the K^+ equilibrium potential, it was, actually, not a pure K^+ current. By applying barium2+ (Ba^{2+}) and K^+ current blockers, I_{K2} could be altered into an inward, hyperpolarisation-activated current with a combination of Na^+ and K^+ permeability, the same as the I_f.[55]

In 1980, a year after the report of I_f in the SAN by Brown *et al.*[54], Yanagihara, Noma and Irisawa developed the first mathematical model for SAN cells, based in rabbit. They called their model the 'YNI' model.[56] It was based on use of the Hodgkin-Huxley model to explore the mechanism of cardiac pacemaker cells. The YNI model has a simple construction, with only a few ion channels, including I_f, I_{Na}, and I_K. The one significant dissimilarity between SAN and Purkinje cells can be seen in the different levels of expression of Na^+ channels. Although I_{Na} is very important and critical for Purkinje cells to sustain a rapid AP upstroke rate and guarantee the strength of electric conduction, I_{Na} is very small in SAN cells, particularly those localised at the SAN centre. The YNI model hypothesised that alterations in K^+ current during DD were quite moderate, and that the primary pacemaking current was I_{Ca} instead of I_f. Yanagihara and colleagues found that I_{Ca} played a critical role in the generation of the pacemaker potential and AP. The I_{Ca} equations in the YNI model were adjusted from Beeler and Reuter's model of ventricular myocytes.[57] I_{Ca} was the largest inward current and was

responsible for the DD and AP upstroke, while I_{Na} and I_f contributions were predicted to be relatively small.

In 1982, Bristow and Clark [58] constructed a SAN model by modifying the (MNT) model of the cardiac Purkinje fibre, with considering the electrical activity of the primary pacemaking preipheral cell of the SAN in the heart. In the same year, Irisawa and Noma [59] updated the Yanagihara *et al.* model by incorporation of a new current, the 'slow inward current' (I_{si}), to the rabbit SAN model. This study was further improved by Noble and Noble in 1984.[60], when the slow inward current (I_{si}) was separated into two components, namely the sodium-calcium exchanger current (I_{NaCa}) and Ca^{2+}-dependent inactivation Ca^{2+} current (I_{Ca}). This mathematical model accounted for the variety of intracellular ion concentrations and introduced the sodium-potassium pump current (I_{NaK}). In 1985, DiFrancesco *et al.*[61] constructed an improved Purkinje cell model (the DN model) based on fresh findings regarding I_f and the new interpretation of I_{K2} as the dominant mechanism behind the M-clock. However, during 1980s the development of SAN models were mostly relied on adaptation of the Purkinje fibre model, using available data from experimental and clinical studies on electrophysiological characteristics within the SAN, under normal and intervention conditions.[62] In 1989, Noble *et al* [63] constructed the first single cell rabbit SAN model.

In 1991, Wilders *et al.*[64] published a new quantitatively model which described the pacemaker activity of a single pacemaker cell isolated from the rabbit sinoatrial node. Model equations employed the most recently available experimental data from voltage clamp experiments on single cells to describe the function of the Ca^{2+} channel in terms of two separate components, I_{CaL} and I_{CaT}. In addition, the model suggested that a small amount of inward background current in addition to the I_f played a role in the slow diastolic depolarisation of the AP during normal pacemaker activity. In 1994, Demir *et al.*[65] demonstrated the possible influence of the sarcolemmal Ca^{2+} pump current and exchanger current and Ca^{2+} buffering in the SAN pacemaker rate. The model equations described by Demir provided an explanation for the electrophysiological activity in the rabbit SAN cell based on voltage-clamp and action potential fitting. At the same time, both Demir *et al.*(1994) [65] and, later, Dokos *et al.*(1996) [66], investigated the role of acetylcholine (ACh) during the pacemaking activities of the rabbit SAN. Moreover, Lei and Brown (1996) [67] found that the delayed rectifier potassium current, I_K devided into two components, based on different kinetics in the rabbit SAN model, namely the rapidly activating I_{Kr}, and slowly activating I_{Ks}.

In 2000, Zhang *et al.*[68] introduced new model of SAN as a complex heterogeneous tissue. The Zhang *et al.* model incorporated two cell types with distinct action potential properties: a central cell, and a peripheral cell, in which 13 ion currents, exchangers, and ionic pumps were computed in each model based on voltage-clamp experiments with respect to regional differences in the central and peripheral SAN with a membrane capacitance of 20 pF in the centre and 65 pF in the periphery. The simulation results were in good agreement with published experimental voltage-clamp data derived from isolated cells in the periphery and centre of the SAN. Moreover, the model accurately mimicked the majority of the effects of ion-channel current blockers on pacemaker activity. This work was farther investigated by Zhang *et al.* (2002) [69] to address the chronotropic effects of acetylcholine on different SAN cells and later, in 2012, to investigate the chronotropic effects of isoprenaline on the rabbit SANs.[70] Later, Kurata *et al.* (2002) [71] introduced the intracellular Ca^{2+} dynamics to the mathematical model for rabbit SAN cells. The model not only considered incorporation of new equations for the I_{st}, voltage- and Ca^{2+}-dependent inactivation of I_{CaL}, but also showed an improvement in the kinetics of certain ion-channel formulations such as I_{Kr}, I_{to}, I_{sus} and I_{NaK}. In 2005, Granny *et al.* [72] modified the Zhang model by transforming the 1D model into 2D and 3D models of SAN and the surrounding atrial cells. Moreover, the role of ionic-current systems in the SAN were investigated in different species. Sarai *et al.* (2003) [73,74] and Mangoni *et al.* (2006)[75] published mathematical models of the principal cardiac pacemakers for mice.

In 2010, Butter *et al.*[76] investigated the link between loss-of-function mutations of the SCN5A gene, which led to a decreased inward current I_{Na}, with sinus node dysfunction. Two groups of SCN5A gene mutations, including the activation and inactivation of I_{Na}, were incorporated into the single-cell model of rabbit SAN developed by Zhang *et al.*[68] to determine mechanisms of the SCN5A mutation impairment of the driving ability of the SAN. The investigation was further extended to produce an anatomically detailed 2D model of the intact healthy SAN atrium. The effects of the SCN5A mutations and vagal nerve activity on cardiac pacemaking at the tissue level were predicted in this study. The simulation results for the 2D-tissue model were validated to the experimental observation of rabbit SAN and surrounding tissue. Their findings also revealed that, in addition to compromising AP conduction across the SAN, the mutations slowed down pacemaking, leading to a possible SAN exit block or sinus arrest.

During the development of cardiac pacemaking models, there was a continuous debate surrounding the cellular basis of cardiac pacemaking in terms of the exact mechanisms that were responsible for the initiation of the spontaneous AP of the SAN pacemaker cells. What initiates the heartbeat remains a controversial discussion: it is unclear whether it is due to cell membrane events, the 'membrane clock' (M clock) or intracellular Ca^{2+} activities, the 'Ca^{2+} clock' (C clock). The theory of the M clock suggests that a set of voltage- and time-dependent transmembrane ionic channels, such as the funny current (I_f), the L-type Ca^{2+} current (I_{CaL}) and the T-type Ca^{2+} current (I_{CaT}), not only generate the spontaneous AP, but also determine when the next AP will occur. This hypothesis is built on a wealth of experimental proofs; the I_f is thought to be the most important ion channel responsible for heart-rate regulation, and may even be specifically committed to this function.[43]

Inspired by the success of the Hodgkin-Huxley model, many of the mathematical models of cardiac cells highlighted the focus on the cell membrane that is discussed above. However, subsequent studies have found that the internal Ca^{2+} mechanism makes a crucial contribution to the AP of cardiac cells and is necessary to conceptualise excitation-contraction coupling. Additionally, the abovementioned M-clock, an internal oscillator coupled with Ca^{2+} cycling across the sarcoplasmic reticulum (SR) membrane (or Ca^{2+} clock) is present in all cardiac cells.[63] Various experimental studies have suggested that the Ca^{2+} clock might play an important role in the cardiac pacemaking processes [77-79], only recently have mathematical representations of the SAN that include integrated SR membranes and thus Ca^{2+} clocks been published. Maltsev and Lakatta *et al.* [80] in 2009 developed a model of a coupled-membrane with Ca^{2+} clock to explain the ionic mechanism of cardiac pacemaking. Notably, they highlighted quantitatively the contribution of spontaneous Ca^{2+} release during late DD (via the Na^+/Ca^{2+} exchange current, I_{NCX}). They arrived at the conclusion that only a coupled system of SAN pacemaking, by activation of an inward $Na^{+/}Ca^{2+}$ exchange membrane and Ca^{2+} clocks, provided both the strength and adaptability needed to sustain a normal pacing function. This ML model hypothesises that the vital pacemaker current that underlies DD is the inward I_{NCX}, not I_f. Updated versions of the ML model have recently been developed to account for additional experimental findings [77, 81]. I_{NCX} is the dominant current during the clock. In the absence of the Ca^{2+} clock, the M clock alone is incapable of DD.

In 2011, Kharche *et al.*[82] published a mathematical model that illustrated the spontaneous electrical AP of the mouse SAN, as informed by experimental findings for the molecular basis of ion channels. The model formulations considered the major ionic currents using isoform-specific expressions: for example, the T-type Ca^{2+} channel current was represented by the $I_{CaT,3.1}$ isoform; the L-type Ca^{2+} channel was composed of two isoforms, $I_{CaL,1.2}$ and $I_{CaL,1.3;}$ and the sodium channel was composed of two isoforms, $I_{Na,1.1}$ and $I_{Na,1.5}$. The results of their simulations showed good agreement with the experimental models, which enabled a better understanding for further studies into complex mechanisms of cardiac arrhythmia. However, in the same year another model was established for a different species. Tao *et al.*[83] developed a mathematical model for rats SAN cells. The model investigated the mechanisms that underlay sympathetic control of the cardiac pacemaker, and their association with hypertension. The simulation results provided satisfactory agreement between experimental and model results for the AP of the SAN and normalised I/V relations for major individual ion-channel currents; I_{CaL}, I_{Kr}, I_{Ks}, and I_f.

In 2012, Severi and colleagues [84] constructed an updated model of a rabbit SAN cell based on new experimental findings, with an updated representation of intracellular Ca^{2+} dynamics. This became known as the 'SD model'. The formulations of membrane ionic currents, ionic pumps and exchangers were revised on the basis of published experimental data. The AP waveforms that were generated successfully reproduced the typical physiological and pharmacological characteristics of rabbit SAN cells. The simulation results implied a qualitative validation of the model, and the details of the intracellular Ca^{2+} dynamics were found to be compatible with I_f as the dominant pacemaker current, contributing both to pacemaking activities and to rate modulation. It was developed through use of a similar Hodgkin-Huxley model to that employed to produce the Purkinje cell model [63,84]. In this model, I_f was considers as a main component of pacemaking and rate modulation.

Most recently, in 2014 Colman [33] attempted to develop a human SAN pacemaker cell model, based on the use of an available mRNA data model, this was followed by a new updated mathematical model of the spontaneous electrical activity of a human SAN was subsequently described by Fabbri *et al.*[85] The model incorporated the 2012 SD model of rabbit SAN cells, which relied on electrophysiological data from the isolated human SAN. The simulation results showed that the characteristics of the electrical AP and calcium transients closely matched those recorded experimentally. The model

highlighted the prominent role of the 'funny current' (I_f) in the setting of the pacing rate in human SAN pacemaker cells, despite its notably low amplitude compared with that in the rabbit.

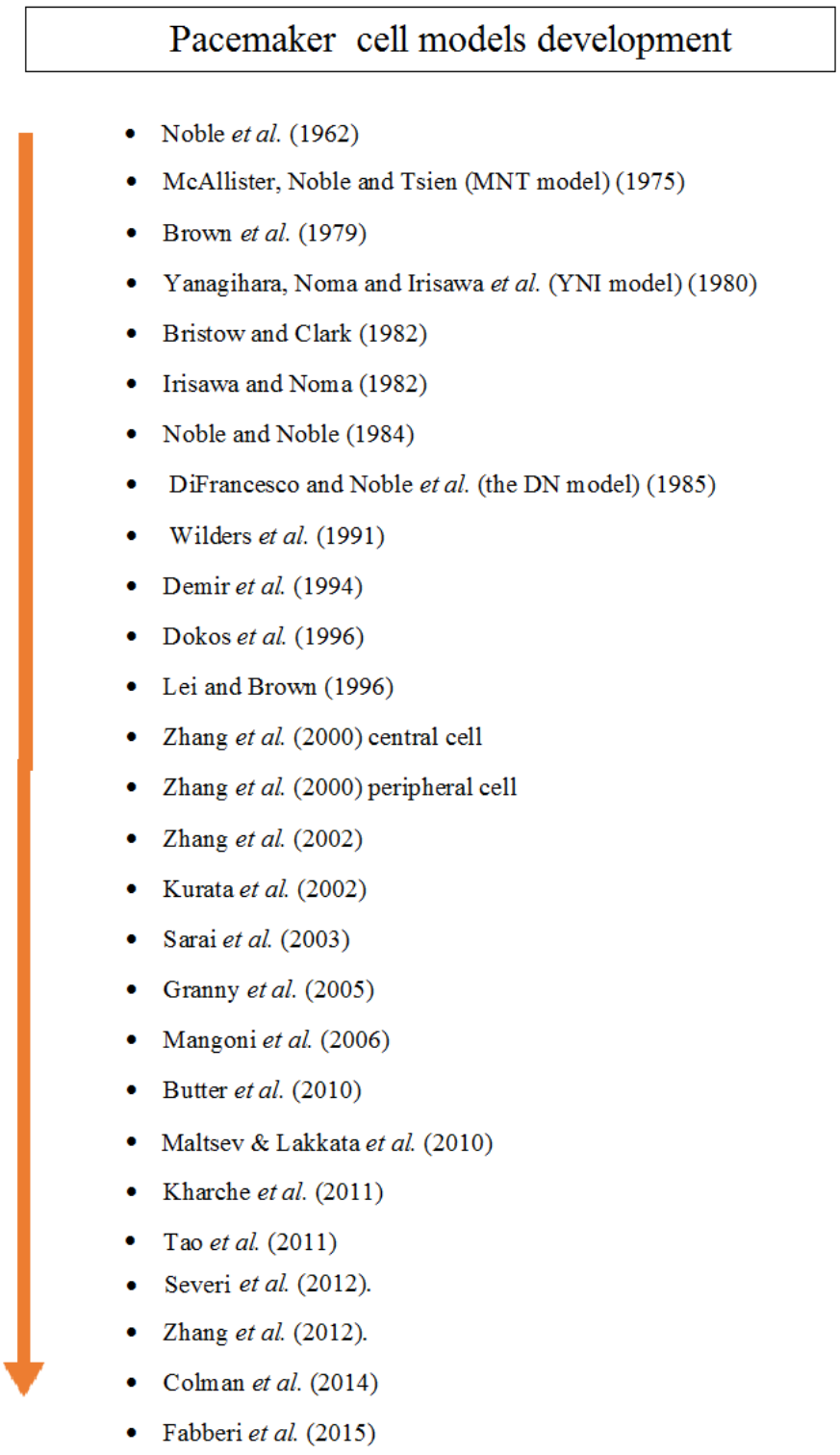

Figure 2.12. Chronological development of mathematical models in pacemaker cells.

2.4 Sinus node dysfunction and relevant arrhythmias

Sinoatrial node dysfunction (arrhythmia) refers to various conditions that manifest as an abnormal generation of the action potential of the sinus node, which may consequently lead to a reduction in cardiac output.[86] They include bradycardia, tachycardias, sinus pause, sinus arrest and sinus exit block, and in some cases result in sudden death. Since this thesis is focussed on SAN-tissue modelling, this summary reviews the most common aetiologies that surround SAN dysfunction, and illustrates that diverse pathophysiology may be caused by the same phenotype.

2.4.1 What are bradycardia and tachycardia?

Bradycardia is defined as the abnormal condition whereby the heart rate at rest is slow (the heart rate can drop below 50 bpm in adults). Symptoms associated with bradycardia include fatigue, dizziness, weakness, and even fainting (syncope) at very low heart rates.[87] Severe bradycardia may cause complications, such as lack of oxygen and nutrient supply to the heart, which can cause cardiac arrest, heart failure and sudden cardiac death because the heart is unable to pump enough blood. Bradycardia is mostly seen in athletes or aged people, and management of the condition requires the implantation of an artificial pacemaker.[88] Tachycardia, by contrast, is a condition in which the heart exhibits fast rates, often at greater than 100 bpm. Symptoms associated with tachycardia include chest pain, palpitations, hypotension (low blood pressure), shortness of breath, and syncope due to the increase in workload of the heart. It may lead to high incidences of sudden death. Tachycardia, also, can be classified based on its origin; atrial tachycardia is known as narrow complex tachycardia, and ventricular tachycardia is known as wide complex tachycardia. The width descriptions refer to the width of the QRS complexes as observed in ECGs.

SAN dysfunction may arise from a variety of conditions, including multiple factors and widespread remodelling of the ion-channel currents that is likely to change the SAN function, evidence for which is discussed below and summarised in Figure 2.13.

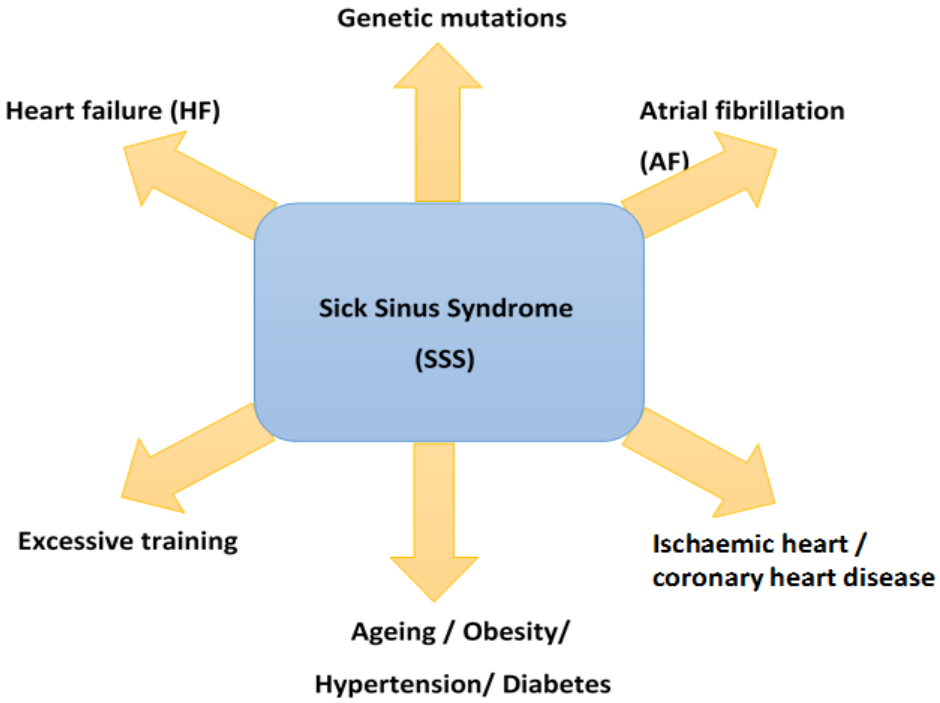

Figure 2.13. Summary of the different cases of ion-channel remodelling observed in sinus node dysfunction.

2.4.2 Remodelling of the sinus node in heart failure

Heart failure (HF) is defined as an inability of the heart to pump and maintain the blood flow necessary to supply the organs' needs, such as those of nutrition and oxygen. The incidence of heart failure can be acute (sudden) or chronic (ongoing). Patients with HF may experience various signs or symptoms, which include rapid or irregular (slow) heartbeat, and shortness of breath associated with chest pain or fainting.[89] There is evidence that HF is linked to the SND that is correlated with electrical remodelling of the ion channels in the various SAN studies performed in different species including humans, dogs, and rabbits [90-93]. These studies elucidated the fact that the electrical remodelling of the expression of key ion channels in the SAN resulted in the dysfunction of normal SAN pacemaker activity, thereby decreasing the intrinsic heart rate. Study on HF in dogs that involved quantitative measurements of mRNA and protein levels found that an electrical remodelling in the SAN manifested an 80% reduction of the HCN2 and HCN4 protein subunits. [92] Another study of rabbit SAN demonstrated a decrease in sinus node pacemaking due to a 40% reduction in I_f current density and 20% in I_{Ks} current density .[93]

2.4.3 Atrial fibrillation (AF)

Atrial fibrillation is the term for common cardiac arrhythmias that are characterised by irregular and rapid electrical activity in the heartbeat. In a clinical setting, atrial fibrillation is the most common form of cardiac arrhythmia.[95] AF has also been associated worldwide with stroke, sudden death, heart failure and a high prevalence of cardiovascular diseases. AF is more common in people aged 60 and older compared with among people younger than 60, and various factors can increase the risk of development of AF, such as diabetes, obesity, genetic mutations, and hypertension. Clinical studies have shown that structural remodelling of the SAN may result in significant damage to both the node itself and, indeed, the nodal artery, and is associated with atrial flutter, and AFalso known as 'bradycardia-tachycardia syndrome'.[93-95]

Several studies have highlighted the association between AF and SND. [96-98] For example, during the treatment of patients suffering from AF, a significant improvement in SAN function after pacemaker implantation has been reported, including an increase in heart rate and maximal heart rate, and a decrease in cSNRT. This indicates a recovery of the SAN due to the remodelling performed to treat AF.[96] In another example, SAN function was altered after rapid atrial pacing within 10-15 minutes.[97] Moreover, comparable data have been shown in dog models in which the animals suffer from chronic AF. Rapid atrial pacing for 16 days at 400 bpm caused nodal dysfunction when the intrinsic and maximal heart rates were reduced [98] and the sinus node recovery time(cSNRT) was prolonged.

2.4.4 Inherited cardiac arrhythmias (gene mutation)

Cardiac arrhythmias can be hereditary, some mutations can cause dysfunction in different properties of the heart. For instance, various forms of mutation in the SCN5A gene, which codes for I_{Na}, can cause a reduction in excitability of the heart, which predisposes it to an array of cardiac diseases, including Brugada syndrome and Long QT syndrome. In the SAN cells, the Nav1.5 channel is present in the peripheral cells but not the centre[76]. Therefore, mutations in the SCN5A may impair the AP in the periphery, which controls the surrounding atrium, and this impairment can lead to a heightened risk of delayed conduction, sinus node exit block, and sinus arrest. [99] Likewise, familial sick sinus syndrome has been attributed to a number of point mutations or deletions within the HCN4 gene, which is responsible for the I_f current. These genetic mutations can cause severe bradycardia and AV-node block.[100, 101]

2.4.5 Excessive training and SND

Athletes who perform fitness training intensely often experience low heart rates and can thus exhibit profound sinus bradycardia. Recent study suggested that intrinsic bradycardia caused by fitness training in rats and mice has led to a down-regulation of HCN4 and TBX3 gene expression in these animals compared with controls.[102] This suggests that electrical remodelling is the mechanism behind bradycardia among athletes, who require pacemaker implantation for SND later in life. Consequently, it raises the question as to whether this could be a prodrome of SND.

2.4.6 Ischaemic heart disease or coronary heart disease

Ischaemia is a condition in which blood supply to one or multiple areas of tissue is restricted, thus, may induce cell death. Acute myocardial ischaemia that involves the cardiac conduction routes is generally associated with bradycardia owing to impaired automatic tone, injury to SAN tissue, or decreased perfusion.[103] SND has often been attributed to ischaemia, and is associated with the diseases that affect the major coronary vessels and sinus node artery. The prevalence of both coronary artery disease and SND rises with age, or patients may suffer from the two concurrently.[88] However, research has demonstrated that the occlusion of the sinus node artery can lead to a range of dysrhythmias, including sinus slowing and sinoatrial block.[104] With a falling sinus rhythm, cardiac output and blood pressure decline, and in some severe cases sinus arrest occurs, causing sudden death. Although ischaemia-caused SAN impairment can cause death, the exact mechanism of this condition has yet to be understood.

References

1. Monfredi O, Tsutsui K, Ziman B, Stern MD, Lakatta EG, Victor X, et al. Electrophysiological heterogeneity of pacemaker cells in the rabbit intercaval region, including the SA node: insights from recording multiple ion currents in each cell. Am J Physiol Hear Circ Physiol [Internet]. 2018 [cited 2019 Mar 7];314:403–14. Available from: http://models.cellml.org/workspace/
2. Komuro I, Izumo S. *Csx*: a murine homeobox-containing gene specifically expressed in the developing heart. Proc. Natl. Acad. Sci USA. [Internet]. 1993 [cited 2019 Feb 11];90:8145-9. . Available from: https://pdfs.semanticscholar.org/198a/2a56e3fb5885009e1e6d0fc87fb7919d37a4.pdf

3. Circulatory system copy.jpg (550×843) [Internet]. [cited 2019 Nov 20]. Available from: https://revisionworld.com/sites/revisionworld.com/files/rw_files/circulatorysystem copy.jpg

4. Brown H, Kozlowski R, Davey P. Physiology and pharmacology of the heart [Internet]. Blackwell Science; 1997 [cited 2019 Mar 7]. p.126 Available from: https://www.wiley.com/en-us/Physiology+and+Pharmacology+of+the+Heart-p-9780865427228

5. Trayanova NA. Computational Cardiology: The Heart of the Matter. ISRN Cardiol [Internet]. 2012;1–15. Available from: http://www.hindawi.com/journals/isrn/2012/269680/

6. Xin M, Olson EN, Bassel-Duby R. Mending broken hearts: cardiac development as a basis for adult heart regeneration and repair. Nat Rev Mol Cell Biol [Internet]. 2013 [cited 2019 Mar 7];14(8):529–41. Available from: http://www4.utsouthwestern.edu/olsonlab/index.html

7. Gomez JF, Cardona K, Trenor B. Lessons learned from multi-scale modeling of the failing heart. J Mol Cell Cardiol [Internet]. 2015 [cited 2018 Jan 5];89:146–59. Available from: http://www.jmmc-online.com/article/S0022-2828(15)30087-0/pdf

8. Abdel-Nasser. Heart: The pump of life [Internet]. 2009 [cited 2019 Nov 20]. Available from: https://www.quranandscience.com/quran-science/signs-of-god/196-heart-the-pump-of-life

9. Katz AM. Physiology of the heart [Internet]. [cited 2019 Mar 7]. p.576 Available from: https://books.google.co.uk/books/about/Physiology_of_the_Heart.html?id=24CcilHdzC4C&redir_esc=y

10. Boyett MR, Honjo H, Kodama I. The sinoatrial node, a heterogeneous pacemaker structure. Cardiovasc Res [Internet]. 2000 [cited 2017 Jul 20];47:658–87. Available from: www.elsevier.com

11. Dobrzynski H, Anderson RH, Atkinson A, Borbas Z, D'souza A, Fraser JF, et al. Structure, function and clinical relevance of the cardiac conduction system, including the atrioventricular ring and outflow tract tissues. Pharmacol Ther [Internet]. 2013 [cited 2019 Mar 7];139:260–88. Available from: http://dx.doi.org/10.1016/j.pharmthera.2013.04.010

12. Brette F, Orchard C. T-Tubule Function in Mammalian Cardiac Myocytes. Circ Res. 2003; 92:1182-1192. [cited 2019 Aug 19]; Available from: http://www.circresaha.org

13. Li P, Lines GT, Maleckar MM, Tveito A. Mathematical models of cardiac pacemaking function. Front Phys [Internet]. 2013 Oct 30 [cited 2019 Aug 1];1:20. Available from: http://journal.frontiersin.org/article/10.3389/fphy.2013.00020/abstract

14. Severi S, Sobie E. A 2-Dimensional model to analyze the effects of cellular heterogeneity on cardiac pacemaking. [Internet]. [cited 2019 Aug 9]. Available from: https://amslaurea.unibo.it/8596/1/campana_chiara_tesi.pdf

15. Opthof T. The mammalian sinoatrial node [Internet]. Cardiovascular Drugs and Therapy. 1988 [cited 2019 Mar 7];1:573-97. Available from: https://link.springer.com/content/pdf/10.1007%2FBF02125744.pdf

16. Courtemanche M, Ramirez RJ, Nattel S. Ionic mechanisms underlying human atrial action potential properties: insights from a mathematical model. Am J Physiol Circ Physiol [Internet]. 1998 Jul [cited 2019 Mar 7];275(1):H301–21. Available from: http://www.physiology.org/doi/10.1152/ajpheart.1998.275.1.H301

17. Mangoni ME, Nargeot J. Genesis and Regulation of the Heart Automaticity. Physiol Rev [Internet]. 2008 [cited 2019 Mar 7];88(3):919–82. Available from: www.prv.org

18. Alberts B, Johnson A, Lewis J, Raff M, Roberts K, Walter P. Molecular biology of the cell. Garland Science; 2002.

19. Atkinson A, Inada S, Li J, Tellez JO, Yanni J, Sleiman R, et al. Anatomical and molecular mapping of the left and right ventricular His–Purkinje conduction networks. J Mol Cell Cardiol [Internet]. 2011 Nov 1 [cited 2019 Apr 5];51(5):689–701. Available from: https://www.sciencedirect.com/science/article/pii/S0022282811002513

20. Haissaguerre M, Vigmond E, Stuyvers B, Hocini M, Bernus O. Ventricular arrhythmias and the His–Purkinje system. Nat Rev Cardiol [Internet]. 2016 Mar 4 [cited 2019 Apr 5];13(3):155–66. Available from: http://www.nature.com/articles/nrcardio.2015.193

21. Sherwood L. Human Physiology: From Cells to Systems. CENGAGE Learning, 2008

22. The Conduction system of heart-27-728.jpg (728×546) [Internet]. [cited 2019 Nov 21]. Available from: https://image.slidesharecdn.com/150heart-100127094500-phpapp02/95/150-heart-27-728.jpg?cb=1290489437

23. CV Physiology: Non-Pacemaker Action Potentials [Internet]. [cited 2019 Apr 6]. Available from: https://www.cvphysiology.com/Arrhythmias/A006.htm

24. Unudurthi SD, Wolf RM, Hund TJ, Billman GE, Winslow RL. Role of sinoatrial node architecture in maintaining a balanced source-sink relationship and synchronous cardiac pacemaking. Frontiers in Physiology 5. doi:10.3389/fphys.2014.00446 [cited 2019 Aug 19]; Available from: www.frontiersin.org

25. Bleeker WK, Mackaay AJ, Masson-Pévet M, Bouman LN, Becker AE. Functional and morphological organization of the rabbit sinus node. Circ Res [Internet]. 1980 Jan 1 [cited 2018 Jan 5];46(1):11–22. Available from: http://www.ncbi.nlm.nih.gov/pubmed/7349910

26. Honjo H, Boyett MR, Kodama I, Toyama J. Correlation between electrical activity and the size of rabbit sino-atrial node cells. J Physiol [Internet]. 1996 Nov 1 [cited 2018 Feb 20];496 (Pt 3):795–808. Available from: http://www.ncbi.nlm.nih.gov/pubmed/8930845

27. Boyett MR, Honjo H, Yamamoto M, Nikmaram MR, Niwa R, Kodama I. Downward gradient in action potential duration along conduction path in and

around the sinoatrial node. American Journal of Physiology - Heart and Circulatory Physiology, 1999: 276; 2 45-2.Downloaded [Internet]. [cited 2019 Mar 7]. Available from: www.physiology.org/journal/ajpheart

28. James TN, Sherf L, Fine G, Morales AR. Comparative ultrastructure of the sinus node in man and dog. Circulation [Internet]. 1966 Jul [cited 2019 Mar 7];34(1):139–63. Available from: http://www.ncbi.nlm.nih.gov/pubmed/5942665

29. Dobrzynski H, Li J, Tellez J, Greener I, Nikolski V, Wright S, et al. Computer Three-Dimensional Reconstruction of the Sinoatrial Node. Circulation. 2005; 111:846-854. [cited 2019 Mar 7]; Available from: http://www.circulationaha.org

30. Dobrzynski H, Boyett MR, Anderson RH. New Insights Into Pacemaker Activity: Promoting Understanding of Sick Sinus Syndrome. Circulation [Internet]. 2007 Mar 26 [cited 2018 Jan 5];115(14):1921–32. Available from: http://www.ncbi.nlm.nih.gov/pubmed/17420362

31. Verheijck EE, Wessels A, van Ginneken AC, Bourier J, Markman MW, Vermeulen JL, et al. Distribution of atrial and nodal cells within the rabbit sinoatrial node: models of sinoatrial transition. Circulation [Internet]. 1998 Apr 28 [cited 2018 Jan 5];97(16):1623–31. Available from: http://www.ncbi.nlm.nih.gov/pubmed/9593568

32. Aslanidi O V, Boyett MR, Dobrzynski H, Li J, Zhang H. Mechanisms of transition from normal to reentrant electrical activity in a model of rabbit atrial tissue: interaction of tissue heterogeneity and anisotropy. Biophys J [Internet]. 2009 Feb [cited 2018 Jan 30];96(3):798–817. Available from: http://www.ncbi.nlm.nih.gov/pubmed/19186122

33. Colman MA. Mechanisms of Atrial Arrhythmias Insights from the Development of a Biophysically Detailed Model of the Human Atria. Springer Theses. Springer International Publishing, Cham. 2014.

34. Bronzino JD, Peterson DR. Biomedical engineering fundamentals. CRC Press, 2014; 2nd Edition. Available from: doi:10.1201/b15482.

35. Blunck R, Batulan Z. Mechanism of Electromechanical Coupling in Voltage-Gated Potassium Channels. Front Pharmacol [Internet]. 2012 [cited 2019 Apr 6];3. Available from: http://journal.frontiersin.org/article/10.3389/fphar.2012.00166/abstract

36. Satoh H. Sino-Atrial Nodal Cells of Mammalian Hearts: Ionic Currents and Gene Expression of Pacemaker Ionic Channels [Internet]. J. Smooth Muscle Res. 2003: 39 (5); 175-193. [cited 2019 Mar 7]; Available from: https://www.jstage.jst.go.jp/article/jsmr/39/5/39_5_175/_pdf/-char/en

37. Grant AO. Cardiac Ion Channels. Circ Arrhythmia Electrophysiol [Internet]. 2009 [cited 2019 Mar 8];2:185–94. Available from: http://ahajournals.org

38. Li Y, Wang F, Zhang X, Qi Z, Tang M. b-Adrenergic Stimulation Increases Cav3.1 Activity in Cardiac Myocytes through Protein Kinase A. PLoS One [Internet]. 2012 [cited 2019 Mar 8];7(7):39965. Available from: www.plosone.org

39. Bers DM. Calcium Cycling and Signaling in Cardiac Myocytes. Annu. Rev. Physiol. 2008; 70:23–49 [cited 2019 Mar 8]; Available from: http://physiol.annualreviews.org

40. Li Q. Mathematical modelling of intracellular Ca 2+ alternans in atrial and ventricular myocytes. PhD thesis [Internet]. [cited 2019 Mar 8]. Available from: https://www.research.manchester.ac.uk/portal/files/54516417/FULL_TEXT.

41. Bers DM. Cardiac excitation–contraction coupling. Nature [Internet]. 2002 [cited 2019 Mar 8];415:198-205. Available from: www.nature.com

42. Lei, M., Zhang, H., Grace, A. A., & Huang, C. L. H. SCN5A and sinoatrial node pacemaker function. Cardiovascular Research. .2007: *74; 356–365*. 2007 Available from: https://doi.org/10.1016/j.cardiores.01.009

43. Noble D, O'Rourke B, Difrancesco D. Mapping Cardiac Pacemaker Circuits: Methodological Puzzles of the Sinoatrial Node Optical Mapping. Circulation Research. 2010; 106:255–71. [cited 2019 Apr 7]; Available from: http://circres.ahajournals.org

44. Bers DM. The Beat Goes On: Diastolic Noise That Just Won't Quit. Circ Res [Internet]. 2006; 99(9): 921–923 [cited 2019 Apr 7]; Available from: http://circres.ahajournals.org/content/99/9/921

45. Bogdanov KY, Maltsev VA, Vinogradova TM, Lyashkov AE, Spurgeon HA, Stern MD, et al. Membrane Potential Fluctuations Resulting From Submembrane Ca $^{2+}$ Releases in Rabbit Sinoatrial Nodal Cells Impart an Exponential Phase to the Late Diastolic Depolarization That Controls Their Chronotropic State. Circ Res [Internet]. 2006 Oct 27 [cited 2019 Apr 7];99(9):979–87. Available from: https://www.ahajournals.org/doi/10.1161/01.RES.0000247933.66532.0b

46. The ECG in assessment of myocardial reperfusion – ECG learning [Internet]. [cited 2019 Mar 8]. Available from: https://ecgwaves.com/the-ecg-in-assessment-of-reperfusion/

47. Lipman BC, Cascio T. ECG assessment and interpretation. F.A. Davis Co; 1994. p.295

48. Hampton JR. The ECG made easy. Churchill Livingstone/Elsevier; 2013. p.200

49. Morita H, Wu J, Zipes DP. The QT syndromes: long and short [Internet]. The Lancet. 2008: 750–763. [cited 2019 Mar 8]. Available from: https://doi.org/10.1016/S0140-6736(08)61307-0

50. Noble D, Garny A, Noble PJ. How the Hodgkin-Huxley equations inspired the Cardiac Physiome Project. J Physiol [Internet]. 2012 Jun 1 [cited 2019 Aug 19];590(11):2613–28. Available from: http://doi.wiley.com/10.1113/jphysiol.2011.224238

51. Hodgkin AL, Huxley AF. A quantitative description of membrane current and its application to conduction and excitation in nerve. J Physiol I [Internet]. [cited 2017 Jul 25];7:500–44. Available from: https://www.ncbi.nlm.nih.gov/pmc/articles/PMC1392413/pdf/jphysiol01442-0106.pdf

52. Nobel D. A modification of the Hodgkin--Huxley equations applicable to Purkinje fibre action and pace-maker potentials. J Physiol [Internet]. 1962 Feb [cited 2019 May 3];160(2):317–52. Available from: http://www.ncbi.nlm.nih.gov/pubmed/14480151

53. McAllister RE, Noble D, Tsien RW. Reconstruction of the electrical activity of cardiac Purkinje fibres. J Physiol [Internet]. 1975 Sep 1 [cited 2019 Aug 19];251(1):1–59. Available from: http://www.ncbi.nlm.nih.gov/pubmed/1185607

54. Brown HF, DiFrancesco D, Noble SJ. How does adrenaline accelerate the heart? Nature [Internet]. 1979 Jul 1 [cited 2019 Aug 19];280(5719):235–6. Available from: http://www.nature.com/articles/280235a0

55. DiFrancesco D. A new interpretation of the pace makeer current in calf Purkinje fibres [Internet]. J. Physiol. 1981; 314:. 359-376. [cited 2019 Aug 19]. Available from: https://www.ncbi.nlm.nih.gov/pmc/articles/PMC1249439/pdf/jphysiol00703-0358.pdf

56. Yanagihara K, Noma A, Irisawa H. Reconstruction of Sino-atrial Node Pacemaker Potential Based on the Voltage Clamp Experiments [Internet]. Japanese Journal of Physiology. 1980;30: 841-857. [cited 2019 Mar 8] Available from: http://www.ele.uri.edu/faculty/vetter/BME307/Projects/Yanagihara-JpnJPhysiol-1980.pdf

57. Beeler GW, Reuter H. Reconstruction of the action potential of ventricular myocardial fibres. J Physiol [Internet]. 1977 Jun 1 [cited 2019 Aug 19];268(1):177–210. Available from: http://www.ncbi.nlm.nih.gov/pubmed/874889

58. Bristow DG, Clark JW. A mathematical model of primary pacemaking cell in SA node of the heart. Am J Physiol [Internet]. 1982 Aug [cited 2019 Mar 8];243(2):H207-18. Available from: http://www.ncbi.nlm.nih.gov/pubmed/6287854

59. Irisawa H, Noma A. Pacemaker Mechanisms of Rabbit Sinoatrial Node Cells. In Springer, Dordrecht; 1982 [cited 2019 Mar 8]. p. 35–51. Available from: http://www.springerlink.com/index/10.1007/978-94-009-7535-4_4

60. Noble D, Noble SJ. A model of sino-atrial node electrical activity based on a modification of the DiFrancesco-Noble (1984) equations. Proc R Soc London Ser B Biol Sci [Internet]. 1984 Sep 22 [cited 2019 Mar 8];222(1228):295–304. Available from: http://www.ncbi.nlm.nih.gov/pubmed/6149553

61. DiFrancesco D, Noble D. A Model of Cardiac Electrical Activity Incorporating Ionic Pumps and Concentration Changes. Philos Trans R Soc B Biol Sci [Internet]. 1985 Jan 10 [cited 2019 Aug 19];307(1133):353–98. Available from: http://rstb.royalsocietypublishing.org/cgi/doi/10.1098/rstb.1985.0001

62. Wilders R. Computer modelling of the sinoatrial node. Med Bio Eng Comput. 2007; 45:189–207 [cited 2017 Jul 20]; Available from: https://link.springer.com/content/pdf/10.1007%2Fs11517-006-0127-0.pdf

63. Noble D., DiFrancesco D.,Neuronal and cellular oscillators (cellular clocks series, vol. 2): edited by Jon W. Jacklet, Marcel Dekker, 1989. (xiii + 553 pages) ISBN 0 8247 8030 2. Trends in Neurosciences . 1989: 12, 521–522. doi:10.1016/0166-2236(89)90114-8

64. Wilders R, Jongsma HJ, Van Ginneken ACG. Pacemaker activity of the rabbit sinoatrial node: a comparison of mathematical models [Internet]. Biophys. J. o Biophysical Society. 1991; 60: 1202-1216 [cited 2019 Mar 8]. Available from: https://www.ncbi.nlm.nih.gov/pmc/articles/PMC1260175/pdf/biophysj00108-0216.pdf

65. Demir SS, Clark JW, Murphey CR, Giles WR. A mathematical model of a rabbit sinoatrial node cell. Am J Physiol [Internet]. 1994 Mar [cited 2019 Apr 5];266(3 Pt 1):C832-52. Available from: http://www.ncbi.nlm.nih.gov/pubmed/8166247

66. Dokos S, Celler B, Lovell N. Ion Currents Underlying Sinoatrial Node Pacemaker Activity: A New Single Cell Mathematical Model. J Theor Biol [Internet]. 1996 Aug [cited 2019 Mar 8];181(3):245–72. Available from: http://linkinghub.elsevier.com/retrieve/pii/S0022519396901290

67. Lei M, Brown H. Two components of the delayed rectifier potassium current, IK, in rabbit sino-atrial node cells. Exp Physiol [Internet]. 1996 Sep 1 [cited 2019 Mar 8];81(5):725–41. Available from: http://doi.wiley.com/10.1113/expphysiol.1996.sp003972

68. Zhang H, Holden A V, Kodama I, Honjo H, Lei M, Varghese T, et al. Mathematical models of action potentials in the periphery and center of the rabbit sinoatrial node. Am J Physiol Hear Circ Physiol. 2000;279(2000):H397–H421.

69. Zhang H, Holden A V., Noble D, Boyett MR. Analysis of the Chronotropic Effect of Acetylcholine on Sinoatrial Node Cells. J Cardiovasc Electrophysiol [Internet]. 2002 May 1 [cited 2018 Feb 5];13(5):465–74. Available from: http://doi.wiley.com/10.1046/j.1540-8167.2002.00465.x

70. Zhang H, Butters T, Adeniran I, Higham J, Holden A V., Boyett MR, et al. Modeling the chronotropic effect of isoprenaline on rabbit sinoatrial node. 2012.Front Physiol.;3 JUL(July).

71. Kurata Y, Hisatome I, Imanishi S, Shibamoto T. Dynamical description of sinoatrial node pacemaking: improved mathematical model for primary pacemaker cell. Am J Physiol Heart Circ Physiol. 2002; 283: H2074–H2101

72. Garny A, Noble D, Kohl P. Dimensionality in cardiac modelling. Prog Biophys Mol Biol [Internet]. 2005 Jan 1 [cited 2019 Jul 28];87(1):47–66. Available from: https://www.sciencedirect.com/science/article/pii/S0079610704000616?via%3Dihub

73. Matsuoka S, Sarai N, Kuratomi S, Ono K, Noma A. Role of individual ionic current systems in ventricular cells hypothesized by a model study. Jpn J Physiol [Internet]. 2003 Apr [cited 2019 Apr 8];53(2):105–23. Available from: http://www.ncbi.nlm.nih.gov/pubmed/12877767

74. Sarai N, Matsuoka S, Kuratomi S, Ono K, Noma A. Role of individual ionic current systems in the SA node hypothesized by a model study. Jpn J Physiol [Internet]. 2003 Apr [cited 2019 Apr 8];53(2):125–34. Available from: http://www.ncbi.nlm.nih.gov/pubmed/12877768

75. Mangoni ME, Traboulsie A, Leoni A-L, Couette B, Marger L, Le Quang K, et al. Bradycardia and Slowing of the Atrioventricular Conduction in Mice Lacking Ca V 3.1/ 1G T-Type Calcium Channels Circ Res. 2006; 98:1422–1430.[cited 2019 Apr 7]; Available from: http://circres.ahajournals.org

76. Butters TD, Aslanidi O V., Inada S, Boyett MR, Hancox JC, Lei M, et al. Mechanistic links between Na+ channel (SCN5A) mutations and impaired cardiac pacemaking in sick sinus syndrome. Circ Res. 2010;107:126-137

77. Yaniv Y, Stern MD, Lakatta EG, Maltsev VA. Mechanisms of beat-to-beat regulation of cardiac pacemaker cell function by Ca^{2+} cycling dynamics. Biophys J [Internet]. 2013 Oct 1 [cited 2019 Aug 19];105(7):1551–61. Available from: https://linkinghub.elsevier.com/retrieve/pii/S0006349513009715

78. Lakatta EG, Vinogradova T, Lyashkov A, Sirenko S, Zhu W, Ruknudin A, et al. The integration of spontaneous intracellular Ca2+ cycling and surface membrane ion channel activation entrains normal automaticity in cells of the heart's pacemaker. Ann N Y Acad Sci [Internet]. 2006 Oct 1 [cited 2019 Aug 19];1080(1):178–206. Available from: http://doi.wiley.com/10.1196/annals.1380.016

79. Vinogradova TM, Maltsev VA, Bogdanov KY, Lyashkov AE, Lakatta EG. Rhythmic Ca2+ oscillations drive sinoatrial nodal cell pacemaker function to make the heart tick. Ann N Y Acad Sci [Internet]. 2005 Jun [cited 2019 Aug 19];1047(1):138–56. Available from: http://doi.wiley.com/10.1196/annals.1341.013

80. Maltsev VA, Lakatta EG. Synergism of coupled subsarcolemmal Ca^{2+} clocks and sarcolemmal voltage clocks confers robust and flexible pacemaker function in a novel pacemaker cell model. Am J Physiol Circ Physiol [Internet]. 2009 Mar [cited 2019 Apr 6];296(3):H594–615. Available from: http://www.ncbi.nlm.nih.gov/pubmed/19136600

81. Maltsev VA, Lakatta EG. Numerical models based on a minimal set of sarcolemmal electrogenic proteins and an intracellular Ca(2+) clock generate robust, flexible, and energy-efficient cardiac pacemaking. J Mol Cell Cardiol [Internet]. 2013 Jun [cited 2019 Aug 19];59:181–95. Available from: https://linkinghub.elsevier.com/retrieve/pii/S0022282813000850

82. Kharche S, Yu J, Lei M, Zhang H. A mathematical model of action potentials of mouse sinoatrial node cells with molecular bases. Am J Physiol Circ Physiol. 2011;301(3):H945–63.

83. Tao T, Paterson DJ, Smith NP. A model of cellular cardiac-neural coupling that captures the sympathetic control of sinoatrial node excitability in normotensive and hypertensive rats. Biophys J [Internet]. 2011;101(3):594–602. Available from: http://dx.doi.org/10.1016/j.bpj.2011.05.069

84. Severi S, Fantini M, Charawi LA, DiFrancesco D. An updated computational model of rabbit sinoatrial action potential to investigate the mechanisms of heart rate modulation. J Physiol. 2012;59018:4483–99.

85. Fabbri A, Fantini M, Wilders R, Severi S. A Novel Computational Model of the Human Sinoatrial Action Potential. Computing in Cardiology 2015; 42:877-880.

86. Antzelevitch C, Burashnikov A. Overview of Basic Mechanisms of Cardiac Arrhythmia. Card Electrophysiol Clin. 2011; 3(1): 23–45. [cited 2019 Apr 5]; Available from: https://www.ncbi.nlm.nih.gov/pmc/articles/PMC3164530/pdf/nihms266695.

87. Desanctis RW, Rubenstein JJ, Schulman CL, Yurchak PM. Clinical Spectrum of the Sick Sinus Syndrome. Circulation [Internet]. 1972;46:5–13. Available from: http://circ.ahajournals.org/content/46/1/5

88. Choudhury M, Boyett MR, Morris GM. Biology of the Sinus Node and its Disease. Arrhythmia and Electrophysiology Review. [Internet]. 2015 [cited 2019 Mar 12];4(1): 28-34. Available from: www.AERjournal.com

89. Dobrzynski H, Boyett MR, Anderson RH. New insights into pacemaker activity: Promoting understanding of sick sinus syndrome. Circulation. 2007;115:1921-1932.

90. Sanders P, Kistler PM, Morton JB, Spence SJ, Kalman JM. Remodeling of sinus node function in patients with congestive heart failure: Reduction in sinus node reserve. Circulation. 2004;110(8):897–903.

91. Jose AD, Taylor RR. Autonomic Blockade by Propranolol and Atropine to Study Intrinsic Myocardial Function in Man [Internet]. The journal of Clinical Investigation. 1963; 48: 2019-2030. [cited 2019 Apr 5]. Available from: https://www.ncbi.nlm.nih.gov/pmc/articles/PMC297454/pdf/jcinvest00248-0067.pdf

92. Zicha S, Fernández-Velasco M, Lonardo G, L'Heureux N, Nattel S. Sinus node dysfunction and hyperpolarization-activated (HCN) channel subunit remodeling in a canine heart failure model. Cardiovascular Research. 2005; 66: 472–481 [cited 2019 Apr 5]; Available from: www.elsevier.com/locate/cardiores

93. Verkerk AO, Wilders R, Coronel R, Ravesloot JH, Verheijck EE. Ionic Remodeling of Sinoatrial Node Cells by Heart Failure. Circulation. [Internet].2003 [cited 2019 Apr 5];108(6):760-6. Available from: http://www.circulationaha.org

94. Gomes JA, Kang PS, Matheson M, Gough WB, El-Sherif N. Coexistence of sick sinus rhythm and atrial flutter-fibrillation. Circulation [Internet]. 1981 Jan [cited 2019 Apr 5];63(1):80–6. Available from: http://www.ncbi.nlm.nih.gov/pubmed/7438410

95. Thery C, Gosselin B, Lekieffre J, Warembourg H. Pathology of sinoatrial node. Correlations with electrocardiographic findings in 111 patients. Am Heart J [Internet]. 1977 Jun 1 [cited 2019 Apr 5];93(6):735–40. Available from: https://www.sciencedirect.com/science/article/pii/S0002870377800707?via%3Dihub

96. Hocini M, Sanders P, Deisenhofer I, Jaïs P, Hsu L-F, Scavée C, et al. Reverse Remodeling of Sinus Node Function After Catheter Ablation of Atrial Fibrillation in Patients With Prolonged Sinus Pauses. Circulation. 2003;108:1172-1175. [cited 2019 Apr 5]; Available from: http://www.circulationaha.org

97. Hadian D, Zipes DP, Olgin JE, Miller JM. Short-Term Rapid Atrial Pacing Produces Electrical Remodeling of Sinus Node Function in Humans. J Cardiovasc Electrophysiol [Internet]. 2002 Jun 1 [cited 2019 Apr 5];13(6):584–6. Available from: http://doi.wiley.com/10.1046/j.1540-8167.2002.00584.x

98. Elvan A, Wylie K, Zipes DP. Pacing-Induced Chronic Atrial Fibrillation Impairs Sinus Node Function in Dogs. Circulation [Internet]. 1996 Dec 1 [cited 2019 Apr 5];94(11):2953–60. Available from: https://www.ahajournals.org/doi/10.1161/01.CIR.94.11.2953

99. Lei M, Goddard C, Liu J, Léoni AL, Royer A, Fung SS, Xiao G, Ma A, Zhang H, Charpentier F, Vandenberg JI, Colledge WH, Grace AA, Huang CL. Sinus node dysfunction following targeted disruption of the murine cardiac sodium channel gene Scn5a. J Physiol. 2005:1;567(Pt 2):387-400.

100. Schulze-Bahr E, Pongs O, Isbrandt D. Pacemaker channel dysfunction in a patient with sinus node disease. J Clin Invest [Internet]. 2003 [cited 2019 Apr 5];111(10). Available from: http://jci.me/16387/pdf

101. Duhme N, Schweizer PA, Thomas D, Becker R, Schröter J, Barends TRM, et al. Altered HCN4 channel C-linker interaction is associated with familial tachycardia–bradycardia syndrome and atrial fibrillation. Eur Heart J [Internet]. 2013 Sep 14 [cited 2019 Apr 5];34(35):2768–75. Available from: http://www.ncbi.nlm.nih.gov/pubmed/23178648

102. D'Souza A, Bucchi A, Johnsen AB, Jit S, Logantha RJ, Monfredi O, et al. Exercise training reduces resting heart rate via downregulation of the funny channel HCN4. Nat Commun [Internet]. 2014 [cited 2019 Apr 5];5. Available from: www.nature.com/naturecommunications

103. Ando' G, Gaspardone A, Proietti I. Acute thrombosis of the sinus node artery: arrhythmological implications. Heart [Internet]. 2003 [cited 2019 Apr 5];89:e5. Available from: www.heartjnl.com

104. Bai X, Wang K, Yuan Y, Li Q, Dobrzynski H, Boyett MR, *et al.* simulation study Mechanism underlying impaired cardiac pacemaking rhythm during ischemia : A simulation study. 2017;093934.

Chapter Three - Mathematical Basis of the Electrophysiology of the Heart

Due to the shortcomings of experimental studies to investigate different aspects of heart function and dysfunction, biophysically detailed mathematical models can be employed as an alternative strategy. These mathematical models are a substitute approach to understand the correlation between the ionic channels and the action potentials of cardiac myocytes. In addition, they can be used to map out genetic mutations, the mechanism of arrhythmias, or of ion-channel remodelling which causes cardiovascular diseases. This chapter presents the published literature on physical laws and principles that relate to biophysically detailed mathematical representations of cardiac cells and tissues.

3.1 Mathematical electrophysiology

The development of the computational models of cardiac cells and organs, are based on formulations of the ionic currents movement mathematically. Hodgkin and Huxley (1952) introduced the first bio-physiologically detailed computational model of the squid-nerve AP.[1] This became known as H-H model. This mathematical model improve our understanding about the mechanistic interactions among ionic mechanism, different molecular components, and physiological function of the action potential. The voltage-clamp method of electrophysiology of different ionic currents was utilised in the development of their model. This was done through recording the ionic currents to study the contribution of the AP in neurons. The H-H model effectively described the interaction between the cell membrane and ionic currents as a component of a single electric circuit. Later, H-H became a framework that inspired the development of many models. [2] One notable aspect of the H-H model is that it has had numerous applications and has inspired many researchers to employ the basic concept for all computational models of APs. This is because, although the Hodgkin-Huxley model was based on studies performed on the squid giant axon, it could be employed widely for computational cardiac AP models owing to similarities in basic electrophysiology and biophysical mechanism.[2] For instance, Noble (1962) utilised the Hodgkin-Huxley design to model cardiac APs computationally for the Purkinje fibre. Noble's model initiated a sustained depolarisation stage of APs in Purkinje fibre, using an available data

from ionic channels voltage clamp record.[3] For their ground-breaking study, Hodgkin and Huxley were awarded the Nobel Prize in Physiology or Medicine in 1963.

3.1.1 Equilibrium potential

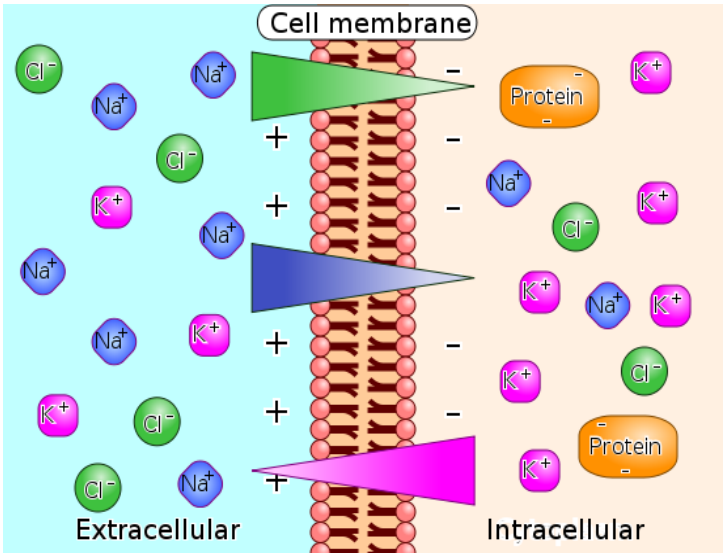

Figure 3.1. Representation of the cell membrane, in which at the Nernst potential no ionic gradient can move across the membrane.

The Nernst equilibrium, known as 'reversal potential', describes how a difference in ionic concentration gradients across cell membranes can lead to a potential difference in a balanced state.[4] The role of the Nernst potential in ionic modelling is to determines the direction of ion-current flow. Assume that there are two reservoirs which contain various types of ions with different concentrations on each side. The reservoirs are separated by a semi-permeable membrane (Figure 3.1). The two sides of the cell membrane contain electrically neutral solutions. The flow of ionic currents from one side to the other is influenced by the two states of concentration difference. Temperature influences the Nernst potential (as shown in the Nernst equation 3.1, below). Consequently, imbalanced charge will cause ions to diffuse through the membrane. The potential difference, *Es*, across the membrane at the equilibrium state is illustrated by the following Nernst equation:

$$Es = \frac{RT}{zF} \ln\left(\frac{[X]_{out}}{[X]_{in}}\right) \tag{3.1}$$

where:

R is the universal gas constant

T is the absolute temperature

z is the ion charge

F is Faraday's constant

$[X]_{out}$ and $[X]_{in}$ are the concentrations of the ions outside and inside the cell, respectively.

3.1.2 Electric circuit model

Figure 3.2A demonstrates the basic design for all electric-circuit models of cardiac myocytes. The cell membrane is displayed as an equivalent circuit, which consists of various components of the cell that considered to be an electrical element.[5] The cell membrane illustrated by the lipid bi-layer shape and split into intracellular and extracellular media, separates the charges over a short distance. The capacitance of the lipid bi-layer mimics that of a capacitor with a constant value of the capacitance, C_m. The ion channels, exchangers, and pumps enable the ions to diffuse through the cell membrane either actively or passively. They play the role of resistors. Given that the 'resistors' operate independently, they should follow a parallel set-up in the model.[6] Therefore, the electric-circuit design of the cell membrane can be modelled as illustrated in Figure 2.3B. Therefore, the complexity of the transmembrane potential and ion-driven currents can be conceptualised and studied using basic electric-circuit design.

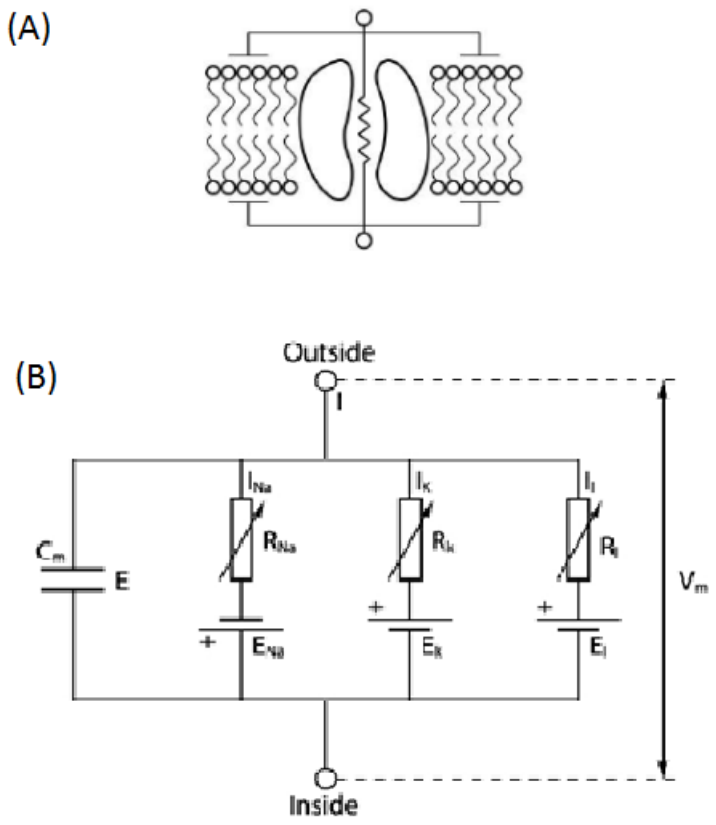

Figure 3.2. (A) A schematic representation of the transmembrane potential and ionic currents using the electric-circuit model. (B) A diagram of the electric-circuit model developed from the Hodgkin-Huxley model of the cell membrane, in which the cell membrane is represented by capacitance, C_m, and E_{Na} , E_K, and E_L. represent the Nernst potentials of each individual ion.

The ion current (I_m) that flows through cell membranes corresponds to the ionic capacitor (I_{cm}) and the resistance ionic currents (I_{ion}), which latter pass through the resistive pathway.[3] The total membrane current (I_m) can then be defined as:

$$I_m = I_{ion} + I_{Cm} \tag{3.2}$$

Based on Kirchhoff's law, the total current of the electrical circuit I_m (the sum of the ionic currents and the capacitive current) should be zero, so:

$$I_{ion} + I_{Cm} = 0 \tag{3.3}$$

Since the cell membrane acts as a capacitor, the relationship between the membrane potential of this cell membrane V_m and the charge Q can be written as:

$$Q \alpha\, V_m \tag{3.4}$$

$$Q \;=\; C_m\, V_m \tag{3.5}$$

The rate of change of the membrane potential with time can be expressed in the following equation:

$$\frac{dQ}{dt} = C_m \frac{dV_m}{dt} \tag{3.6}$$

I_{Cm} can be obtained using the transmembrane potential V_m, where:

$$I_{Cm} = \frac{dQ}{dt}$$

$$I_{Cm} = C_m \frac{dV_m}{dt} \tag{3.7}$$

Thus to calculate the transmembrane potential dependence over time, the equation (3.3) and equation (3.7) are combined:

$$I_{ion} = - C_m \frac{dV_m}{dt} \tag{3.8}$$

This equation represents the change in transmembrane potential in relation to the total ionic current and integrated to calculate the AP of the electrical-circuit model.[6]

To define a form for the ionic current, which is the simplest form that can be given, as they are dependent on passive processes. The formulation of the ion channels is described here using Ohm's Law while accounting for the ion concentration gradient:

$$V \alpha I \tag{3.9}$$

$$V = R\, I \tag{3.10}$$

The resistance, R, can be replaced with the conductance, g, based on the following equation: $R = \frac{1}{g_{ion}}$

$$I = g_{ion} V \tag{3.11}$$

It is worth noting that V in the equation is not the transmembrane potential V_m, but the driving force for the ionic currents. Each of the distinct ionic currents can be modelled in this general way, and then added together to obtain the total ionic current.[7] The form of V must now be examined. The driving force, $V$is linked to the Nernst equilibrium potential (equation 3.1), highlighted above in section 3.2. This is particularly useful because it allows us to formulate the driving force behind such passive processes through purely electrical way. The variation in the transmembrane potential and the reversal potential play the role of an electromotive force on the ion. This allows a form to be obtained for the V term in equation (3.11), and hence the ionic current can be represented as:

$$I_{ion} = g_{ion} (V_m - E_{ion}), \tag{3.12}$$

The equation above is referred to as the 'driving force equation' and describes the of ion currents transportations in both the intracellular and extracellular fluids across the cell membrane. V_m is the resultant membrane potential across membranes, and E_{ion} is the reversal potential.

3.1.3 The Hodgkin-Huxley Model

As discussed above, the H-H designed the is first mathematical model of excitable cells, known as 'conductance-based model', which describes the initiation and propagation of the AP in neurons cells.[1] Their model utilises non-linear ordinary differential equations (ODEs), to give an approximation the AP characteristics in these excitable cells based on ionic mechanisms. It was suggested that the AP activities of SAN cells in cardiac system can be modelled in similar manner of the H-H model of the electrical circuits that form a biophysical system (Figure 3.2).[6] Hodgkin and Huxley demonstrated that the ionic current across the membrane carries potassium currents (I_K), sodium currents (I_{Na}), and a small leakage current (I_L). A concentration gradient for each ion across the cell membrane is described as a battery (electromotive force) in the electrical circuit. Therefore, each ion channel can be considered as a resistor connected in series with this battery.[7] The driving force for each ion channel is calculated by the electrical potential difference and a conductance. The following equations show mathematical definition of the ionic current components:

$$I_{Na} = g_{Na}(V_m - E_{Na}) \quad (3.13)$$

$$I_K = g_K(V_m - E_K) \quad (3.14)$$

$$I_L = g_L(V_m - E_L) \quad (3.15)$$

g_K represents the ionic conductance of potassium currents I_K, g_{Na} represents the ionic conductance of sodium currents I_{Na}, g_L represents the ionic conductance of leakage current I_L. Similarly, E_{Na}, E_K and E_L represent the equilibrium potentials of potassium, sodium and leakage ions. The ion channels are connected in parallel with each other and considered as variable resistors based on their inconstant (open and close) state.[2] The total ionic current of a cell membrane is calculated from the net of different ion channels as the following equation:

$$I_{ion} = I_{Na} + I_K + I_L \quad (3.16)$$

The conductance of the ion channel is voltage-dependent, and can be stated as:

$$I_{ion} = g_{i,max} \quad m^{\alpha} h^{\beta}(V_m - E_{ion}) \quad (3.17)$$

In this equation, $g_{i,max}$ refers to the maximum conductance value; *m* and *h* represent the activation and inactivation variables; α and β refer to empirically fit the form of the activation and inactivation gates observed experimentally. It is worth noting that some ion channels do not feature two types of activation and inactivation gates, for example a number of potassium channels do not present activation variable and thus, they only have an inactivation gate.[7] In the same manner, some channels display two different time courses of activation or inactivation, and this can be demonstrated using two separate activation or inactivation gates which exhibit distinct properties. This type of ion channel can be seen in Chapter Four in modelling the $I_{K,Ach}$, which features two inactivation variables.

To describe how voltage and time dependent channel can be incorporated intomodel: consider an activation gating variable, *q*, where *q* refers to the proportion of channels in an activated state and their gates are open. Therefore, the proportion of channels not in the activated state and with their gate closed must be (1-*q*). Rate coefficients, α_q and β_q, are dependent on the transitions between the two states. when α_q correlates to the opening of the gate, this implies that the rate of change of opening can be expressed as

$\alpha_q(1\text{-}q)$, and the rate of change of shutting can be expressed as $\beta_q q$, thus the transition equation can be described as follows:

$$1 - q \overset{\alpha_q \beta_q}{\rightleftarrows} q \tag{3.18}$$

Where q refers to the fraction of open channels, 1-q represents the fraction of closed channels. Therefore, the rate of change of gating variable q can be determined as a differential equation as shown below:

$$\frac{dq}{dt} = \alpha_q(1 - q) - \beta_q q \tag{3.19}$$

If the values of either α_q or β_q are determined by V_m, then the state of the gate can be considered as a voltage-dependent as well as a time-dependent gate. This can give a useful indication of the activity of a channel at various voltages, as a determination of its ability to respond to alterations in potential.[7] Consequently, the differential equation that demonstrates the gating kinetics can be expressed as:

$$\frac{\mathrm{d}q}{\mathrm{d}t} = \frac{q_\infty - q}{\tau_q} \tag{3.20}$$

where q_∞ represents the steady-state value of gating variable q (the number of opening channels in a steady-state system). The steady state of the gate q denotes the value to which the gating variable tends at a certain voltage.

$$q_\infty = \frac{\alpha_q}{\alpha_q + \beta_q} \tag{3.21}$$

If the voltage is altered suddenly, the rate at which the gate reaches its steady-state value for the updated voltage is demonstrated by the time constant, expressed as:

$$\tau_q = \frac{1}{\alpha_q + \beta_q} \tag{3.22}$$

It is common to record and fit steady-state values and time constants directly in experimental and modelling studies. The steady-state is often represented by a sigmoidal function as shown below:

$$q_\infty = \frac{1}{1 + e(v_m - v_{0.5}/a)} \tag{3.23}$$

Both $v_{0.5}$ and a are determined quantitatively and may be positive or negative value.

3.2 Autonomic regulation of the heart

While spontaneous activity of the SAN is responsible for the initiation of the rhythmic contractions of the heart, the automatic nervous system, which controls much of an animal's bodily functions by transmitting signals, normally known as hormones, to and from various organs, is also responsible for regulation of the heart rate.[8,9] These hormones can affect the physiological activities in the target cell through binding them to a special receptor protein, and thus, controlling the behaviour of the target organ.[7] Hormonal effects vary from one region of the body to another. Cardiac-related hormones are regulated by the sympathetic and parasympathetic nerves, both of which arise in the automatic nervous system.[10]

Sympathetic regulation involves the release of the β-adrenergic stimulation, an essential isomer of adrenaline that is known to accelerate the spontaneous activity of the SAN and the contraction force in cardiac myocytes and therefore, increase the heart rate.[7,11] Studies have shown that β-adrenoceptor stimulation occurs through alteration of ionic currents that contribute to pacemaker activity of the SAN.[11,12] Another study have revealed that isoprenaline (ISO), a β- adrenergic agonist, influences the morphology of the APs of a rabbit SAN cell and increases its firing rate.[13] ISO is utilised primarily as a sympathomimetic drug, as it mimics the effects of adrenaline. Zhang *et al.*[14] simulated the effect of ISO on the SAN by modelling the effects of many of the ion channels such as I_{CaL}, I_f, I_{st}, I_{Kr}, and I_{Ks} in detailed description, whereby a rise in the rate of deactivation of I_{Kr} plays a critical role, although the impact of ISO on the kinetics of I_{Kr}, I_f and $Ca^{2+}{}_i$ also have an impact.

The parasympathetic system, in contrast, regulates the release of acetylcholine, ACh, the effects of which on the pacemaker potentials contradict those of ISO; that is, it triggers a reduction of the pacing rate.[15] It also slows the APs through the activation of the ACh-activated potassium channel, I_{KACh}, and affects the kinetics of the conductance of L-type Ca^{2+} channels and the funny current.[16] The detailed impact of ACh on the heart is shown in detail and explored in Chapter Four of this thesis.

3.3 Model development at tissue level

The use of the H-H model helps to calculate the flow of ion channel currents across a cell membrane in single cell. The next step in building tissue model is to simulate the electrical excitation waves that propagate in cardiac tissue through calculating the flow

of currents between individual myocytes. The electrophysiological communication between neighbouring cells in tissue depend on the gap junction coupling. The gap junctional ion channels connect the cytoplasm of the individual cell with the adjacent cells. Ion currents can then enter the adjacent myocytes through these channels. This process may trigger depolarisation of adjacent myocytes or may even initiate an AP, but only if the membrane potential of adjacent myocytes attains the threshold for the activation of I_{Na}. This activity paves the way for the propagation of cardiac electrical activity in myocardial tissue. One such approximation is the bidomain model equation was designed to describe this activity.[17] However, solving this equation demands significant computational intensity. [18] Accordingly, the monodomain model, which is an approximation of the bidomain model, was identified for use to perform the work described in this thesis.

3.3.1 Monodomain equation

In the bidomain model, both extracellular and intracellular spaces are accounted for as two separated spaces with overlapping domains. Therefore, the transmembrane potential V_m can be calculated as the potential difference between these two spaces. However, in the monodomain model, both intracellular and extracellular conductivities are assumed to be proportional, meaning that the ratio between the intra- and extracellular spaces is 1. [19] The bidomain model is thus simplified to the monodomain model. To explain the monodomain model of the APs propagation at the tissue level, we need to calculate the flow of currents between individual cells. Figure3.3 illustrates a simplified diagram of ion current flowing between coupled cells in cardiac tissue. Each cell is represented as an individual electrical circuit separated from the adjacent cell by a distance Δx, $g_c(x)$ represents the conductance of the intercellular connections.

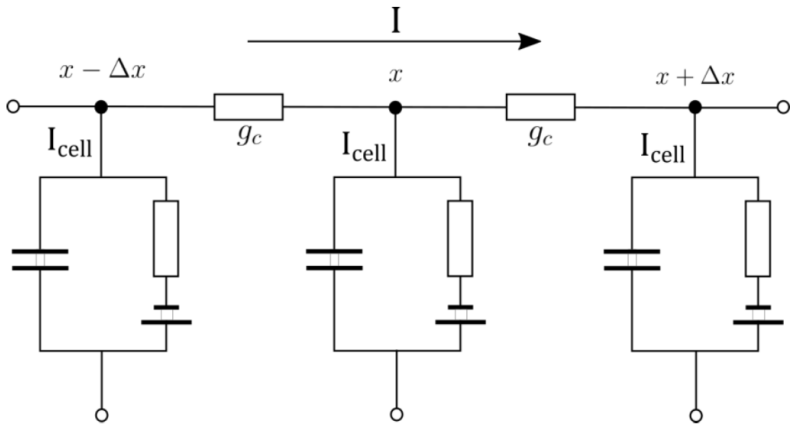

Figure 3.3 Diagram illustration of current flowing between coupled cells in tissue.

Based on Kirchoff's first law, the total current interning node is equal to the total current leaving,

$$I_{ion}(x - \Delta x) - \Delta x\, I_{cell} = I_{ion}(x + \Delta x) + \Delta x\, I_{cell} \tag{3.24}$$

$$I_{ion}(x - \Delta x) = I_{ion}(x + \Delta x) + 2\Delta x\, I_{cell} \tag{3.25}$$

Where I_{ion} is the current per unit length, and Δx is the length of cells in the tissue that are connected end to end. By using the Taylor expansion of $I(x \pm \Delta x)$, equation (3.25) can be written as:

$$I_{ion}(x \pm \Delta x) = I_{ion}(x) \pm \Delta x \frac{dI_{ion}}{dx} + O(\Delta x^2) \tag{3.26}$$

If Δx has a small value, the term $O(\Delta x^2)$ can be excluded. This result can be substituted into equation 3.26 as:

$$\frac{dI_{ion}}{dx} = -I_{cell} \tag{3.27}$$

This result is for one-dimensional representation; thus, for multi-dimensional directions the following equation (3.28) can be written as:

$$\nabla I_{ion}(x) = -I_{cell} \tag{3.28}$$

∇ refers to the special gradient operator. To calculate the membrane potential at x point, the necessary equation is:

$$V_m(x) = V_m(x - \Delta x) - V_m(x + \Delta x) \tag{3.29}$$

According to Ohm's law, $V_m(x)$ will be substituted as equation (3.11)

$$I_{ion}(x) = g_c(x) \left(\frac{(V_m(x) - V_m(\Delta x)) - (V_m(x) + V_m(\Delta x))}{2\Delta x} \right) \tag{3.30}$$

In this equation, $g_c(x)$ represents the coupling conductance. Taylor expansion used in equation (3.25) is used here:

$$I_{ion}(x) = g_c(x) \frac{[(V_m(x) - \Delta x \frac{\partial V_m}{\partial x}] - [(V_m(x) + \Delta x \frac{\partial V_m}{\partial x}]}{2\Delta x} \tag{3.31}$$

The latter equation can be simplified and replaced into equation (3.27) to describe the current flow through one-dimensional tissue,

$$I_{ion} = \frac{\partial}{\partial x} \left(g_c(x) \frac{\partial V_m}{\partial x} \right) \tag{3.32}$$

Or more generally:

$$I_{ion} = \nabla (g_c(x) \nabla V_m) \tag{3.33}$$

By describing the conductance $g_c(x)$ in terms of a diffusion coefficient D:

$$g_c(x) = \frac{Cm}{\partial x^2} D(x) \tag{3.34}$$

This equation is substituted into the following;

$$I_{cell} = Cm \frac{dV_m}{dt} + I_{ion} = \nabla (g_c(x) \nabla V_m) \tag{3.35}$$

$$Cm \frac{dV_m}{dt} = \nabla \left(\frac{Cm}{\partial x^2} D(x) \nabla V_m \right) - I_{ion} \tag{3.36}$$

$$\frac{dV_m}{dt} = (D(x) \nabla^2 V_m) - \frac{I_{ion}}{Cm} \tag{3.37}$$

This equation represents the monodomain model.

In isotropic tissue, the monodomain model treats both the inner and outer spaces of the cell as one environment, therefore D is considered as a constant rather than being position dependent.[20] Thus, the formula can be simplified to:

$$\frac{dV_m}{dt} = (\ D\ \nabla^2\ V_m) - \frac{I_{ion}}{Cm} \tag{3.38}$$

In the case of 1D tissue, this equation is simplified to:

$$\frac{dV_m}{dt} = \left(\ D\frac{d^2V_m}{dx^2}\right) - \frac{I_{ion}}{Cm} \tag{3.39}$$

In the case of anisotropic tissue, which is widely considered in cardiac-tissue models, we take into account the effect on the diffusion of excitation propagation through regions of different conductivity in tissue, hence, the D value will be assumed as a scalar field. Thus we need to consider the diffusion gradient when calculating potential contributions from neighbouring nodes. Scalar fields represent the diffusion and voltage:

$$\nabla \cdot (D\nabla V_m) = D\ \nabla^2\ V_m + \nabla D \cdot \nabla V_m \tag{3.40}$$

In the simple case where D is constant, the gradient of D is zero, hence, the term $\nabla D \cdot \nabla V$ is zero. However, if D is a scalar field we must account for this term. Here;

$$\nabla\ V_m = \frac{\partial V_m}{\partial x}\ \hat{\imath} + \frac{\partial V_m}{\partial y}\hat{\jmath} + \frac{\partial V_m}{\partial z}\ \hat{k} \tag{3.41}$$

$$\nabla\ D = \frac{\partial D}{\partial x}\ \hat{\imath} + \frac{\partial D}{\partial y}\hat{\jmath} + \frac{\partial D}{\partial z}\ \hat{k} \tag{3.42}$$

$$\nabla \cdot (D\nabla V_m) = \frac{\partial V_m}{\partial x}\ \frac{\partial D}{\partial x}\ +\ \frac{\partial V_m}{\partial y}\ \frac{\partial D}{\partial y} + \frac{\partial V_m}{\partial z}\ \frac{\partial D}{\partial z} \tag{3.43}$$

In the case of a 1D tissue, the gradient when Δx is sufficiently small is shown in the equations (3.41) and (3.42):

$$\frac{\partial V_m}{\partial x} \approx \frac{\left(\ V_m(x+\Delta x) - V_m(x-\Delta x)\right)}{2\Delta x} \tag{3.44}$$

$$\frac{\partial D}{\partial x} \approx \frac{\left(\ D(x+\Delta x) - D(x-\Delta x)\right)}{2\Delta x} \tag{3.45}$$

$$\frac{dV_m}{dt} = \nabla.(D(x) \cdot\ \nabla V_m) - \frac{I_{ion}}{Cm} \tag{3.46}$$

$$\frac{dV_m}{dt} = D\ \frac{d^2V_m}{dx^2} + \left[\frac{\left(V_m(x+\Delta x)-V_m(x-\Delta x)\right)}{2\Delta x}\right].\left[\frac{D(x+\Delta x)-D(x-\Delta x)}{2\Delta x}\right] - \frac{I_{ion}}{Cm} \quad (3.47)$$

3.3.2 Boundary conductions

The solution of differential equations requires a definition of the behaviour of the system at the boundary condition. In cardiac modelling, for instance, the 'no-flux' boundary parameters are usually applied as shown below [21]:

$$n\ D\ \nabla\ V_m = 0 \quad (3.48)$$

In this equation, n represents the vector normal to the tissue. See equation (3.38) for D and V_m. The boundary conditions here suggest that the alteration in membrane potential with time is zero at the boundary $\frac{dV_m}{dt} = 0$. It is easy to apply the boundary condition for an idealised square tissue, as the standard to the surface is in the coordinate path. However, the direction of the normal vector is not unique for real tissue. Accordingly, the normal vector is approximated first in this direction, and then the change of membrane potential is adjusted to zero.

3.4 Numerical methods

Numerical methods offer mathematical ways in which continuous equations can be estimated to enable them to be solved iteratively on a computer. Numerous numerical equations are based on estimations of the real solutions of ODEs and PDEs. In this section, only those numerical methods that are utilised in the models developed in this thesis are considered. These include: Euler's method, the Runge-Kutta approach. [22,23] and the finite difference approach. The three approaches are different in complexity and accuracy. They are described in the following sections.

3.4.1 The forward Euler's method

Euler established a numerical method based on a first order integration technique for solving ODEs with one step scheme. Euler's approach has become the most widely used approach in cardiac modelling.[22] Generally, the approach approximates the state of the system based on given an initial value:

$$\frac{dy}{dt} = f(t, y) \quad (3.49)$$

and

$$y(t_0) = y_0 \tag{3.50}$$

Therefore, the estimated solution of ODEs for next time step is expressed as:

$$y_{n+1} = y_n + \frac{dy_n}{dt} h \tag{3.51}$$

In this equation, the terms y and t represent the position and the time, h represents the step size in the same unit as t, n is the step number.[23] This technique is commonly employed in mathematical cardiac models for several reasons: it is simple, so computationally effective for solving ODEs; it has been found to show relatively high suitability for the calculation of APs that are based on the Hodgkin-Huxley equations; and it is easy to apply. One disadvantage is that it occasionally leads to errors in finding solutions. Even so, the errors can be rectified by the use of smaller step sizes.

3.4.2 Runge-Kutta method

The Runge-Kutta approach is a multi-step approximation used to estimate ODE solutions.[23] Mathematicians Runge and Kutta in 1900 described the technique based on application of a 'trial' step at the midpoint of the interval to eliminate lower-order error terms. The second-order technique is expressed as:

$$\frac{dy}{dt} = f(t, y), y(t_0) = y_0 \tag{3.52}$$

The equation can be expressed as:

$$y_{n+1} = y_n + k_2 \tag{3.53}$$

$$k_1 = hf\ (t_0, y_0\ ) \tag{3.54}$$

$$k_2 = hf\left(t_0 + \frac{1}{2}, y_0 + \frac{1}{2}k_1\right) \tag{3.55}$$

In these equations, k_1 is the slope at the beginning of the interval, and k_2 is the slope at the midpoint of the interval. The value of y can be determined by k_1. This is referred to as the second-order Runge-Kutta approach. Similarly, the Runge-Kutta approach can be expanded to higher orders. The fourth-order method (RT4), which is another important method for the approximation of solutions of ODEs, can be expressed as:

$$y_{n+1} = y_n + \frac{1}{6}\, h(k_1 + 2k_2 + 2k_3 + k_4) \tag{3.56}$$

$$k_1 = f(t_n, y_n) \tag{3.57}$$

$$k_2 = f\left(t_n + \frac{1}{2}h, y_n + \frac{1}{2}h\, k_1\right) \tag{3.58}$$

$$k_3 = f\left(t_n + \frac{1}{2}h, y_n + \frac{1}{2}h\, k_2\right) \tag{3.59}$$

$$k_4 = f(t_n + h, y_n + hk_3) \tag{3.60}$$

$$t_{n+1} = t_{n+1} + h \tag{3.61}$$

Equation (3.56) represents the RT4 method, which provides a stable approximation to solve ODEs. the derivative is assessed four times in each time step: the first time at the initial step (k_1), the second and third time at the trial midpoints (k_2 , k_3) and lastly at the trial endpoint (k_4). The RT4 exhibits many advantages. It is reasonably simple and robust. It produces a stable and more accurate solution especially with a large time step, when considered against the Euler approach. However, it is computationally intensive compared with the Euler technique, thus it is commonly used in single cell models, but not in high complexity models.

Both Euler and fourth-order Runge-Kutta methods show advantages and disadvantages. The two compare as follows:

- Euler's approach is simpler and more direct than RT4 in computing ODEs.
- Operating at the equivalent step size, RT4 is more accurate than Euler, but time-consuming.
- RT4 is more stable than the Euler approach, particularly with a large time step.

Although the RT4 offers a more accurate and reliable approach to the solution of ODEs, a majority of cardiac models employ Euler's technique. The popularity of Euler's model over the fourth-order Runge-Kutta method can be explained by the fact that the former is more suitable for computing APs based on Hodgkin-Huxley type problems; it is easy to apply, causes a low computational load, and results can be obtained in reasonable time on personal computers.

3.4.3 Finite difference method (FDM)

In tissue-level modelling, the excitation-wave propagation can be modelled using the partial differential equations (PDEs) as described by equation (3.38). These PDEs over an N-dimensional space can be solved using the finite-difference method (FDM), which is a simple numerical integration method commonly used to approximate the monodomain equation numerically.[24] In this method it is assumed that the cardiac tissue is divided into a number of nodes. The space between each node is Δx in a 1D direction (X). For instance, if a function $f(x)$ varies with both time and a simple 1D case composed of equal point spacing Δx, the approximated change in position of $f(x)$ at the point $x = x_0$ can be calculated based on Taylor's polynomial theorem as follows.[25]

$$f(x_0 + \Delta x) = f(x_0) + \frac{f'(x_0)}{1!}\Delta x + \frac{f''(x_0)}{2!}\Delta x^2 + \cdots + \frac{f^n(x_0)}{n!}\Delta x^n \qquad (3.62)$$

This equation can be simplified by waiting the first two terms:

$$f(x_0 + \Delta x) = f(x_0) + \Delta x\, f'(x_0) \qquad (3.63)$$

The first-order derivative can be rearranged as:

$$f'(x_0) \approx \frac{f(x_0 + \Delta x) - f(x_0)}{\Delta x} \qquad (3.64)$$

By employing the centred difference, the second-order derivative can be estimated as:

$$f''(x_0) \approx \frac{f(x_0 + \Delta x) + f(x_0 - \Delta x) - 2f(x_0)}{\Delta x^2} \qquad (3.65)$$

By using the second-order approximation term in the monodomain equation (3.38), the initial and subsequent order derivative in the X direction can be expressed as:

$$D\,\frac{d^2V_m}{dx^2} \approx \frac{D}{\partial x^2}\,[\,V_m(x + \Delta x, t) - 2V_m(x, t) + V_m(x - \Delta x, t)\,] \qquad (3.66)$$

Therefore, the numerical equation of the finite monodomain is written as:

$$\frac{dV_m}{dt} = \frac{D}{\Delta x^2}\,[\,V_m(x + \Delta x, t) - 2V_m(x, t) + V_m(x - \Delta x, t) - \frac{I_{ion}}{C_m} \qquad (3.67)$$

In the case of an isotropic monodomain model, the diffusion term is represented as a constant value. Therefore, the formulation of the membrane potential of the x-th cell at time t+Δt can be described by:

$$V_m\ (t+\Delta t) \approx V_m(t) + \frac{D\Delta t}{\Delta x^2}\left(V_m(x+\Delta x,t) - 2V_m(x,t) + V_m(x-\Delta x,t)\right) - \frac{\Delta t\ I_{ion}}{C_m} \tag{3.68}$$

In the case of an anisotropic monodomain model, the diffusion term for equation (3.38) can be expressed as a scalar field:

$$\begin{aligned} & V_m\ (t+\Delta t) \\ & \approx V_m(t) + \frac{D\Delta t}{\Delta x^2}\left(V_m(x+\Delta x,t) - 2V_m(x,t) + V_m(x-\partial x,t)\right) \\ & + \Delta t\left[\frac{\left(V_m(x+\Delta x,t) - V_m(x-\Delta x,t)\right)}{2\Delta x}\right].\left[\frac{D(x+\Delta x,t) - D(x-\Delta x,t)}{2\Delta x}\right] \\ & - \frac{\Delta t I_{ion}}{C_m} \end{aligned} \tag{3.69}$$

The stability of the solution as well as the computational time needed to solve the equation is highly dependent on the choice of space step (Δx), time step (Δt), and diffusion coefficient (D). Thus, to solve the monodomain equation in a stable domain it is important to consider the stability in these related factors in this method based on the condition:

$$\Delta t < \frac{1}{D}\frac{\Delta x^2}{2d} \tag{3.70}$$

In this equation, *d* represents the dimension of the simulation.

References

1. Hodgkin AL, Huxley AF. A quantitative description of membrane current and its application to conduction and excitation in nerve. J Physiol I [Internet]. 1952 [cited 2017 Jul 25];7:500–44. Available from: https://www.ncbi.nlm.nih.gov/pmc/articles/PMC1392413/pdf/jphysiol01442-0106.pdf

2. Schwiening CJ. The Journal of Physiology A brief historical perspective: Hodgkin and Huxley. J Physiol [Internet]. 2012 [cited 2019 May 3];590:2571–5. Available from: https://www.ncbi.nlm.nih.gov/pmc/articles/PMC3424716/pdf/tjp0590-2571.pdf

3. Nobel D. A modification of the Hodgkin--Huxley equations applicable to Purkinje fibre action and pace-maker potentials. J Physiol [Internet]. 1962 Feb [cited 2019 May 3];160(2):317–52. Available from: http://www.ncbi.nlm.nih.gov/pubmed/14480151

4. Keener JP, Sneyd J. Mathematical physiology. Springer; 2009.

5. Plonsey R, Barr RC. Bioelectricity: a quantitative approach. Springer; 2007. p.528.

6. Nelson ME. Electrophysiological Models [Internet]. 2004 [cited 2019 May 23]. Available from: https://www.nada.kth.se/kurser/kth/2D1435/2005/lasmaterial/f1/Nelson.pdf

7. Colman MA. Mechanisms of Atrial Arrhythmias Insights from the Development of a Biophysically Detailed Model of the Human Atria. Springer Theses. Springer International Publishing, Cham. 2014.

8. Kerin NZ, Louridas G, Edelstein J, Levy MN. Interactions among the critical factors affecting sinus node function: the quantitative effects of the duration and frequency of atrial pacing and of vagal and sympathetic stimulation upon overdrive suppression of the sinus node. Am Heart J [Internet]. 1983 Feb 1 [cited 2019 May 23];105(2):215–23. Available from: https://www.sciencedirect.com/science/article/pii/0002870383905161

9. Jänig W. Autonomic Nervous System. Human Physiology [Internet]. 1989 [cited 2019 May 23]. p. 333–70. Available from: http://link.springer.com/10.1007/978-3-642-73831-9_16

10. Robinson BF, Epstein SE, Beiser GD, Braunwald E. Control of Heart Rate by the Autonomic Nervous System. Circ Res [Internet]. 1966 Aug [cited 2019 May 23];19(2):400–11. Available from: https://www.ahajournals.org/doi/10.1161/01.RES.19.2.400

11. Jakob H, Nawrath H, Rupp J. Adrenoceptor-mediated changes of action potential and force of contraction in human isolated ventricular heart muscle Br. J. Pharmacol. [Internet]. 1988 [cited 2019 May 23];94(2):584-590. Available from: https://www.ncbi.nlm.nih.gov/pmc/articles/PMC1853982/pdf/brjpharm00285-0311.pdf

12. Lei M, Brown HF, Terrar DA. Modulation of delayed rectifier potassium current, iK , by isoprenaline in rabbit isolated pacemaker cells. Exp Physiol 2000;85:27–35.

13. Lei, M., Cooper, P. J., Camelliti, P., & Kohl, P. Role of the 293b-sensitive, slowly activating delayed rectifier potassium current, iKs, in pacemaker activity of rabbit isolated sino-atrial node cells. *Cardiovascular Research*.2002: *53*(1); 68–79. https://doi.org/10.1016/S0008-6363(01)00459-X

14. Zhang H, Butters T, Adeniran I, Higham J, Holden A V., Boyett MR, *et al.* Modeling the chronotropic effect of isoprenaline on rabbit sinoatrial node. Front Physiol. 2012;3 JUL(July).

15. DiFrancesco D, Ducouret P, Robinson RB. Muscarinic modulation of cardiac rate at low acetylcholine concentrations. Science [Internet]. 1989 Feb 3 [cited 2019 Mar 8];243(4891):669–71. Available from: http://www.ncbi.nlm.nih.gov/pubmed/2916119

16. Zhang H, Holden AV., Noble D, Boyett MR. Analysis of the Chronotropic Effect of Acetylcholine on Sinoatrial Node Cells. J Cardiovasc Electrophysiol [Internet]. 2002 May 1 [cited 2018 Feb 5];13(5):465–74. Available from: http://doi.wiley.com/10.1046/j.1540-8167.2002.00465.

17. Tung L. A bi-domain model for describing ischemic myocardial d-c potentials. PhD thesis. 1978 [cited 2019 May 23]. Massachusetts Institute of Technology Dept of Elect. Eng and Comp. Sci. Available from: https://dspace.mit.edu/handle/1721.1/16177

18. Vigmond EJ, Weber Dos Santos R, Prassl AJ, Deo M, Plank G. Solvers for the Cardiac Bidomain Equations. Prog Biophys Mol Biol [Internet]. 2008 [cited 2019 May 24];96(1). Available from: https://www.ncbi.nlm.nih.gov/pmc/articles/PMC2881536/pdf/ukmss-29782.pdf

19. Sundnes J. Computing the Electrical Activity in the Heart. 2006 [cited 2019 Nov 14];1:978-3-540-33432–3. Available from: http://link.springer.com/10.1007/3-540-33437-8

20. Benson AP, Aslanidi O V., Zhang H, Holden A V. The canine virtual ventricular wall: A platform for dissecting pharmacological effects on propagation and arrhythmogenesis. Prog Biophys Mol Biol [Internet]. 2008 Jan 1 [cited 2019 May 24];96(1–3):187–208. Available from: https://www.sciencedirect.com/science/article/pii/S0079610707000788

21. Benson AP, Bernus O, Dierckx H, Gilbert SH, Greenwood JP, Holden A V, *et al.* Construction and validation of anisotropic and orthotropic ventricular geometries for quantitative predictive cardiac electrophysiology. [Internet]. 2011 [cited 2019 May 3];1:101–16. Available from: https://www.ncbi.nlm.nih.gov/pmc/articles/PMC3262240/pdf/rsfs20100005.pdf

22. Paul Blanchard. Robert L. Devaney, .Glen R. Hall. Differential Equations [Internet]. Fourth Edition. Andrew Coppola, editor. Boston; 2012 [cited 2019 Nov 14]. Available from: http://dl.konkur.in/post/Book/Paye/Differential-Equations-Blanchard-4th-Edition-%5Bkonkur.in%5D.pdf

23. Süli E. Numerical Solution of Ordinary Differential Equations. Maths Inst, University of Oxford. [Internet]. 2014 [cited 2019 May 24]. Available from: https://people.maths.ox.ac.uk/suli/nsodes.pdf

24. Difference IF, Pdes MFOR. Introductory Finite Difference Methods for PDEs. 2010.

25. Kaw A, Nguyen C, Snyde L. Finite Difference Method for Ordinary Differential Equations.2012. p:1-14.

Chapter Four - Mechanistic Insights into the Reduced Pacemaking Rate of the Rabbit Sinoatrial Node During Postnatal Development: Simulation Study

4.1 Introduction

In many species maturation leads to a decrease in the heart rate (HR).[1] The HR of mammals including humans, rabbits, rats, and dogs,[2,3] decrease with age development; in humans, the heart rate average is between 100-150 beats/ min in the neonate,[4] and 60- 100 beats/ min in the adult.[5]

In normal conditions, the HR is determined by the primary pacemaker of the heart, the sinoatrial node (SAN), which possesses intrinsic pacemaking activity.[2,6,7] Spontaneous APs of the sinoatrial pacemaker cells are produced by ion channels and ion transporters, as well as by the intracellular Ca^{2+} dynamics in SAN myocytes. [2] It has been shown that significant developmental changes in the expression and function of ion channels and other cellular elements may be responsible for a postnatal alteration in the spontaneous activity of the transmembrane potential in single cells isolated from rabbit SAN.[2,8] As compared with neonatal SAN cells, spontaneous APs in adult SAN cells show a reduction in spontaneous beating rate, increases in action potential duration (APD) and the intrinsic cycle length (CL), and an increasingly negative maximal diastolic potential (MDP).[1,9]

Although a number of studies have investigated the ionic basis of automaticity in the adult SAN and the age-dependent factors responsible for the changes in the intrinsic heart rate.[10-14] However, there have been far fewer studies on the basis of automaticity of the neonate or immature node cells.[8,14-18] The mechanism(s) that underlie the different pacemaking activities between the neonatal and the adult SAN are unclear, though a number of recent studies have stated categorically that the ionic basis of automaticity in neonate mammalian cells is distinct from that in the adult.[1,14,19]

Prior studies on the developing SAN in rabbits have revealed that the sodium current, I_{Na}, [16,17] and pacemaker current, I_f, [8,18] are associated with an age-dependent decrease of SAN automaticity, as the two currents have been shown to be greater in the

neonate than in the adult. In contrast, the opposite was observed for L-type Ca^{2+} current, $I_{Ca,L}$ [19,20], as the contribution from this current to the automaticity increased in the central cells of adult SAN in rabbits compared with that in the neonate. This may reflect species differences.[21]

Although experimental information regarding age-dependent changes in potassium and other transmembrane currents within the sinoatrial node is lacking, there are experimental data that have considered a molecular marker on other relevant parameters and highlighted the key differences between neonates and adults, including an increase in the fibroblast content of the node and a lack of expression of connexions [14,22], each of which may produce alterations to the electrophysiological properties of the cardiac tissues.

It is unclear whether these differences could account for the different pacemaking activities between the neonate and adult SAN. Computer-based modelling approaches have proved to be powerful tools to gain a further understanding of the behaviour and complexity of electrical, mechanical, structural, and genetic mechanisms of the pacemaker activities in healthy animals [23], and during the development of arrhythmia,[24] They have also offered a means to predict quantitatively the functional roles of altered molecular dynamics and ionic channels in a systematic way that is otherwise difficult to achieve in an experimental setting at the level of ion channels, cells and tissues.[9] These models have usually been constructed and validated against experimental data, and so these approaches are considered reliable.[25]

In this study, we aim to provide a framework to consider the developmental maturation of the rabbit SAN at the single cell level. The project is based on combining different experimental findings from voltage clamp experiments with findings of gene expression of the ion-channel currents and intracellular calcium handling. The objective of this study was to investigate how changes in the expression and function of different ion channels and other cellular elements can contribute to the alteration of the spontaneous AP waveform of the SAN cells and therefore slow the heart rate at the single-cell level of the adult heart. In addition, we have updated a 2D model of the intact SAN and surrounding atrial tissue to determine the functional impact of age-dependent changes in electrical coupling through connexins on the initiation and conduction of SAN APs, and their conduction into the atrium.

4.2 Methods

A framework for investigating the underlying mechanism of fast heart rhythm in the neonate rabbit SA node cells, the ion channel remodelling and intracellular Ca^{2+} handling changes was developed by updating: (1) the electrophysiologically detailed central and peripheral SAN cell models developed by Zhang *et al.*[26] at the single cell level; (2) a 2D anatomical model of the intact SAN-atrium tissue developed by Butters *et al.* [27,28], which incorporated tissue geometry for SAN and the right atrium (RA), including the crista terminalis (CT).[29] These models represented the healthy adult rabbit. Therefore, based on the literature review on the neonate ion channels as summarised in Table 4.1, both models were modified at the single cell and tissue level in order to represent two age groups: neonate and adult.

4.2.1 Model development at the single-cell level

The single-cell models developed by Zhang *et al.*[26], as based on experimental data from isolated rabbit SAN preparations, were used as basal models. In brief, the model was developed to calculate the membrane potential of rabbit SAN cells using Hodgkin-Huxley formulations of ionic currents (see Equation 4.1) at body temperature (37°C). The model consisted of 39 coupled ordinary differential equations (ODEs) that described voltage-gated ion-channel currents, exchanger currents, and an ionic pump (see Equation 4.2) at a cell capacitance of 20pF in the central cells and 65pF in the periphery. The model was solved numerically with a time step of 0.01ms.

$$\frac{dV_m}{dt} = -\frac{1}{C_m} \; I_{\text{tot}} \tag{4.1}$$

$$I_{\text{tot}} = (I_{\text{Na}+} I_{\text{Ca,T}} + I_{\text{Ca,L}} + I_{\text{Kr}} + I_{\text{Ks}} + I_{\text{to}} + I_{\text{sus}} + I_{\text{f}} + I_{\text{b}} + I_{\text{NaK}} + I_{\text{NaCa}}) \tag{4.2}$$

In order to model the AP of the SAN cell of neonatal rabbits, the conductances and kinetics of some of the main ionic channel currents responsible for cellular depolarisation and repolarisation were adjusted, based on a comprehensive literature review of the voltage-clamp experiment data of certain ion-channel currents, such as, $I_{\text{Ca,L}}$ and I_{f}, and gene expression levels of different ion channels, such as I_{Ks}, I_{Kr} and I_{NaCa}, on the neonatal rabbit SAN (see Table 4.1). The integral (inclusive) effect of different ion channels on the APs was simulated and validated by the experimental observations. [16,30]. Table 4.2 and Table 4.3 summarise the two age groups' current densities and

conductances of the central SAN, which matched the experimental observations. Subsequently, the individual (exclusive) effect of each ion current change was individually investigated to determine the major contributor to the greater heart rate of the neonate.

4.2.2 The modelling of I_{Na} in the neonatal rabbit SAN

The sodium-channel current, I_{Na}, is considered to be the main ion channel responsible for the upstroke phase of the APs in non-pacemaking cells.[2] The sodium current is not detected in the central cells of the adult SAN of the rabbit, and therefore this current does not contribute to the slow APs of the central cells of the SAN in adult rabbits.[2,26] In contrast, according to Baruscotti *et al.*[16], voltage clamp measurements from neonatal born SAN cells revealed the presence of sodium-channel current. This ion-channel current decreased gradually to disappear 40 days after birth. Of further interest are the results comparison between the I_{Na} current in the neonate with young isolated cells from rabbit SAN.[16] The sodium-channel current density in the young cells was about 76% reduced from that observed in the neonate, and it ultimately reduced to zero in the adult. There was also a rightward shift of the activation curve (midpoint changed by 7mV from neonate to young) and little or no alteration of the inactivation curve (see Table 4.1). Consistent with this, quantitative PCR analysis of the mRNA of neonatal and adult SAN rabbit cells showed a relative abundance of the isoforms Nav1.1 and Nav1.5 in the neonate rabbit SAN cells, which significantly decreased during postnatal development.[30] It is not yet clear if/how such a decreased I_{Na} helps to explain the slowing of the heart rate with age.

To model the postnatal development of the sodium-channel current in rabbit SAN, age-dependent I_{Na} equations were developed based on experimental data from both newborn and young rabbit SAN cells. In the developed model, the steady-state activation and inactivation curves for neonate and young rabbit SAN cells reported in Baruscotti *et al.*[16] were fitted, , taking into account the shift in the steady-state activation midpoints (as seen in Figures 4.1A-B). These experimental data were obtained at room temperature (20-22°C) while the model was developed at body temperature (37°C) , therefore, a Q_{1O} of 1.7 correction of the current density was considered accounting for the temperature difference.[26,31] The maximal channel conductance of the sodium current ($g_{Na,max}$) was determined by reproducing the experimental data for the I-V relationship.[16] The equations that were developed and choice of parameters were validated by the model's

ability to reproduce voltage-clamp data for the I_{Na} channel, using the following voltage-clamp protocols as used in the experiments: the I_{Na} current was recorded from a holding potential of -65mV by applying a series of testing potentials that each lasted 10ms and were varied between -60mV and +45mV in 5mV increments (see Figure 4.1C). According to the experimental data reported in Table 4.2, these age-related I_{Na} equations were then incorporated into the Zhang SAN model.[26] Figure 4.1D shows the simulated I-V currents for both neonate and young rabbits (black and red lines respectively), which are compared with experimental values (the square points) reported for both neonate and adult rabbits. Simulation data was consistent with the experimental data in showing a peak current density of the neonate I-V curve greater than that of the young, as shown in Table 4.2.

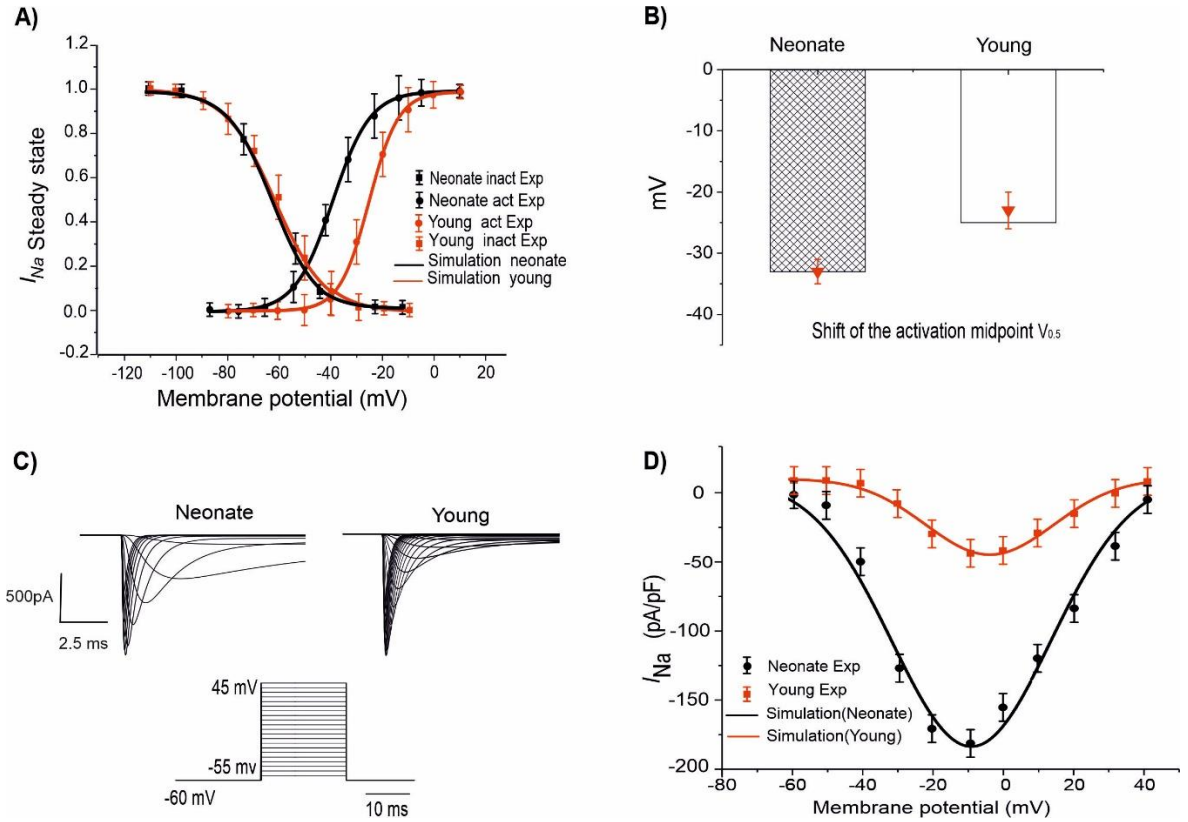

Figure 4.1. Simulation of I_{Na} and validation of the simulation. (A) Model-generated steady-state activation and inactivation curves of the I_{Na} current in two age groups: neonate (black line) and adult (red line), which are compared with experimental data. (B) Shift of the midpoint of the activation and inactivation relations ($V_{0.5}$). (C) Simulated current traces of the I_{Na} in both simulation and experiment for neonate and young SAN cells under the following voltage-clamp protocols: the I_{Na} current was recorded from a holding potential of -60mV by applying a series of testing potentials that each lasted 10ms and were varied between -60mV and +45mV in 5mV increments. (D) Simulated I–V relationship and validation against experimental data by Baruscotti *et al.*[16]

4.2.3 The modelling of I_f

The hyperpolarisation activated current, I_f, is well known as a pacemaking current due to its significant contribution to the pacemaker potential (phase 4) of the AP in the SAN.[32,33] This ionic current consists of sodium, Na^+, and potassium, K^+, ion fluxes, and the channel is comprised of HCN1, HCN2, and HCN4 isoforms, which have been found to be the most abundant isoforms among the various subunits.[34] Postnatal changes of this ion channel in rabbit SAN cells were identified experimentally by Accil *et al.*[18] and Yang *et al.*[8]. According to Accil *et al.*[18], SAN development affects I_f by inducing a decrease in the current density and altering the slope factor of the activation curve of the current, though without changing the midpoint of the activation curve. The decreased I_f is assumed to result from the change to the cAMP during development. In agreement with this, voltage clamp data recorded by Yang *et al.* suggested a relationship between a smaller I_f and the reduced heart rates in adults (12-week-old group) as compared with the neonate group (two weeks old) of the rabbit.[8] The smaller I_f was shown to be attributable to a reduction in the magnitude of the I_f current and a negative shift of the voltage-dependent activation curve (Table 4.1). Moreover, quantitative PCR measurements on the mRNA of the HCN subunit confirmed a 69% reduction in HCN4 expression in adult SAN cells compared with the numbers in neonates.[30] Similar age-induced I_f remodelling during SAN development was also observed in changes of HCN expression in other species, including rats,[35] mice,[1] and canines.[36] These results indicate that the I_f current change with age may be an important contributor to the decline of the SAN function and therefore the decrease in HR. However, this has not yet been shown explicitly.

The role of the remodelled I_f current on the APs of the developing SAN and, therefore, pacemaking activities, was assessed by incorporation of the age-dependent I_f equations into Zhang *et al.*'s model.[26] These age-dependent I_f equations were developed based on experimental data from Yang *et al.*[8] and Accil *et al.*[18], and the model was validated by their ability to reproduce the experimental data derived for the voltage-clamp on the channel. Results are shown in Figure 4.2 for neonatal and adult I_f taking into account the age-related negative shift of the activation midpoint by 7mV based on the experimental data from Yang *et al.*[8] (see Figures 4.2A-B), as well as an increase in the maximal conductances of g_f (e.g. g_{Na}, $g_{f,K}$) by 70%. The time constant for the activation of I_f in neonates was similar to that of adults in the Zhang *et al.* model.[26]

The simulated current traces for the I_f current in both neonate and adult SAN cells were obtained under the following voltage-clamp protocols: the I_f current was recorded from a holding potential of -35mV by applying a series of testing potentials lasting for 600ms and were varied between -45mV and -105mV in 10mV increments at 36^{o}C, as shown in Figure 4.2C. The resultant I-V curve (Figure 4.2D) showed reasonable agreement between the simulation and experimental data obtained for both neonatal and adult cells. The peak current-voltage relationships for I_f from the central SAN cell model in neonates (black line) and adults (red line) are shown in Figure 4.2D, and these were validated against experimental data reported by Protas *et al.*[36] and Honjo *et al.*[37]

4.2.4 Calcium currents and remodelling

In the SAN cells, two types of Ca^{2+} current are present: L-Type and T-Type, which were activated at relatively low and high voltages, respectively.[38] The contributions made by these currents to the pacemaking AP of the rabbit SAN cells have been investigated previously. [2] The L-type calcium current was found to be a major contributor to the phase 0 (upstroke) of the APs, either alone in the central cells of adult rabbits' SAN or in combination with the I_{Na} current in peripheral SAN cells, in addition to its contribution to the late diastolic depolarisation phase of the adult rabbit SAN cells spontaneous AP. [14,39-41] A comparative analysis of the postnatal changes of Ca^{2+} ion currents $I_{Ca,T}$ and $I_{Ca,L}$ in central cells of the rabbit SAN was carried out by Protas *et al.*[20] It was shown that there were no developmental changes in recorded $I_{Ca,T}$ densities, suggesting that, although it contributes to the automaticity of rabbit SAN cells, $I_{Ca,T}$ is not a critical determinant of age-dependent changes the SAN pacemaking.

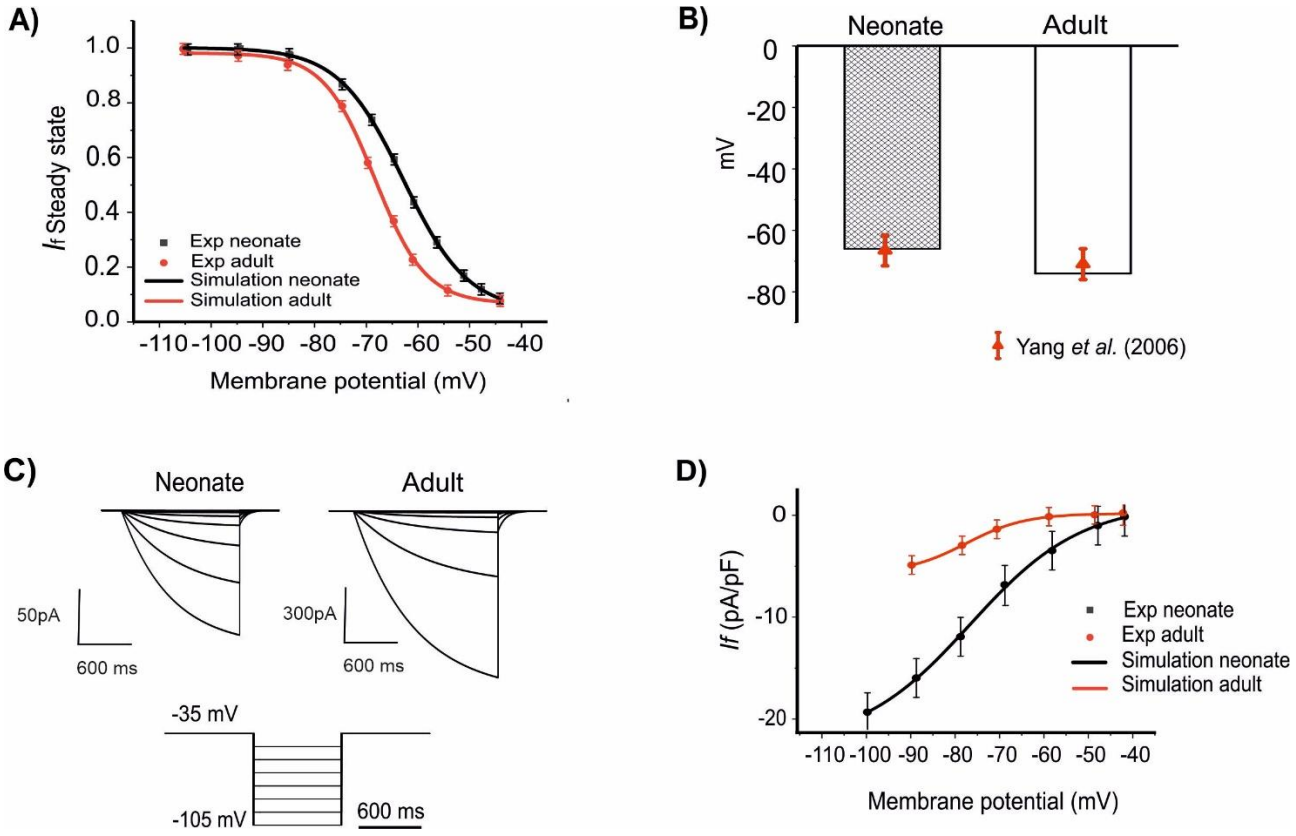

Figure 4.2. Model of I_f and comparison with experimental data. (A) The steady-state activation curves for the I_f current for two age groups: neonates (black line) and adults (red line). (B) Shift of the midpoint of the activation relation. (C) Simulated current traces of the I_f current in both neonate and adult SAN cells under the following voltage-clamp protocols: I_f current was recorded from a holding potential of -35mV by applying a series of testing potentials that each lasted 600ms and were varied between -45mV and -105mV in 10mV increments. (D) Simulated I–V relationship. Results are validated against experimental data reported by Yang *et al.*[8], Protas *et al.*[36] and Honjo *et al.*[37].

There is experimental evidence for the reduction of $I_{Ca,L}$ with age [20]; in particular, a 42% reduction in the current density of $I_{Ca,L}$ has been seen in adults as compared to neonates. However, this was accompanied by a rightward shift of the inactivation curve (midpoint changed by 5mV in adults), and a leftward shift of the activation curve (midpoint changed by 5mV in adults), leading to an increase in the window current (the overlap between the activation and inactivation steady-state curves). The increased window current in the adult would suggest a greater contribution of this current to pacemaking in the adult as compared to the neonate. Additional support for this hypothesis comes from the findings of Jones *et al.*[19], who observed a progressive loss of Cav1.2 with age in guinea-pig SAN. Moreover, molecular identification of the ion channels at the protein level showed an association between heartbeat decline and decrease in $I_{Ca,L}$ transcript by 58% in developing SAN rabbit cells.[30]

To investigate if/how $I_{Ca,L}$ influences age-dependent changes SAN activity development, a model for neonatal $I_{Ca,L}$ was developed, based on the above-mentioned experimental data reported by Protas *et al.*[20] Figure 4.3A illustrates the simulated fitted activation and inactivation of the steady-state curves for neonates (black lines) and adults (red lines). The I-V relationship was computed from the model using a voltage clamp protocol with 10 mV incrementing steps between -60mV and 60mV of 300ms duration, at a temperature of 36°C. The established I-V relationship curve for the $I_{Ca,L}$ of neonate and adult rabbit SAN is illustrated in Figure 4.3D. The magnitude of the neonate (black line) peak current density, 17.30pA/pF, was considerably larger than the peak current density in adults of 12.32pA/pF (see Table 4.3). This result was comparable with values recorded experimentally.[20]

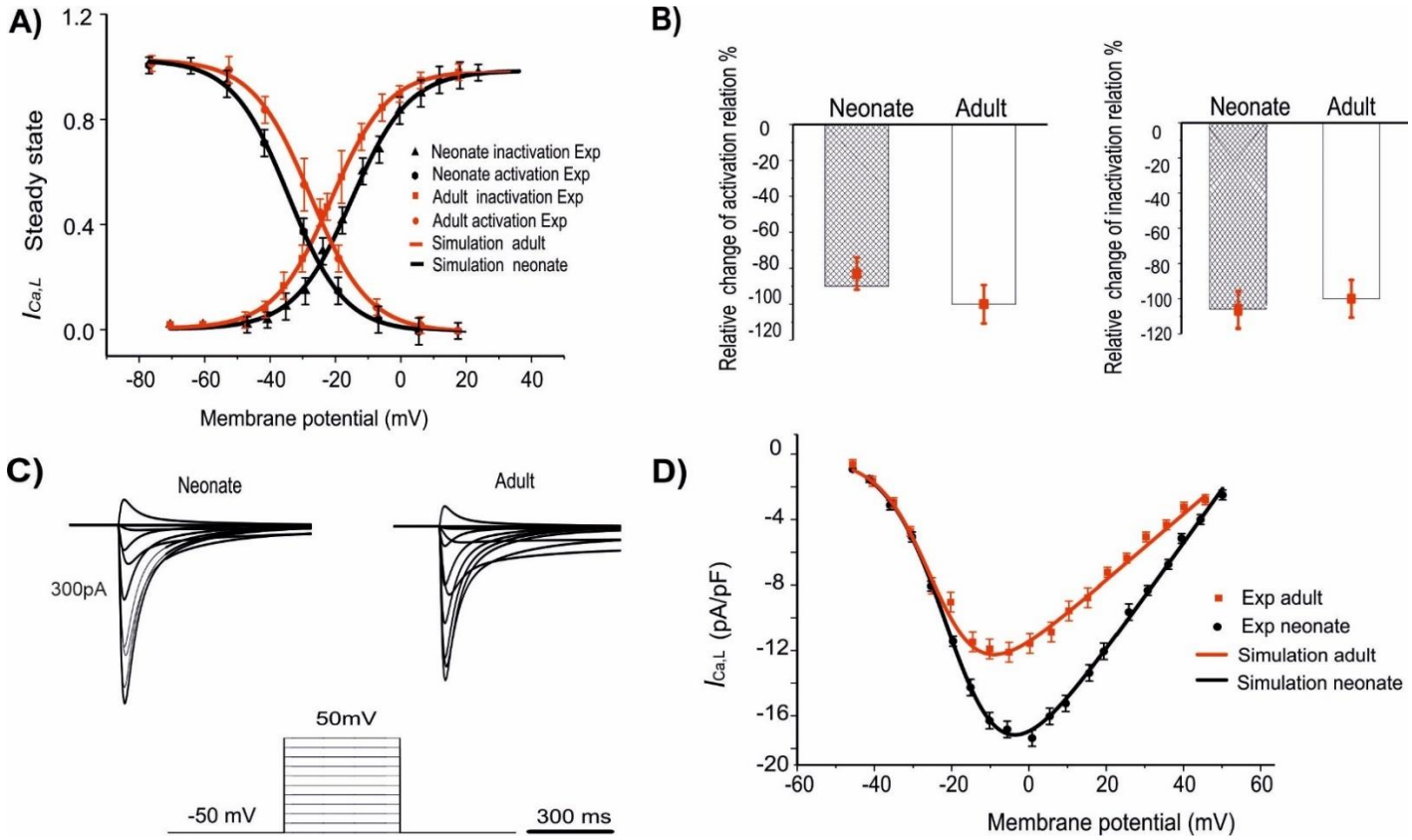

Figure 4.3. Simulation of ICa,L and validation of the simulation. (A) The fitted steady-state activation and inactivation gate curves of the ICa,L current in two age groups: neonates (black line) and adults (red line). (B) The bar chart shows the shifted activation and in activated midpoints. (C) The simulated current traces of the ICa,L current in both neonate and adult SAN cells with the voltage-clamp protocols as shown at the bottom of the diagram. (D) Simulated voltage-clamp protocol used to determine I–V relationship. Results validated against experimental data reported by Protas et al.[20].

Table 4.1. Summary of differences in current densities and kinetic parameters of ion channels between newborn and adult central SAN cells for multiple species. Available data regarding relative abundance of mRNAs that code for some ion channels between neonatal and adult cells are also listed.

Ion channel	Current density (pA/pF)		Midpoint potential for the activation curve (mV)		Midpoint potential for the inactivation curve (mV)		Change in relative abundance of mRNAs for ion channel in central SAN	Species	References
	Neonate	Adult	Neonate	Adult	Neonate	Adult			
I_{Na}	68.51±16.0	9.00±0.3	-38±2.2	-37.50±0.9	-89.70±0.7	-93.42±1.9	-	Canine	(Protas, 2010) [36]
	180.55±16.0	0.00±0.0	-33.9+0.7	-23.21±0.8	-63.51±1.0	-61.75±1.1	-	Rabbit	(Baruscotti,1996) [16]
	-	-	-		-	-	↑ + 64 %	Rabbit	(Allah, 2011) [30]
I_f	-	-	-68.5±4.0	-63.20±0.6	-	-	-	Rabbit	(Yang, 2006) [8]
	0.24±1.5	0.15±0.1	-	-	-	-	-	Rabbit	(Accili, 1997) [18]
	17.23±6.2	9.60±1.0	-82.9±5.2	-84.13±2.9	-	-	-	Canine	(Protas, 2010) [36]
	-	-	-104.7±3.1	-110.66±3.2	-		-	Mouse	(Larson, 2013) [1]
	-		-		-		HCN2↑ +31% HCN4↑ +24%	Rat	(Huang, 2016) [35]

Ion channel	Current density (pA/pF)		Midpoint of the activation curve (mV)		Midpoint of the inactivation curve (mV)		Change in relative abundance of mRNAs for ion channel in central SAN	Species	References
	Neonate	Adult	Neonate	Adult	Neonate	Adult			
$I_{Ca,L}$	17.61±2.5	12.31±1.4	-17.33±1.4	-22.00±0.8	-33.41±1.4	-28.31±1.7	-	Rabbit	(Protas, 2001) [20]
	-	-	-	-	-	-	↑ +42%	Rabbit	(Allah, 2011) [30]
	9.02±3.1	4.60±2.6	-	-	-	-	-	Mouse	(Larson, 2013) [1]
$I_{Ca,T}$	4.55±0.0	4.52±0.0	-33.00± 2.2	-35.11± 2.0	-65.00 ± 2.1	-65.09 ± 2.4	-	Rabbit	(Protas, 2001) [20]
	9.10±2.6	6.36±2.7	-		-	-	-	Mouse	(Larson, 2013) [1]
I_{Kr}	-		-		-		↑ +36%	Rabbit	(Allah, 2011) [30]
I_{Ks}	-		-		-		↑ +27 %	Rabbit	
I_{NaCa}	-		-		-		↑ +66 %	Rabbit	
$I_{K,ACh}$	-		-		-		↑ +60 %	Rabbit	
Cx43	-		-		-		↑ +60 %	Guinea-pig	(Jones, 2004) [19]

4.2.5 I_{NaCa} and remodelling

NCX is believed to be functionally important for pacemaking activity through the release of Ca^{2+} from the SR during late diastole and the consequent activation of the inward Na^{+}–Ca^{2+} exchange current, I_{NaCa}.[7] In the SAN, it was observed that the expression of NCX1 for both mRNA and protein levels was more abundant in the neonate than the adult.[30] In addition, the expression of NCX1 protein was different between the neonate and the adult. This decrease in NCX1 abundance with age suggests a correlation with the decrease in the heart rate during postnatal development.[30] In addition, the expression of NCX1 protein was different in the neonate and the adult. This decrease in NCX1 abundance with age suggests a correlation with the decrease in the heart rate during postnatal development. Consistent with this, several previous studies have observed a similar postnatal decrease in NCX1 in rabbit ventricles, [42-45], rabbit whole hearts[42] and human ventricles.[46] In our model, the I_{NaCa} of the rabbit SAN cells was considered to be greater in neonates compared to adults; therefore, based on Allah *et al.*[30], the magnitude of the I_{NaCa} current density was adjusted by multiplying the maximal value of the scaling factor for I_{NaCa} by a ratio of 1.66, as summarised in Table 4.1 and Table 4.2.

4.2.6 Modelling of the rapid/ slow delayed rectifier K^{+} currents: I_{Kr} / I_{Ks}

There are two components of the potassium delayed rectifier current in rabbit SAN cells: rapidly activating current (I_{Kr}) and slowly activating current (I_{Ks}). These outward currents are crucial during the repolarisation phase of the APs in the SAN. For the neonate condition, limited voltage-clamp experiments for these currents are reported in the literature. However, the postnatal developmental changes have been investigated in the expression of different ion channels in the SAN, including these two components, using quantitative PCR, *in situ* hybridisation and immunohistochemistry from neonatal (two-seven days of age) and adult(~six months of age) New Zealand White rabbits [30]. The results showed that the mRNA expression of ERG (responsible for I_{Kr}) and both KvLQT1 and minK (responsible for I_{Ks}) were more abundant in the SAN compared with the left ventricle for both neonate and adult cases. It was also found that there was a postnatal reduction in mRNAs associated with delayed rectifier K^{+} channels by 36% for the ERG and 27% for the KvLQT1 in the SAN. Therefore, for the purposes of our

simulation, the ratios of the I_{Kr} and I_{Ks} maximal conductances of neonate to adult were adjusted by multiplying these ratios by 1.36 and 1.27 as factors in the conductance in the neonatal SAN model, respectively (see Table 4.1 and Table 4.2).

Table 4.2. Implemented conductances of different ion-channel currents in the neonate and adult central SAN cell models based on experimental data as listed in Table 4.1.

Ion current	Conductance		
	Neonate	Adult	Ratio (neonate/adult)
g_{Na}	0.5350×10^{-6} µS	0	∞
$g_{Ca,L}$	0.841×10^{-2} µS	0.58×10^{-2} µS	1.45
$g_{K,r}$	10.839×10^{-4} µS	7.97×10^{-4} µS	1.34
$g_{K,s}$	6.57×10^{-4} µS	5.18×10^{-4} µS	1.27
$g_{f,Na}$	9.5725×10^{-4} µS	5.47×10^{-4} µS	1.75
$g_{f,K}$	9.5725×10^{-4} µS	5.47×10^{-4} µS	1.75
K_{NaCa}	0.4482×10^{-5} nA	0.27×10^{-5} nA	1.66

Table 4.3. Current densities in the neonate and adult central SAN cell models.

Ion current	Current density, pA/pF		
	Neonate (simulation)	Neonate (experimental)	Adult
I_{Na}	179.56	180.5±16	0.0
$I_{Ca,L}$	17.58	17.6±2.5	12.23
I_f	17.45	17.2±6.2	3.36
I_{Ks}	0.84	-	0.66
I_{Kr}	1.07	-	0.97
I_{NaCa}	0.22	-	0.13

4.2.7 Acetylcholine-activated potassium current: $I_{K,ACh}$

Acetylcholine (ACh) is a neurotransmitter which has a chronotropic effect opposite to that of (nor)adrenaline. It is released from the vagal nerve terminals in the SAN, leading to a negative chronotropic effect which appears as a significant reduction in the HR. The effects of ACh on the HR and CL in both age groups for SAN cells in rabbits are described. The contribution of acetylcholine (ACh) was included in the adult model as a new ionic current, $I_{K,ACh}$, also known as the acetylcholine-activated potassium current. The formulation for this current has been given by Zhang *et al.*[47] as:

$$I_{K,ACh} = g_{K,ACh} * \left(\frac{[K]_e}{10 + [K]_e}\right) * ((V_m - E_K)/1 + \exp[V_m - E_K - 140)F/2.5RT]) \quad (4.3)$$

in which $g_{K,ACh}$ is the conductance; $I_{K,ACh}$ is the ionic current; F and R are the Faraday and universal gas constants, respectively; $[K]_e$ is the extracellular concentration of K^+; V_m is the membrane potential; and E_K is the reversal potential for K^+.

The conductance $g_{K,ACh}$ is given by:

$$g_{K,ACh} = g_{K,ACh\,max} * j\ k * \frac{[ACh]^{nK,ACh}}{K_{0.5,K,ACh}^{nK,ACh} + [ACh]^{nK,ACh}} \quad (4.4)$$

where *j*, *k* refer to the inactivation variables (fast and slow, respectively); $g_{K,ACh\,max}$ is the maximum value of $g_{K,ACh}$; $n_{K,ACh}$ is the Hill coefficient; $K_{0.5,K,ACh}$ is the concentration of ACh that produces a half-maximal activation; and $[ACh]$ is the molar concentration of ACh.

The voltage-dependent inactivation variables *j* and *k* are ODEs of the form given in the following equations:

$$\frac{dj}{dt} = \alpha_j\ (j - 1) - \beta_j\, j \quad (4.5)$$

$$\frac{dk}{dt} = \alpha_k\ (1 - k) - \beta_k\, k \quad (4.6)$$

In these equations, α_j, β_j ,α_k, and β_k are rate constants. The constants α_k and α_j represent voltage-independent constants given by $3.7s^{-1}$and $73.1s^{-1}$, respectively. However, the voltage-dependent constants β_j , and β_k are given by:

$$\beta_j = \frac{120}{1 + \exp(-(v_m + 50)/15)} \quad (4.7)$$

$$\beta_k = \frac{5.82}{1 + \exp(-(v_m + 50)/15)} \quad (4.8)$$

The equation that describes the change of time dependence of the membrane potential is as follows:

$$\frac{dV_m}{dt} = -\frac{I_{tot} + I_{K,ACh}}{C_m} \quad (4.9)$$

in which I_{tot} is the net magnitude of the various ionic currents.

The incorporation of ACh into our model incorporated two additional effects on ionic currents: a shift in the activation curve for the funny current, I_f, and the fractional block of $I_{Ca,L}$, the L-type Ca^{2+} channel.[47]

ACh causes a shift in the activation curve (mV) of the funny current I_f to a more negative potential as follows:

$$S = S_{max} * \frac{[ACh]^{nf}}{K_{0.5,f}^{nf} + [ACh]^{nf}} \quad (4.10)$$

In this equation, S_{max} refers to the maximum shift of the I_f activation curve; $K_{0.5,f}$ is the ACh concentration that produces a half-maximal shift in the funny current activation curve; and nf is the Hill coefficient. This was factored into the model by subtracting s from the exponent in the Boltzmann equation for the steady-state gating variables of the funny current.

The activated ACh also leads to a partial depression of $I_{Ca,L}$, which is given by a dimensionless quantity:

$$b = b_{max} * \frac{[ACh]}{K_{0.5,Ca} + [ACh]} \quad (4.11)$$

where b_{max} is the maximum fractional block of $I_{Ca,L}$, and $K_{0.5,Ca}$ is the concentration of ACh that produces a half-maximal block of $I_{Ca,L}$. This depression can be included in the model by multiplying the $I_{Ca,L}$ ionic current by (1- b).

For the neonatal condition, it was found in patch clamp experiments that the neonatal SAN cells exhibited particular sensitivity to autonomic stimulation compared with adult SAN cells, through the patch-clamp technique. Accili *et al.*[18] examined the activation curves of the I_f in neonate and adult rabbit cells. The investigation showed that cells in both groups exhibited similar shifts in the I_f activation relation of the wild type of SAN in response to maximal concentrations of acetylcholine. Therefore, it was suggested that the greater heart rate and the greater sensitivity of the SAN to ACh was partly the result of the greater magnitude of the hyperpolarisation-activated current (I_f). Another study[30], which measured changes in the mRNA expression of Kir3.1 that is responsible for $I_{K,ACh}$, found that the relative abundance of mRNAs for Kir3.1 in the SAN was greater (60%) than in the right atrium and left ventricles in the neonates, but not in the adults. In order to model the effect of ACh, the dose dependency of ACh-affected ion channels, including $I_{K,ACh}$, $I_{Ca,L}$, and I_f, were considered and incorporated into our newly developed neonate (central and peripheral) SAN models, while taking into consideration the fact that $g_{K,ACh}$ is greater in neonates (60%) by incorporating this percentage as a factor in $g_{K,ACh}$.

4.2.8 Tissue model for AP propagations

In order to investigate the consequences of postnatal changes due to different ion-channel properties on the propagation and conduction in the intact SAN-atrium, we used the reconstructed 2D anatomical model of the intact SAN-atrium tissue described in previous study [27] This model provided valuable insight into the behaviour of the SAN and surrounding tissues in healthy adult rabbits.[27] The model was designed to consider the heterogeneities of the AP characteristics and the anisotropy of the tissue, including distinct regions of the SAN-atrium together with central and peripheral cells of the SAN, and atria. The models introduced by Zhang *et al.*[26] were used for both the central and peripheral SAN cells. The model produced by Aslanidi *et al.*[48] was used to represent the AP of the right atria cells. The geometry of the 2D model was extracted using histological and immunohistochemistry-imaging data from anatomical models of rabbit SAN cells.[38] The geometry represented the whole intact SAN-atrium meshing from the endo-cardiac surface with a high spatial resolution of 0.04 mm to form a Cartesian grid which was divided into 385 × 250 nodes. [27,29]

Since the intact SAN-atrial tissue is anisotropic, the 2D model was produced to consider the local variations of the diffusion coefficient (*D*), which determines the conduction velocity. This was performed by incorporating the gradient distribution of the diffusion (*D*) in both the longitudinal and transverse directions. The regional differences in cell-membrane capacitance (C_m) in the SAN-atrium tissue were also introduced according to Zhang *et al.*'s model.[26] (Figure 4.4A-B).The spatial distributions of current densities for different ion channels were correlated with the cell membrane capacitance (C_m), which increased gradually from the centre to the periphery of the SAN.[49] The 2D model used the monodomain equation to simulate the propagation of the AP and describe the transmembrane potential changes with time. The equation was solved using the finite partial differential equation (PDE) solver with a time step of 0.01ms and space step of 0.04 mm, which gave accurate numerical solutions. [27,29]

To investigate the functional impact of postnatal development in the intact SAN-atrium at the tissue level, the 2D model for the SAN-atrium at the tissue level was used to simulate both the neonatal and adult conditions. In the instance of the neonate, the electrophysiology of the cells in the 2D model was adjusted in the same way as for the single-cell level. In addition, changes to intercellular coupling that arose from the connexin remodelling were considered, as explained in the following section. Further, the pacemaking activity of the AP propagation, activation time and conduction velocity were analysed, as presented in the results section.

4.2.9 Remodelling of connexins

Researchers have proposed that connexins play a critical role in intercellular electrical coupling through the movement of ion channels and intracellular exchange via the gap junction.[50] In the SAN tissue, Dobrzynski *et al.*[2] found that Cx43 was present in the peripheral cells of adult rabbits. Another study measured the relative abundance of each Cx43, Cx40 and Cx45 in different tissues including the SAN, right atrium and left ventricle of the rabbit heart, from birth to adulthood. These measurements showed that the Cx45 protein was distributed similarly in the different tissues but at decreased levels in the adult; only 45% of that found in adult compared to neonates.[30] This observation was corroborated by Jones *et al.*'s [22] study of guinea-pig SAN cells for different age groups; results of this study revealed a substantial rearrangement of Cx43, showing a 60% decrease in Cx43 levels in adults compared with neonates (see Figure

4.5).Therefore, in this simulation, the connexin remodelling was considered by applying the guinea-pig data above to represent the neonate condition of rabbit SAN cells. This was achieved by adjustment of the diffusion coefficient values, which represented the electrical coupling within the 2D tissue

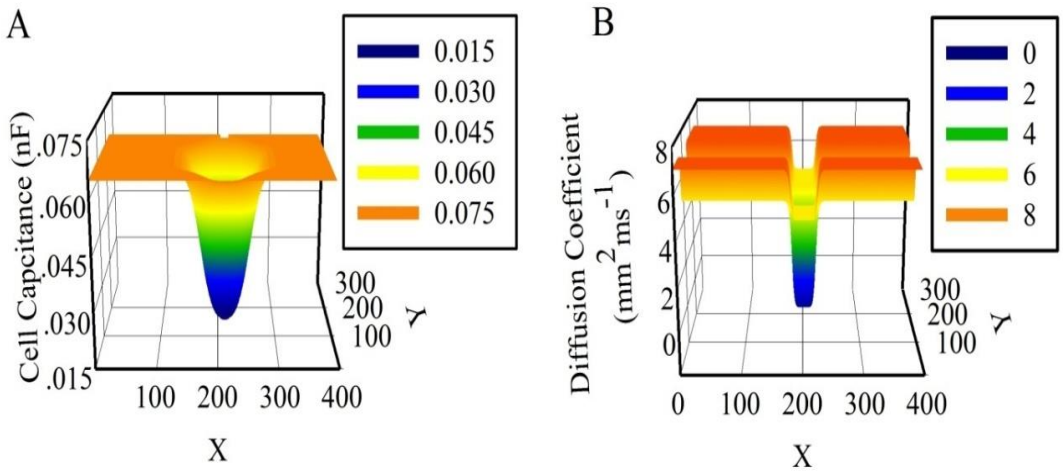

Figure 4.4. The gradient distribution in (A) cell capacitance (C_m) and (B) diffusion D in both longitudinal and transverse directions of the 2D tissue slice. Figure adapted from [28].

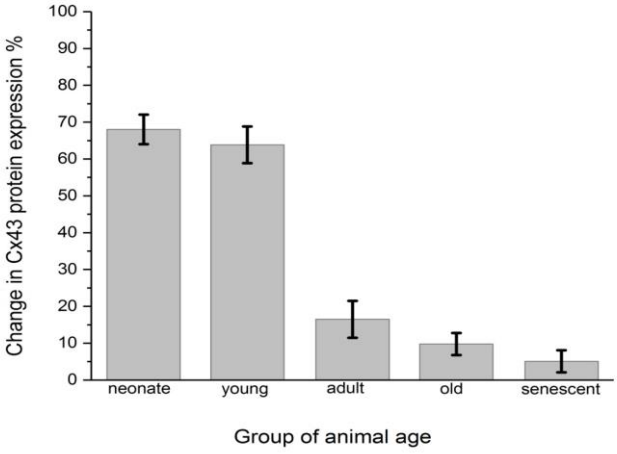

Figure 4.5. The decline of the Cx43 protein expression in the SAN of rat represented as percentage during age development.[22] The expression of the junctional protein Cx43 in the SAN of Duncan-Hartley guinea pigs were evaluated by immunofluorescence analysis. The area lacking Cx43 signal, calculated from 2D reconstruction of the whole SAN obtained from sequential slices, increased linearly with the age of the animal. The quantification of the expression of Cx43 was accomplished by Western blot and densitometric analysis and normalized to desmin expression, which is not influenced by development or aging.

4.3 Results

4.3.1 The integral effects of ion-channel remodelling during the development of the SAN at the single cell level

Age-related remodelling of the different ion channels (I_{Na}, $I_{Ca,L}$, I_f, I_{Kr}, I_{Ks} and I_{NaCa}) was incorporated into the adult single-cell model of the central SAN developed by Zhang *et al.* [26] Figure 4.6 illustrates the simulated APs and time course of age-remodelled ionic channel currents for the neonatal condition, which were superimposed on those from the adult condition, for the central SAN model. The simulation results showed that the neonatal model reproduces the characteristic AP shapes of neonatal cells as compared with the adult equivalent.

In general, the neonatal APs had faster spontaneous activities, shorter durations and greater amplitudes than the adult. The resultant CL (the time interval between two successive pacemaking APs) for the neonatal SAN was smaller than the CL in adults: 277ms in the neonate compared with 327ms in the adult, which showed an 18% prolongation of CL with age. The computed maximal upstroke velocity of AP (dV/dt_{max}) was 11.9V/s in the neonate compared with 2.7V/s in the adult condition. The greater dV/dt_{max} in the neonatal SAN cells can be attributed to the presence of the I_{Na}. The action potential peak amplitude, PA, of the neonate was greater than that of the adult (32mV compared with 21mV) in the central SAN model. This is consistent with experimental observations, as summarised in Table 4.4.

Our simulation showed a reduction of spontaneous AP rate with development, with the measured pacemaking rate of 217 min^{-1} in neonates and 170 min^{-1} in adults (Figure 4.7). The simulation results were in agreement with the experimental observations, which showed that the heartbeat of the rabbit SAN was around 200±50min^{-1} for neonates, but then reduced by 21.6% in the adult.[30] The bar charts in Figure 4.7 show a comparison of the AP characteristics of the neonatal and adult central SAN from simulations, which quantitatively matched to experimental data, validating the model development. The simulated time course of the major ion-channel currents in both neonate and adult states of the central rabbit SAN cells are also included in Figure 4.6. As most available experimental data were acquired in the central SAN cells of neonatal rabbits, data on the peripheral SAN cells were lacking.

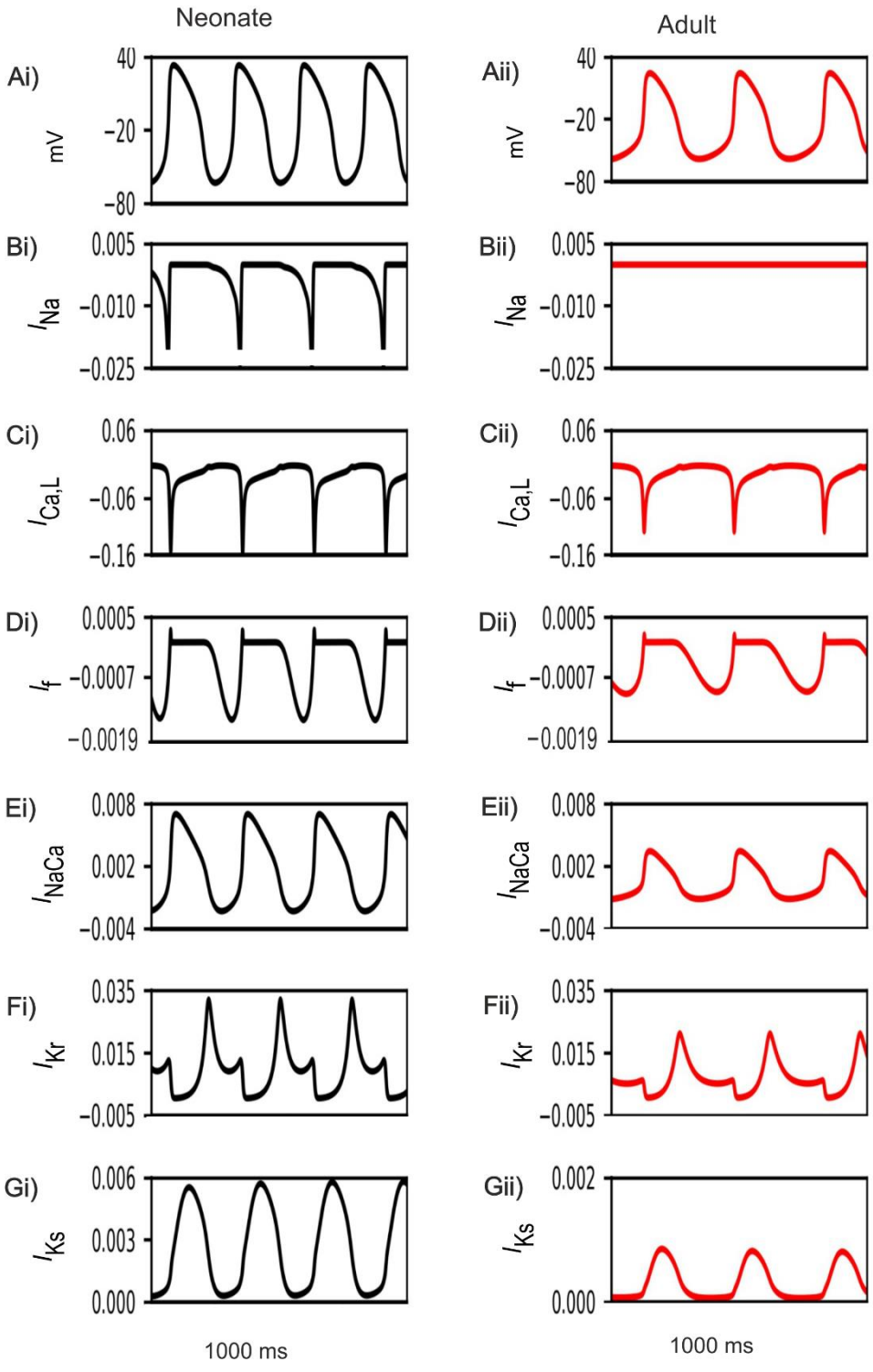

Figure 4.6. (Ai-Aii) Simulated central SAN action potentials in the neonate (black lines) and adult (red lines) and (Bi-Gii) underlying ionic currents I_{Na}, $I_{Ca,L}$, I_f, I_{NaCa}, I_{Kr} and I_{Ks}.

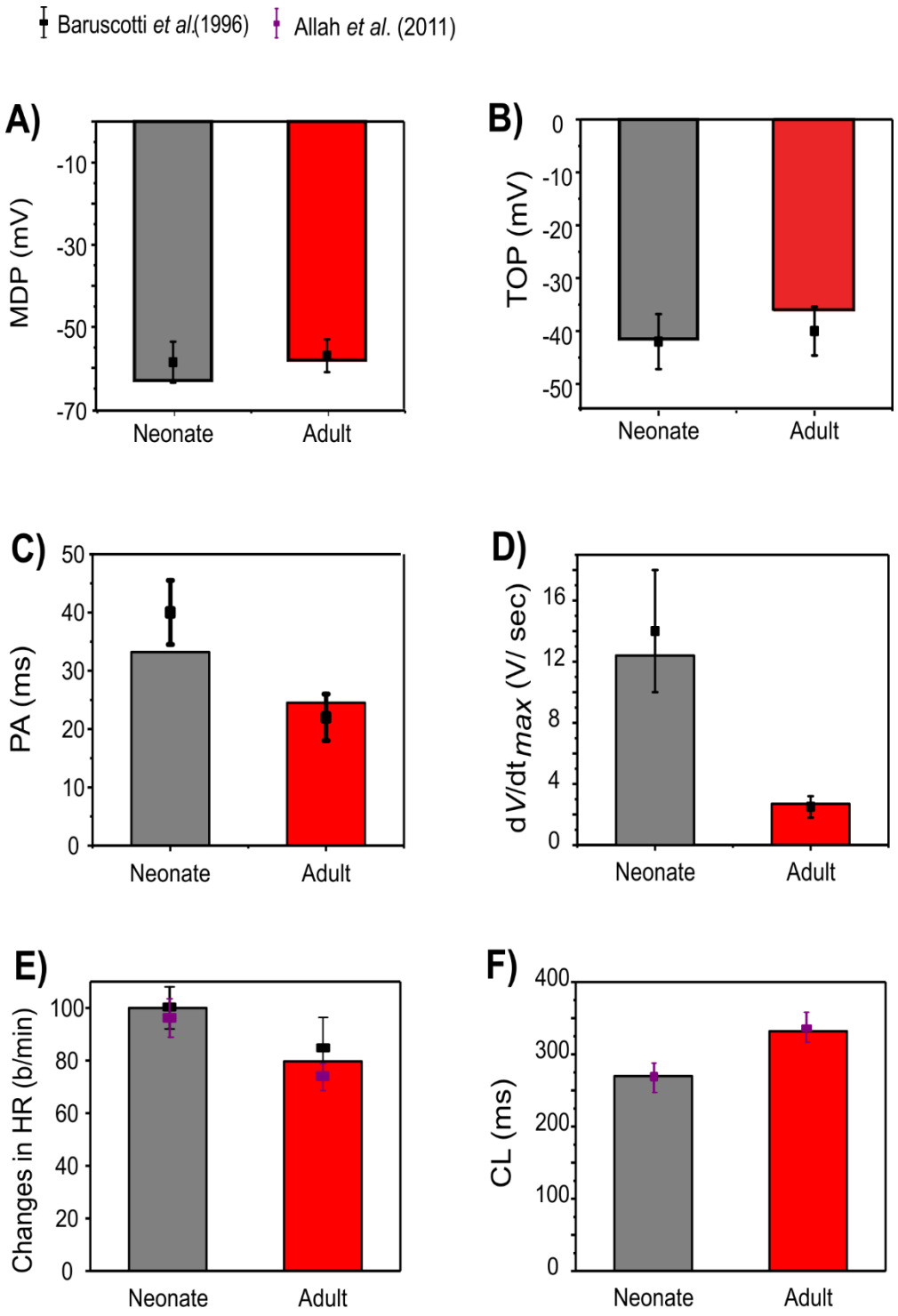

Figure 4.7. Bar chart comparison of the main AP characteristics of central SAN. (A) MDP, (B) TOP, (C) PA, (D) dV/dtmax, (E) HR, and (F) CL in neonate (grey) and adult (red) rabbits. All characteristics were compared against experimental values from Baruscotti et al.[16]

In simulations, the same modification to ion channels as was implemented in the neonatal central cells was assumed to be applicable to the peripheral model. The resultant APs and the underlying ion channel currents are illustrated in Figure 4.8.

Simulation results showed that the morphology of the neonatal APs of peripheral SAN cells was similar to that of the adult, but with some changed characteristics. The simulated CL in the neonate was smaller than that in the adult: 156ms compared with 175ms, and therefore the pacemaking rate was reduced by 12% following development. This was attributable to the integral actions of altered I_{Na}, $I_{Ca,L}$, and I_f. The measured peak amplitude of the AP in the neonatal condition was greater than that in the adult condition, changing from 31mV to 23mV with age. The reduced amplitude can be explained by the remodelled $I_{Ca,L}$. Most importantly, in both age groups, the peripheral-cell model considered I_{Na}, but with a greater conductance and changes in the kinetics in neonates as compared with adults. This contributed to the decreased maximal upstroke velocity of APs with age. Furthermore, the age-related remodelling during the development of I_{Ks}, I_{Kr} and NCX had only small effects on the peripheral AP characteristics, which is discussed in the following section. Characteristics of simulated APs for both peripheral neonatal and adult SAN models are summarised in Table S4.1 and Figure 4.9.

Table 4.4. AP characteristics of neonatal and adult central and peripheral SAN cell model

		References	PA (mV)	CL(ms)	MDP (mV)	dV/dt_{max} (V/s)
Centre	Neonate	Experiment Baruscotti *et al.* [16]	40.22±8	280	-59.2±2.2	14 ±4.5
		Experiment Allah *et al.* [30]	-	246±50	-53.5±2.2	-
		Simulation (Our model)	32.22	277	-63	11.99
	Adult	Simulation Zhang *et al.* [26]	21.2	327	-57.31	2.76
Periphery	Neonate	Our model	31.69	156.23	-78.45	72.83
	Adult	Zhang *et al.*	23.07	175.39	-77.96	70.16

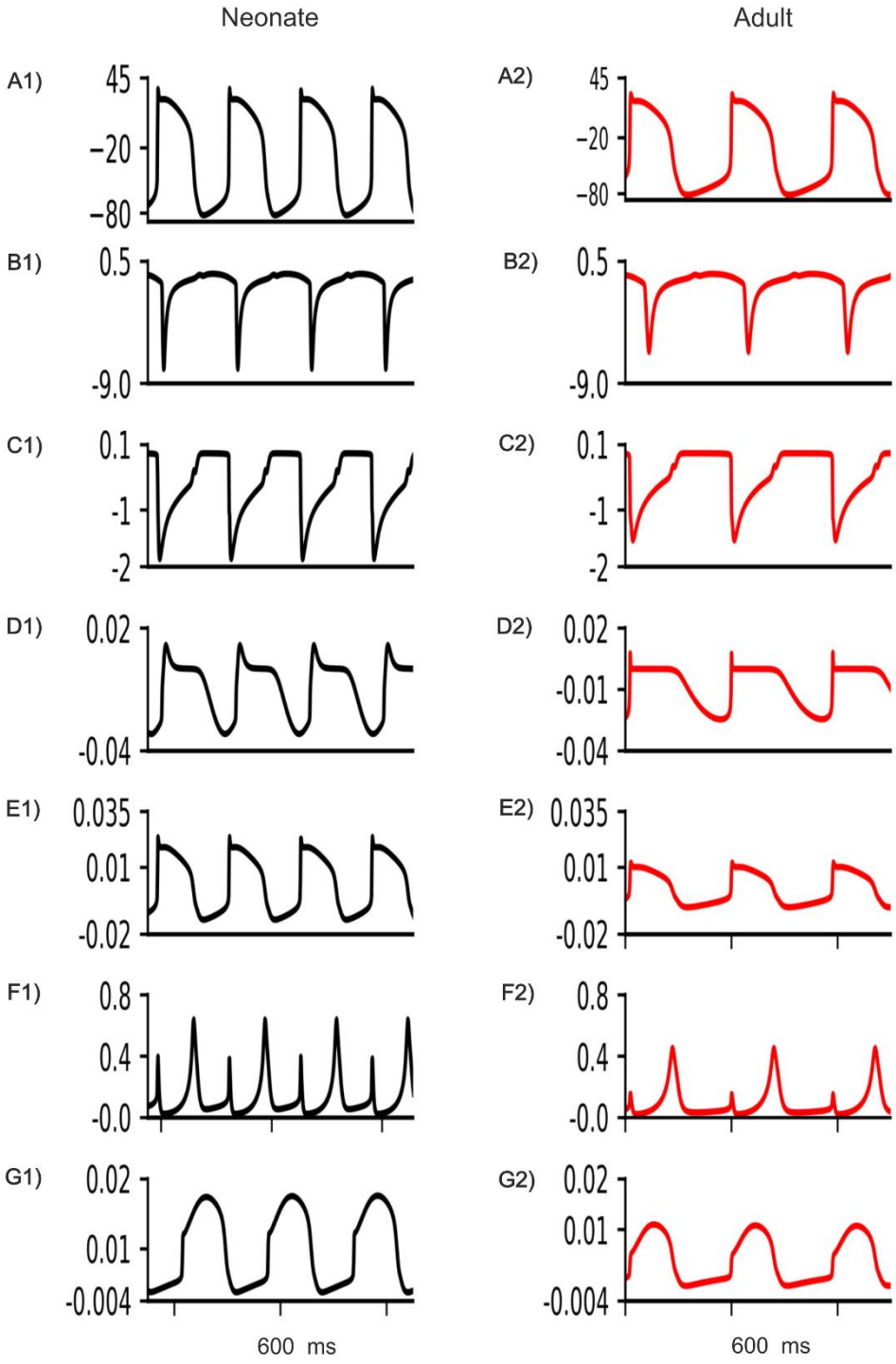

Figure 4.8. (Ai-Aii) Simulated peripheral SAN action potentials in the neonate (black lines) as compared with the adult (red lines) and (Bi-Gii) their underlying time courses of ionic channel currents I_{Na}, $I_{Ca,L}$, I_f, I_{NaCa}, I_{Kr} and I_{Ks}.

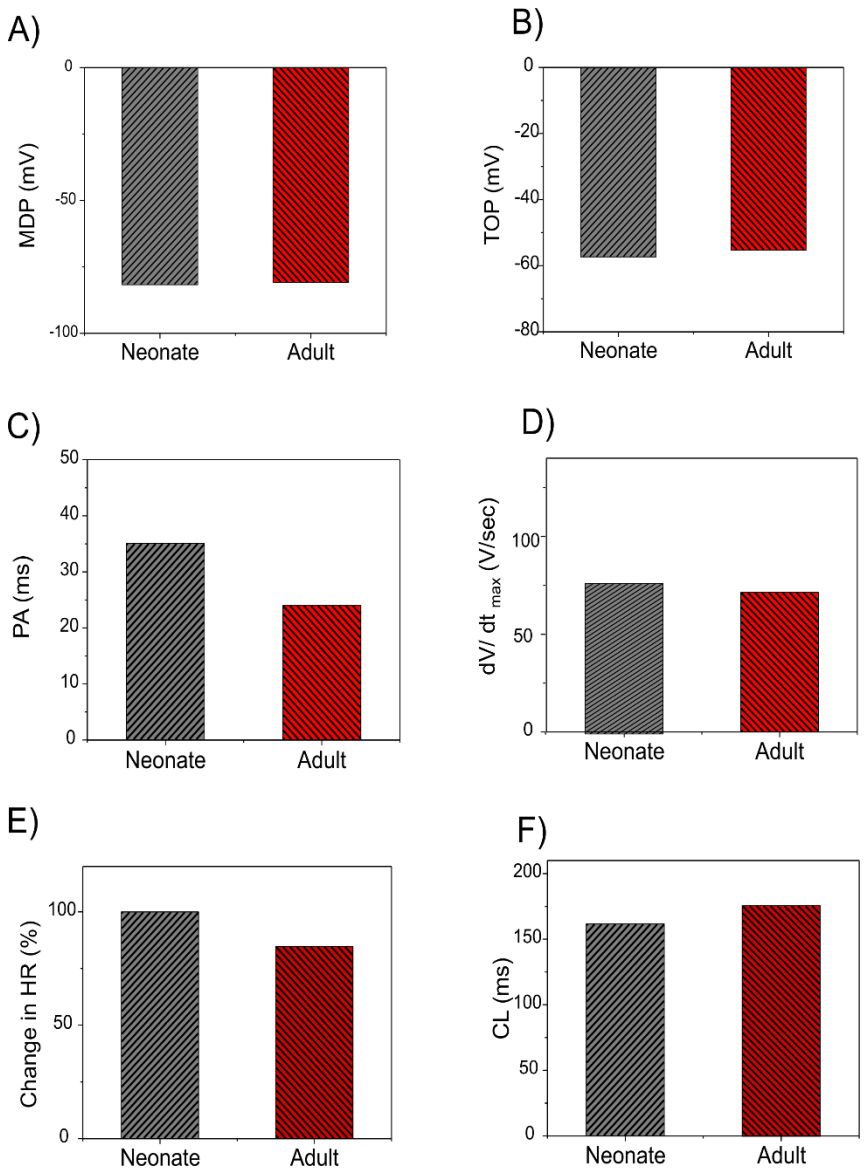

Figure 4.9. Bar chart comparison of the main AP characteristic of peripheral SAN cells: (A) MDP, (B) TOP, (C) PA, (D) dV/dt_{max}, (E) reduction of HR, and (F) CLin the neonate (grey) corresponding to the adult (red).

4.3.2 Functional role of individual remodelling of ion channels in the neonate condition

The central and peripheral cell models were used to investigate the individual roles of each remodelled ion channel in modulating the SAN cell APs, in order to identify the major contributor to the fast neonatal AP rate. This was done by the exclusive method (each individual remodelled ion channel action was considered in turn), with results being compared to those from the inclusive method (i.e., all remodelled ion channel

currents were considered) for the neonate case. Results are shown in Figure 4.10A-B and summarised in Table 4.5.

To evaluate the functional roles of the age-dependent differences of I_{Na} on spontaneous APs, the results are shown in Figure 4.11Ai-Aii for the central and Figure 4.12Ai-Aii for the peripheral SAN cells. In simulations, when the shift of the activation midpoint was considered alone (the AP and time course of the I_{Na} represented by green lines compared with the adult red lines), there was a marked reduction in neonatal CL in both central (by 99ms) and peripheral (by 29ms) cells compared with CL in the adult. When a reduced I_{Na} magnitude was considered alone (the AP and time course of I_{Na} are represented by blue lines compared with the adult red lines), the recorded CL was reduced by 62ms in the centre and 9ms in the periphery compared with CL values in the adult. When both developmental effects on I_{Na} were considered (the AP and time course of the I_{Na} are represented by black lines compared with the adult red lines), the resultant APs were found to be faster than both of the previous changes, with an increase in the diastolic depolarisation (phase 0), and a smaller CL by 123ms in the centre and 30ms in the periphery compared to CL in the adult condition. Thus, a combined effect of the shifted activation curve and reduced current density of I_{Na} in neonatal SAN cells played a crucial role in influencing AP rate.

Figure 4.11Bi-Bii and Figure 4.12Bi-Bii show the effect of age-related change of $I_{Ca,L}$ alone on the pacemaking APs for central and peripheral cell models. In simulations, the shift in the activation and inactivation midpoints alone reduced the CL by 20ms in the centre and 15ms in the peripheral model as compared with the adult (represented by green lines compared with the adult red lines). When the current density of $I_{Ca,L}$ was increased (i.e., by modifying the conductance), a decrease in the CL by 12ms was observed in the centre, but an increase of the CL by 20ms in the peripheral model were observed (represented by blue lines) as compared to the adult APs (represented by red lines), which was due to the regional different contribution of $I_{Ca,L}$. [26] When the shift in activation/inactivation curves and $I_{Ca,L}$ densities were considered together, the resultant APs were faster (represented by black lines) (CL being reduced by 24ms in the centre and by 5ms in the periphery) with a decreased diastolic depolarisation phase. This demonstrates that the opposite shift of the steady-state activation and inactivation curves is an important contributor as compared with the current density changes in modulating the pacemaking rate. It was also noted that the PA was greater in the neonate than in the

adult by 7mV in the centre and 8mV in the periphery, indicative of the contribution of the $I_{Ca,L}$ current to the diastolic depolarisation phase (phase 0) and the plateau phase (phase 2).

Figure 4.11Ci-Cii and Figure S4.12Ci-Cii elucidate the modulatory effect of the I_f current on spontaneous APs in the neonatal SAN. A shift of the steady-state activation curve by -7mV reduced the CL by 5ms in the centre and 2ms in the periphery (represented by green lines compared with the adult red lines). An increase in I_f density alone produced a notable decrease in CL: by 16ms in the centre and by 12ms in the periphery (represented by blue lines). A combined action of the shifted activation curve and increased current density of I_f produced a CL reduction by 21ms in the centre and 16ms in the peripheral cell models (represented by blue lines).

Figures 4.11Di-Dii, Ei-Eii and Fi-Fii illustrate the effects of remodelled I_{Kr}, I_{Ks} and I_{NaCa} on pacemaking APs of the central cell model, while their effects on the APs of the peripheral cell model are shown in Figures 4.12Di-Dii, Ei-Eii, and Fi-Fii. An increase of the I_{Ks} by 27% as seen in the neonate did not lead to a significant change in the CL or the APs' morphology. When I_{Kr} was increased by 36%, there was a CL increase by 10ms in the centre, and by 2ms in the periphery. An increase of the I_{NaCa} alone decreased the CL by 17ms in the central model and caused a small change (5ms) in the peripheral model. The overall ion channel remodelling effect on the computed CL is summarised in Table 4.5.

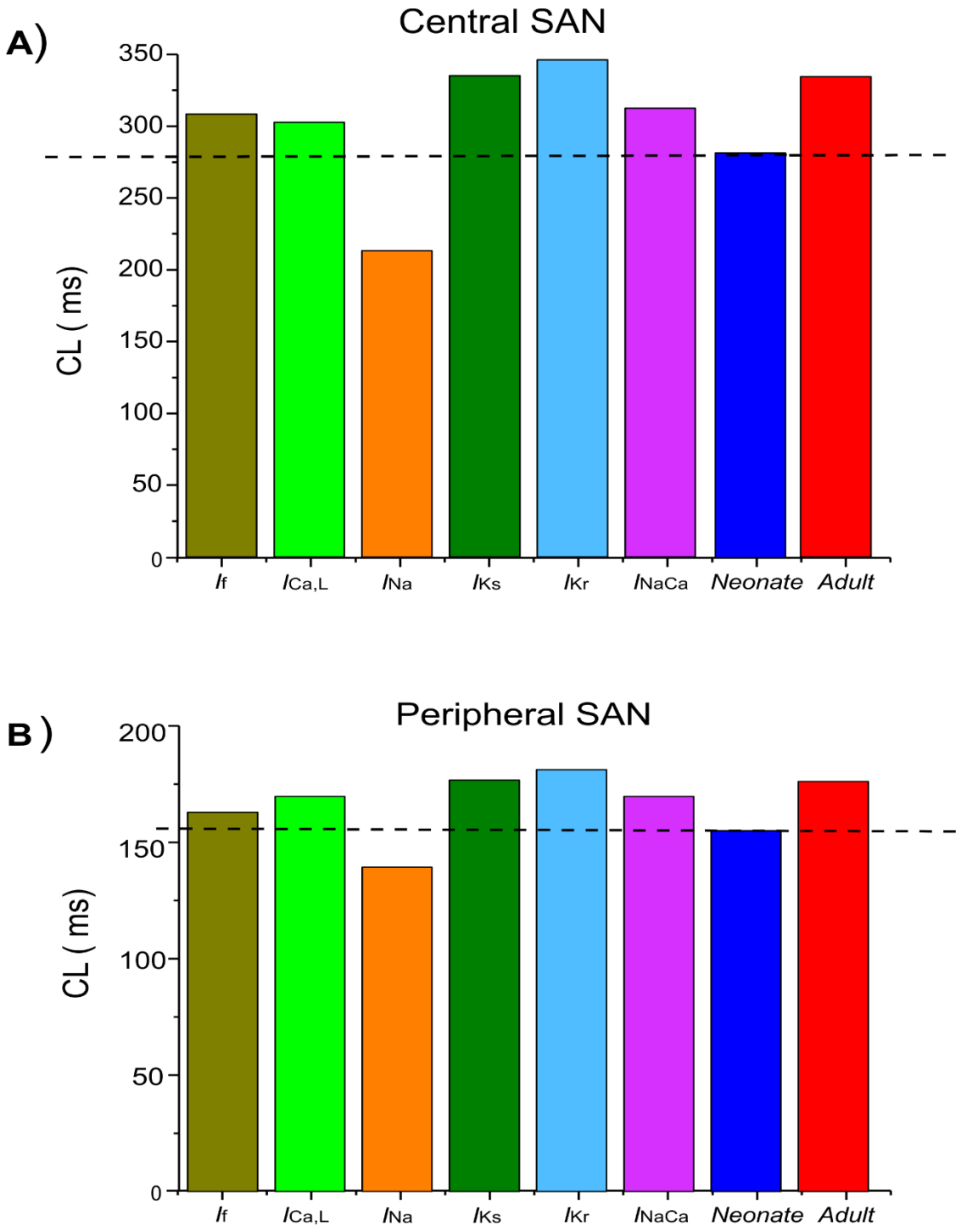

Figure 4.10. Computed CL from (A) central, and (B) peripheral SAN-cell models, when age-related change to each of the remodelled ionic-channel currents was considered alone.

Table 4.5. Effect of individual age-related remodelled ionic-channel currents on the CL of central and peripheral SAN-cell models.

	Centre		Periphery	
	CL (ms)	Change in CL compared with adult (ms)	CL (ms)	Change in CL compared with adult (ms)
I_f	306	-21	159	-16
$I_{Ca,L}$	303	-24	170	-5
I_{Na}	204	-123	145	-30
I_{Ks}	327	0	175	0
I_{Kr}	337	+10	177	+2
I_{NaCa}	310	-17	170	-5
Neonate	277	-50	156.23	-18.77
Adult	327	0	175	0

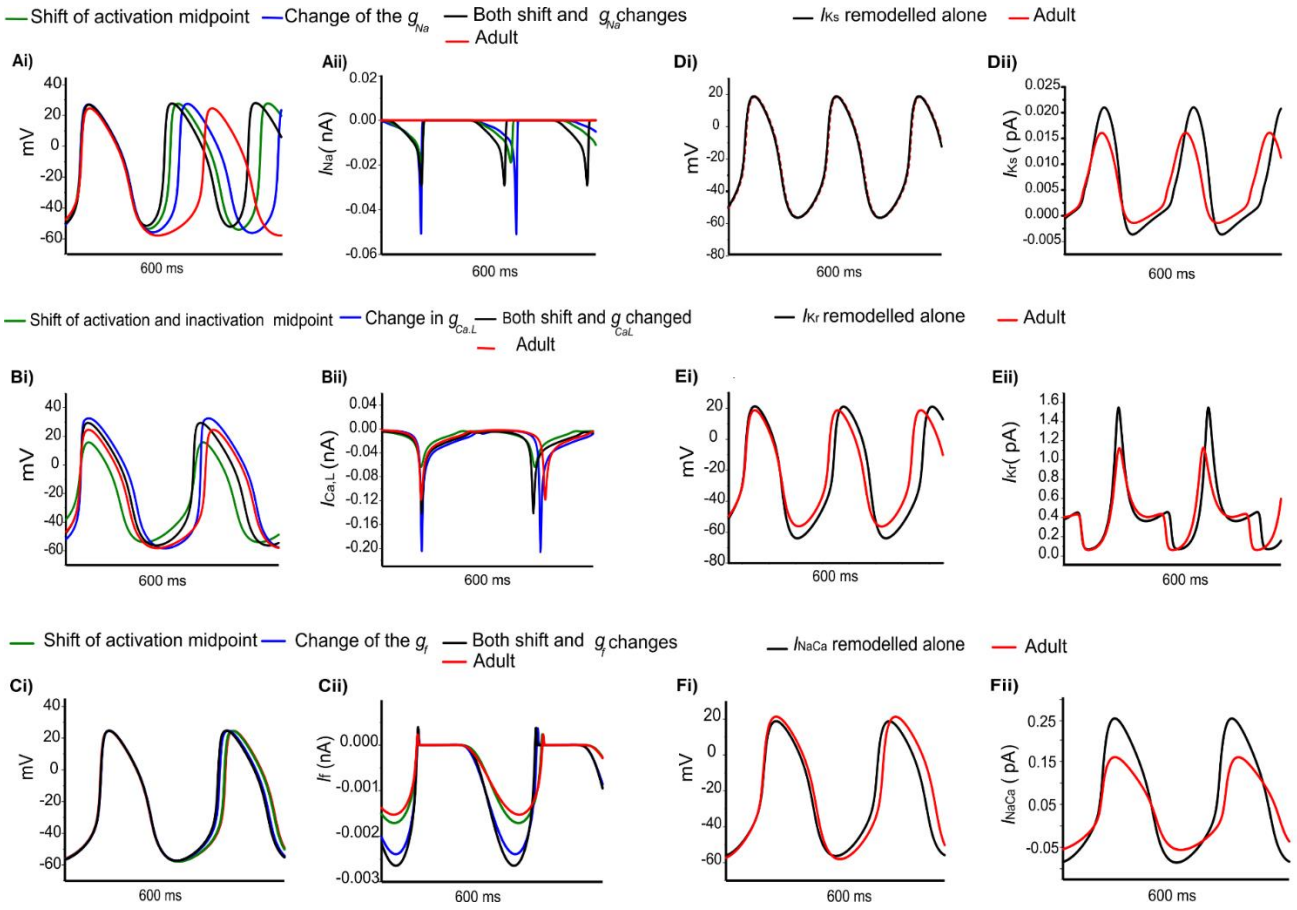

Figure 4.11. Simulations of the effects of individual remodelled ion channels on modulation of pacemaking APs in the central SAN-cell model. Corresponding action potentials and underlying ionic currents are shown for (Ai-Aii) I_{Na}, (Bi-Bii) $I_{Ca,L}$, (Ci-Cii) I_f, (Di-Dii) I_{Kr}, (Ei-Eii) I_{Ks} and (Fi-Fii) I_{NaCa}.

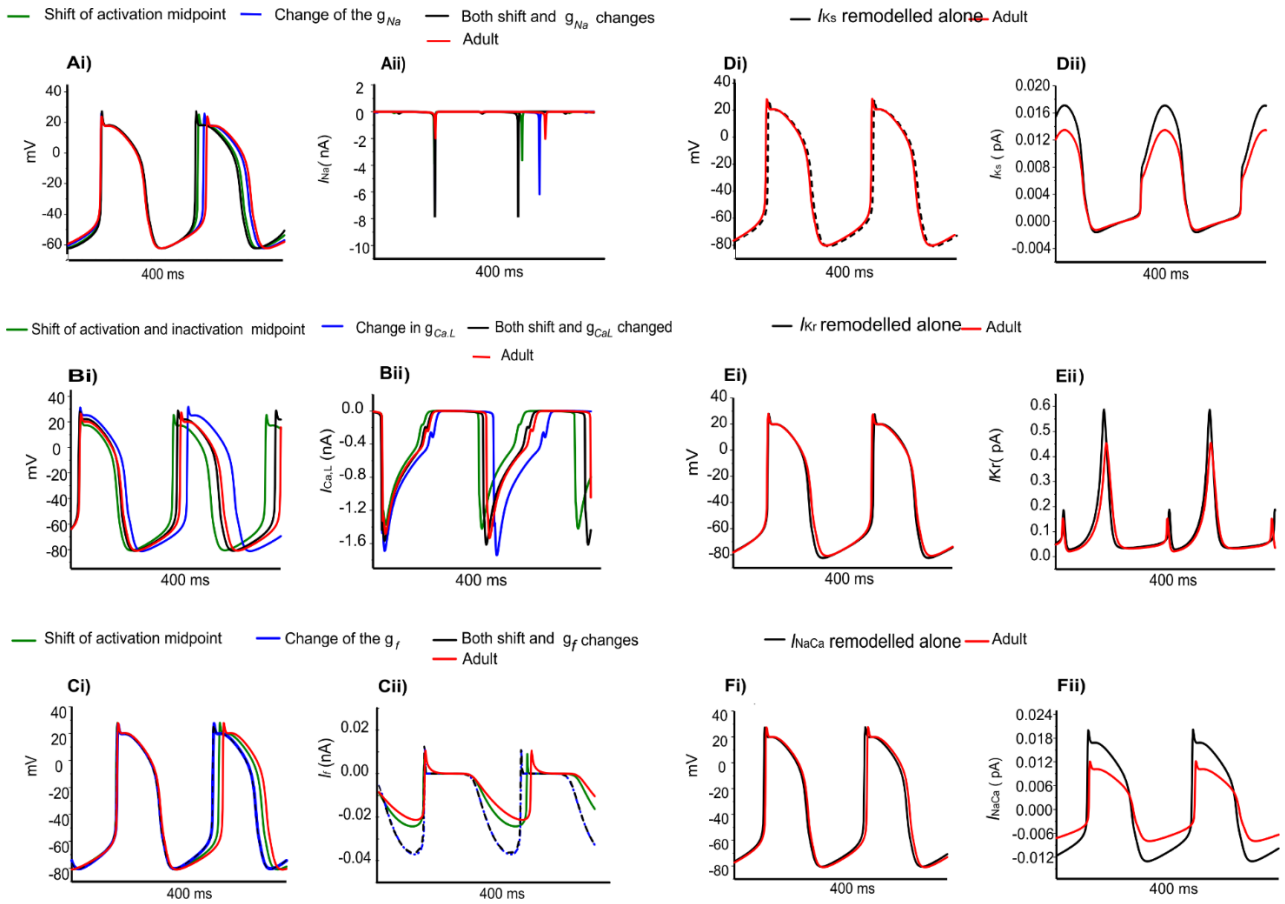

Figure 4.12. Simulated individual effects of ion-channel remodelling on peripheralal SAN action potentials in the adult and the underlying ionic currents (Ai-Aii) I_{Na}, (Bi-Bii) $I_{Ca,L}$, (Ci-Cii) I_f, (Di-Dii) I_{Kr}, (Ei-Eii) I_{Ks} and (Fi-Fii) I_{NaCa}

4.3.3 Effects of ACh on SAN cell activity

It is not known whether the negative chronotropic action of ACh is similar between adult and neonate rabbit SAN cells. Simulations were conducted to address this question, in which actions of ACh on APs were simulated at a physiological concentration of $5x10^{-8}$M for the neonate and adult conditions. Results are shown in Figure 4.13.

In the adult condition, ACh slowed down the pacemaking APs: the measured CL increased from 327ms to 430ms (by 30.4%) for the central cells, and from 175ms to 219ms (by 23%) for the peripheral cells (Figure 4.13Ai-Aii). It reduced the PA (from 23.8mV to 18.38mV, a decrease of 21.11% in the central cells, and in the peripheral cells (from 24.4mV to 21.5mV, a decrease of 10.6%). It also reduced the APD_{50} (by 13.33% in the centre and by 11.9% in the periphery). It hyperpolarised the MDP, which changed from -57mV to -61mV in the centre and from -80.88mV to -81.4mV in the periphery. This resultant negative chronotropic effect of ACh on the APs was attributed to the combination of the activation of $I_{K,ACh}$, partial depression of $I_{Ca,L}$ and the I_f activation shift.

ACh had a greater effect on modulating simulated APs in the neonatal than in the adult SAN cell models, which is consistent with previous experimental observations. [47,51] The changes in the CL under the influence of ACh were markedly greater in the neonatal condition: see the bar-chart comparison on the computed CL under WT and ACh effects for both cases in the central and peripheral cells, in Figure 4.13Ei-Eii. This demonstrates that the negative chronotropic effects of ACh were grater in both the centre and the peripheral cells of the neonatal models than in the adult ones. The PA changed from 32.5mV to 14.5mV (by 55.38%) in the central cells and from 30mV to 28mV (by around 13%)in the peripheral cells. There was a reduction in the APD_{50} values by 23.4% in the centre and 13% in the periphery. The simulated MDP values for the APs were hyperpolarised from -62.8mV to -64.6mV in the centre and from -82.04mV to -83.53mV in the periphery in the neonate. These changes were 2.8% and 1.8% for the central and peripheral cell models in the neonate condition. All these values are summarised in Table4.6.

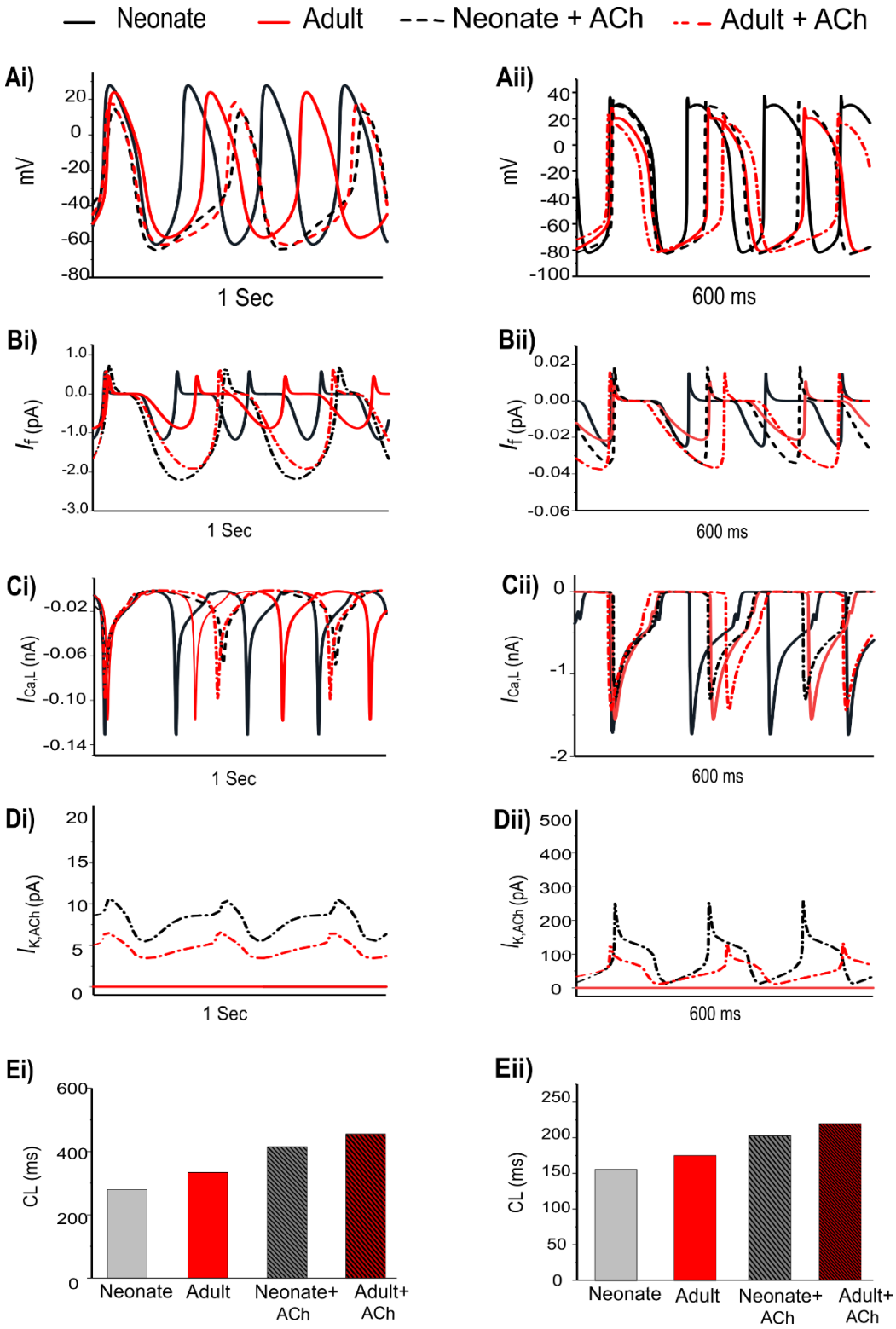

Figure 4.13. Effect of ACh on the SAN pacemaking APs. Both neonate and adult conditions are shown for (Ai) the central and (Aii) the peripheral SAN cells; ACh concentration for both conditions was [ACh] = 5×10^{-8} M. (Bi-Bii) Time course of I_f current.(Ci-Cii) Time course of the $I_{Ca,L}$ current. (Di-Dii) Time course of $I_{K,Ach}$ current. (Ei-Eii) bar-chart comparison on the computed CL under WT and ACh effects for both cases in the central and peripheral cells.

Table 4.6. The negative chronotropic effect of ACh is shown on the pacemaking APs in central and peripheral rabbit SAN cells, at a physiological concentration of 5x10-8M for the neonate and adult conditions.

		Neonate			Adult		
		No ACh	**Ach 5×10^{-8} M**	**Change %**	**No ACh**	**Ach 5×10^{-8} M**	**Change %**
Centre	MDP (mV)	-62.08	-64.6	↑2.8	-57	-61	↓7
	PA (mV)	32.5	14.5	↓55.38	23.8	18.38	↓21.11
	CL (ms)	277	403	↑47	327	430	↑30.0
Periphery	MDP (mV)	-82.04	-83.53	↓1.8	-80.88	-81.0	↓2.4
	PA (mV)	30	28	↓13	24.4	21.5	↓10.6
	CL (ms)	156	202.37	↑27	175	219	↑ 23.0

The dose-dependent effects of ACh on pacemaking APs in developing SAN were also investigated. Figure 4.14 illustrates the results obtained from the central and peripheral cell models for both age groups under three different "physiological" ACh concentrations. Increase of the ACh concentration resulted in a monotonic increase of CL of the APs for both cell types, with greater effects in the neonate condition. At an ACh concentration of 7.0×10^{-8}M (Figure 4.14Ci-Cii), pacemaking was still occurred in the adult central SAN cells (though with a prolonged CL compared with the control condition), but became quiescent in the neonatal condition. The results for the peripheral cells showed less sensitivity to ACh at a concentration of 7.0×10^{-8}M compared with the central model, although the neonate was more affected than the adult. Figure 4.14Di-Dii summarises the simulated dose-dependent effect of ACh on the CL recorded in both conditions. The concentration-response relation of the CL shifted leftwards with age, indicating an amplified effect of ACh on SAN cells in neonates.

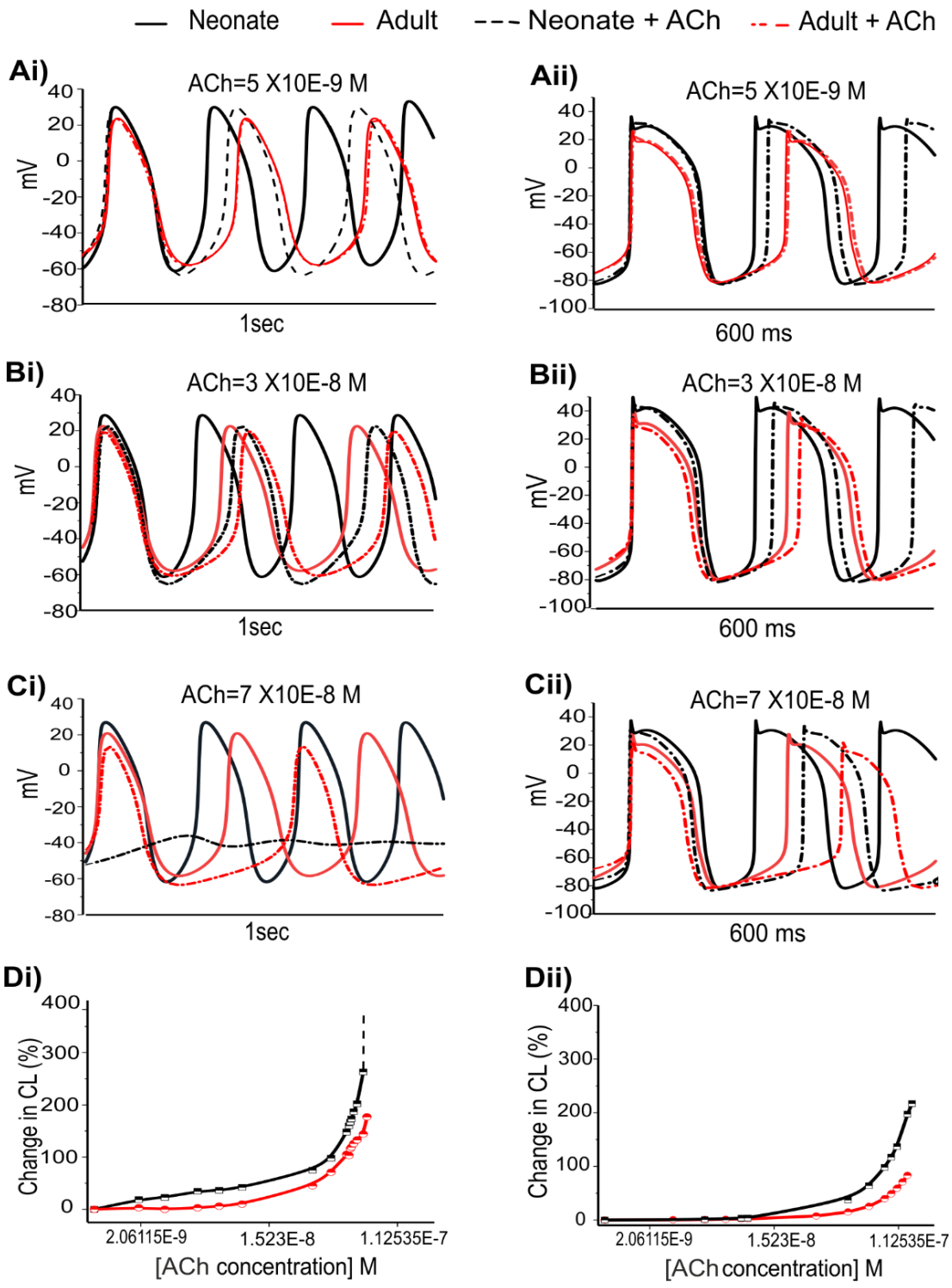

Figure 4.14. Dose-dependent effects of ACh on spontaneous APs of the SANs for the neonate and adult. (Ai-Aii) at [ACh] = $5x10^{-9}$M. (Bi-Bii) at [ACh] = $3x10^{-8}$M. (Ci-Cii) at [ACh]= $7x10^{-8}$M. (Di-Dii) dose-dependent effects of ACh on pacemaking CL for the central and peripheral SAN cells, respectively. The black line represents the neonate condition and the red line represents the adult condition.

Figure 4.15 shows the effects of various ACh concentrations on the primary AP characteristics of the neonate cell models (black symbols) compared with the adult cell models (red symbols). Figure 4.15Ai-Aii shows the changes in AP amplitude; Figure 4.15Bi-Bii shows the changes in APD_{50}; and Figure 4.15Ci-Cii shows the changes in MDP. For both age groups, all these changes in AP characteristics illustrate that the central cell shows more sensitivity to ACh than the peripheral cell.

4.3.4 AP conduction in the two-dimensional tissue model during SAN development

Figure 4.16A-B shows snapshots of the initiation and conduction patterns of pacemaking APs in the 2D SAN-atrium model for both neonate and adult conditions at different time-points after impulse initiation. In both age groups, the AP propagation displayed a similar conduction sequence, but with a shorter conduction time and thus a greater conduction velocity in the neonate with respect to the adult. In both cases, the AP propagation first started slowly in the centre of the SAN. Once initiated, it propagated preferentially from the centre towards the periphery of the SAN, and then parallel to the crista terminalis (CT) before entering rapidly into the atrium in a direction towards the atrial septum. The AP conduction was blocked in the block zone, which was encircled by excitation waves from the superior and inferior tissues that surrounded the zone. Such simulated activation and conduction patterns are consistent with experimental observations.[29]

The isochrones of the activation timing sequence of the SAN-atrium tissue for both conditions are shown in Figure 4.17A-B. The computed time taken to activate the whole tissue was less in the neonate (55-65ms) than in the adult (75-95ms). In association with this, the computed pacemaking CL showed an age-dependent increase, which changed from 290ms in the neonate to 376ms in adult tissue, equivalent to a decrease in the heart rate from 210 min^{-1} to 160 min^{-1} in the neonate and adult tissue respectively. This age-related change in HR was qualitatively close to that observed experimentally from the intact SAN-atrial tissue of guinea pigs (Figure 17C).[22,28] The measured conduction velocity (CV) was also reduced by age in the 2D SAN-atrium model (Figure 4.17D).

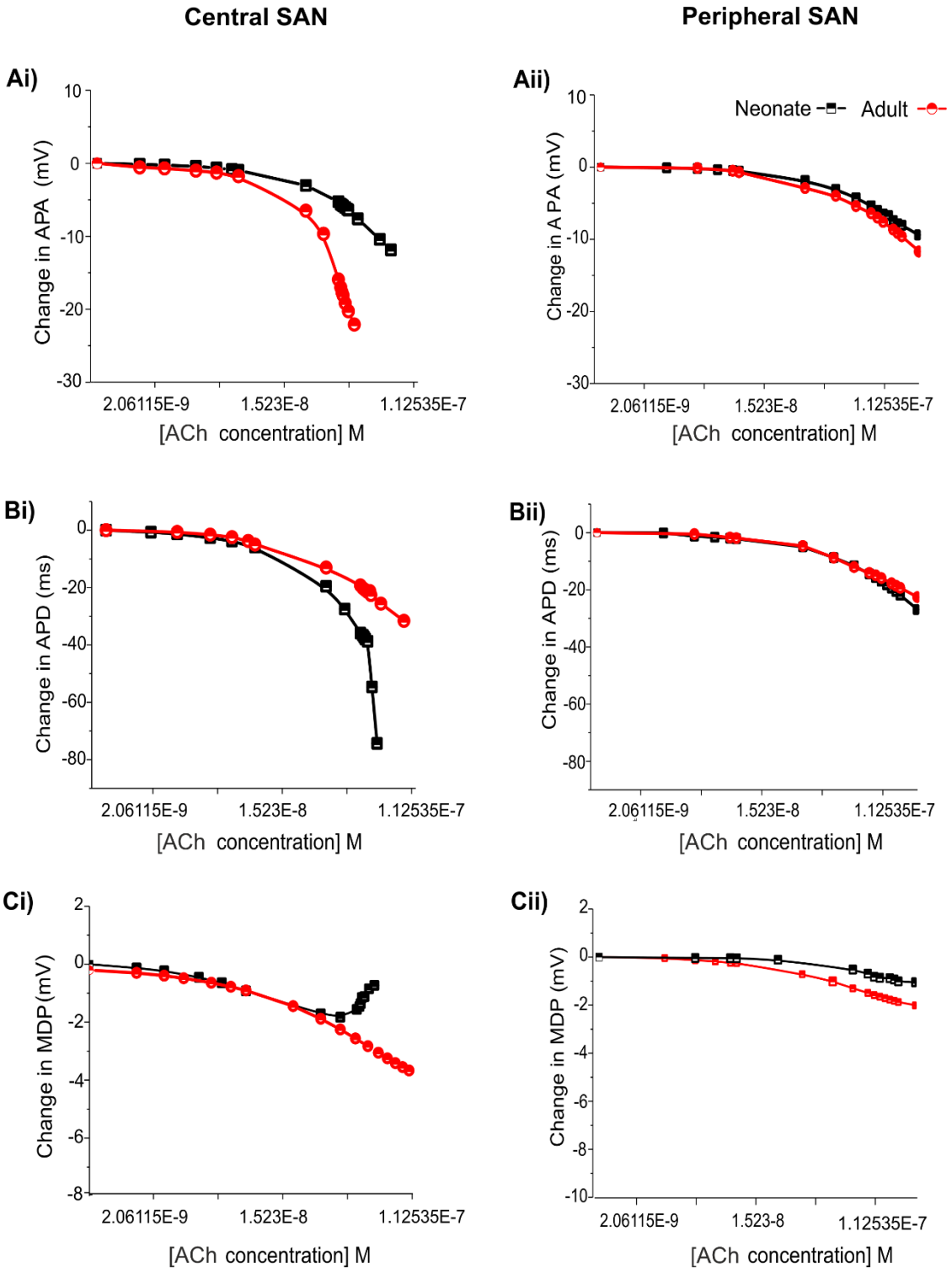

Figure 4.15. Concentration-dependent effects of ACh on the AP characteristics of rabbit central and peripheral SAN cells for neonate (black squares) and adult (red circles) conditions. (Ai-Aii) action potential peak amplitude (PA). (Bi-Bii) action potential duration (APD_{50}). (Ci-Cii) maximal diastolic potential (MDP).

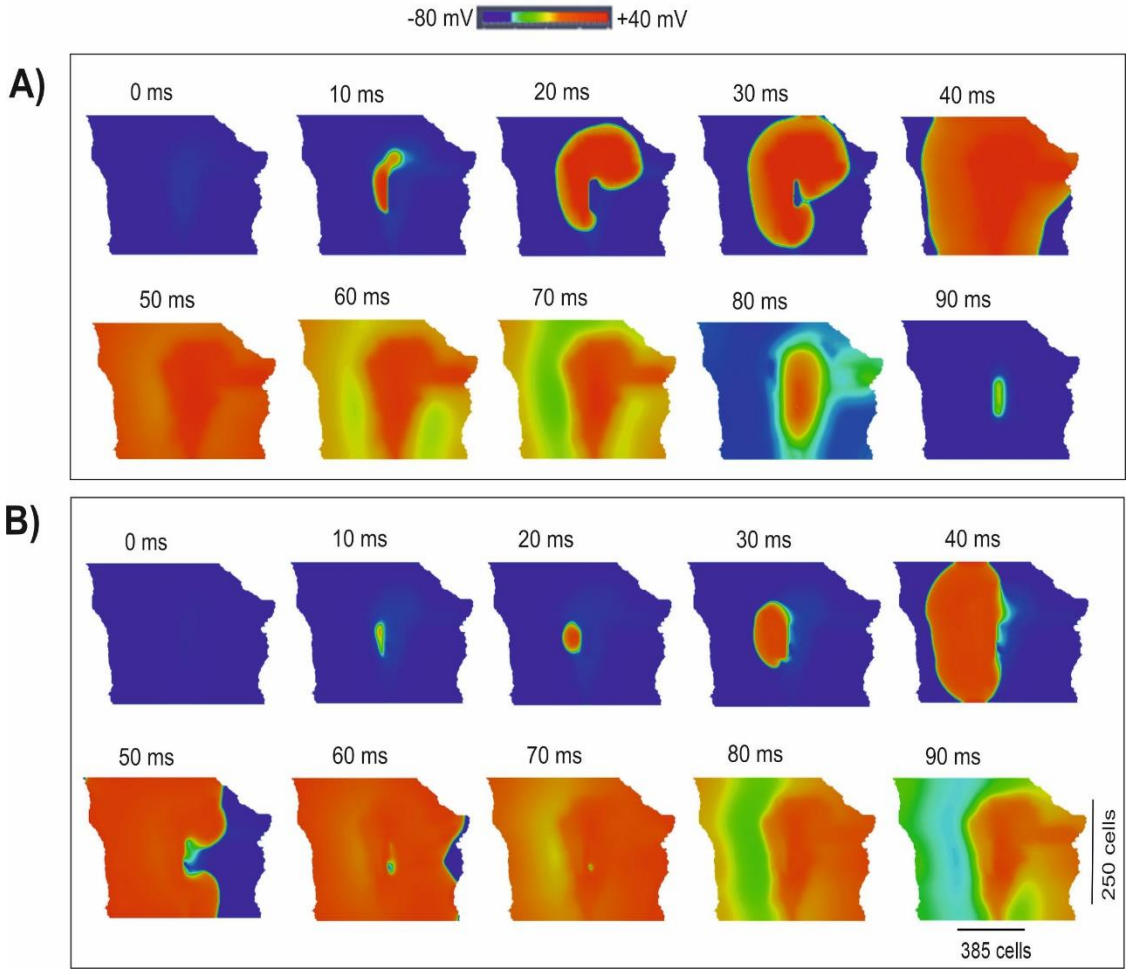

Figure 4.16. Snapshots of AP initiation and conduction patterns in the 2D model of intact SAN-atrial tissue in the (A) neonate and (B)adult conditions.

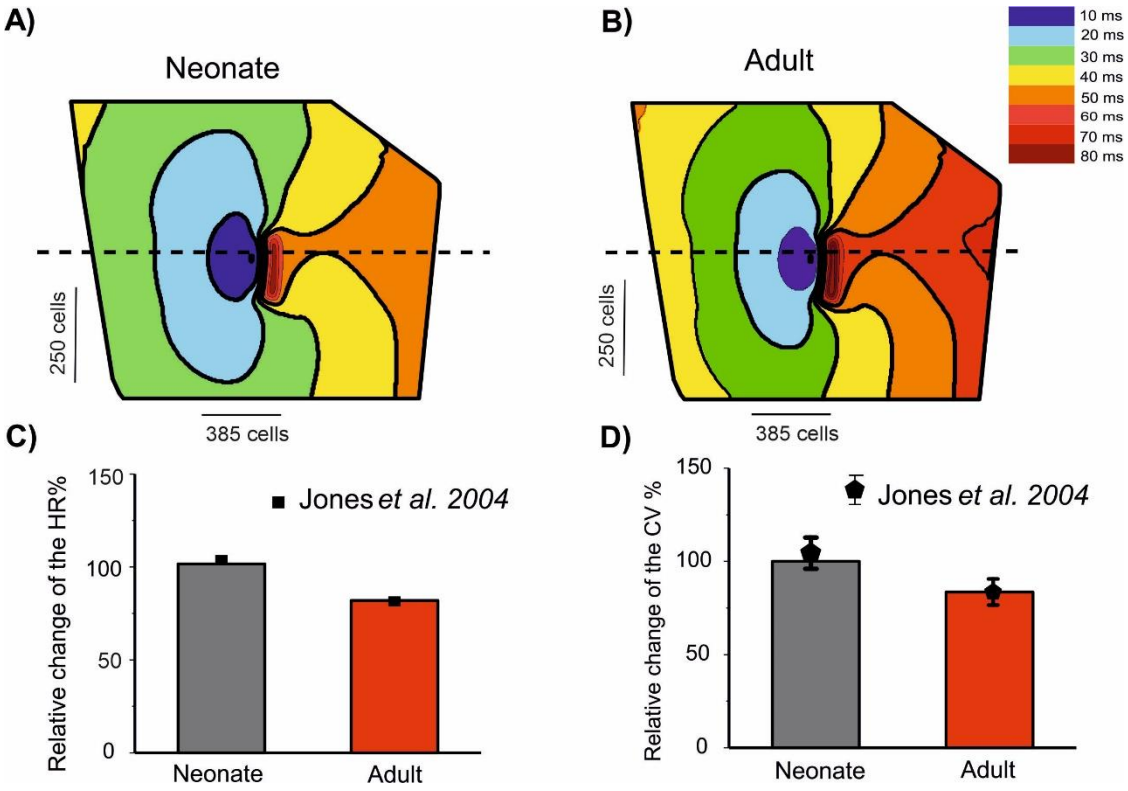

Figure 4.17. Isochrones of the activation map in 2D rabbit intact SAN-atrial models for both (A) neonatal and (B) adult conditions. The activation timing in the model was recorded every 10ms, as illustrated with various colours, which changed from blue at 0ms to dark red at 80ms. The bar chart (C) shows the reduction of HR and (D) the conduction velocity (CV) with age in the 2D SAN-atrium, compared with experimental values from [22].

4.3.5 The effect of ACh on two-dimensional SAN-atrial tissue with increasing age

The single cell simulations showed higher sensitivity of neonatal SAN cells to ACh as compared to the adult, which has also been observed experimentally.[8,51] Further simulations were conducted to evaluate the functional consequence of ACh on AP conduction in the 2D model of intact SAN-atrium in neonatal and adult conditions.

As at the single cell level, our simulation results implied that when the ACh concentration value was above $8x10^{-8}$M in the neonatal condition, the AP of the central model was suppressed. Therefore, in the 2D model simulations, two physiological values for ACh ($3x10^{-8}$M, $8x10^{-8}$M) were used.

Figure 4.18 provides snapshots of the AP initiation and conduction sequences in the 2D model for both neonate and adult conditions. With application of ACh ([ACh] = $3x10^{-}$

^{8}M), in both cases, the wave propagation pattern is similar to that seen in the control condition, but with a slower conduction velocity and pacemaking rates (the measured CL changed from 290ms to 454ms (by 30%) in the neonate; and changed from 366ms to 411ms (by 12.3%) in the adult tissue). The greater effect of the ACh in the neonate as compared with the adult in the tissue simulations was consistent with the simulation results at the single-cell level.

When ACh concentration was increased as shown in Figure 4.19, with [ACh]= 8×10^{-8}M, there was a further reduction in the wave propagation velocity within the SAN and atrium tissue, but a more marked increase in the computed pacemaker CL (by 49%). The resulting decreased conduction velocity and increased CL have been observed experimentally for the adult rabbit SAN.[52] Interestingly, ACh caused a shift of the leading pacemaker site to the peripheral region in the neonatal condition. As the new leading pacemaker was far from the original location, the conduction pathway was altered, leading to differences in the activation timing and conduction velocity in the neonate tissue between the control and ACh conditions (for details see Table 4.7). The simulated pacemaking shift in response to ACh was consistent with previous experimental observations, in which the leading pacemaker was shifted in response to vagal nerve stimulation. [53-55]

Quantitative analyses were also performed to investigate the effect of postnatal development effect on AP activation timing and the AP conduction velocity in the intact SAN-atrial tissue model. Figure 4.20A plots the measured activation timings from the representative cells across the middle of the 2D neonate tissue for control (black curve) and ACh =$8x10^{-8}$M conditions (blue line), which were compared with those obtained from the adult tissue in control (red curve) and ACh=$8x10^{-8}$M conditions (green line). In the adult, the activation timings across the tissue increased. With ACh, the activation time for the neonate was reduced in the direction towards the atrial septum (blue line) due to the shift of leading pacemaking site. The corresponding average conduction velocity across the tissue is shown in Figure 4.20B. The conduction velocity under control for the neonate condition was found to be greater than that for the adult: approximately 0.30m/s in the neonate and 0.26m/s in the adult along the CT. This age-dependent reduction in the CV is in accordance with the increased activation time in the direction towards the CT during ageing. Application of higher ACh concentrations may

lead to a further reduced conduction velocity and increased CL, and may even impair the SAN to drive the atrial muscle, leading to a “SAN conduction exit block”. Both age-dependent changes of the activation time and conduction velocity seen in simulations were reasonably comparable with the experimental observations from guinea-pig SAN tissue as seen in Figure 4.20C-D.[22]

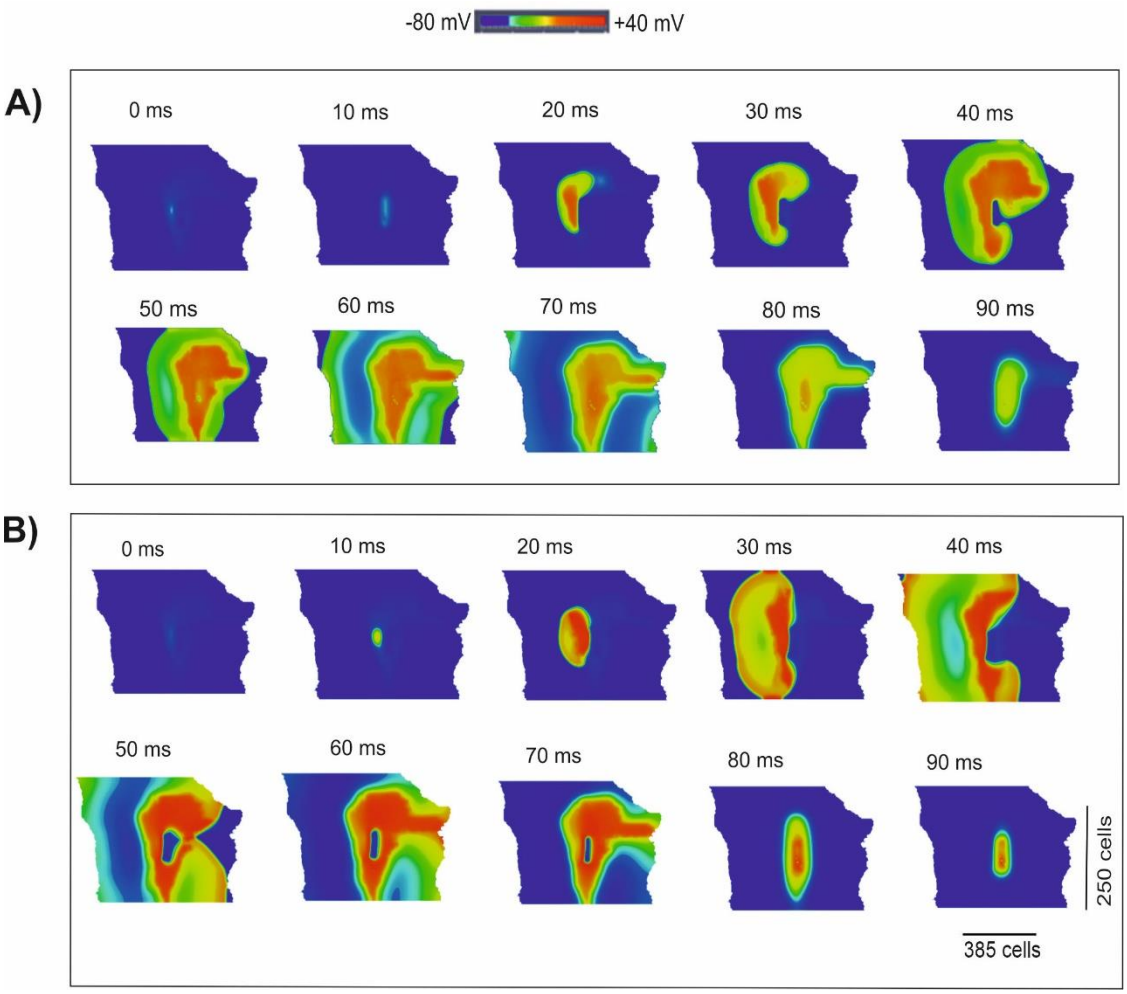

Figure 4.18. ACh effect at a concentration of 3×10^{-8}M on the propagation of the SAN and surrounding area of the (A) neonate and (B) adult rabbit 2D tissue. Snapshots of the activation pattern at various timings are shown.

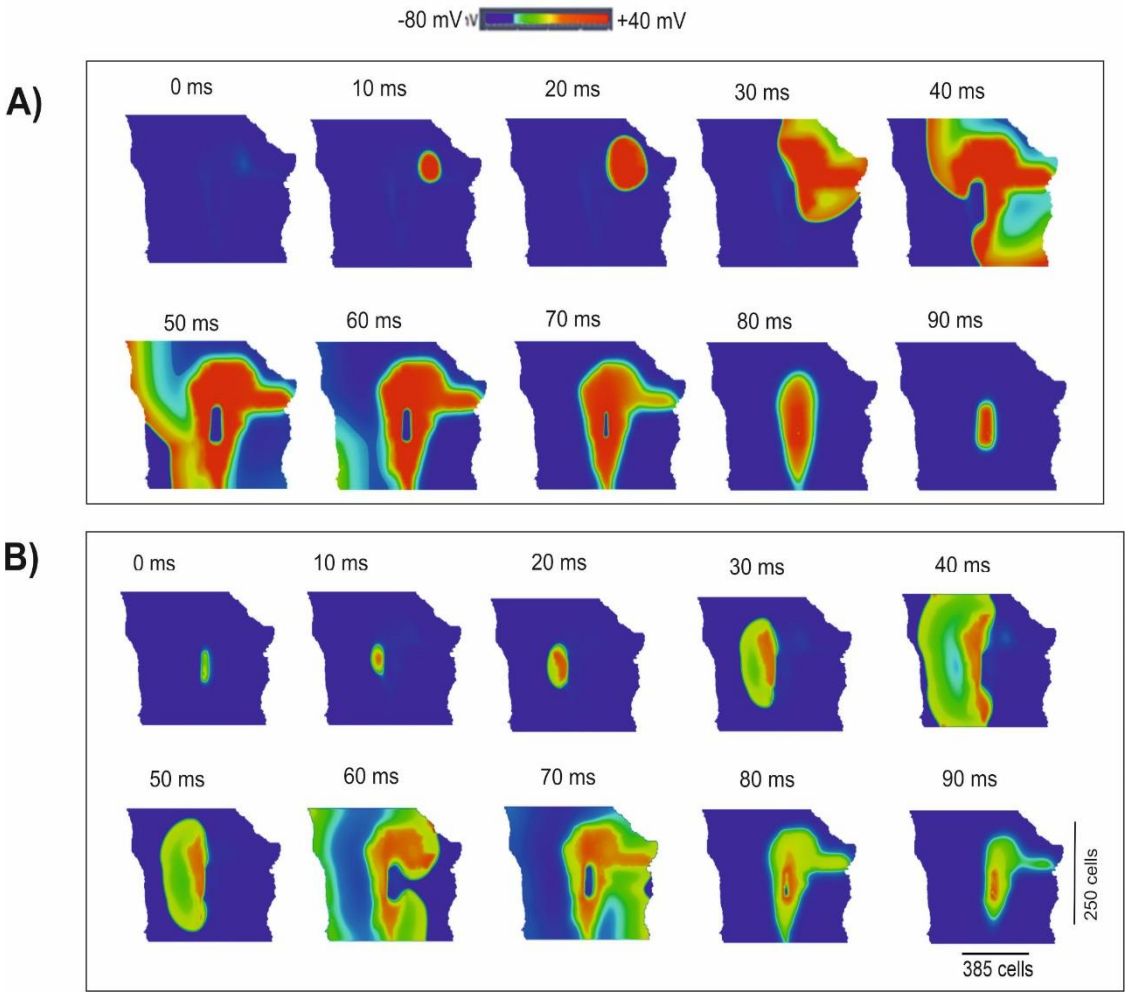

Figure 4.19 ACh effect at a concentration of 8×10^{-8}M on the propagation of the SAN and surrounding area of the (A) neonate and (B) adult rabbit 2D tissue. Snapshots of the activation pattern at various times are shown.

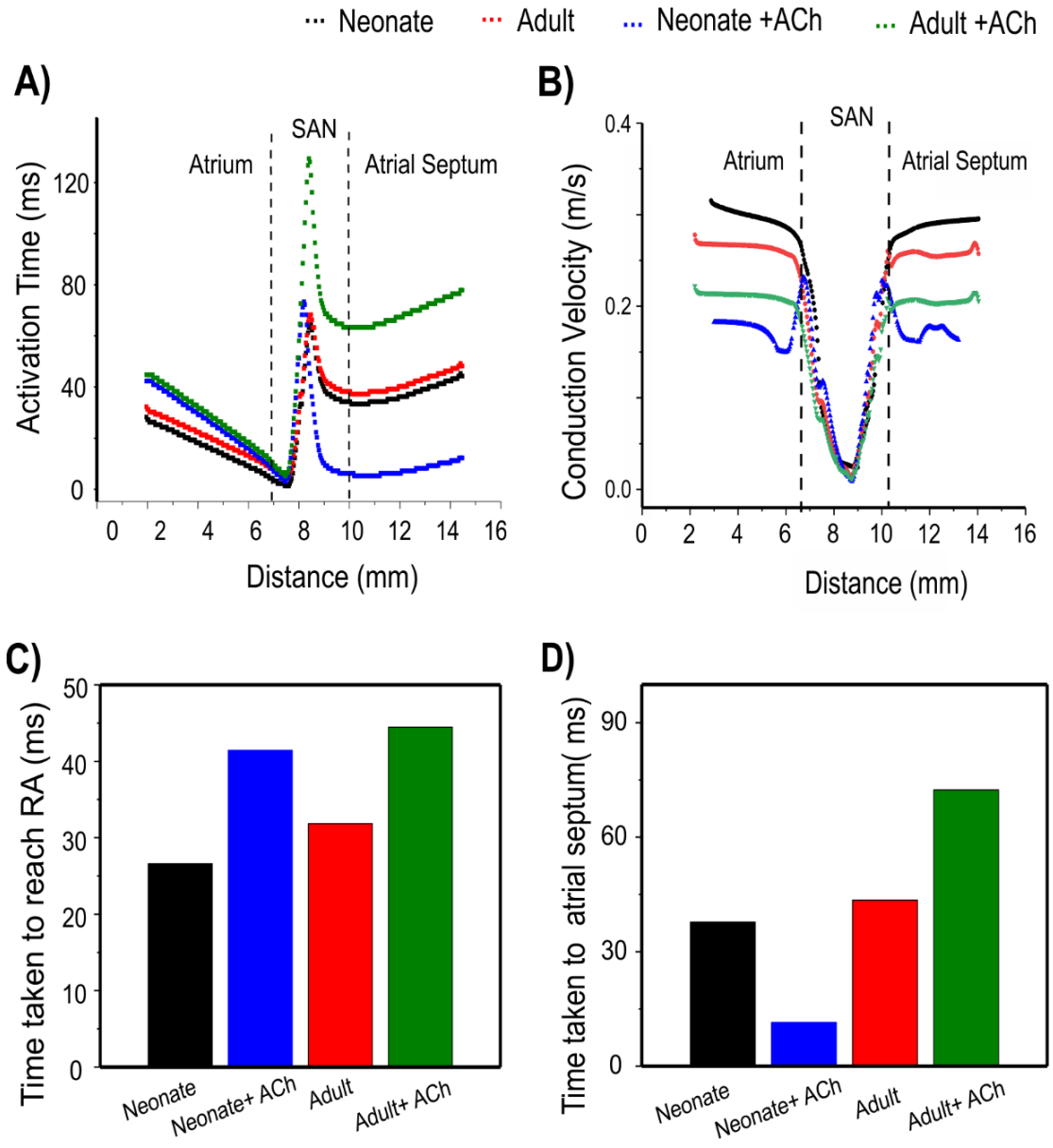

Figure 4.20. Postnatal development effects on AP conduction across the tissue in the 2D intact SAN-atrium slice. (A) Activation time profile and (B) conduction velocity of the neonate (black line) as compared with those in the adult (red line) under the effect of WT and ACh at a concentration of [ACh] $=8\times10^{-8}$M on the neonate (blue line) and adult (green line). (C-D): Bar charts showing the increase in time taken for APs to reach the RA, and the relative change of the conduction velocity with age.

Table 4.7. Simulated CL and averaged CV in control and ACh for both neonate and adult central SAN cell models.

	Cycle length (ms)	Conduction velocity along the SAN-Atrium (m/s)	HR (b/m)	Reduction of the HR under ACh (%)	HR (b/m) [22]
Neonate	290.7	0.30	206.0	0.0	250.0± 60.0
Neonate + ACh ($3x10^{-8}$ M)	377.21	-	159.1	22.8	-
Neonate + ACh ($8x10^{-8}$ M)	569.00	0.18	105.4	49.0	-
Adult	366.21	0.26	163.0	0.0	160.0± 20.06
Adult + ACh ($3x10^{-8}$ M)	411.32	-	150.0	8.0	-
Adult + ACh ($8x10^{-8}$ M)	536.1	0.21	111.9	31.13	-

4.4 Discussion

In this study, we have developed a new neonatal SAN cell mathematical model based on available experimental data from immature rabbit cells (details are reported in Tables 4.1, 4.2 and 4.3) on some major underlying ionic channel currents. The developed model successfully reproduces the morphology of neonate APs with their characteristics quantitatively matching experimental data, validating the cell model development [16]. This may have important implications for the diagnosis and treatment of cardiac rhythm disorders in the immature, adult, and aged individuals. Using the "exclusive" method, the functional role of individual post-developmental ion-channel remodelling on the APs has been investigated in order to elucidate the major contributor to the fast pacemaking rhythm of the neonate hearts. The functional impact of age-related ion-channel remodelling on AP propagation in a 2D model of the intact rabbit SAN-atrium tissue

were also investigated. Effects of ACh on pacemaking APs and their conduction were also investigated to elucidate the mechanisms that underlie the post-developmental difference of vagal tone modulation on cardiac pacemaking activities.

The major findings of this study are: (1) at the single cell level, neonatal mathematical models produced higher frequency APs in both the central and peripheral SAN cells with a higher upstroke phase as compared to adult APs. These differences may be attributable to the ion channel remodelling of I_{Na} and I_f in the developing SAN. The resultant APs at neonatal age showed greater peak amplitude values and smaller APD values, which can be attributed to the post-developmental changes of $I_{Ca,L}$ and I_{NaCa}; (2) at the tissue level, the post-neonatal changes in cellular APs are reflected by a decrease in the pacemaking rate and AP conduction velocity across the SAN-atrium; (3) acetylcholine had a greater effect on modulating AP pacemaking and conduction in the neonate compared to the adult. A high concentration of ACh in the neonate not only slowed down AP propagation, but also compromised the ability of the SAN to pace and drive the atrium. It could also produce a leading pacemaking site shift to the periphery. These findings may be of relevance to underlying mechanisms responsible for a possible risk of cardiac arres in new-born babies during sleep when the vagal tone is more active.

4.4.1 Role of postnatal ion-channel remodelling on pacemaking activity

At the cellular level, our simulation results reproduced the age-dependent changes in pacemaking APs and their characteristics, such as the pacemaking rates, between neonatal and adult SAN as observed experimentally.[16] Further analyses of the role of each individual remodelled ion channel of I_{Na}, $I_{Ca,L}$, I_f, I_{Kr}, I_{Ks} and I_{NaCa} by the "exclusive method" elucidated the contribution of each of these channels to the faster pacemaking APs observed in the neonatal group compared with the adult group.

Role of I_{Na}. Our simulation results suggested that (i) the presence of I_{Na} in the neonate central cells is the one of the major factors responsible for their faster pacemaking activity (i.e., short CL) than that in the adult. This finding is consistent with a previous study,[16] showing that I_{Na} was present in rabbit central SAN cells at birth, but fully disappeared by the 40th postnatal day. In the earlier experimental study, the functional role of the current was assessed by applying a Na^+ channel blocker, TTX, at a

concentration of 3μM and measuring the spontaneous activity of the APs in both the neonatal and adult cells in the SAN. It was found that TTX modified the action potential parameters of the neonatal cells, including a reduction of the upstroke velocity, a decrease in the diastolic depolarisation slope from 0.035 to 0.015V/s, and the consequent slowing down of the pacemaking rate by 60%. However, in the adult cells from the central SAN, I_{Na} was absent and application of TTX did not show changes in their APs; (ii) the marked age-dependent change in the I_{Na} channel properties also contributes to the faster pacemaking APs in the central neonate SAN cells. In the neonatal SAN cells, a noticeable window I_{Na} current, resulting from the overlap between activation and inactivation curves of the current, provides a depolarising current in the diastolic phase, accelerating pacemaking APs in neonates. However, with development, the position of the activation curve shifts in the positive direction while the inactivation curve remains, resulting in a reduced overlap of the two curves and hence the window current slowing down the depolarisation.

Role of $I_{Ca,L}$ and $I_{Ca,T}$. Our simulation results showed that the age-related modulation of $I_{Ca,L}$ has a secondary contribution to the faster pacemaking rate of the neonate. The greater $I_{Ca,L}$ density in the neonate and the modulation of $I_{Ca,L}$ kinetics with age (activation curve shifted to the left, steady-state inactivation curve shifted to the right) also play an important role in the high peak value of the APs in the neonate. However, in the adult, although the current density of the $I_{Ca,L}$ in the central cells was found to be smaller than in the neonate, the opposite shift in activation and inactivation curves during the developmental course resulted in a greater window current in the adult, providing more depolarising Ca^{2+} current during the depolarisation phase of the AP in the adult [20], which slowed down the repolarisation phase, forming the secondary cause of the fast HR in neonates. Despite the fact that there were recorded changes to the HR between the neonate and adult SAN cells, the absence of developmental changes in $I_{Ca,T}$ may indicate that this current does not make a major contribution to the different ion currents regulating the APs in central rabbit SAN during development. However, this can vary among different species, as cellular electrophysiology experiments on mice in different age groups showed an age-dependent decline of the heart rate accompanied by a significant decrease of $I_{Ca,T}$ conductance densities in aged SAN currents.[1]

Role of I_f. The present study also demonstrated an association between the age-dependent difference in current density and the modulation of the I_f activation curve in SAN cells, causing a slowing of pacemaking rate during postnatal development. Previous studies demonstrated that the pacemaker current, I_f, exhibited an age-dependent decrease in current density which was assumed to result from a reduction in baseline cAMP levels in the SA node, suggesting that the combined action between the I_f channels and the reduced number of cAMP molecules are the main cause of the shift in the activation curve towards hyperpolarisation in older age groups, leaving fewer I_f channels available to initiate diastolic depolarisation, a key determinant of the heart rate decrease of the SA node [8,18].

Role of other channel currents. Based on the measurement of gene-expression levels, the great abundance of I_{Kr}, I_{Ks} and I_{NaCa} in neonate SAN is of small consequence for age differences in pacemaking.[56] In addition, the mechanism of the Na^+/Ca^{2+} exchange merits study as it is intimately associated with other components of Ca^{2+} homeostasis, such as sarcoplasmic reticular Ca^{2+} stores and release mechanisms, both of which change with postnatal development in other cardiac regions, but not in neonatal SAN.[57] The contribution of the delayed rectifier K^+ currents and Na^+/Ca^{2+} exchange current to SAN pacemaking in adults has been previously studied. [57-59], but the role of developmental changes in K^+ currents in the sinus node remains unexplored. [56,60]

4.4.2 Postnatal effect on AP conduction in SAN-atrial tissue

At the tissue level, our results show that the combined effect of ion-channel remodelling and the reduced intercellular electrical coupling alters the conduction properties of the APs across the tissue, thereby impairing the function of the SAN with age. The simulation results on the increased conduction time and reduced conduction velocity in the adult tissue are consistent with experimental observations of changed conduction velocity and time taken for the APs to travel toward the RA from guinea pigs [22], which demonstrated a link between the progressive increase in the area of SAN tissue lacking the Cx43 protein and the decrease in the intrinsic HR A previous study of intact SAN-atria in guinea pigs during their lifespan.[22] Without considering the connexin remodelling, ionic-channel remodelling alone resulted in multiple leading pacemaking sites (Figure 4.21), which implied a functional role of connexin remodelling with age to ensure a normal pacemaking AP initiation and conduction in the intact SAN-atrium

tissue. According to a number of experimental studies [3,28,61], the electrotonic interaction between the SAN and the atrium affects the pacemaking APs of the SAN cells, leading to a depression in the pacemaking APs. Thus, the magnitude of the CL at the tissue level is greater than that of the isolated single SAN cells.

4.4.3 Effects of acetylcholine on the SAN during age development

The chronotropic responsiveness of developing sinoatrial myocytes to acetylcholine (ACh) has been studied.[18,51] This study elucidated possible mechanisms underlying the increased responsiveness of the neonate SAN cells to ACh. Our simulation results show that the large current density of $I_{K,ACh}$ in the neonate SAN cells plays a major role in this responsiveness, together with greater densities of I_f and $I_{Ca,L}$, which play an important secondary contribution to this significant effect of ACh in neonate SAN cells. At both cellular and 2D-tissue levels, a more suppressive effect of ACh on the neonate pacemaking rate in SAN has been observed with increased ACh concentrations, which is comparable with experimental observation.[51] Above a critical concentration (> $7x10^{-8}$ M), ACh not only slows down the pacemaking rate in SAN cells, but also shifts the leading pacemaking site from the SAN to the periphery (Figure S4.8). In comparison, in the adult tissue, previous studies have demonstrated that the leading pacemaker can be shifted within the SAN in response to vagal nerve stimulation. [53-55] These studies revealed that the application of specific concentrations of ACh (above $15x10^{-8}$M) may trigger a leading pacemaker site shift alongside the CT, usually towards the superior vena cava but occasionally towards the interior vena cava. The observed increase in the activation timing and decrease in the AP conduction velocity underlies the conduction failure from the SAN to the atrium, providing a potential mechanistic insight into bradycardia-related dysfunction under conditions of high vagal tone.

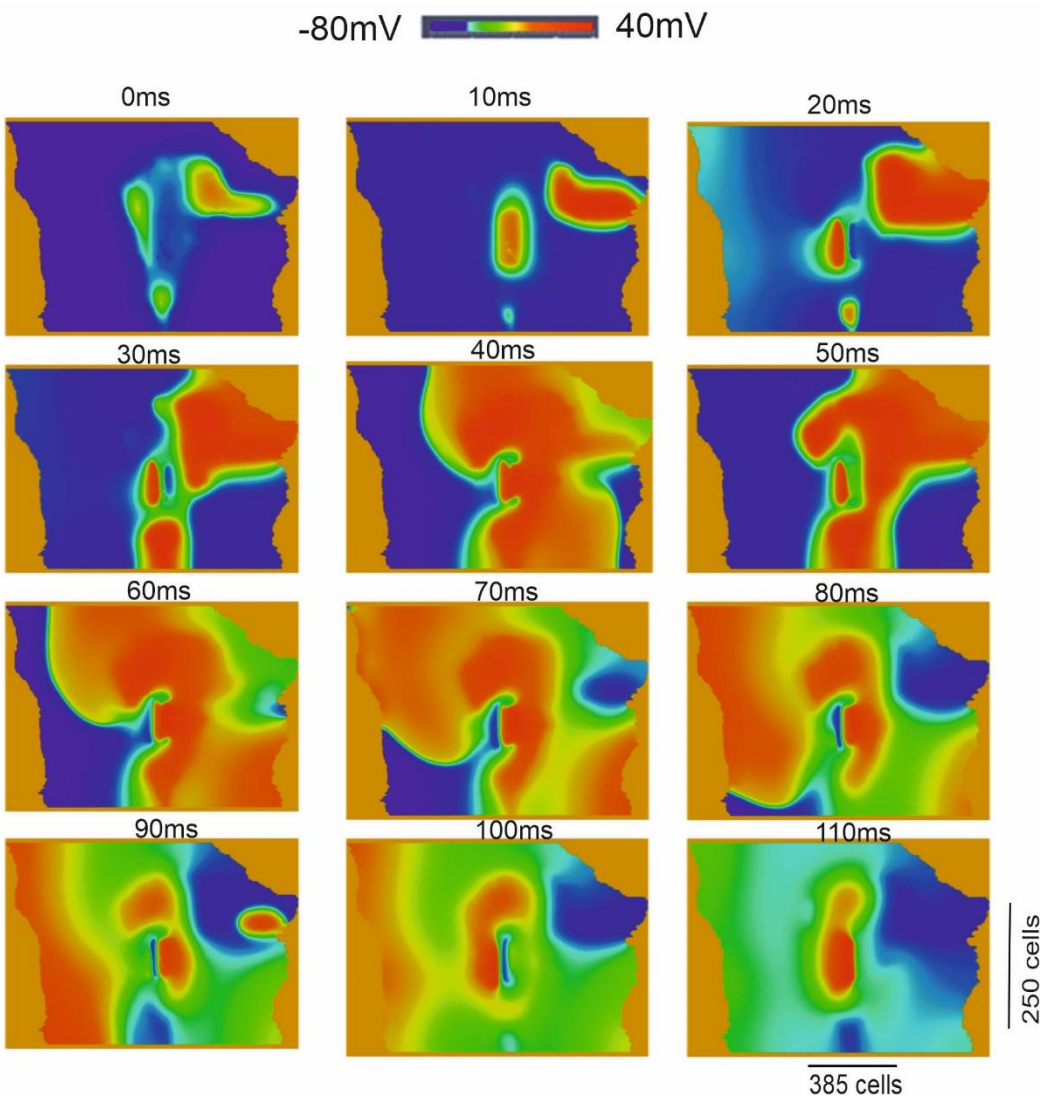

Figure 4.21. Multi-leading pacemaking sites resulting from ion-channel remodelling in the absence of connexin remodelling. Snapshots of the activation pattern at various timings are shown.

4.4.4 Limitations of the study

This study was based on mathematical models of the APs of adult rabbit SAN cells, which inherited some limitations that have been described previously in the literature.[26,28] The model developed for the neonatal SAN cells was based on data from various sources. Specifically, the formulations and the current densities of I_{Na}, $I_{Ca,L}$ and I_f were based on voltage-clamp data from newborn rabbit SAN cells, while data on I_{Kr}, I_{Ks}, $I_{K,ACh}$ and I_{NaCa} were based on data from messenger RNA gene expression or protein levels, as no experimental data on their kinetic or current densities in the SAN

cell is available. In model development, we assumed there is a correlation between the gene expression or protein level for certain ion channel subunits and their current densities. However, such correlation may be nonlinear and is still unclear. Remodelling in connexin Cx43 was based on data from guinea-pig SAN tissue. Though it is necessary to make clear these limitations, it is an accepted practice in computational modelling to use data from other species when there is a lack of data from the target species.[28] In addition, our simulation was based on extant data on ion-channel remodelling, but other factors such as remodelling in calcium handling, ionic homeostasis and energy metabolism, have not been considered due to lack of available data. They may also be of significance in modulation of postnatal pacemaking APs. However, it is notable that the simulated neonatal pacemaking APs matched well prior experimental data from newborn rabbit SAN cells,[16,30] which validates the model development and justifies the use of parameters for the mathematical model of neonatal rabbit SAN cells.

The 2D anatomical tissue model considered the anisotropic and electrical heterogeneity of the SAN-atrial tissue, providing valuable insights into the age-related effect on the AP initiation and conduction pathway in the SAN and surrounding tissue. However, further 3D anatomical models that considered tissue anisotropy, heterogeneity and spatial structure might be more useful to investigate the initiation and conduction of APs in control or ACh conditions (e.g., the phenomenon of leading pacemaking site shift). Moreover, the tissue geometry used in the neonatal case here was similar to that in the adult. It has been reported that during the growth of the rabbit, the heart weight and cell diameter increases for the central and peripheral SAN and/or atrial tissue, suggesting that the AP conduction distance may increase with development.[16,30] Further research is therefore required to determine the tissue geometry in neonate rabbit intact SAN-atrial tissue.

4.5 Conclusion

This simulation study is of significance for three reasons. First, it provides a novel computational model for neonatal rabbit SAN cells. The model has been well validated and can be further used to study the key mechanism responsible for the fast heart rate in neonatal hearts, which may have value for the understanding and treatment of cardiac rhythm disorders in the immature, adult, and aged individuals. Second, the results of the study help understand the dramatic differences in the initiation and conduction of APs

at the cellular and tissue levels between neonates and adults. Third, ionic mechanisms responsible for the high sensitivity of neonatal SAN cells to acetylcholine were elucidated. The observation of an amplified effect of ACh in the neonates leading to possible sinus arrest or conduction exit block may be of relevance to cardiac dysfunction in the very young, under situations of high vagal tone.

References

1. Larson ED, St Clair JR, Sumner WA, Bannister RA, Proenza C. Depressed pacemaker activity of sinoatrial node myocytes contributes to the age-dependent decline in maximum heart rate. Proc Natl Acad Sci U S A [Internet]. 2013 Oct 29 [cited 2018 Mar 16];110(44):18011–6. Available from: http://www.ncbi.nlm.nih.gov/pubmed/24128759

2. Dobrzynski H, Boyett MR, Anderson RH. New Insights Into Pacemaker Activity: Promoting Understanding of Sick Sinus Syndrome. Circulation [Internet]. 2007 Mar 26 [cited 2018 Jan 5];115(14):1921–32. Available from: http://www.ncbi.nlm.nih.gov/pubmed/17420362

3. Yanni J, Tellez JO, Sutyagin P V., Boyett MR, Dobrzynski H. Structural remodelling of the sinoatrial node in obese old rats. J Mol Cell Cardiol. 2010;48((2010)):653–662.

4. John Mersch, MD F. Pediatric Vital Signs: Charts of Normal Ranges [Internet]. [cited 2019 Nov 10]. Available from: https://www.emedicinehealth.com/pediatric_vital_signs/article_em.htm

5. Your heart rate - British Heart Foundation [Internet]. [cited 2019 Nov 10]. Available from: https://www.bhf.org.uk/informationsupport/how-a-healthy-heart-works/your-heart-rate

6. Boyett MR, Honjo H, Kodama I. The sinoatrial node, a heterogeneous pacemaker structure. Cardiovasc Res [Internet]. 2000 [cited 2017 Jul 20];47:658–87. Available from: www.elsevier.com

7. Satoh H. Sino-atrial nodal cells of mammalian hearts: ionic currents and gene expression of pacemaker ionic channels. J Smooth Muscle Res [Internet]. 2003 Oct [cited 2018 Jan 30];39(5):175–93. Available from: http://www.ncbi.nlm.nih.gov/pubmed/14695028

8. Yang ZF, Sun Y, Li CZ, Wang HW, Wang XJ, Zheng YQ, *et al.* Reduced sinoatrial cAMP content plays a role in postnatal heart rate slowing in the rabbit. Clin Exp Pharmacol Physiol. 2006;33((8)):757–62.

9. Roberts BN, Yang P-C, Behrens SB, Moreno JD, Clancy CE. Computational approaches to understand cardiac electrophysiology and arrhythmias. Am J Physiol Heart Circ Physiol [Internet]. 2012 Oct 1 [cited 2018 Jan 29];303(7):H766-83. Available from:

http://www.ncbi.nlm.nih.gov/pubmed/22886409

10. Campbell DL, Rasmusson RL, Strauss HC. Ionic Current Mechanisms Generating Vertebrate Primary Cardiac Pacemaker Activity at the Single Cell Level: An Integrative View. Annu Rev Physiol [Internet]. 1992 Oct 28 [cited 2018 Feb 22];54(1):279–302. Available from: http://www.annualreviews.org/doi/10.1146/annurev.ph.54.030192.001431

11. Jose AD, Collison D. The normal range and determinants of the intrinsic heart rate in man. Cardiovasc Res [Internet]. 1970 Apr 1 [cited 2019 Nov 10];4(2):160–7. Available from: https://academic.oup.com/cardiovascres/article-lookup/doi/10.1093/cvr/4.2.160

12. Opthof T. The normal range and determinants of the intrinsic heart rate in man. Cardiovasc Res [Internet]. 2000 Jan 1 [cited 2019 Nov 10];45(1):177–84. Available from: https://academic.oup.com/cardiovascres/article-lookup/doi/10.1016/S0008-6363(99)00322-3

13. Toda N. Age-related changes in the transmembrane potential of isolated rabbit sino-atrial nodes and atria. Cardiovasc Res [Internet]. 1980 Jan 1 [cited 2019 Nov 10];14(1):58–63. Available from: https://academic.oup.com/cardiovascres/article-lookup/doi/10.1093/cvr/14.1.58

14. Baruscotti M, Robinson RB. Electrophysiology and pacemaker function of the developing sinoatrial node. Am J Physiol Hear Circ Physiol [Internet]. 2007 [cited 2017 Dec 26];293:2613–23. Available from: http://www.physiology.org/doi/pdf/10.1152/ajpheart.00750.2007

15. Yang Z-F, Li C-Z, Li Q, Wang X-J, Liu Y-M. [The sinus node itself also plays a role in heart rate slowing down during postnatal development]. Sheng Li Xue Bao [Internet]. 2002 Aug 25 [cited 2019 Nov 10];54(4):282–6. Available from: http://www.ncbi.nlm.nih.gov/pubmed/12195274

16. Baruscotti M, DiFrancesco D, Robinson RB. A TTX-sensitive inward sodium current contributes to spontaneous activity in newborn rabbit sino-atrial node cells. J Physiol [Internet]. 1996 Apr 1 [cited 2018 Jan 30];492 (Pt 1(Pt 1):21–30. Available from: http://www.ncbi.nlm.nih.gov/pubmed/8730579

17. Baruscotti M, Difrancesco D, Robinson RB, Generali B. Single-channel properties of the sinoatrial node Na + current in the newborn rabbit. 2001;192–6.

18. Accili EA, Robinson RB, DiFrancesco D. Properties and modulation of If in newborn versus adult cardiac SA node. Am J Physiol Circ Physiol [Internet]. 1997 Mar [cited 2017 Dec 26];272(3):H1549–52. Available from: http://www.physiology.org/doi/10.1152/ajpheart.1997.272.3.H1549

19. Jones SA, Boyett MR, Lancaster MK. Declining into failure: The age-dependent loss of the L-type calcium channel within the sinoatrial node. Circulation. 2007;115(10):1183–90.

20. Protas LE V, Difrancesco D, Robinson RB, Difrancesco D, Rob- RB. L-type but not T-type calcium current changes during postnatal development in rabbit sinoatrial node. Am J Physiol Hear Circ Physiol. 2017;10032:1252–9.

21. Adachi T, Shibata S. The mechanism of increased postnatal heart rate and sinoatrial node pacemaker activity in mice. J Physiol Sci. 2013;(63:):133–46.

22. Jones SA, Lancaster MK, Boyett MR. Ageing-related changes of connexins and conduction within the sinoatrial node. J Physiol [Internet]. 2004 Oct [cited 2017 Jul 26];560(2):429–37. Available from: http://doi.wiley.com/10.1113/jphysiol.2004.072108

23. Fabbri A, Fantini M, Wilders R, Severi S. A Novel Computational Model of the Human Sinoatrial Action Potential.

24. Fabbri A, Fantini M, Wilders R, Severi S. Computational analysis of the human sinus node action potential: model development and effects of mutations. J Physiol [Internet]. 2017 Apr 1 [cited 2018 Mar 16];595(7):2365–96. Available from: http://doi.wiley.com/10.1113/JP273259

25. Wilders R. Computer modelling of the sinoatrial node. Med Bio Eng Comput [Internet]. 2007 [cited 2017 Jul 20];45:189–207. Available from: https://link.springer.com/content/pdf/10.1007%2Fs11517-006-0127-0.pdf

26. Zhang H, Holden A V, Kodama I, Honjo H, Lei M, Varghese T, *et al.* Mathematical models of action potentials in the periphery and center of the rabbit sinoatrial node. Am J Physiol Hear Circ Physiol. 2000;279(2000):H397–H421.

27. Butters TD, Aslanidi O V., Inada S, Boyett MR, Hancox JC, Lei M, *et al.* Mechanistic links between Na+ channel (SCN5A) mutations and impaired cardiac pacemaking in sick sinus syndrome. Circ Res. 2010;107(1):126–37.

28. Bai X, Wang K, Yuan Y, Li Q, Dobrzynski H, Boyett MR, *et al.* simulation study Mechanism underlying impaired cardiac pacemaking rhythm during ischemia : A simulation study. 2017;093934.

29. Dobrzynski H, Li J, Tellez J, Greener ID, Nikolski VP, Wright SE, *et al.* Computer three-dimensional reconstruction of the sinoatrial node. Circulation. 2005;111(7):846–54.

30. Allah EA, Tellez JO, Yanni J, Nelson T, Monfredi O, Boyett MR, *et al.* Changes in the expression of ion channels, connexins and Ca2+-handling proteins in the sino-atrial node during postnatal development. Exp Physiol. 2011;96(4):426–38.

31. Lindblad DS, Murphey CR, Clark JW, Giles WR. A model of the action potential and underlying membrane currents in a rabbit atrial cell. Am J Physiol - Hear Circ Physiol. 1996;271(4 40-4).

32. DiFrancesco D. Pacemaker Mechanisms in Cardiac Tissue. Annu Rev Physiol [Internet]. 1993 Oct 28 [cited 2018 Feb 22];55(1):455–72. Available from: http://www.annualreviews.org/doi/10.1146/annurev.ph.55.030193.002323

33. Baruscotti M, Bucchi A, DiFrancesco D. Physiology and pharmacology of the cardiac pacemaker (“funny”) current. Pharmacol Ther [Internet]. 2005 Jul 1 [cited 2018 Feb 20];107(1):59–79. Available from: https://www.sciencedirect.com/science/article/pii/S0163725805000252?via%3D

ihub

34. Brioschi C, Micheloni S, Tellez JO, Pisoni G, Longhi R, Moroni P, *et al.* Distribution of the pacemaker HCN4 channel mRNA and protein in the rabbit sinoatrial node. J Mol Cell Cardiol [Internet]. 2009;47(2):221–7. Available from: http://dx.doi.org/10.1016/j.yjmcc.2009.04.009

35. Huang X, Yang P, Yang Z, Zhang H, Ma A. Age-associated expression of HCN channel isoforms in rat sinoatrial node. Exp Biol Med [Internet]. 2016 Feb [cited 2018 Mar 14];241(3):331. Available from: http://www.ncbi.nlm.nih.gov/pubmed/26341471

36. Protas L, Oren R V., Clancy CE, Robinson RB. Age-dependent changes in Na current magnitude and TTX-sensitivity in the canine sinoatrial node. J Mol Cell Cardiol [Internet]. 2010 Jan [cited 2018 Mar 22];48(1):172–80. Available from: http://www.ncbi.nlm.nih.gov/pubmed/19665465

37. Honjo H, Boyett MR, Kodama I, Toyama J. Correlation between electrical activity and the size of rabbit sino-atrial node cells. J Physiol [Internet]. 1996 Nov 1 [cited 2018 Feb 20];496 (Pt 3)(Pt 3):795–808. Available from: http://www.ncbi.nlm.nih.gov/pubmed/8930845

38. Verheijck EE, Wessels A, van Ginneken AC, Bourier J, Markman MW, Vermeulen JL, *et al.* Distribution of atrial and nodal cells within the rabbit sinoatrial node: models of sinoatrial transition. Circulation [Internet]. 1998 Apr 28 [cited 2018 Jan 5];97(16):1623–31. Available from: http://www.ncbi.nlm.nih.gov/pubmed/9593568

39. Verheijck E, Van Ginneken ACG, Wilders R, Bouman LN. Contribution of L-type Ca 2*ƈ* current to electrical activity in sinoatrial nodal myocytes of rabbits. Am J Physiol. 1999;276(3Pt2):H1064-77.

40. Mangoni ME, Couette B, Bourinet E, Platzer J, Reimer D, Striessnig J, *et al.* Functional role of L-type Cav1.3 Ca channels in cardiac pacemaker activity. Proc Natl Acad Sci [Internet]. 2003;100(9):5543–8. Available from: http://www.pnas.org/content/100/9/5543.long

41. Zaza A, Robinson RB, DiFrancesco D. Basal responses of the L-type Ca2+ and hyperpolarization- activated currents to autonomic agonists in the rabbit sino-atrial node. J Physiol. 1996;491(2):347–55.

42. Artman M. Sarcolemmal Na(+)-Ca2+ exchange activity and exchanger immunoreactivity in developing rabbit hearts. Am J Physiol Circ Physiol [Internet]. 1992 Nov [cited 2018 Feb 21];263(5):H1506–13. Available from: http://www.physiology.org/doi/10.1152/ajpheart.1992.263.5.H1506

43. Artman M, Ichikawa H, Avkiran M, Coetzee WA. Na+/Ca2+ exchange current density in cardiac myocytes from rabbits and guinea pigs during postnatal development. Am J Physiol [Internet]. 1995 Apr [cited 2018 Feb 21];268(4 Pt 2):H1714-22. Available from: http://www.ncbi.nlm.nih.gov/pubmed/7733375

44. Chen F, Mottino G, Klitzner TS, Philipson KD, Frank JS. Distribution of the Na+/Ca2+ exchange protein in developing rabbit myocytes. Am J Physiol Physiol [Internet]. 1995 May [cited 2018 Feb 21];268(5):C1126–32. Available

from: http://www.physiology.org/doi/10.1152/ajpcell.1995.268.5.C1126

45. Dan P, Lin E, Huang J, Biln P, Tibbits GF. Three-Dimensional Distribution of Cardiac Na+-Ca2+ Exchanger and Ryanodine Receptor during Development. Biophys J [Internet]. 2007 Oct 1 [cited 2018 Feb 21];93(7):2504–18. Available from: http://www.ncbi.nlm.nih.gov/pubmed/17557789

46. Qu Y, Ghatpande A, el-Sherif N, Boutjdir M. Gene expression of Na+/Ca2+ exchanger during development in human heart. Cardiovasc Res [Internet]. 2000 Mar [cited 2018 Feb 21];45(4):866–73. Available from: http://www.ncbi.nlm.nih.gov/pubmed/10728412

47. Zhang H, Holden A V., Noble D, Boyett MR. Analysis of the Chronotropic Effect of Acetylcholine on Sinoatrial Node Cells. J Cardiovasc Electrophysiol [Internet]. 2002 May 1 [cited 2018 Feb 5];13(5):465–74. Available from: http://doi.wiley.com/10.1046/j.1540-8167.2002.00465.x

48. Aslanidi O V, Boyett MR, Dobrzynski H, Li J, Zhang H. Mechanisms of transition from normal to reentrant electrical activity in a model of rabbit atrial tissue: interaction of tissue heterogeneity and anisotropy. Biophys J [Internet]. 2009 Feb 4 [cited 2018 Jan 5];96(3):798–817. Available from: http://www.ncbi.nlm.nih.gov/pubmed/19186122

49. Zhang H, Zhao Y, Lei M, Dobrzynski H, Liu JH, Holden A V., *et al.* Computational evaluation of the roles of Na^+ current, i_{Na}, and cell death in cardiac pacemaking and driving. Am J Physiol Circ Physiol [Internet]. 2007 Jan [cited 2018 Jan 5];292(1):H165–74. Available from: http://www.physiology.org/doi/10.1152/ajpheart.01101.2005

50. Boyett MR, Inada S, Yoo S, Li J, Liu J, Tellez J, *et al.* Connexins in the Sinoatrial and Atrioventricular Nodes. In: Cardiovascular Gap Junctions [Internet]. Basel: KARGER; 2006 [cited 2018 Jan 30]. p. 175–97. Available from: http://www.ncbi.nlm.nih.gov/pubmed/16646591

51. Atkins DL, Marvin WJ. Chronotropic Responsiveness of Developing Sinoatrial and Ventricular Rat Myocytes to Autonomic Agonists Following Adrenergic and Cholinergic Innervation In Vitro. [cited 2018 Mar 9]; Available from: https://pdfs.semanticscholar.org/5e2c/d47c14e24cdeb44908bab64850dec745e1a6.pdf

52. Rana OR, Schauerte P, Kluttig R, Schröder JW, Koenen RR, Weber C, *et al.* Acetylcholine as an age-dependent non-neuronal source in the heart. Auton Neurosci [Internet]. 2010 Aug 25 [cited 2018 Mar 14];156(1–2):82–9. Available from: https://www.sciencedirect.com/science/article/pii/S1566070210000809?via%3Dihub

53. Spear JF, Kronhaus KD, Moore EN, Kline RP. The effect of brief vagal stimulation on the isolated rabbit sinus node. Circ Res [Internet]. 1979 Jan 1 [cited 2018 Mar 9];44(1):75–88. Available from: http://www.ncbi.nlm.nih.gov/pubmed/758234

54. Shibata N, Inada S, Mitsui K, Honjo H, Yamamoto M, Niwa R, *et al.* Pacemaker Shift in the Rabbit Sinoatrial Node in Response to Vagal Nerve

Stimulation. Exp Physiol [Internet]. 2001 Mar 1 [cited 2018 Mar 9];86(2):177–84. Available from: http://doi.wiley.com/10.1113/eph8602100

55. Sciences P. Simulation of Cardiac Pacemaker Dysfunction Arising from Genetic Mutations. 2011;

56. Vinogradova TM, Zhou YY, Bogdanov KY, Yang D, Kuschel M, Cheng H, *et al.* Sinoatrial node pacemaker activity requires Ca(2+)/calmodulin-dependent protein kinase II activation. Circ Res [Internet]. 2000 Oct 27 [cited 2018 Mar 12];87(9):760–7. Available from: http://www.ncbi.nlm.nih.gov/pubmed/11055979

57. Kaplan P, Jurkovicova D, Babusikova E, Hudecova S, Racay P, Sirova M, *et al.* Effect of aging on the expression of intracellular Ca2+ transport proteins in a rat heart. Mol Cell Biochem [Internet]. 2007 Jun 4 [cited 2018 Mar 12];301(1–2):219–26. Available from: http://link.springer.com/10.1007/s11010-007-9414-9

58. Tibbits GF, Xu L, Sedarat F. Ontogeny of excitation-contraction coupling in the mammalian heart. Comp Biochem Physiol A Mol Integr Physiol [Internet]. 2002 Aug [cited 2018 Mar 12];132(4):691–8. Available from: http://www.ncbi.nlm.nih.gov/pubmed/12095856

59. Janowski E, Cleemann L, Sasse P, Morad M. Diversity of Ca2+ Signaling in Developing Cardiac Cells. Ann N Y Acad Sci [Internet]. 2006 Oct 1 [cited 2018 Mar 12];1080(1):154–64. Available from: http://doi.wiley.com/10.1196/annals.1380.014

60. Irisawa H, Brown HF, Giles W. Cardiac pacemaking in the sinoatrial node. Physiol Rev [Internet]. 1993 Jan [cited 2018 Mar 12];73(1):197–227. Available from: http://www.ncbi.nlm.nih.gov/pubmed/8380502

61. Woods WT, Urthaler F, James TN, Lin S-F. Spontaneous action potentials of cells in the canine sinus node. Circ Res [Internet]. 1976 Jul 5 [cited 2018 Jan 5];39(1):76–82. Available from: http://www.ncbi.nlm.nih.gov/pubmed/1277407

Chapter Five - Cardiac Pacemaker Dysfunction Arises from Different Pathways of Electrical Remodelling in the Ageing Rat Heart

5.1. Introduction

The sinoatrial node (SAN) is the primary pacemaker of the heart. It is situated in the superior right atrium and produces a sequence of auto-rhythmic electrical activities that control the heartbeat.[1] Dysfunction of the sinoatrial node (SND) associated with "sick sinus syndrome" (SSS) manifests as pathological bradycardia or systolic pauses[2], producing inadequate blood supply to satisfy the demands of the body. This condition leads to symptoms such as dizziness and syncope[2], though the initial stages of SND may be latent and asymptomatic.[3]

Various physiological and pathological mechanisms (intrinsic, extrinsic or a combination of the two) are responsible for SND.[4] Among them is the failure of a specific part of the SAN to achieve impulse generation[5], or the impulse conduction from the SAN to the surrounding atrial muscle, due to genetic mutations[6,7] or ischaemic conditions.[8] Increased fibrosis and degenerative changes in physiological properties of the SAN may also cause SND. [1,3,9]

SND is also associated with ageing [10,11]. Whilst it can occur at any age, the occurrence of SND significantly increases with age.[12] In a retrospective research study of 277 participants with compromised bradycardia, 51% of the cases were attributed to extrinsic causes (such as adverse drug reactions, imbalance of electrolytes or acute myocardial infarction, etc.), and 49% were attributable to either intrinsic or idiopathic [13] conditions, such as cardiac ischaemia, gene mutations, excessive training and particularly ageing. [3,4] More than 600,000 pacemaker implants are performed worldwide each year [8,14,15], of which the older adult account for the largest percentage.

Experimental data from animal models [16-20] and human studies [21,22] have demonstrated an association between SND and ageing. It has been shown that during

the ageing process, changes occur to SAN functions, manifested by increased pacemaking cycle length (CL) (i.e., slower heart rate) and reduced conduction of action potentials (i.e., an increased sinoatrial node-atrium conduction time (SACT)). Both of these contribute to the reduced aerobic capacity of older adults, leading to an increased incidence of abnormal pacemaker symptoms and atrial arrhythmia. [23] Further investigations have also revealed that such ageing-associated SND is related to changes in the cellular electrical properties of the SAN [9,10, 24-29] in a similar way to ageing-induced cellular changes in atrial and ventricular cells [29] and intercellular electrical coupling. [30]

A complex and variable patterns of ion channels and calcium-handling proteins have been observed in ageing-induced SND rat models. [31-33] In their study, Tellez *et al.*[31] found that ageing-SND was associated with a considerable changes of gene expression in the SAN including: a significant increase in the relative abundance of mRNA for many ion channels (e.g Nav1.5, Navβ1 and Cav1.2, Cav1.3 and KvLQT1, Kv4.2, which are responsible for I_{Ks} and I_{to} .in addition to an increase of the Ca^{2+} handling proteins; Sarcoplasmicreticulum Ca^{+2}-ATPase (SERCA2a), that responsible for Ca uptake process. The study showed , also, a depression in some ion channels (e.g. in Kv1.5, NCX, and HCN1) and in the Ca^{2+} clock gene; Ryanodine receptor, (RYR2) of the SAN during ageing (Ageing Study-1). This implied changes of them, though there is no explicit link between mRNA levels and channel activity.[34] However, other studies showed conflicting data, suggesting significant down-regulation trend of some ion channels (e.g. decreases Cav1.2, Cav1.3 and HCN4, and decrease in Ca^{2+} clock gene RYR2, and an increase of NCX and SERCA) in aged SAN cells (Ageing Study-2). [32,33,35]

The ionic mechanisms that underlie the ageing-associated SND are as yet unclear. It is possible that SND is associated with different "pathways" of ionic and molecular mechanisms, including up-regulation or down-regulation of particular ion channels as identified in previous studies. [31-35] The aim of the present study was to:

I. determine whether the age-induced changes in ion channels as identified in Ageing Study-1 and Ageing Study-2 were sufficient to account for the observed SND;
II. investigate the relative role of a particular remodelled ion channel on

modulation of the characteristics of pacemaking APs, including the cycle length (CL), action potential duration (APD_{50}), peak amplitude (PA), maximal upstroke velocity (dV/dt_{max}) and maximal diastolic potential (MDP); and

III. address the question of how differently remodelled $I_{Ca,L}$ could lead to SND.

5.2. Method

5.2.1. Mathematical models of single SAN cells

The consequence of ageing-induced electrophysiological changes in ion-channel currents in rat SAN cells was investigated using the model developed by Tao *et al.*[36] for rat pacemaking APs. The model was based on modifications of the rabbit SAN models [37,38] by incorporating experimental data for major ion channels obtained from rat SAN cells by Satoh *et al.*[39] and Shinagawa *et al.*[40]. In the Tao *et al.* model, the membrane potential V_m is dependent on a set of voltage-gated ion-channel currents, exchanger currents, and ionic pump currents, in the form of the following equations (5.1) and (5.2):

$$\frac{dV_m}{dt} = -\frac{1}{C_m} I_{tot} \tag{5.1}$$

$$I_{tot} = (I_{Ca,T} + I_{Ca,L} + I_{Kr} + I_{Ks} + I_{st} + I_{sus} + I_{to} + I_{K,ACh} + I_f + I_{b,Na} + I_{NaCa}) \tag{5.2}$$

where C_m is the cell capacitance (set at 32pF); I_f is the hyperpolarisation-activated current; $I_{Ca,L}$ and $I_{Ca,T}$ are the inward L-type and T-type Ca^{2+} currents; I_{Kr} and I_{Ks} are the rapid and slow delayed rectifier K^+ currents; I_{to} is the Ca^{2+}-independent transient outward K^+ current; I_{st} is the sustained inward current (carried by Na^+); I_{sus} is the sustained outward K^+ current; $I_{K,ACh}$ is the muscarinic K^+ channel current; I_{NaK} is the Na^+-K^+ pump current; I_{NaCa} is the Na^+-Ca^{2+} exchanger current; and $I_{b,Na}$ is the background inward Na^+ current.

Details of the equations and parameters of the model are documented in Tao *et al.*[36] Numerically, the equations for the rat SAN cell model were described by use of the classical Hodgkin-Huxley formalism at 37ºC, with a time step of 0.01ms, which was sufficiently small to ensure a stable numerical solution.

5.2.2. Ageing SAN model

To simulate the functional impact of ageing-induced changes on membrane ion channels and intracellular Ca^{2+} handling on cardiac pacemaking potentials, experimental data from two independent studies on ageing rat SAN cells, as conducted by Tellez *et al.*[31] (noted as Ageing Study-1) and Hatch *et al.* [32], Huang *et al.*[33] and Jones *et al.*[35] (noted as Ageing Study-2) were incorporated into the Tao *et al.* model.[36] Both datasets were obtained from SAN cells isolated from the right atrium of Wistar Hannover rats with ages of ≥ 25 or ≥ 24 months (equivalent to about a 70-year-old human). In both studies, cellular APs and ECGs were recorded. These showed reductions in heart rates in the older adult rat SAN preparations by 18% [31] and 11% [32], respectively, as compared with adult preparations. Such a change in heart rate is associated with changes in cellular ion channels, as summarised in Table 5.1.

In simulation, AP characteristics including CL (and hence HR), maximal diastolic potential (MDP), peak amplitude (PA) and action potential duration (APD_{50}) were computed in adult and older adult conditions, which were compared with the relevant experimental data. [32-34] In order to elucidate the primary factor(s) responsible for the slower heart rate in the older adult cells, the relative impacts of different remodelled ionic channels on CL were analysed via two distinct methods: the inclusive, and the exclusive simulation methods. With the inclusive method, all changes in the remodelled ion channels and Ca^{2+} handling due to ageing were considered for the older adult condition. With the exclusive simulation method, only a specific remodelled ion channel or subsets of all the remodelled ion channels were considered for the older adult condition, while the rest of the ageing-induced changes were not included in the models. Details of ion channels considered in each case are described in the following sections.

Table 5.1. Relative changes in mRNA, protein expression levels and current density/channel conductance of ion channels and intracellular Ca^{2+} handling between adult and older adult rat SAN. Data are from studies on rat central SAN cells by Tellez *et al.*[31] (Ageing Study-1); Hatch *et al.*[32], Huang *et al.*[33], and Jones *et al.*[35] (Ageing Study-2). Arrows indicate up- or down-regulation of the underlying channels, as indicated by changes in mRNA, protein expression levels or measured channel current densities.

Ageing Study -1				**Ageing Study -2**				
Isoform	Underlying ion channel current	|Relative change in mRNA (older adult/ adult)	Reference	Isoform	Underlying ion channel current	Relative change in protein expression (older adult/adult)	Relative change in channel current density (older adult/adult)	Reference
Cav1.2	$I_{Ca,L}$	↑25%	Tellez *et al.*[31]	Cav1.2	$I_{Ca,L}$	↓66%	↓50%	Jones *et al.*[35]
Cav1.3	$I_{Ca,L}$	↑30%		Cav1.3	$I_{Ca,L}$	↓50%	-	Hatch *et al.*[32]
RyR2	Ca_release	↓80%		RyR2	Ca_release	↓67%	↓24%	
SERCA2a	Ca_uptake	↑15%		SERCA2a	Ca_ uptake	↓83%	↓29%	
NCX	I_{NaCa}	↓6%		NCX	I_{NaCa}	↑72%	↑42%	
HCN4	I_f	↓16%		HCN4	I_f	↓30%		Huang *et al.*[33]
KvLQT1	I_{Ks}	↑60%		HCN2	I_f	↓49%		
ERG	I_{Kr}	↓8%						
Kv4.2	I_{to}	↑50%						
Cav3.1	$I_{Ca,T}$	↓12%						
Na+/K+ pump	I_{NaK}	↑50%						

5.3. Results

5.3.1 Effects of ion-channel remodelling on pacemaking APs

Figure 5.1 shows the simulated effects of ageing on the pacemaking AP of rat SAN cells based on the experimental data set of Ageing Study-1 (left panels) and Ageing Study-2 (right panels). It has been shown that both data sets produce a similar consequence of ageing, i.e., a slower pacemaking rate in the older adult compared with the adult condition, though they show dramatic differences in remodelling of membrane ion channels and the intracellular Ca^{2+} handling system (see Table 5.1). Using the dataset Ageing Study-1, the CL that was computed under controlled conditions of 230ms was increased to 310ms in the older adult condition, illustrating a ~16% decrease in pacemaking rate. Similarly, using the dataset of Ageing Study-2, a 35ms increase in CL was observed, corresponding to ~12.9% decrease in HR. Such simulated effects of ageing on slowing the cardiac pacemaking APs are in agreement with those observed experimentally. [32-34]

Although the experimental data sets produced similar effects on reduction of the pacemaking rate, each of the data-sets produced different changes in the characteristics of the simulated APs. In the case of Ageing Study-1, the simulated pacemaking APs in the older adult condition (Figure 5.1Ai) presented a more hyperpolarised maximum diastolic potential (MDP) (by -12.8mV), a greater dV/dt_{max} (by 60%), PA (by 20%) and APD_{50} (by 14%). These changes in AP characteristics were attributable to changes in the underlying ion-channel currents and the Ca^{2+} handling processes, which manifested as a decreased I_f (Figure 5.1Bi) and increased $I_{Ca,L}$ (Figure 5.1Ci), decreased I_{NaCa} (Figure 5.1Di), as well as an increased I_{NaK} (Figure 5.1Ei) and Ca^{2+} uptake (Figure 5.1Fi), but a decreased Ca^{2+} release (Figure 5.1Gi).

However, in the case of Ageing Study-2, the simulated pacemaking APs (Figure 5.1Aii) presented an elevated maximum diastolic potential value (by +9.3mV), decreased dV/dt_{max} (by 64%), PA (by 70%) and abbreviated APD_{50} (by 17%). These changes were attributable to decreased I_f (Figure 5.1Bii) and I_{CaL} (Figure 5.1Cii), increased I_{NaCa} (Figure5.1Dii), and Ca^{2+} uptake (Figure 5.1Fii) but decreased Ca^{2+} release (Figure 5.1Gii). The decrease in PA was attributable to the reduction of the L-Type calcium current.

Simulated effects of ageing on the pacemaking APs and their characteristics were validated by quantitative comparison of the simulation with experimental data when possible. Results are shown in Figure 5.2 and summarised in Table 5.2. In the case of Ageing Study-1, simulations showed that there was an increase in CL of 80ms (34.3%), leading to a 16% reduction in HR. This is quantitatively consistent with Tellez *et al.*[31], who observed an increase in CL (by 35.3%) that corresponded to an 18% reduction in HR. Simulation observed increases in APD_{50} and maximal dV/dt_{max} that were also quantitatively consistent with the results of Tellez *et al.*[31]

In Ageing Study-2, simulations showed that ageing caused an increased CL by 35ms (15.2%), which corresponded to a reduction in HR of about 12.9%. This was also quantitatively comparable with data from Hatch *et al.*[32] They observed a CL increase of 43 ± 12ms (by 23%; corresponding to an 11% decrease in HR). In simulations, we also observed decreases in APD_{50}, dV/dt_{max} and the amplitude of action potentials. However, there was no experimental data available for quantitative comparison with these values.

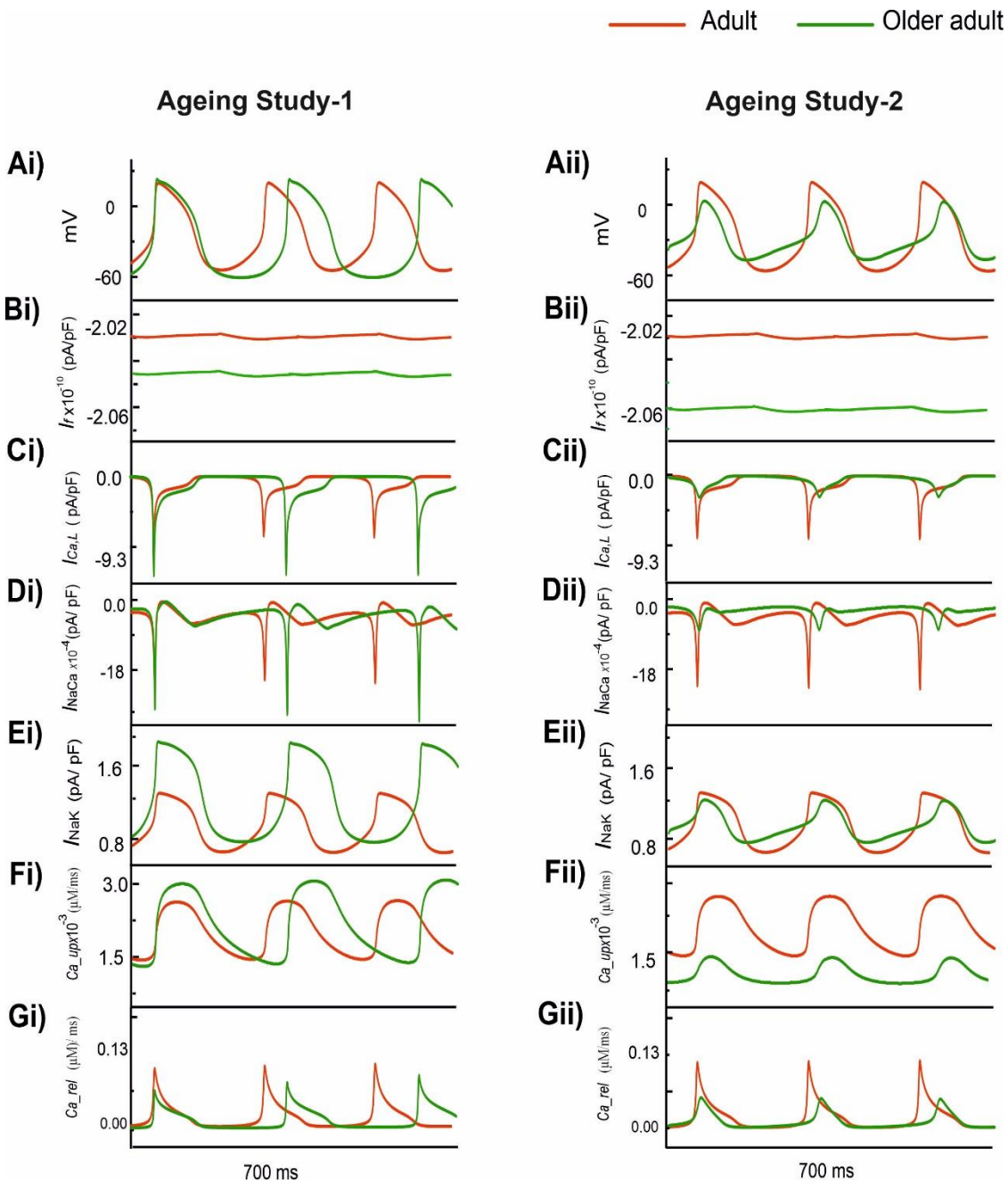

Figure 5.1. (Ai, Aii): Action potentials computed from rat SAN myocytes in adult (red) and older adult (green) conditions using the Ageing Study-1 (left panels) and Ageing Study-2 (right panels) datasets. The data were produced by use of the rat SAN cell model developed by Tao *et al.*[36]. (Bi-Gii): Underlying ionic channel currents and Ca^{2+} handling during APs: I_f, I_{CaL}, I_{NaCa}, I_{NaK}, Ca^{2+} release, and Ca^{2+} uptake.

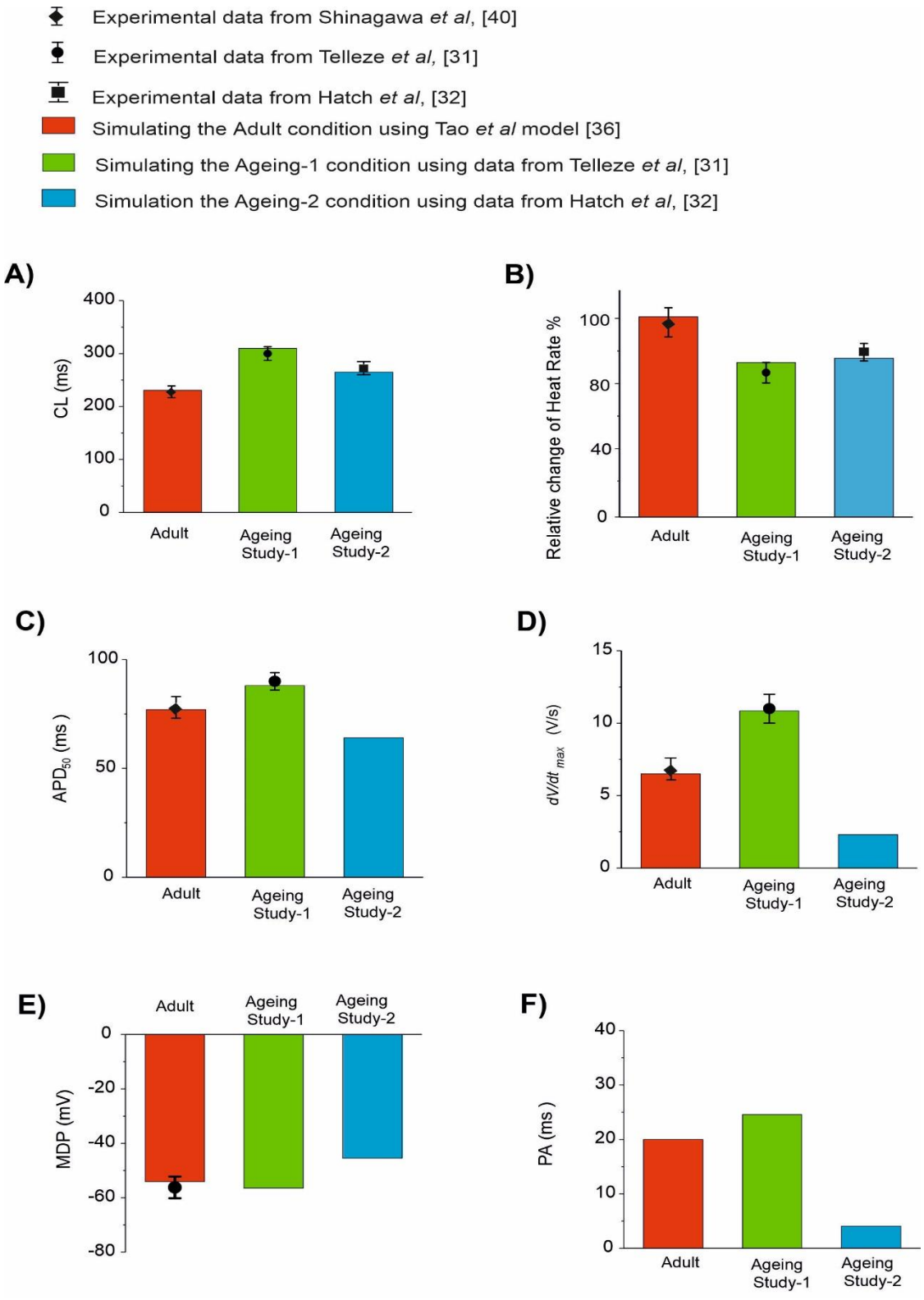

Figure 5.2. Quantitative comparison between experimental and simulated data of the functional effects of ageing on the pacemaking APs and their characteristics. (A) CL; (B) HR; (C) APD_{50}; (D) dV/dt_{max}; (E) MDP; and (F) PA. Data for adult is shown in red, and from Ageing Study-1 and -2 in green and blue, respectively. Experimental data with error bars are from Tellez *et al.*[31] and Hatch *et al.*[32]

Table 5.2. Characteristics of action potentials and heart rates in adult and older adult conditions based on experimental data of Ageing Study-1 and Ageing Study-2, which were incorporated into the Tao *et al.*[36]model. Simulation data were compared with the experimental data of Tellez *et al.*[31] for Ageing Study-1 and Hatch *et al.*[32] for Ageing Study-2. Data with error bars were from the experimental studies of Tellez *et al.*[31] and Hatch *et al.*[32]

	Adult **Simulation** Tao *et al.*[36]	**Adult** **Experiment** Shinagawa *et al.*[40]	**Ageing study -1** **Simulation**	**Ageing study -1** **Experiment** Tellez *et al.* [31]	**Ageing study -2** **Simulation**	**Ageing study -2** **Experiment** Hatch *et al.*[32]
dV/dt_{max}(V/s)	6.50	7.00 ± 1.0	10.85	11.00 ±1.0	2.31	-
MDP (mV)	-54.01	-56.02 ± 2.0	-56.84	-	-45.70	-
PA (mV)	20.00	-	24.58	-	4.16	-
APD_{50} (ms)	77.06	78.00 ± 1.0	88.00	90.14 ± 2.2	64.00	-
CL (ms)	230.00	232.23 ± 10.0	310.44 (↑34%)	300.00 ± 12.0(↑35%)	265.22 (↑15.2%)	275.0 ± 12.0(↑23.1%)
HR (bpm)	260.00	258.62 ± 17.0	210.12 (↓16%)	200.17 ± 14 (↓18%)	226.45 (↓12.9%)	230.1 ± 8.2 (↓11.0 %)

5.3.2. Relative role of individual (or a subset of) remodelled ion channel(s) in ageing bradycardia

Simulation results using the data sets from Ageing Studies 1 and 2 produced similar ageing bradycardic effects that both qualitatively and quantitatively matched to their experimental observations, although there were marked differences in the underlying remodelled ion channels and the intracellular Ca^{2+} handling processes. In order to elucidate the primary factor(s) that contributed to ageing bradycardia, the relative roles of individual, or a subset of, remodelled ion channels and Ca^{2+} handling on pacemaking APs were simulated and analysed using the exclusive method. Through this method, only ageing-induced changes of interest were considered, while other remodelling factors were ignored.

After analysis of the differences and similarities in the ageing-induced remodelling patterns between Ageing Studies 1 and 2, three different cases were analysed, as shown below.

5.3.2.1 Case 1: Effects of remodelled I_f and RyR2

Both ageing studies showed similar down-regulated expressions of mRNA coding for I_f and Ca^{2+} release channels. Therefore, in Case 1, simulations were conducted to evaluate the effects of a reduced I_f and Ca^{2+} release-channel current (flux) from the sarcoplasmic reticulum (SR) on the pacemaking APs using the exclusive approach. Results drawn up in Figure 5.3 show the computed APs for the control (adult) and for the older adult conditions from the Tao *et al.*[36] model based on Ageing Study-1 (left panels (Ai)) and Ageing Study-2 (right panels (Aii)). During the APs, the time traces of I_f and Ca^{2+} release flux from the SR are also shown in panels (Bi) and (Bii), and (Ci) and (Cii), for the adult and older adult conditions, respectively.

In both data sets, reduced I_f and Ca^{2+} release from the SR had a limited effect on slowing down the pacemaking rate of APs. With a combined action of reduced I_f and Ca^{2+} release, the HR was reduced when considering the data set from Ageing Study-1, but unchanged when considering the data set from Ageing Study-2.

Simulation results from both data sets suggested a limited role of combined action of remodelled I_f and Ca^{2+} release in the bradycardia. Further analysis was conducted to analyse the individual role of a wide-range reduction of I_f or SR Ca^{2+} release. When I_f

reduction alone was considered from 16% (Ageing Study-1) to 30% (Ageing Study-2), there was no noticeable change in the pacemaking APs. This result was in agreement with the results of Bers *et al.*[41], who observed that I_f played only a minor role in the primary and central SAN cells, though a critical role in the peripheral SAN cells.

When a reduced SR Ca^{2+} release alone was considered by 80% (Ageing Study-1) or 24% (Ageing Study-2), there was a small increase in the measured CL. With an 80% reduction in the RyR2 alone, as suggested by Ageing Study-1, CL was increased by 2.45%, while with a 24% reduction in the RyR2 alone as seen in Ageing Study-2, no noticeable change in the CL was observed. The time traces of Ca^{2+} release flux during the APs are shown in panels (Ci) and (Cii) for the adult (red) and older adult (green) conditions. Panels (Di) and (Dii) compare the simulated and experimental results of relative changes in HR when the age-induced remodelling of I_f and RyR2 alone were considered.

5.3.2.2 Case 2: Effects of remodelled $I_{Ca,L}$, I_{NaCa}, and SERCA2a

Both the Ageing Study datasets showed a common set of changes in $I_{Ca,L}$, I_{NaCa} and Ca^{2+} uptake from the SR, though with dramatic differences. In Ageing Study-1, up-regulation of $I_{Ca,L}$ and Ca^{2+} uptake, but down-regulation of I_{NaCa}, were observed; whilst in Ageing Study-2, down-regulation in $I_{Ca,L}$ and Ca^{2+} uptake, but an up-regulation of I_{NaCa}, were shown.

It is unclear how such contradictory behaviours of remodelled ion channels can lead to the same consequence. To address this question, simulations were conducted to investigate the role of the altered $I_{Ca,L}$, I_{NaCa} and Ca^{2+} uptake in generating ageing bradycardia based on the two studies

Results are shown in Figure 5.4 for the computed APs (Ai and Aii) in the adult and older adult conditions, as well as the underlying time courses of $I_{Ca,L}$ (Bi, Bii), I_{NaCa} (Ci, Cii), and Ca^{2+} uptake (Di, Dii) based on data of Ageing Study-1 (left panels) and -2 (right panels). Figure 5.4Ai shows the simulated pacemaking APs in Ageing Study-1, with considerations only of an increase of $I_{Ca,L}$ by 25%, Ca^{2+} uptake by 15%, and a decrease in I_{NaCa} by 6% for the older adult condition. As compared with the adult condition, the computed CL increased by 23.4% (i.e., a decrease in HR of 11%), and this was accompanied by changes in other AP characteristics, including an increase in PA of 17.5% and in APD_{50} of 23.4%.

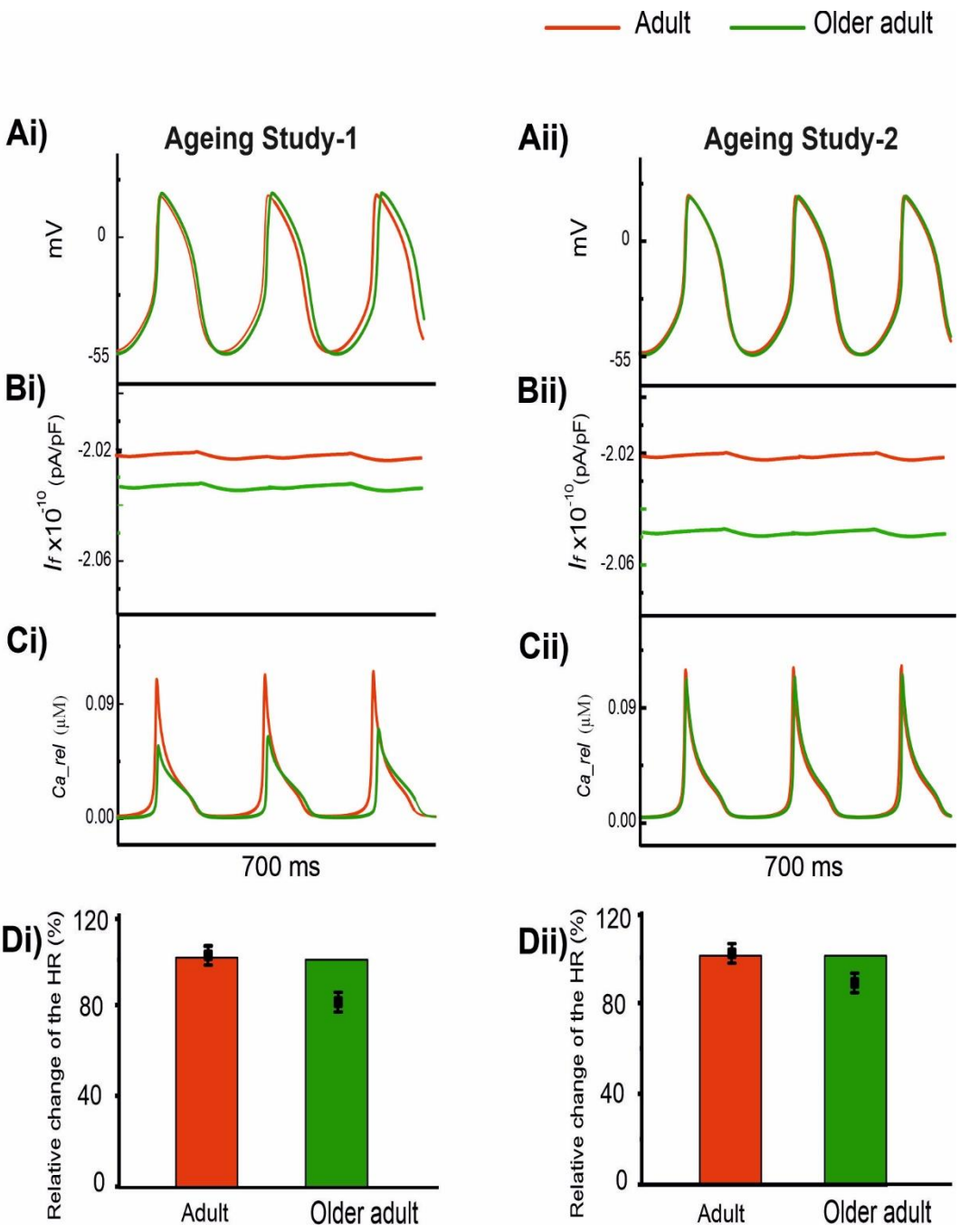

Figure 5.3. Role of reduced I_f and Ca^{2+} release from the SR in ageing bradycardia. Changes in other ion-channel currents as reported by Tellez *et al.*[31] in Ageing Study-1 (right panels) and by Hatch *et al.*[32] and Huang *et al.*[33] in Ageing Study-2 (left panels) were omitted. (Ai, Aii) APs. (Bi, Bii) Ionic current profiles for I_f, and (Ci, Cii) for Ca^{2+} release, for adult (red) and older adult (green) conditions. (Di, Dii) Bar charts showing the simulated relative changes of the age-dependent changes in HR for this case; error bars show the experimental HR reduction due to ageing.

In this case, the observed changes in CL and AP characteristics were comparable with those obtained when all remodelled factors were considered, as well as close to experimental observations.[31] The results seem to suggest that the ageing-induced up-regulations of $I_{Ca,L}$ and Ca^{2+}-uptake, and down-regulation of I_{NaCa}, are sufficient to account for the ageing bradycardia seen experimentally in Ageing Study-1.

Figure 5.4Aii shows simulated APs in Ageing Study-2 when a decrease of $I_{Ca,L}$ by 50% and of Ca^{2+} uptake by 29%, and an increase of I_{NaCa} by 42%, were considered. As compared with the APs in the adult condition, the implemented changes also reproduced bradycardia, resulting in a 7% increase in CL (i.e., a 6.9% HR decrease), which was accompanied by other changes in AP characteristics. These included an MDP elevated by 6mV, a reduction of PA by 55% and an APD_{50} shortening by 14%. Those observed changes in APs were also close to the experimental observations of Hatch *et al.*[32], which implied that the subset of remodelled $I_{Ca,L}$, I_{NaCa} and Ca^{2+} uptake, as seen in Ageing Study-2, were also sufficient to produce the ageing-related bradycardia.

In both datasets of Ageing Study-1 and Ageing Study-2, the same bradycardia effect was produced, although different ionic pathways were considered. In Ageing Study-1, bradycardia was associated with an increased $I_{Ca,L}$ (Figure 5.4Bi) and increased SR Ca^{2+} uptake (Figure 5.4Ci), and a decreased I_{NaCa} (Figure 5.4Di). In contrast, in Ageing Study-2 it was associated with a decreased $I_{Ca,L}$ (Figure 5.4Bii) and decreased SR Ca^{2+} uptake (Figure 5.4Cii), and an increased I_{NaCa} (Figure 5.4Dii). Quantitatively, the computed HR reductions in the older adult condition were close to the experimental data of Tellez *et al.*[31] and Hatch *et al.*[32] for Ageing Study-1 (Figure 5.4Ei) and Ageing Study-2 (Figure 5.4Eii) respectively.

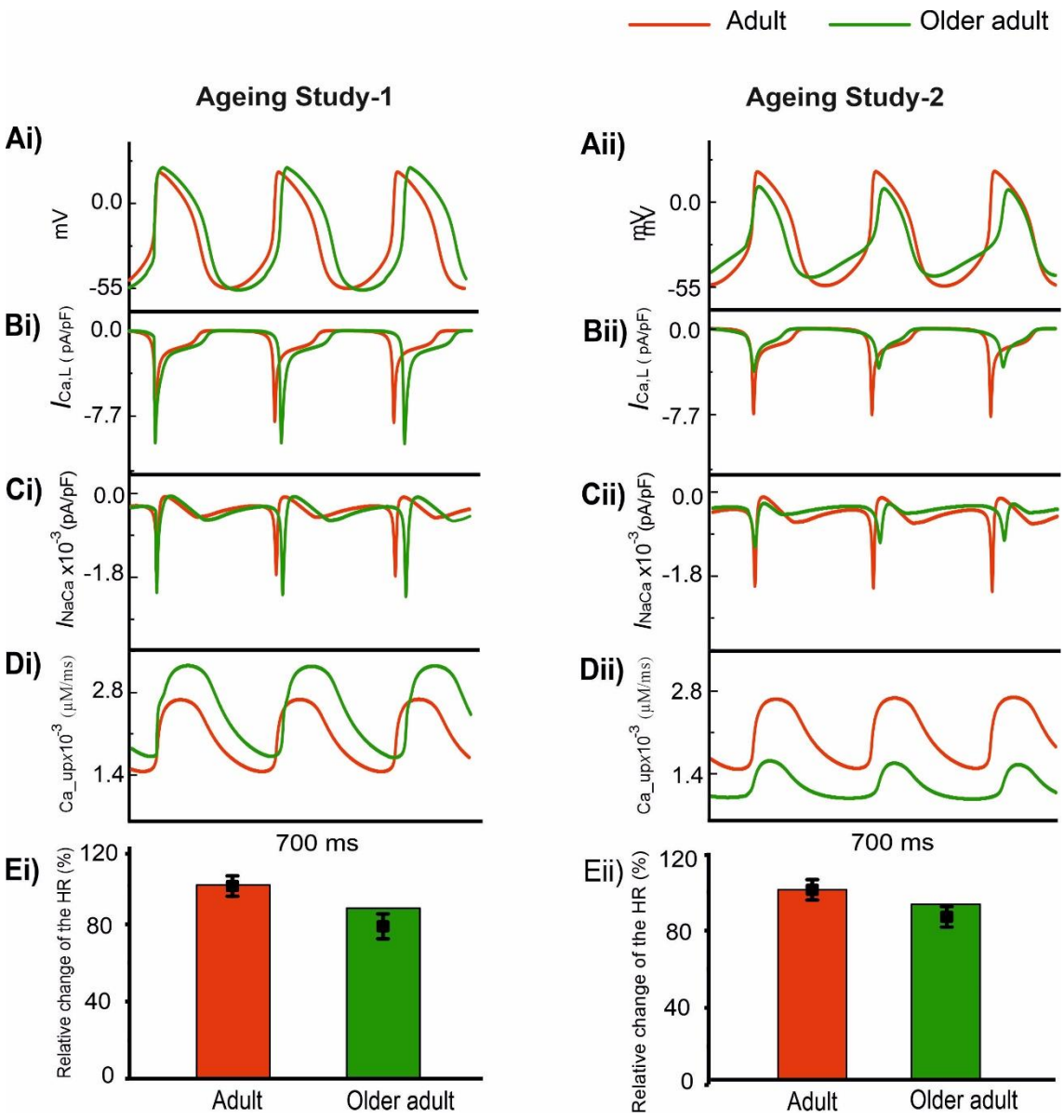

Figure 5.4. Effect of remodelled $I_{Ca,L}$, $I_{NaCa,}$ and Ca^{2+} uptake on pacemaking APs (red: adult; green: older adult). Other ion channel changes, as seen by Tellez *et al.* [31] in Ageing Study-1 (right panels), and by Hatch *et al.* [32] in Ageing Study-2 (left panels), were ignored in simulations. (Ai, Aii) APs. (Bi, Bii) $I_{Ca,L}$. (Ci, Cii) I_{NaCa}. (Di, Dii) Ca^{2+} uptake. (Ei, Eii) HR reduction. Data with error bars show the experimental data.

5.3.2.3 Case 3: Effect of remodelled I_{Kr}, I_{Ks}, I_{to}, I_{NaK}, and $I_{Ca,T}$. (Specific for data set 1)

Ageing Study-1 also found changes in certain ion channels including I_{Kr}, I_{Ks}, I_{to}, I_{Nak} and $I_{Ca,T}$, which were absent in Ageing Study-2. Further simulations were conducted to investigate the effects of such a subset of remodelled ion channels on ageing bradycardia. In simulations, we considered changes to I_{Kr} (a 6% reduction), I_{Ks} (a 25% increase), I_{to} (a 60% increase), I_{NaK} (a 50% increase) and $I_{Ca,T}$ (a 12% decrease).

Simulation results of APs for the adult and older adult conditions are shown in Figure 5.5A. In this case, the remodelled ion channels produced a 9.13% increase in CL (i.e., a 6.9% decrease in HR). It also produced changes in other AP characteristics, including a more hyperpolarised MDP (by -3mV), and a prolonged APD_{50} (by 26ms).

Panels B-F in Figure 5.5 show the time traces of the relevant ion-channel currents for I_{Kr}, I_{Ks}, I_{to}, $I_{Ca,T}$, and I_{NaK} in the adult and older adult conditions. It was shown that during APs, the decreased PA might be attributable to the change in I_{to} and I_{Ks}; the more hyperpolarised MDP might be attributable to the increased I_{NaK}; the prolonged APD_{50} was attributable to the decreased I_{Kr}; and the decreased DD phase was partially attributable to the integral action of the decreased $I_{Ca,T}$ and I_{Kr}. The prolonged APD_{50} slowed down the repolarisation phase and, together with the slowed DD depolarisation phase and the increased time interval required for membrane potential to reach the take-off potential from the MDP, resulted in a slowed HR.

The individual roles of each remodelled I_{Ks}, I_{to}, I_{NaK} and $I_{Ca,T}$ ion channels were also simulated, generating a 1.3%, 1.7%, 6.7%, and 5.6% change in CL, respectively, as shown in Figure 5.5G. The simulation showed that the remodelled I_{NaK} and $I_{Ca,T}$ currents alone made notable contributions to an increased CL, in which the remodelled I_{Kr} current was responsible for the increase in APD_{50}, slowing the repolarisation phase of the APs.

.

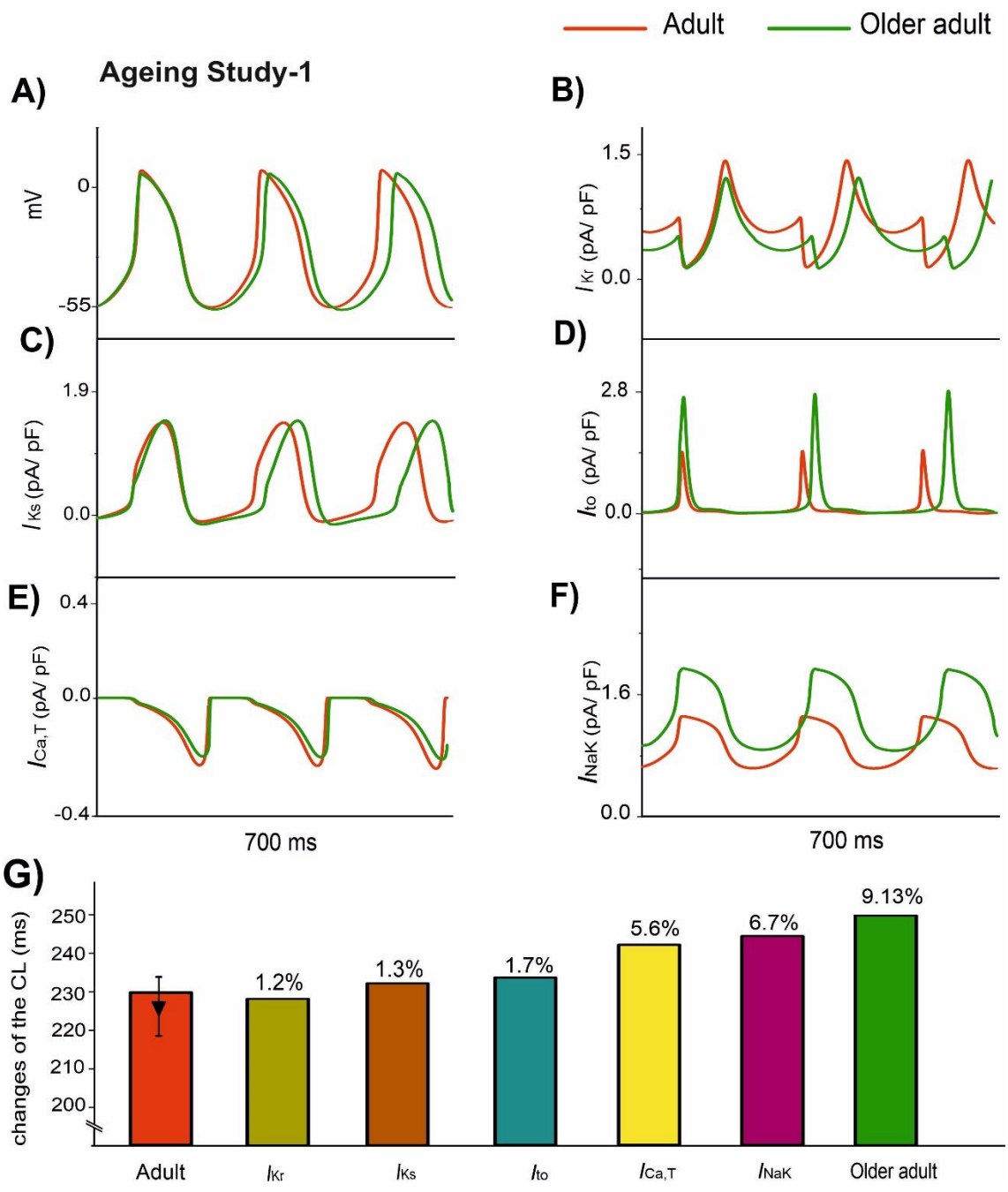

Figure 5.5. APs for the adult and older adult conditions with the subset of changes to the ion-channel currents involved in Ageing Study-1, namely I_{Kr}, I_{Ks}, I_{to}, $I_{Ca,T}$, and I_{NaK} (A). Panels (B-F) show the time traces for the relevant ion-channel currents, namely I_{Kr}, I_{Ks}, I_{to}, $I_{Ca,T}$ and I_{NaK} in the adult and older adult conditions. (G) illustrates the role of the individual remodelled ionic channels on CL values.

5.4. Discussion

The main findings of this study are the following:

(1) heart-rate reduction in aged rat sinoatrial myocytes can be sufficiently accounted for by the age-induced ionic-channel remodelling of $I_{Ca,L}$, I_f, I_{NaCa}, SERCA2a, and RYR;

(2) whilst all remodelled channels and Ca^{2+} handling contribute to the heart-rate reduction in the older adult, the remodelled $I_{Ca,L}$ plays the most significant role; and

(3) remodelled $I_{Ca,L}$, either up-regulated or down-regulated during the ageing, leads to a similar bradycardia effect, suggesting that the age-related SAN dysfunction can be a result of different ionic pathways.

Mechanism underlying age-related SAN dysfunction: Possible mechanism(s) underlying the age-related SAN dysfunction were investigated by both the inclusive and exclusive methods in simulations. With the inclusive method, when all remodelling of ion channels and Ca^{2+} handling identified in Ageing Study-1 [32] and Ageing Study-2 [31,34] were considered, a similar bradycardial effect was produced, which was manifested by a slower pacemaking rate of APs in the older adult as compared with the adult rat SAN cell. This observation suggested that the identified age-related changes in ion channels ($I_{Ca,L}$, I_f, I_{NaCa}) and Ca^{2+} handling (SERCA2a and RYR) in both studies were adequately responsible for the experimentally observed age-related changes in APs, which were consistent to the experimental data of the two studies. Note that, though a similar bradycardial effect was produced, changes in some other AP characteristics, such as the maximal upstroke velocity (dV/dt_{max}), AP amplitude and duration (APD_{50}), were different between the two cases of simulations. While the computed dV/dt_{max} and APD_{50} in the older adult condition were increased in the case of Ageing Study-1, they were decreased in the case of Ageing Study-2.

Further analyses were conducted by the exclusive method to elucidate the major contributor(s) responsible for the age-related bradycardia.

Role of I_f and Ca^{2+} RyR release: When down-regulations of I_f and Ca^{2+} RyR release were considered for the older adult conditions as seen in both Ageing Studies 1 and 2, no apparent effect was observed on modulating the APs. This suggested a limited role of remodelled I_f and Ca^{2+} RyR release in generating the age-related bradycardial effect.

A limited role of I_f in pacemaking APs in the rat SAN, as seen in this study, is consistent with the experimental observation of Shinagawa *et al.*[40], who reported that I_f activated at a very negative threshold, -90mV, in the central cells of the rat SAN. As such, the hyperpolarisation-activated channel remains inactivated under the normal AP threshold range (-70mV to -50mV), and therefore contributes only slightly to the pacemaking APs of the rat SAN cells.

In both data sets of Ageing Studies 1 and 2, substantial down-regulation of RYR2 in the SAN during the ageing process was observed, which was believed to be responsible for a reduced heart rate in the aged rat.[31] However, in simulations, a reduction of SR Ca^{2+} release from 30% to 80% as observed in the two experimental studies showed only limited effects in slowing down the heart rate. A complete block of Ca^{2+} release from the SR only produced a 3.5% increase in CL. This finding was in agreement with previous experimental observations, which showed that the effect of SR Ca^{2+} release on pacemaker activity in adult rat central SAN cells was small due to the poor development of SR in these cells.[36]

There has been an ongoing debate as to the leading mechanism responsible for the pacemaking activity in the SAN. [42,43] One theory is that the role is played by the membrane clock, in which I_f plays an important role [44,45]. The other is that the Ca^{2+} clock plays an important role, by which SR pumping kinetics are thought to regulate spontaneous beating in rabbit SAN. [46] The rate of SR replenishment defines the cycle length of each natural beat. Its occurrence is based on the cytosolic Ca^{2+} availability and SERCA2a activity due to RYR2 release flux and Cav1.2 influx, as described by Vinogradova *et al.*[47] Even though the SR's role in initiating an AP is debatable, there are distinct changes in SR proteins that are clearly related to ageing.

Role of $I_{Ca,L}$, I_{NaCa} and SR Ca^{2+} uptake: There are contradictory changes in $I_{Ca,L}$, I_{NaCa} and Ca^{2+} uptake from the SR between the datasets of the ageing studies. The relative role of these remodelled factors in the generation of age-related bradycardia was evaluated by the exclusive method. In both Ageing Studies 1 and 2, the altered $I_{Ca,L}$ showed notable effects on the modulation of the pacemaking AP profiles and rates, leading to bradycardia, through different actions. In Ageing Study-1, the up-regulated $I_{Ca,L}$ increased the amplitude of the AP and prolonged the APD_{50}, which slowed down the time course for repolarisation and consequently led to a slowing down in the pacemaking as seen in ageing bradycardia. [10,12] It also produced a more hyperpolarised maximal diastolic

membrane potential, which led to an increased voltage difference between the MDP and the take-off potential. This contributed to increased time taken to generate a successive action potential, though the depolarisation I_{NaCa} current during the diastolic depolarisation (DD) phase was increased. Overall, this led to an increased time interval between two successive APs (i.e., CL), leading to a slowed heart rate.

However, in Ageing Study-2, a decreased $I_{Ca,L}$ also produced bradycardia. In this case, the decreased $I_{Ca,L}$ was associated with a decreased AP amplitude and abbreviated $APD_{50.}$ Both accelerated the repolarisation process but produced an incomplete repolarisation as a consequence of reduced AP amplitude and abbreviated APD_{50}. Consequentially, an elevated MDP was produced, leading to a reduced depolarisation current in the DD phase (such as I_{NaCa}), which slowed down the time course between the MPD and the take-off potential, leading to an increased time interval between two successive pacemaking APs, resulting in bradycardia.

Our results suggest the importance of the remodelled $I_{Ca,L}$ to generate ageing-related bradycardia. This is consistent with a previous study, which showed that I_{CaL} was a critical pacemaking current in adult rat SAN, as demonstrated by spontaneous beating being halted by Ca^{2+} antagonists.[34] This is consistent with the present simulation, by which a complete $I_{Ca,L}$ block abolished the pacemaker activity in the model.

When the age-related remodelling of $I_{Ca,L}$ alone was considered, in both datasets, a dramatic bradycardial effect was observed, which was comparable to the case when all ion channel and Ca^{2+} handling remodelling were considered. Results are shown in Figure 5.6. These results further support the notion that the remodelled $I_{Ca,L}$ has the most significant influence on slowing down of the pacemaking rates in the older adult rat SAN myocytes.

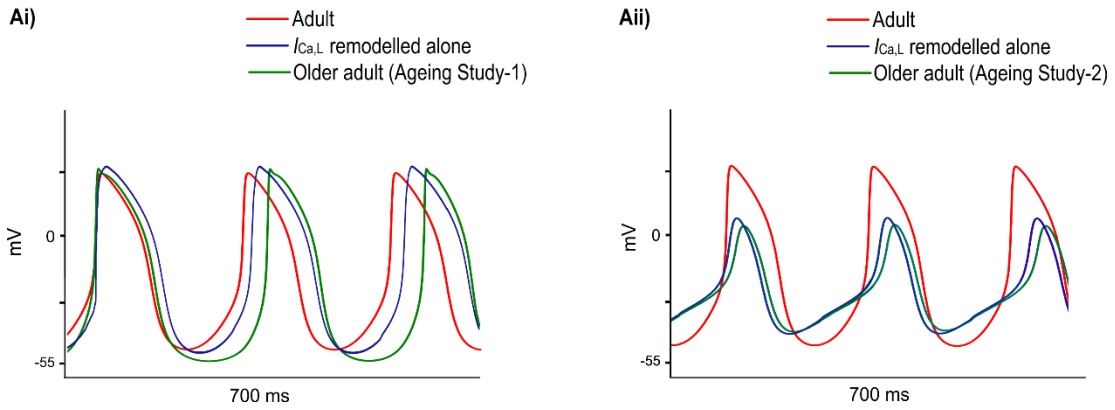

Figure 5.6. Simulated APs when the age-related remodelling of $I_{Ca,L}$ alone (blue) was considered (other ion channel and Ca^{2+} handling changes, as seen by Tellez *et al.*[31], in Ageing Study-1 (right panels), and by Hatch *et al.*[32] in Ageing Study-2 (left panels), were ignored). The obtained APs were compared with those of adult (red) and those with all ion channel and Ca^{2+} handling remodelling were considered (green).

In Ageing Study-1, a small age-related increase in SERCA2a (by 15%), and decrease in NCX (by 6%), were observed. This is in contrast to the case of Ageing Study-2, in which a decrease in SERCA2a (by 29%) and an increase in NCX (by 42%) were observed in the older adult SAN. The changes in SERCA2a and NCX could alter the SR Ca^{2+} uptake and SR Ca^{2+} content, modulating the Ca^{2+} release that affects the pacemaking APs.[49] However, in both cases, their contribution to age-related bradycardia was limited, as observed in the present study.[50]

Role of remodelled I_K, I_{to}, I_{Ks}, I_{NaK}, and $I_{Ca,T}$. The role of each individual remodelled ion channel of I_{Kr}, I_{to}, I_{Ks}, I_{NaK}, and $I_{Ca,T}$, as seen in Ageing Study-1, was also investigated. The functional effect of these remodelled ion channels prolonged the time course of APs, leading to a reduced pacemaking rate, some of which was associated with a secondary action. For example, the reduction in I_{Kr} prolonged the APD_{50}, therefore slowing down the repolarisation phase of the APs. In the adult rat SAN model, I_{Kr} is considered to be another important pacemaking current. It has been observed that during diastole, I_{Kr} is slowly deactivated and the decreased outward current enables self-activated depolarisation. Therefore, in combination with other currents, remodelling of this current might play a secondary role in reducing the HR of the aged SAN. [33,52,53,54] Decreased spontaneous activity and sinus arrest were observed in rat SAN cells when I_{Kr} was completely blocked by E-4031.[25]

5.5. Limitations of the study

The rat SAN model used in our simulations had certain inherent limitations, as described previously.[36] Our simulation incorporated age-induced changes in ion channels and intracellular Ca^{2+} handling from two independent studies into the rat SAN model. [31-32] The data was derived from mRNA gene expression or protein levels whenever experimental data on their kinetic or current densities in the SAN cell were unavailable. However, the correlation between the gene expression or protein levels for certain ion channel subunits and their current densities remains unclear. Another limitation of this study was that the results were determined at the single-cell level. Consequently, other factors associated with age-induced changes, such as remodelling the electrical coupling between cells via the gap junction [26], or connexion, and the possible incidence of fibrosis [1,4], might also play a specific role in production of the bradycardia effect that is more pronounced at the tissue level. Nevertheless, without considering age-induced changes in the connexions and fibrosis, such changes in various ionic channel conductances can nevertheless increase CL and reduce HR in a manner that is quantitatively comparable with experimental data.

5.6. Conclusions

In this study, the mechanism underlying the age-related SAN dysfunction was elucidated. Our results suggest that while it is an integral action of all remodelled ion channels and Ca^{2+} handling, the remodelled $I_{Ca,L}$, either via a gain or loss of function, contributes primarily to age-related bradycardia. Therefore, ageing-related bradycardia can be linked to different remodelling "pathways" (see Figure 5.7), which may affect clinical treatment strategies.

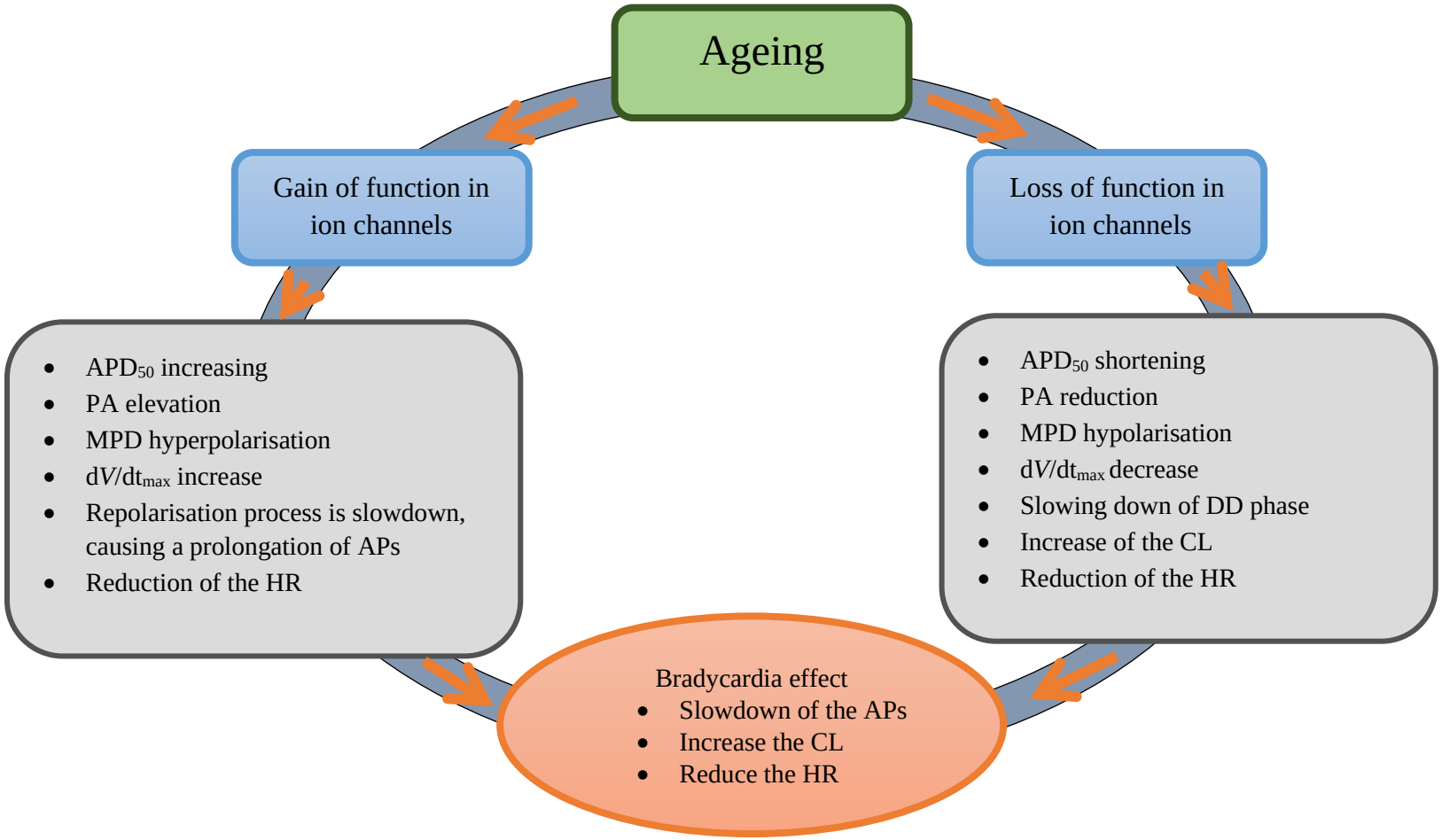

Figure 5.7. Diagrammatic representation to summarise the two 'pathways' investigated in this study and the mechanisms associated with each process.

References

1. Baruscotti M, Robinson RB. Electrophysiology and pacemaker function of the developing sinoatrial node. Am J Physiol Hear Circ Physiol [Internet]. 2007 [cited 26 Dec 2017];293:2613–23. Available from: http://www.physiology.org/doi/pdf/10.1152/ajpheart.00750.2007

2. Haqqani HM, Kalman JM. Aging and sinoatrial node dysfunction: Musings on the not-so-funny side. Circulation. 2007;115(10):1178–9.

3. Choudhury M, Boyett MR, Morris GM. Biology of the Sinus Node and its Disease. Arrhythmia Electrophysiol Rev [Internet]. 2015 May [cited 16 May 2018];4(1):28. Available from: http://www.radcliffecardiology.com/articles/biology-sinus-node-and-its-disease

4. Semelka M, Gera J, Usman S. Sick sinus syndrome: A review. Am Fam Physician [Internet]. 2013;87(10):691–6. Available from: http://www.aafp.org/afp/2013/0515/p691.pdf http://ovidsp.ovid.com/ovidweb.cgi?T=JS&CSC=Y&NEWS=N&PAGE=fulltext&D=emed11&AN=2013536120 http://nt2yt7px7u.search.serialssolutions.com/?sid=OVID:Embase&genre=article&id=pmid:&id=doi:&issn=0002-838X&volume=87&iss

5. Fenske S, Krause SC, Hassan SIH, Becirovic E, Auer F, Bernard R, *et al.* Sick sinus syndrome in HCN1-Deficient mice. Circulation. 2013;128(24):2585–94.

6. Choudhury M, Black N, Alghamdi A, Souza A D', Wang R, Yanni J, *et al.* TBX18 overexpression enhances pacemaker function in a rat subsidiary atrial pacemaker model of sick sinus syndrome. J Physiol [Internet]. 2018 [cited 22 Mar 2019];596:6141–55. Available from: https://www.ncbi.nlm.nih.gov/pmc/articles/PMC6292813/pdf/TJP-596-6141.pdf

7. Butters TD, Aslanidi O V., Inada S, Boyett MR, Hancox JC, Lei M, *et al.* Mechanistic Links Between Na^+ Channel (SCN5A) Mutations and Impaired Cardiac Pacemaking in Sick Sinus Syndrome. Circ Res [Internet]. 2010 Jul 9 [cited 2019 Nov 4];107(1):126–37. Available from: https://www.ahajournals.org/doi/10.1161/CIRCRESAHA.110.219949;

8. Choudhury M, Boyett MR, Morris GM. Biology of the Sinus Node and its Disease. Arrhythmia & Physiol. Rev. [Internet]. 2015 [cited 12 Mar 2019];4(1);28-34. Available from: www.AERjournal.com/articles/biology-sinus-node. http://dx.doi.org/10.15420/aer.2015.4.1.28

9. Zhang H, Zhao Y, Lei M, Dobrzynski H, Liu JH, Holden AV, *et al.* Computational evaluation of the roles of Na^+ current, i_{Na}, and cell death in cardiac pacemaking and driving. Am J Physiol Circ Physiol [Internet]. 2007 Jan [cited 5 Jan 2018];292(1):H165–74. Available from: http://www.physiology.org/doi/10.1152/ajpheart.01101.2005

10. Tohno Y, Tohno S, Viwatpinyo K, Minami T, Chaisuksunt V, Mahakkanukrauh P, *et al.* Age-related changes of elements in the human sinoatrial nodes. OA Anat Aug [Internet]. 2014 [cited 2018 Mar 29];172(3).

Available from:
http://www.oapublishinglondon.com/images/article/pdf/1417622077.pdf

11. Alghamdi AM, Testrow CP, Whittaker DG, Zhang H. The Mechanism Underlying Heart Rate and Pacemaking Activity Decline in Developing Sinoatrial Node of the Rabbit Heart. Comp. in Cardiol. [Internet] 2018 [cited 22 Mar 2019];45;1-4. Available from: http://www.cinc.org/archives/2018/pdf/CinC2018-224.pdf

12. Härtel G, Talvensaari T. Treatment of sinoatrial syndrome with permanent cardiac pacing in 90 patients. Acta Med Scand [Internet]. 1975 Nov [cited 20 May 2018];198(5):341–7. Available from: http://www.ncbi.nlm.nih.gov/pubmed/1199808

13. Sodeck GH, Domanovits H, Meron G, Rauscha F, Losert H, Thalmann M, *et al.* Compromising bradycardia: Management in the emergency department. Resuscitation [Internet]. 2007 [cited 18 May 2018];73:96–102. Available from: http://www.akutkliniken-utbildning.se/EKG-bok/pace/Compromising bradycardia Management in the emergency department.pdf

14. Lamas GA, Lee K, Sweeney M, Leon A, Yee R, Ellenbogen K, *et al.* The Mode Selection Trial (MOST) in sinus node dysfunction: Design, rationale, and baseline characteristics of the first 1000 patients. Am Heart J [Internet]. 2000 Oct [cited 19 May 2018];140(4):541–51. Available from: http://www.ncbi.nlm.nih.gov/pubmed/11011325

15. Wood MA, Ellenbogen KA. Cardiology patient pages. Cardiac pacemakers from the patient's perspective. Circulation [Internet]. 2002 May 7 [cited 8 Jun 2018];105(18):2136–8. Available from: http://www.ncbi.nlm.nih.gov/pubmed/11994244

16. Moghtadaei M, Jansen HJ, Mackasey M, Rafferty SA, Bogachev O, Sapp JL, *et al.* The impacts of age and frailty on heart rate and sinoatrial node function. J Physiol [Internet]. 2016;594(23):7105. Available from: http://www.ncbi.nlm.nih.gov/pubmed/27598221

17. Satoh H, Tohno S, Azuma C, Minami T, Ohishi T, Hayashi M, *et al.* Age-Related Attenuation in the Elements in Monkey Sino-atrial Node. Biol Trace Elem Res [Internet]. 2005 [cited 29 Mar 2018];43(107). Available from: https://link.springer.com/content/pdf/10.1385%2FBTER%3A107%3A1%3A043.pdf

18. Alings AMW, Bouman LN. Electrophysiology of the ageing rabbit and cat sinoatrial node -- a comparative study. Eur Heart J [Internet]. 1993 Sep 1 [cited 7 Jun 2018];14(9):1278–88. Available from: https://academic.oup.com/eurheartj/article-lookup/doi/10.1093/eurheartj/14.9.1278

19. Toda N. Age-related changes in the transmembrane potential of isolated rabbit sino-atrial nodes and atria. Cardiovasc Res [Internet]. 1980 Jan 1 [cited 6 Jan 2018];14(1):58–63. Available from: https://academic.oup.com/cardiovascres/article-lookup/doi/10.1093/cvr/14.1.58

20. Du J, Deng S, Pu D, Liu Y, Xiao J, She Q. Age-dependent down-regulation of hyperpolarization-activated cyclic nucleotide-gated channel 4 causes deterioration of canine sinoatrial node function. Acta Biochim Biophys Sin (Shanghai) [Internet]. 2017 May 1 [cited 16 May 2018];49(5):400–8. Available from: http://www.ncbi.nlm.nih.gov/pubmed/28369243

21. Opthof T. Gap junctions in the sinoatrial node: Immunohistochemical localization and correlation with activation pattern. J of cardio electrophysiol. [Internet]. . 1994 [cited 2018 May 20];(5);138-143 Available from: https://www.narcis.nl/publication/RecordID/oai%3Apure.amc.nl%3Apublications%2F1452d468-fd43-4b0a-80da-945018db400a

22. Dobrev D. Ion Channel Portrait of the Human Sinus Node: Useful for a Better Understanding of Sinus Node Function and Dysfunction in Humans? Circulation [Internet]. 2009;119:1556–8. Available from: http://circ.ahajournals.org/content/119/12/1556

23. Sharpe EJ, Larson ED, Proenza C. Cyclic AMP reverses the effects of aging on pacemaker activity and I_f in sinoatrial node myocytes. J Gen Physiol [Internet]. 2017 Feb [cited 2018 Mar 27];149(2):237–47. Available from: http://www.ncbi.nlm.nih.gov/pubmed/28057842

24. Moghtadaei M, Jansen HJ, Mackasey M, Rafferty SA, Bogachev O, Sapp JL, *et al.* The impacts of age and frailty on heart rate and sinoatrial node function. J Physiol [Internet]. 2016;594(23):7105. Available from: http://www.ncbi.nlm.nih.gov/pubmed/27598221

25. Mitsuiye T, Shinagawa Y, Noma A. Sustained Inward Current During Pacemaker Depolarization in Mammalian Sinoatrial Node Cells. Am Hear Assoc Inc Circ. 2000;87:88–91.

26. Huang X, Du Y, Yang P, Lin S, Xi Y, Yang Z, *et al.* Age-dependent alterations of voltage-gated Na + channel isoforms in rat sinoatrial node. Mech Ageing Dev [Internet]. 2015 [cited 28 Mar 2018];152:80–90. Available from: https://ac.els-cdn.com/S0047637415300208/1-s2.0-S0047637415300208-main.pdf?_tid=cda93b3e-29ba-4def-bb37-602bfa113342&acdnat=1522245232_6ccf1b8b8bbbae013579a80f3e5af3f3

27. Larson ED, St Clair JR, Sumner WA, Bannister RA, Proenza C. Depressed pacemaker activity of sinoatrial node myocytes contributes to the age-dependent decline in maximum heart rate. Proc Natl Acad Sci USA [Internet]. 2013 Oct 29 [cited 16 Mar 2018];110(44):18011–6. Available from: http://www.ncbi.nlm.nih.gov/pubmed/24128759

28. Hao X, Zhang Y, Zhang X, Nirmalan M, Davies L, Konstantinou D, *et al.* TGF-β1-mediated fibrosis and ion channel remodeling are key mechanisms in producing the sinus node dysfunction associated with SCN5A deficiency and aging. Circ Arrhythmia Electrophysiol [Internet]. 2011 Jun 1 [cited 2018 Mar 27];4(3):397–406. Available from: http://www.ncbi.nlm.nih.gov/pubmed/21493874

29. Congxin Huang, MD; Wenmao Ding, MD; Lan Li, MD*; Dongdong Zhao M. C. Differences in the Aging-Associated Trends of the Monophasic Action

Potential Duration and Effective Refractory Period of the Right and Left Atria of the Rat. Circ J. 2006;70:352–357.

30. Jones SA, Lancaster MK, Boyett MR. Ageing-related changes of connexins and conduction within the sinoatrial node. J Physiol [Internet]. 2004 Oct [cited 26 Jul 2017];560(2):429–37. Available from: http://doi.wiley.com/10.1113/jphysiol.2004.072108

31. Tellez JO, Ma˛czewski M, Yanni J, Sutyagin P, Mackiewicz U, Atkinson A, *et al.* Ageing-dependent remodelling of ion channel and Ca 2+ clock genes underlying sino-atrial node pacemaking. Exp Physiol. 2011;96(11):1163–78.

32. Hatch FS. Age-associated changes to calcium handling proteins across the whole heart. PhD thesis, University of Hull. December 2012 Abstract.

33. Huang X, Yang P, Yang Z, Zhang H, Ma A. Age-associated expression of HCN channel isoforms in rat sinoatrial node. Exp Biol Med [Internet]. 3 Feb 2016 [cited 22 Mar 2018];241(3):331–9. Available from: http://journals.sagepub.com/doi/10.1177/1535370215603515

34. Brioschi C, Micheloni S, Tellez JO, Pisoni G, Longhi R, Moroni P, *et al.* Distribution of the pacemaker HCN4 channel mRNA and protein in the rabbit sinoatrial node. J Mol Cell Cardiol [Internet]. 2009;47(2):221–7. Available from: http://dx.doi.org/10.1016/j.yjmcc.2009.04.009

35. Jones SA, Boyett MR, Lancaster MK. Declining into failure: The age-dependent loss of the L-type calcium channel within the sinoatrial node. Circulation. 2007;115(10):1183–90.

36. Tao T, Paterson DJ, Smith NP. A model of cellular cardiac-neural coupling that captures the sympathetic control of sinoatrial node excitability in normotensive and hypertensive rats. Biophys J [Internet]. 2011;101(3):594–602. Available from: http://dx.doi.org/10.1016/j.bpj.2011.05.069

37. Zhang H, Holden A V, Kodama I, Honjo H, Lei M, Varghese T, *et al.* Mathematical models of action potentials in the periphery and center of the rabbit sinoatrial node. Am J Physiol Hear Circ Physiol. 2000;279(2000):H397–H42.

38. Kurata Y, Hisatome I, Imanishi S, Shibamoto T. Dynamical description of sinoatrial node pacemaking: improved mathematical model for primary pacemaker cell. Physiol Hear Circ Physiol [Internet]. 2002;283:H2074–H2101. Available from: 10.1152/ajpheart.00900.2001.

39. Satoh H. Sino-Atrial Nodal Cells of Mammalian Hearts: Ionic Currents and Gene Expression of Pacemaker Ionic Channels. J Smooth Muscle Res [Internet]. 2003;39(5):175–93. Available from: http://joi.jlc.jst.go.jp/JST.JSTAGE/jsmr/39.175?from=CrossRef

40. Shinagawa Y, Satoh H, Noma A. The sustained inward current and inward rectifier K+ current in pacemaker cells dissociated from rat sinoatrial node. J Physiol [Internet]. 2000;523 Pt 3:593–605. Available from: http://www.pubmedcentral.nih.gov/articlerender.fcgi?artid=2269831&tool=pmcentrez&rendertype=abstract

41. Bers DM. Excitation-Contraction Coupling and Cardiac Contractile Force [Internet]. Dordrecht: Springer Netherlands; 2001 [cited 4 Jul 2018]. (Developments in Cardiovascular Medicine; vol. 237). Available from: http://link.springer.com/10.1007/978-94-010-0658-3

42. Lakatta EG, DiFrancesco D. What keeps us ticking: a funny current, a calcium clock, or both? J Mol Cell Cardiol [Internet]. 2009;47(2):157–70. Available from: http://dx.doi.org/10.1016/j.yjmcc.2009.03.022

43. Li P, Lines GT, Maleckar MM, Tveito A. Mathematical models of cardiac pacemaking function. Front Phys [Internet]. 2013 Oct 30 [cited 2019 Aug 1];1:20. Available from: http://journal.frontiersin.org/article/10.3389/fphy.2013.00020/abstract

44. DiFrancesco D. Pacemaker Mechanisms in Cardiac Tissue. Annu Rev Physiol [Internet]. 1993 Oct 28 [cited 22 Feb 2018];55(1):455–72. Available from: http://www.annualreviews.org/doi/10.1146/annurev.ph.55.030193.002323

45. Accili EA, Proenza C, Baruscotti M, DiFrancesco D. From Funny Current to HCN Channels: 20 Years of Excitation. Physiology [Internet]. 2002 Feb [cited 26 Dec 2017];17(1):32–7. Available from: http://www.physiology.org/doi/10.1152/physiologyonline.2002.17.1.32

46. Maltsev VA, Lakatta EG. Synergism of coupled subsarcolemmal Ca $^{2+}$ clocks and sarcolemmal voltage clocks confers robust and flexible pacemaker function in a novel pacemaker cell model. Am J Physiol Circ Physiol [Internet]. 2009 Mar [cited 6 Apr 2019];296(3):H594–615. Available from: http://www.ncbi.nlm.nih.gov/pubmed/19136600

47. Vinogradova TM, Zhou YY, Bogdanov KY, Yang D, Kuschel M, Cheng H, *et al.* Sinoatrial node pacemaker activity requires Ca(2+)/calmodulin-dependent protein kinase II activation. Circ Res [Internet]. 2000 Oct 27 [cited 12 Mar 2018];87(9):760–7. Available from: http://www.ncbi.nlm.nih.gov/pubmed/11055979

48. Satoh H, Sino-Atrial Nodal Cells of Mammalian Hearts: Ionic Currents and Gene Expression of Pacemaker Ionic Channels. J Smooth Muscle Res. 2003;39(5):175–93.

49. Szentesi P, Pignier C, Egger M, Kranias EG, Niggli E. Sarcoplasmic Reticulum Ca 2 Refilling Controls Recovery From Ca 2 -Induced Ca 2 Release Refractoriness in Heart Muscle. Circ Res. 2004;1–7.

50. Katz B, Miledi R. The role of calcium in neuromuscular facilitation. J Physiol. 1968;195(2):481–92.

51. Talano JV., Euler D, Randall WC, Eshaghy B, Loeb HS, Gunnar RM. Sinus node dysfunction. Am J Med [Internet]. 1978 May [cited 1 Apr 2017];64(5):773–81. Available from: http://linkinghub.elsevier.com/retrieve/pii/0002934378905168

52. Hagiwara N, Irisawa H, Kameyama M. Contribution of two types of calcium currents to the pacemaker potentials of rabbit sino-atrial node cells. J Physiol [Internet]. 1988 Jan [cited 5 Jul 2018];395:233–53. Available from: http://www.ncbi.nlm.nih.gov/pubmed/2457676

53. Zhou Z, Lipsius SL. T-Type Calcium Current in Latent Pacemaker Cells Isolated from Cat Right Atrium. J Mol Cell Cardiol [Internet]. 1994 [cited 5 Jul 2018];26(9):1211–9. Available from: https://www.sciencedirect.com/science/article/pii/S0022282884711394

54. Lei M, Cooper PJ, Camelliti P, Kohl P. Role of the 293b-sensitive, slowly activating delayed rectifier potassium current, i, in pacemaker activity of rabbit isolated Ks sino-atrial node cells. Cardiovasc Res [Internet]. 2002 [cited 5 Jul 2018];53:68–79. Available from: www.elsevier.com

55. Bround MJ, Asghari P, Wambolt RB, Bohunek L, Smits C, Philit M, *et al.* Cardiac ryanodine receptors control heart rate and rhythmicity in adult mice. Cardiovasc Res [Internet]. 2012 Dec 1 [cited 20 May 2018];96(3):372–80. Available from: https://academic.oup.com/cardiovascres/article-lookup/doi/10.1093/cvr/cvs260

Chapter Six - A Novel Computational Rat Sinoatrial Model for the Study of Sinus Node Dysfunction in STZ-diabetes

6.1 Introduction

Cardiovascular complications are the major cause of morbidity and mortality in diabetic patients.[1] Clinical observations and experiments have found that diabetes mellitus (DM) is linked with a variety of contractility and heart arrhythmias that may occur in the absence of atherosclerosis, hypertension or valvular dysfunction.[2] Ventricular arrhythmias such as prolongation of the QT interval as measured on electrocardiograms are the most common type of cardiac arrhythmia observed in DM patients.[3] However, sinoatrial node dysfunction (SND), which include bradycardia and tachycardia, are frequently seen in both type 1 and type 2 DM patients.[4] Other research has demonstrated that there is a high prevalence of atrioventricular node block [5] and fibrillation with bradycardia in the DM patients, and consequently, often require artificial pacemakers. Experimental studies have shown that the cycle length (CL) of APs in sinoatrial node (SAN) cells was prolonged and the beating rates of the isolated SAN preparations from streptozotocin (STZ)-induced DM animal models were significantly decreased.[6] This indicates that reduced SAN function is an important complication in DM.[7] Although STZ-induced diabetic SAN dysfunction can be fatal, the exact underlying ionic mechanisms of SAN electrical remodelling associated with DM remain unclear.

Arecent experimental evidence assessed the function of the CCS in rat *ex vivo* and key proteins involved in pacemaker mechanisms in induced-STZ in DM. The study involved the following tissues; SAN, atrioventricular junction (AVJ), left atrium (LA), right ventricle (RV), and left purkinje fibre (LPF). [1] Voltage-clamp records have shown that the cell capacitance and the funny current density, (I_f) are significantly decreased in type 1 DM SAN cells. Moreover, western-blot measurements have concluded that complex functional and cellular changes occur in protein expression of ion channels involved in the function of the CCS in diabetic rats. They have shown that, for SAN cells, HCN4, Cav1.3, Cav3.1, RyR2 and NCX1, as well as intercellular

electrical coupling Cx45, decrease; at the AVJ, protein expression of RyR2 and NCX1 decreases; and in the LPF, RyR2 and Cx40, Cx43 and Cx45 are also reduced. All these findings have revealed electrical remodelling in the diabetic heart, and each of them produces alterations to the electrophysiological properties of cardiac cell and tissues. However, the electrical remodelling in the SAN caused by DM has rarely been studied experimentally, due to its complicated and heterogeneous anatomy. It is also unclear whether the remodelling identified at the cellular ion-channel level is sufficient to account for the STZ-induced diabetic sinus bradycardia. The role of remodelled ion channels associated with STZ-induced diabetic in SAN slow pacemaking activity and the impired ability of the SAN to drive the surrounding atrial muscle need to be addressed.

Computational models of the heart form a complementary approach to investigate cardiac arrhythmias that cannot be studied by experiment. They also have provided powerful tools to study the mechanism of genetic mutations, ageing and heart failure on cardiac pacemaker activities.[8,9] These models are normally constructed based on experimental data and validated against experimental data, providing a means to quantitatively predict the functional roles of altered molecular dynamics and ionic channels in a systematic way that is difficult to achieve in an experimental setting. In previous computational work, various models were developed to simulate the propagation of action potentials (APs) and the electrical conduction system in healthy and disease hearts for most regions of the SAN tissue and other heart tissues from a variety of species such as mouse [10], rabbit [9,11], sheep [12] and human [13], however, there is a lack of tissue models for rat SAN tissue. Although rat cells and tissues are extensively used as animal model [14-16] to investigate diseases such as heart failure (HF) [17], atrial fibrillation (AF) [18], diabetes [19, 20] and in some cases for risk-factor examination such as obesity [21,22], a search of the literature reveals a lack of mathematical models of the rat SAN and surrounding tissue that describe the physiological behaviour of cardiac cells.

The main objectives in this study are:1) to develop a new mathematical model for rat SAN that considered regional differences in the capacitances and ion-current densities to develop the peripheral rat SAN model; 2) to update the available neonatal rat atrial model to represent the adult condition; 3) to develop what we believed would be the first detailed mathematical model of the rat one-dimensional (1D) SAN-atrium model

and to include the typical physiological and pathophysiological characteristics of the tissue.

The model could be used as a tool to analyse the complex structure and behaviour of the rat SAN. To this end, we investigated the functional impact of STZ-induced diabetes on the initiation of SAN APs and their conduction through use of our model, and studied how this impaired the spontaneous activity of the heart and weakened cardiac impulse propagation from the SAN to the atrial tissue.

6.2 Method

6.2.1 Development of the peripheral rat SAN models

The biophysically detailed mathematical model for rat SAN (used in Chapter Five) was chosen to simulate the regional variations in the cardiac pacemaker. The model of the rat central SAN developed by Tao *et al.* was directly adapted to build the peripheral SAN, taking into account the absence of I_{Na} in the centre of the rat SAN.[23] The peripheral SAN rat model was constructed based on modification of cell capacitance and the primary currents densities by altering the maximal conductances of the ionic channel currents in the central cell model, to reproduce the faster pacemaking activities of peripheral SAN cells. Due to the lack of experimental findings from peripheral SAN cells in rat, the kinetics of ionic channels were slightly adjusted based on existing SAN model findings from Zhang *et al.*[24] Table 6.1 illustrates the variations of the ionic conductances and the scaling ratios deployed to produce the central and peripheral SAN cell models.

Owing to the absence of experimental studies on peripheral rat SAN ion-channel currents, I_{Na} was incorporated into the peripheral model based on the I_{Na} formulations from the peripheral model of rabbit SAN [24]. A total of 13 passive ion-channel currents were considered in the model, one being an ionic pump, one being an ionic exchanger and the remaining 11 being passive ionic channels. The membrane potential is illustrated by this equation:

$$\frac{dV_m}{dt} = -\frac{1}{C_m}\left(I_{Ca,T}+I_{Na}+I_{Ca,L}+I_{Kr}+I_{Ks}+I_{st}+I_{sus}+I_{to}+I_{K,ACh}+I_{f}+I_{b,Na}+I_{NaCa}+I_{NaK}\right) \qquad (6.1)$$

C_m refers to cell capacitance, which has a value of 32pF for the central SAN model and 65pF for the peripheral SAN model. Additionally, the various intracellular ionic

concentrations of Ca^{2+}, Na^{+} and K^{+}, and the Ca^{2+} handling formulations, in the new peripheral model were taken from the central SAN model.

Table 6.1: Adjustments of ionic current conducunces from central to peripheral SAN models based on previous study by Zhang *et al.*[24]

Ion channel	**Zhang *et al,* 2000** [24]			**Our model**	
	Centre	Periphery	Ratio* P/C	Centre	Periphery
g_{Na}	0.0 µS	1.24×10^{-6} µS	∞	0.0 nS	$1.24e^{-3}$ nS
$g_{Ca,L}$	5.07 µS	65.88 µS	12.97	0.7 nS	9.079 nS
$g_{Ca,T}$	4.27 µS	13.88 µS	3.245	0.458 nS	1.49 nS
g_{sus}	0.06 µS	11.38 µS	171.31	0.01 nS	1.71 nS
g_{to}	4.0 µS	36.49 µS	7.44	0.18 nS	1.34 nS
g_{Kr}	0.79 µS	16.0 µS	20.07	0.428 nS	8.56 nS
g_{Ks}	0.34 µS	10.4 µS	30.18	0.026 nS	0.75 nS
$g_{f,Na}$	0.54 µS	6.87 µS	12.58	0.357 nS	4.47 nS
$g_{f,K}$	0.54 µS	6.87 µS	12.58	0.357 nS	4.47 nS
$g_{b,Na}$	0.05 µS	0.18 µS	3.2	0.003 nS	0.01 nS
K_{pump}	4.73 nA	161.19 nA	3.245	3.6 pA	11.682
K_{NaCa}	27×10^{-5} nA	88×10^{-5} nA	3.24	0.0005	0.00162

(*ratio of conductance in peripheral to central SAN cell models in Zhang model[24])

6.2.2 Update of the neonatal rat atrial model to represent the adult condition

The neonatal right atrial cells (RA) in rat developed by Majumder *et al.*[25] was chosen in the developmentof the 1D mathematical model of rat SAN- atrium tissue. The ionic currents formulations of the RA model were primarily based on patch-clamp records derived from neonatal rat atrial cells. The generated AP in this model resulted from a

single electrical pulse at 100pA and lasting for 5ms time duration from a simulated resting membrane potential (RMP) of -85mV. Since this model represented the electrophysiological AP of the healthy neonatal condition, we updated the model to represent the adult rat atrial cells based on the following literature.

Existing experimental results: Several groups have reporteed the effect of age-related remodelling of ion-channel currents and intracellular on the charctristics APs and beating rates of rat atrial single cells (Leuranguer *et al.*[26]; Avila *et al.*[27]; Hatch *et al.*[28]; Kaplan *et al.*[29]). Different mechanisms can cause the slowdown of APs in rat atrial cells: 1) alteration of the activation midpoint and slope factor in L-type and T-type currents, with a drop in T-type current density and an increase in L-type current density.[27]; 2) an increase in current density of I_{NaCa} and the expression of protein level of RyR was reported by Hatch *et al.*[28]. Although the SERCA activity was reduced during age development [28, 29], no substantial difference was observed in the expression of the protein level and mRNA between neonate and adult groups [28]; and 3) the Ca_ATPase related to I_{NaK} decreased in the study by Kaplan *et al.*[29] All these measurements are summarised in Table 6.2.

Basal numerical model: The Majumder *et al.* [25] model for neonatal rats was updated to represent the adult atrial cells. The membrane potential,(V_m) of this model is subject to a set of voltage-gated ion-channel currents, ionic pump current and exchanger currents as illustrated by equations (6.2) and (6.3):

$$\frac{dV_m}{dt} = -\frac{I_{tot} + I_{stim}}{C_m} \tag{6.2}$$

$$I_{tot} = (I_{Na} + I_{Ca,T} + I_{Ca,L} + I_{K1} + I_{Kr} + I_{Ks} + I_{sus} + I_{to} + I_{K,ACh} + I_f + I_{b,Na} + I_{NaCa} + I_{NaK}) \tag{6.3}$$

C_m represents the cell capacitance (set at 100pF). Numerically, the equations for the neonatal rat atrial cell model were described by using the classical Hodgkin-Huxley formalism at 37ºC under 1Hz pacing, with a time step of 0.01ms, which was sufficiently small to guarantee a stable numerical solution. The L-type and T-type calcium ionic currents were simulated and modified based on available experimental data on age-related change of Ca^{2+} measurements from Leuranguer *et al.* [26], as summarised in Table 6.1. The maximal conductance of $I_{Ca,L}$ was increased by 30% while it decreased by 70% for $I_{Ca,T}$. The shifts of activation midpoint $V_{0.5}$ for both currents were fitted and

simulated as shown in the following equations and Figure 6.1(A-B) below. No significant changes were observed with age advancement for inactivation midpoint. Figure 6.1(Ci-Cii) illustrates I-V curves obtained from the simulations for both adult and neonate plotted against the recorded values that were obtained experimentally.[26,27] The equations and related parameters are documented below:

T-type Ca^{2+} current in neonate:

$$I_{Ca,T} = G_{CaT} * bg(V - E_{Ca} + 106.5) \tag{6.4}$$

$$b_{\infty} = \frac{1.0}{1 + e^{\left(-\frac{V+36}{6.1}\right)}} \tag{6.5}$$

$$g_{\infty} = \frac{1.0}{1 + e^{\left(\frac{V+66}{6}\right)}} \tag{6.6}$$

T-type Ca^{2+} current in adult:

$$I_{CaT} = 0.3 * G_{CaT} * bg(V - E_{Ca} + 106.5) \tag{6.7}$$

$$b_{\infty} = \frac{1.0}{1 + e^{\left(-\frac{V+40}{7.8}\right)}} \tag{6.8}$$

$$g_{\infty} = \frac{1.0}{1 + e^{\left(\frac{V+66}{6}\right)}} \tag{6.9}$$

L-type Ca^{2+} current in neonate:

$$I_{Ca,L} = 4G_{CaL}dff_{Ca}\frac{VF^2}{RT}\left(\frac{[Ca]_i e^{\left(\frac{2VF}{RT}\right)} - 0.341[Ca]_o}{e^{\left(\frac{2VF}{RT}\right)} - 1}\right) \tag{6.10}$$

$$d_{\infty} = \frac{1.0}{1 + e^{\left(\frac{-1.8-V}{8.6}\right)}} \tag{6.11}$$

$$f_{\infty} = \frac{1.0}{1+e^{\left(\frac{22+V}{6.1}\right)}} \tag{6.12}$$

L-type Ca^{2+} current in adult:

$$I_{CaL} = 1.3 * 4G_{CaL}dff_{Ca}\frac{VF^2}{RT}\left(\frac{[Ca]_i e^{\left(\frac{2VF}{RT}\right)} - 0.341[Ca]_o}{e^{\left(\frac{2VF}{RT}\right)} - 1}\right) \quad (6.13)$$

$$d_\infty = \frac{1.0}{1 + e^{\left(\frac{-6-V}{9.37}\right)}} \quad (6.14)$$

$$f_\infty = \frac{1.0}{1+e^{\left(\frac{22+V}{6.1}\right)}} \quad (6.15)$$

In addition, the following changes were made to the original model: the I_{NaK} was changed to decrease by 20%, in accordance with Kaplan *et al.* [29] I_{NaCa} was increased by 3% as found by Hatch *et al.* [28] Similarly to the I_{NaCa}, the formulation of J_{rel}, which describes the Ca^{2+}-release rate, was increased by 30% [28]. Finally, Na^+, K^+ and Ca^{2+} intracellular intensities were kept constant as outlined in the original model. Such a variation in heart rate could be attributed to changes in cellular-ion channels, as shown in Table 6.2.

Na^+/K^+ ATPase in neonate:

$$I_{NaK} = \bar{I}_{NaK}\frac{f_{NaK}}{\left(1+\left(\frac{K_{mNai}}{[Na]_i}\right)^{n_{NaK}}\right)\left(1+\frac{K_{mKo}}{[K]_o}\right)} \quad (6.16)$$

Na^+/K^+ ATPase in adult:

$$I_{NaK} = 1.2 * \bar{I}_{NaK}\frac{f_{NaK}}{\left(1+\left(\frac{K_{mNai}}{[Na]_i}\right)^{n_{NaK}}\right)\left(1+\frac{K_{mKo}}{[K]_o}\right)} \quad (6.17)$$

Na^+/Ca^{2+} exchanger current in neonate rat:

$$I_{NCX} = k_{NCX}\frac{{[Na]_i}^3[Ca]_o e^{0.03743\gamma V} - {[Na]_o}^3[Ca]_i e^{0.03743(\gamma-1)V}}{1+d_{NCX}\left({[Na]_o}^3[Ca]_i + {[Na]_i}^3[Ca]_o\right)} \quad (6.18)$$

Na^+/Ca^{2+} exchanger current in adult rat:

$$I_{NCX} = 1.03 * k_{NCX}\frac{{[Na]_i}^3[Ca]_o e^{0.03743\gamma V} - {[Na]_o}^3[Ca]_i e^{0.03743(\gamma-1)V}}{1 + d_{NCX}\left({[Na]_o}^3[Ca]_i + {[Na]_i}^3[Ca]_o\right)} \quad (6.19)$$

To validate our simulation, the AP characteristics of RMP, peak amplitude (PA) and action potential duration (APD_{50}), obtained from the newly updated adult atrial model, were computed and plotted to be compared with neonatal conditions, which were plotted with the relevant experimental data. [28,30]

Table 6.2: Summary of experimental ion-channel remodelling and Ca^{2+} channelling proteins across age advancement in rat atrial cells.

Ion current	**Age -related changes (Experiments)**			**Simulation**
$I_{Ca,L}$	Current density (pA/pF)	3.7 to7 (↑ 30%)	Leuranguer *et al.* [26]	↑ 30%
	Activation midpoint (mV)	Negative shift by 5mv		-1.8 to -6
	Slope factor	↑ 30%		6 to 7.8
$I_{Ca,T}$	Current density (pA/pF)	5 to 2 (↓ 60%)		↓ 60%
	Activation midpoint (mV)	Negative shift by 5mv		-36 to -40
	Slope factor	↑ 9%		8.6 to 9.37
RYR2	The expression in protein level (↑ 30%)		Hatch *et al.* [28]	↑ 30%
SERCA2a	No significant changes in protein level ↔			
I_{NaCa}	The expression in protein level (↑ 3.2%)			↑ 3.2%
I_{NaK}	The expression in protein level (↓ 20.3%)		Kaplan *et al.*[29]	↓ 20.3%

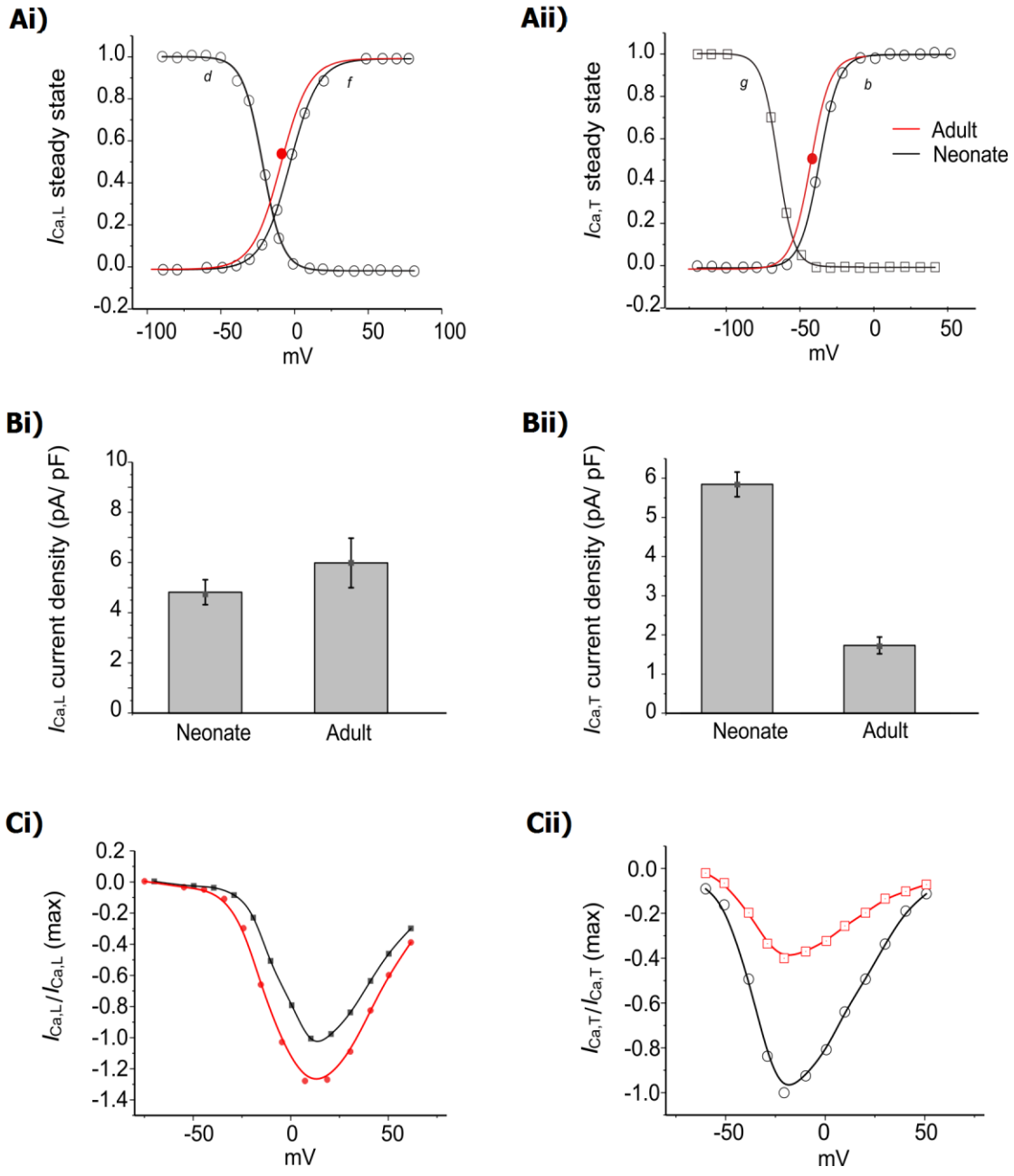

Figure 6.1. (A) Simulation of I-V curve relationship for $I_{Ca,L}$ and $I_{Ca,T}$ and their validation. The computed steady-state activation and inactivation gate curves of the Ca^{2+} current among two age groups: neonate (black line) and adult (red line) for (Ai) $I_{Ca,L}$ and (Aii) $I_{Ca,T}$. (B) The bar charts illustrate the variation in current densities shown for $I_{Ca,L}$ and $I_{Ca,T}$. (C) Computer-generated I-V relationships as authenticated against experimental findings by Avila *et al* [27] for (Ci) $I_{Ca,L}$, and for (Cii) $I_{Ca,T}$, according to Leuranguer *et al.* [26]

6.2.3 The development of 1D model of the SAN and the atrial muscle

The autonomic pacemaker cells in the SAN produce spontaneous APs that travel through gap junctions, and these facilitate the diffusion of ions, enabling the potentials of the cells to interact. SAN APs can be further transmitted to contractile cells such as atrial cells. Therefore, the stimulus of the APs from the SAN triggers the atrial cells to be excitable when the atrial cells reach the excitation threshold. [31] A 1D model of healthy SAN-atrium tissue was developed while taking into account the heterogeneity of AP properties, the anisotropy of tissue-conducting characteristics of the SAN and the RA to illustrate the cell-to-cell interaction, and AP diffusion between the SAN and atrial cells.

6.2.3.1. Anatomical SAN-atrium design

The rat multi-cellular 1D SAN-atrium tissue model was constructed as a tissue string. Owing to the lack of experimental observations on rat SAN cells, the geometry of tissue model described in this chapter was adapted from the rabbit SAN model developed by Zhang *et al.* [24], which suggested use of a gradient 1D model of the SAN based on the central and peripheral SAN-cell models. Furthermore, the rabbit SAN 1D string model was characterised by length (L) to12.9mm. This total length was divided into: SAN string tissue with length (L^s) of 3mm; atrial string tissue with length (L^a) of 9.6mm.[24] Owing to the differences between species, Zhang's 1D strand model was rescaled for rat by shortening the total length of the string to 6.5mm and adjusting the L^s to 1.5mm and L^a to 5mm to match the length of the rat SAN based on experimental findings by Hatch *et al.* [28]

6.2.3.2 Mathematical 1D string model

The proposed model indicated a gradient 1D model of the SAN based on the central and peripheral SAN and RA models. The monodomain differential equation was used in this idealised 1D SAN model and is described by the following equation:

$$\frac{\partial V}{\partial t} = \nabla \cdot (D \nabla V) - \frac{I_{tot}}{C_m} \tag{6.20}$$

D denotes the tensor of diffusion coefficients that describe the spread of electrical activity, the I_{tot} denotes the total ionic membrane current derived from different cell

models, ∇ is the spatial gradient operator, and C_m is the cell capacitance. In this 1D tissue model, the entire current for SAN cells was calculated using rat central and peripheral SAN cell models designed by this study, whilst for atrial cells, the biophysically comprehensive rat atrium model was modified as explained in the last section. [25]

Within the SAN string, the ordinary differential equations of the 1D SAN model are captured in the following formula:

$$\frac{dV^s}{dn} = 0\,, for\ x = 0\text{mm} \tag{6.21}$$

For $x > 0$ and ≤ 1.5mm

It is assumed that $C_m^s(x)$ shifts from 32pF (C_m in the central SAN cell model) to 65pF (C_m in the peripheral SAN cell model) exponentially. Therefore, the capacitance $C_m^s(x)$can be described in terms of the following formulas:

$$C_m^s(x) = 32 + \frac{1.07\,(x-0.1)}{L^s[1+0.7747\exp-(x-2.05)/(0.295)]}(65-32) \tag{6.22}$$

The conductance $g^s(x)$ at a certain distance *x* is shown by Equation (6.23) for different ion channels (Na^+, Ca^{2+}, and K^+). The conductance value $g^s(x)$ is dependent on the value of $C_m^s(x)$.

$$g^s(x) = \frac{[65 - C_m^s(x)]\ g_c + \ (\ C_m^s(x) - 32\ )g_P}{65\ -\ 32} \tag{6.23}$$

$$\frac{dV^s(x)}{dt} = -\ \frac{1}{C_m^s(x)}\ \left[i_{tot}^s(x) + \ D^s\ \frac{d^2V^s(x)}{dx^2}\ \right] \tag{6.24}$$

The SAN cell voltage $V^s(x)$ varies with distance *x* from the SAN centre. D^s refers to the scale of the conduction velocity of AP in the SAN cells.

For $x > 1.5 < 6.5$mm:

$$\frac{dV^a(x)}{dt} = -\ \frac{1}{C_m^a(x)}\ \left[i_{tot}^a(x) + \ D^a\ \frac{d^2V^a(x)}{dx^2}\ \right] \tag{6.25}$$

$$\frac{dV^a}{dn} = 0\ , for\ x = 6.5\text{mm} \tag{6.26}$$

$V^a(x)$ represents the atrial cell voltage from the end of the SAN to x. D^s and D^a are the diffusion coefficients that determine the conduction velocity of the APs in both the SAN and the atrial muscle. The D^s and D^a scale the conduction velocity, (CV) for the oropageted AP from rat SAN to atril cells. The recorded CV of SAN was measured as 5.7± 0.3cm/s.[7] D^s is set at 0.6 cm^2/s, which results in a CV of 6cm/s in the SAN, and D^a was set at 1.25cm^2/s, which generates a CV of 62.0cm/s in the atrial muscle.[25,32] Coupling at the junction of the SAN- atriaum is indicated by the diffusion coefficient D^s . Moreover, a time step 0.1ms and space steps of 0.05mm were used into our model. These time and space steps were chosen to be sufficiently small for a stable and accurate solution

Equations (6.21) and (6.26) represent the non-flux boundary conditions, which assume no ion exchange between the 1D tissue and the external environment of 1D tissue at the two poles of the 1D model. The non-flux boundary conditions suggest absence of concentration gradient at the boundary. Thus, there is no ion (or voltage) exchange between the SAN and the external environment.

6.2.4 Simulation of the electrical remodelling in STZ-induced diabetic rats: a case study

A recent experimental study, conducted by Zhang *et al.*[1], suggests that STZ-induced diabetes in rat can modulate ion-channel function in SAN cells, producing depressions in capacitance C_m of 20% and in I_f current density of 30%. Protein expression in $Ca_v1.3$, $Ca_v3.1$, and NCX is also significantly decreased, as summarised in Table 6.3. All these changes were incorporated into our rat SAN model at single-cell level to investigate the functional effect of this electrical remodelling of ion-channel proteins that are involved in STZ-induced diabetes on generation of APs and on the beating rate of the SAN. Our newly developed 1D model was used to simulate the same parameters in single cells. In addition, it was found that the expression of C_X45 deceased significantly by 50%, therefore, we decreased the diffusion coefficient of the 1D SAN model by 50% to address the effect of the ion channels expression changes in the protein level on the function of this electrical system and their contribution of Aps propagation, the activation time, and conduction velocity of the electrical conduction system.

Table 6.3: Summary of experimental measurements of the cell capacitance and remodelled ion-channels in STZ-diabetic rat.

Ion channel	Isoform	Changes in the protein investigated	References
I_f	HCN4	Current density from (-21 to -15) pA/pF ↓30%	Zhang *et al.*[1]
$I_{Ca,L}$	$Ca_V1.3$	↓33%	
$I_{Ca,T}$	$Ca_V3.1$	↓16%	
I_{NaCa}	NCX	↓40%	
Gap junction	C_X40	↑40%	
	C_X43	↓50%	
	C_X45	↓50%	

6.3 Results

6.3.1 Simulation of the pacemaking APs of peripheral rat SAN

In this study, the cell capacitance of the peripheral and central models were assumed to be 65pF and 32pF correspondingly. Figure 6.2 illustrates various pacemaking activities of the simulated APs and major ionic currents using the models of a central and a peripheral cell at 37°C from the rat SAN. The AP from the peripheral model exhibited an early rapid phase (phase 1) of repolarisation following the AP upstroke. Such an occurrence (early rapid phase of repolarisation) can be seen also in the periphery of a healthy SAN of a rabbit but not in the centre. [33, 34]

The morphology of simulated APs of peripheral cells was the same as those modelled from rabbit peripheral SAN. [24] When compared with the central SAN (see Figure 6.2Ai-Aii), the peripheral model exhibited faster spontaneous activity: the cycle length in the central model was 230ms, while that of the peripheral model was calculated at 178ms. Furthermore, the AP produced in the peripheral model also showed a more negative take-off potential, a faster upstroke velocity, a greater amplitude, shorter duration, a more positive peak value, and a more negative maximum diastolic potential than the AP of the central node Figure 6.2 (Bi-Bii) and (Ci-Cii) show changes in major

ionic currents (I_{Na}, $I_{Ca,L}$, I_{to}, I_{Kr}) and ($I_{Ca,T}$, I_{Ks} and I_f), respectively, during the APs generated by the peripheral and central models. Due to the regional differences in cell capacitance and ionic current densities outlined above, the amplitudes of the ionic currents varied between the central and peripheral models. All these characteristic differences are summarised in Figure 6.3.

6.3.2 Simulated action potential of the adult rat atrial cells

The age-related remodelling of the different ion channels ($I_{Ca,L}$, $I_{Ca,T}$, I_{NaK} and I_{NaCa}) and the Ca^{2+} handling component RyR2 were incorporated into the neonatal single-cell model of rat atrial cells developed by Majumder *et al.* [25] Figure 6.4A illustrates the simulated APs for adult rat RA (red), overlaid on a neonatal AP (black), obtained from 1Hz electrical pacing. Panels B-F display the time courses of ionic channel currents of rat atrial cells in the adult, which were superimposed on those from the neonate condition.

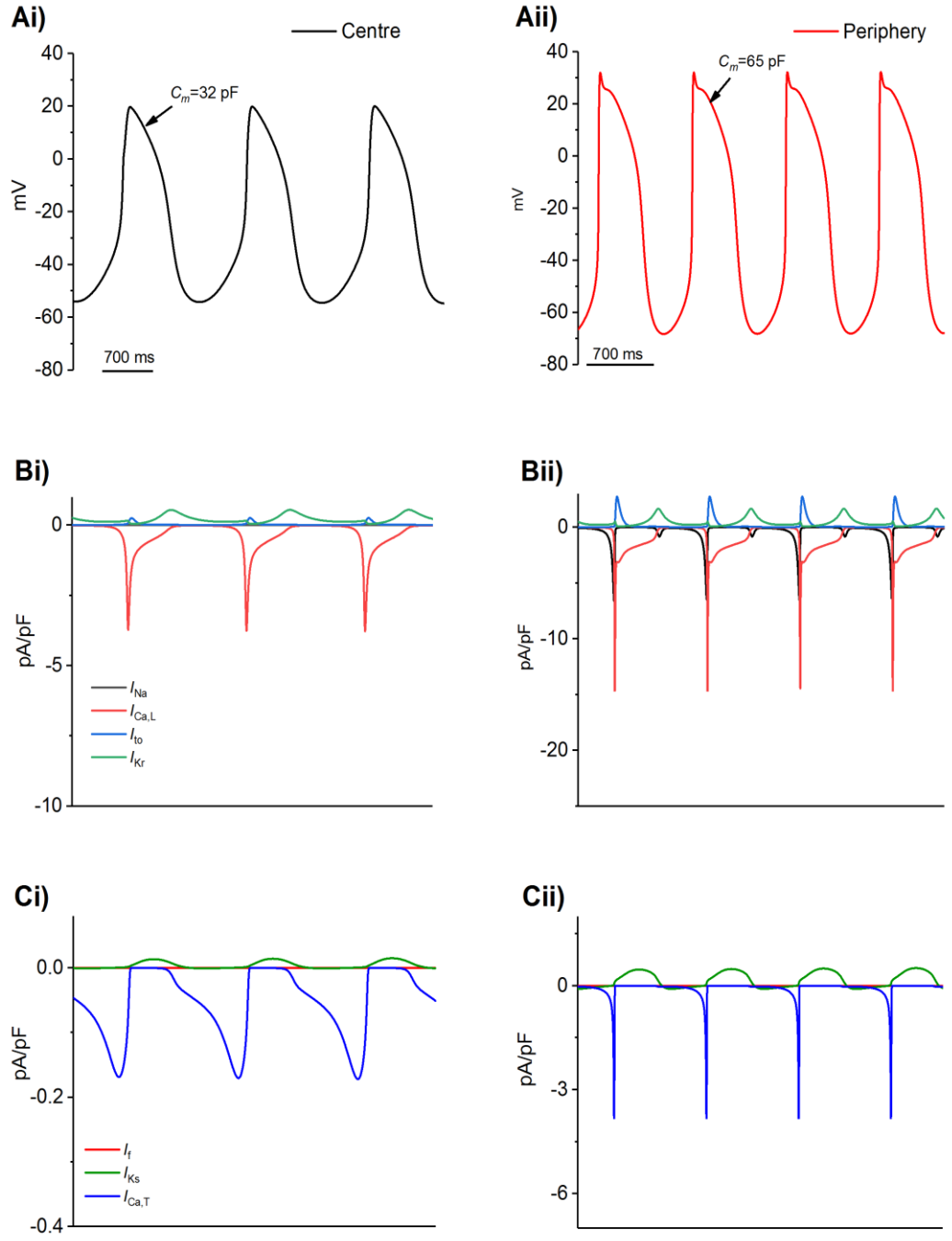

Figure 6.2. (Ai and Aii) Simulated central and peripheral SAN APs. The primary ionic currents (Bi-Bii) I_{Na}, $I_{Ca,L}$, I_{to}, $I_{K,r}$ and (Ci-Cii) $I_{Ca,T}$, $I_{K,s}$, and $I_{f.}$

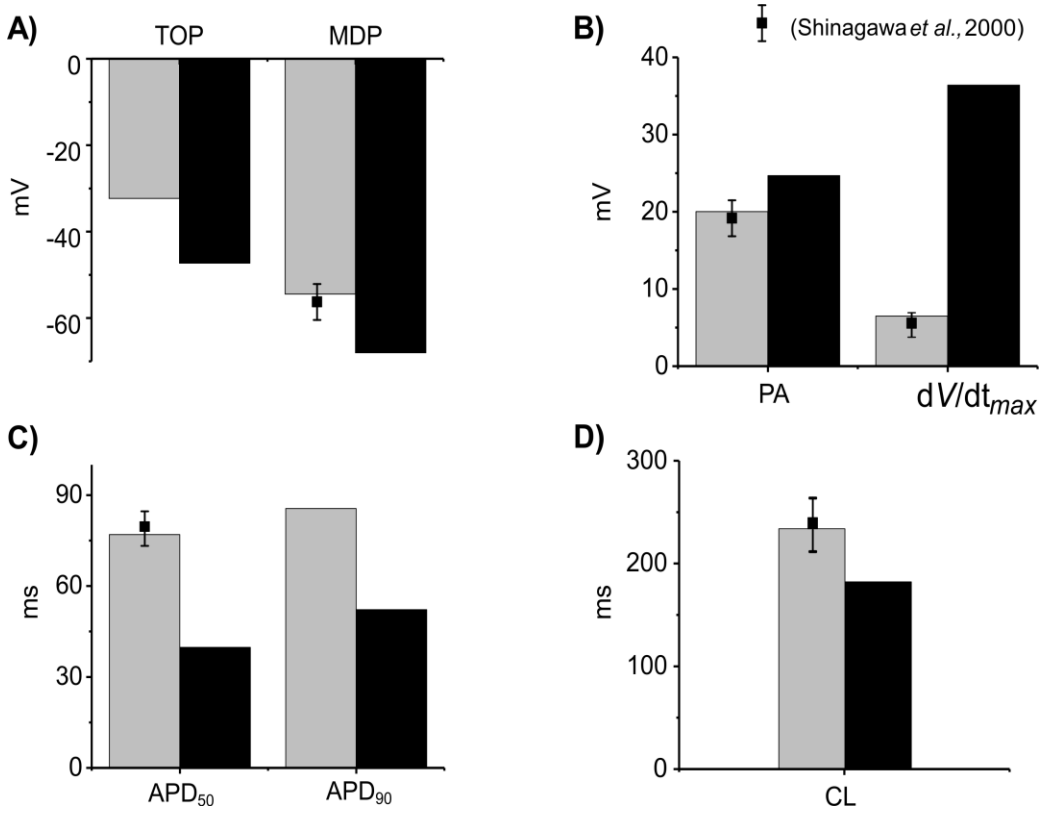

Figure 6.3. Bar chart comparison of the main AP characteristics of the rat central and peripheral SAN. (A) TOP and MDP; (B) OS and dV/dt $_{max}$; (C) APD_{50} and APD_{90}; (D) CL in central (grey) and peripheral cells (black).

The simulation results show that the adult-like model reproduced the characteristic shapes of the APs seen in adult cells as compared with experimental records.[7, 30] In general, the adult APs showed characteristics of sharp upstroke with repolarisation phase, which was the same as seen in the AP of the neonate condition, but they exhibited slower activities, longer durations, and smaller amplitudes than those of the neonate. The resultant APD_{50} for the adult was greater than the APD_{50} in the neonate: 38ms in the adult compared with 27ms in the neonate, showing a 40.7% prolongation of APD_{50} with age. Similarly for APD_{90}, our simulation results show that the APD_{90} in the adult was 109ms compared with 86ms in neonate cells. The computed maximal upstroke velocity of AP (dV/dt_{max}) was 83.6mV/ms in the adult compared with 114mV/ms in the neonate. The AP amplitude, APA, of the adult was smaller than that of the neonate (121mV compared with 131mV) in the rat atrial cell model. The simulation results were in agreement with the experimental observations as summarised in the bar charts shown in Figure 6.5, which shows a comparison of the AP characteristics of the adult rat atria

obtained from simulations. These could be quantitatively compatable with experimental records [7, 30] validating the model development.

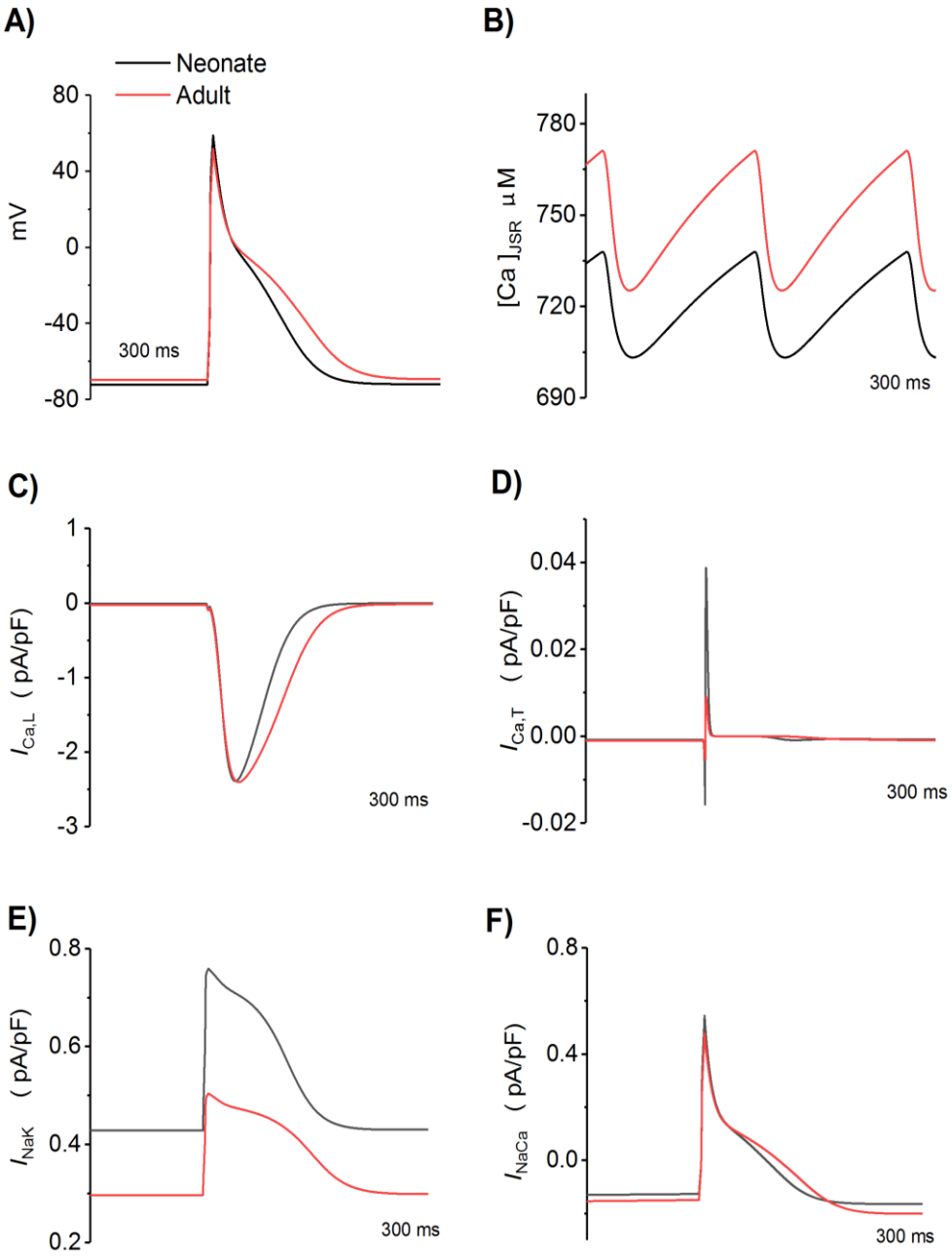

Figure 6.4. Time course of the APs and major ionic channel currents in neonate and adult rats atrial cell model generated during 1 Hz pacing. (A) APs profile. (B) Ca^{2+} - release in the junctional sarcoplasmic reticulum $[Ca^{2+}]_{JSR}$.(C) L-type current ($I_{Ca,L}$). (D) T-type current ($I_{Ca,T}$). (E) Na^{+}-K^{+} pump current (I_{NaK}). (F) exchanger current (I_{NaCa}).

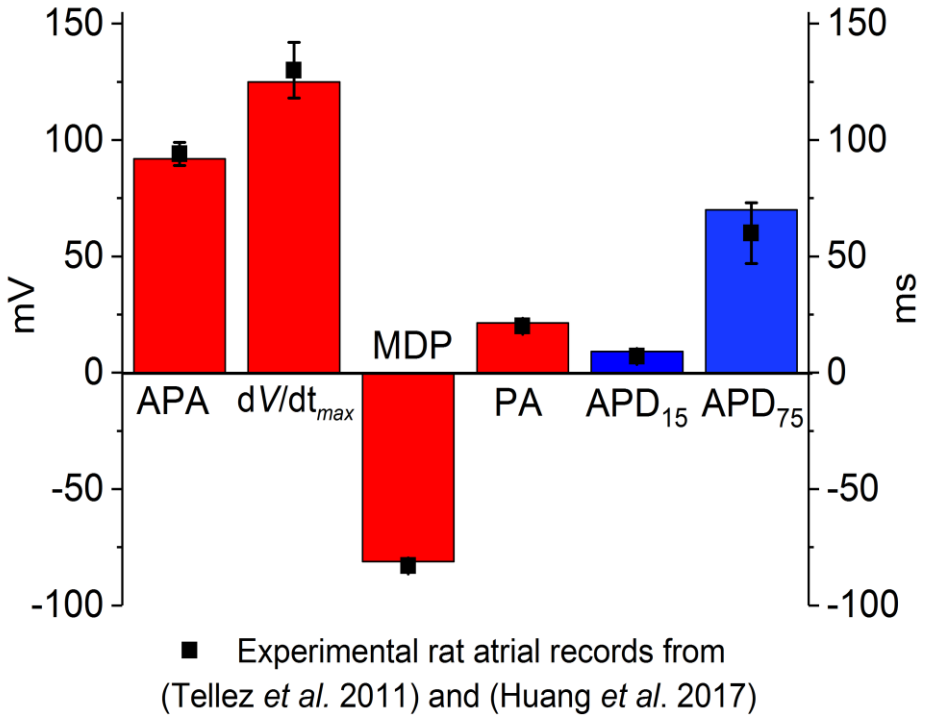

Figure 6.5. Bar chart of model findings of the main AP attributes of rat adult atrial cell. The attributes modelled were: APA, dV/dt_{max}, MDP, PA, APD_{15} and APD_{75}. All attributes were compared against experimental records [7, 30].

6.3.3 Simulated 1D SAN-atrium tissue model and comparison with the experimental data

The complex multi-cellular nature of the SAN and the electrotonic interaction between the SAN and the surrounding atrial myocytes determine many characteristics of the SAN tissue such as conduction, conduction disturbances, and leading pacemaker shift, suppression of the SAN affected by the atrial muscle. [31] The complex structure of the intact SAN tissue and the surrounding atrial muscle, and an anatomically realistic model of the intact SAN, was beyond the scope of the present study. However, a simple model, which disregarded the intricate structure of the SAN and considered the tissue as a 1D idealised tissue strand stretching from the SAN centre to the periphery and then onto the atrial muscle, could be employed to simulate qualitatively the activity and behaviour of the intact SAN -atrium tissue (see Figure 6.6A). Our 1D cell string tissue model of the SAN included the $C_m^s(x)$ that was assumed to show a gradient change in an exponential fashion from 32pF to 65pF, and similarly the ionic channel current densities

were dependent functions of C_m. Electronic coupling that occurred between cells was demonstrated by diffusion coefficients D^s and D^a for the SAN and the RA, respectively. The diffusion coefficient values were chosen to obtain appropriate conduction velocities within the SAN-atrium tissue (D^s was set at 0.6cm^2/s for SAN and D^a at 1.25cm^2/s for RA) (see section 6.2.3). These figures were consistent with experimental measurements of conduction velocities in the rat SAN.[7]

Figure 6.6 illustrates the simulation results of the propagation of APs using the 1D model of the SAN-atrium tissue. APs from different points along the tissue strand are shownin figure 6.6A**.** The junction of the atrium and the SAN were 1.5mm from the centre. Figure 6.6B demonstrates that the initiation of spontaneous APs began from the centre SAN (see arrow) and then spread to the periphery of the SAN and on to the atrial muscle. This activation sequence is similar to behaviour observed experimentally.[7, 28] The computed CL of SAN in our 1D model was 280ms, which was markedly larger than the CL of action potentials in the central (230ms) and peripheral (178ms) single-cell models, this is due to electronic interaction between SAN cells and the atrial cells. However, the CL of our 1D model was similar to that found experimentally in the healthy SAN of the rat at 37°C: 275

±30ms. [7] The SAN conduction time, (SNCT) (time taken for the AP to be conducted from the SAN) was 19ms, which was consistent with to experimental range between (17.2± 0.2ms - 21± 1ms). [7,35]

Figure 6.6C illustrates the activation time curve (the time taken for the AP to propagate from the leading pacemaker site in the centre to the atrial muscle) plotted against the distance from 0mm in the centre to the junction of the SAN-RA muscle at 1.5mm and on to the atrial muscle. The model results were similar to experimental data.[1, 7, 28, 35] Therefore, the 1D model of the intact SAN exhibited an array of activities that were comparable with those of the rat SAN.

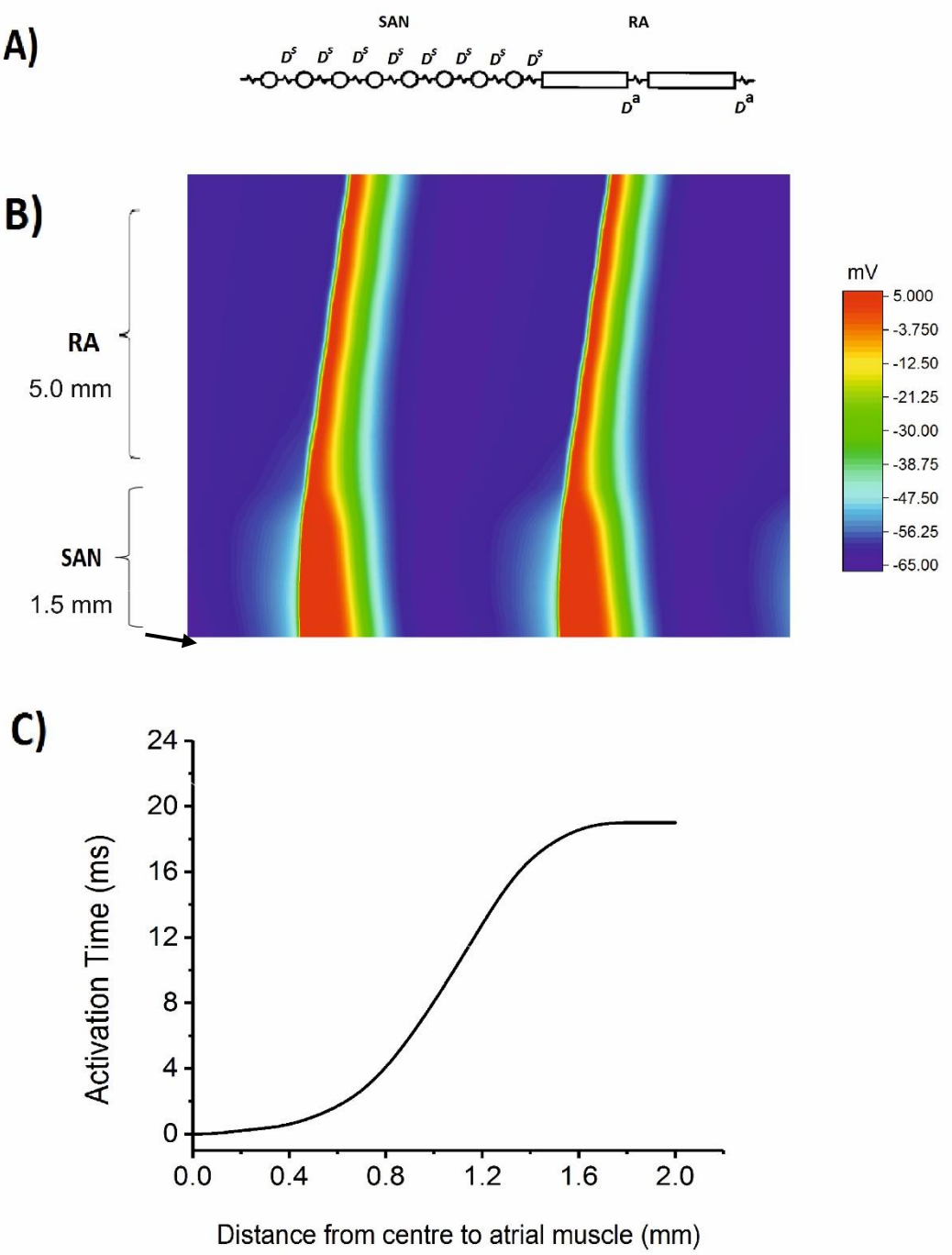

Figure 6.6. 1D model of the SAN. (A) Diagram of the idealised 1D model of the SAN and RA, in which D^s and D^a refer to diffusion coefficients for the SAN and the RA respectively. (B) Propagation of APs along the 1D model, starting from the centre of the SAN at 0mm to the junction of the SAN-RA muscle at 1.5 mm and on to the atrial muscle, which is up to 5mm from the SAN. (C) Activation time plotted against distance from the centre to the conjunction of SAN-RA (1.5mm).

6.3.4. STZ-induced diabetes and impaired pacemaking activity

The newly developed 1D tissue model of the rat SAN-atriaum was used to investigate the bradycardia effect associated with electrical remodelling of ion channels in STZ-induced diabetic rats.[1,7] In this section, simulation results presented the electrophysiological properties of APs at the single-cell for diabeties condition in comparison with control condition. Then, the functional effect of the STZ-induced diabetes on the spontaneous rhythmic pacemaking and conduction activity of the SAN tissue was illustrated.

The functional effects of HCN4, Cav1.3, Cav3.1 and NCX deficiencies on pacemaking APs at a single-cell level were investigated in both the central and peripheral models by reducing the maximal ionic current density simulations. Figures 6.7 and 6.8 illustrate the simulated APs, together with the main AP characteristics, under control and diabetic conditions in the central and peripheral cells. The simulation results show that integral effect of remodelled ion-channel deficiencies slowed down the pacemaker activity in both the central and peripheral cell models. To be more specific, the measured CL increased from the control value of 230ms to 255ms (10.9%) for the central model, and from 178.8ms to 197.2ms (11.3%) for the peripheral model. Apart from slowing the pacemaker activity, STZ-induced diabetes also caused changes in other characteristics of AP morphology, including a reduction of the PA and dV/dt_{max} and an elevation of the MDP, as shown in Table 6.4.

At tissue level, the 1D model was used to study how ionic channel deficiency in STZ-induced diabetes affected the AP propagation across the SAN-RA. Figure 6.9A-B illustrates the spontaneous APs propagated across the tissue under control and diabetic conditions**.** Figure10A illustrates the activation time curve plotted against the distance from the centre to the conjunction of SAN-RA for the diabetic rats compared with the control rat. As explained above, APs in the control condition originated from the central region of the SAN with a CL of 280ms, whereas the CL in the diabetic model was 330ms (17.8% increase)(see Figure 6.10B), leading to a decrease in the HR from 214bpm to 181.8bpm, 15% fall. It is worth noting that the negative effects of ionic channel deficiency on the spontaneous pacemaking activity were enhanced in the SAN tissue model; this was due to the electrotonic interactions between the SAN and atrium cells. In addition, the 1D model also indicated a reduction of the conduction velocity in

the SAN with STZ-induced diabetes,(6cm/s compared to 5.2cm/s in control condition, these values are compatible with evperimental records of SAN's CV; 5± 0.5cm/s.[7] in diabetes and : 5.7± 0.3cm/s.[7] in control, as shown in Figure 6.10B. It can be seen also that the SNCT in the diabetic rat condition was slightly longer (~25ms) than that of the control model (19ms) (Figure 6.10C). These results are consistent with experimental observations from diabetic rats. [7] The decrease of conduction velocity observed in the simulation may be attributed to the elevation of the MDP and the reduction in DD phase. With these two effects, the time course between the MPD and the take-off potential would slow down, leading to an increase in the time required for SAN currents to charge the cell membrane and pass the electrical signal to the neighbouring cell. In turn, this would lead to an increase in the time taken to reach the required threshold potential for the initiation of an AP, thereby resulting in a bradycardia effect.

Table 6.4. The APs characteristics for both control and STZ-induced diabetes in central and peripheral single cells models.

Cell type of SAN		MDP(mV)	PA(mV)	dV/dt_{max}(V/s)	APD_{50}(ms)	CL(ms)
Centre	Control	-56.01	20.00	6.50	77.06	230
	STZ	-54.9	3.9	2.4	65.2	255
Periphery	Control	-68.06	32.06	35.23	40.94	177.7
	STZ	-67.6	21.55	12.88	35.52	197.2

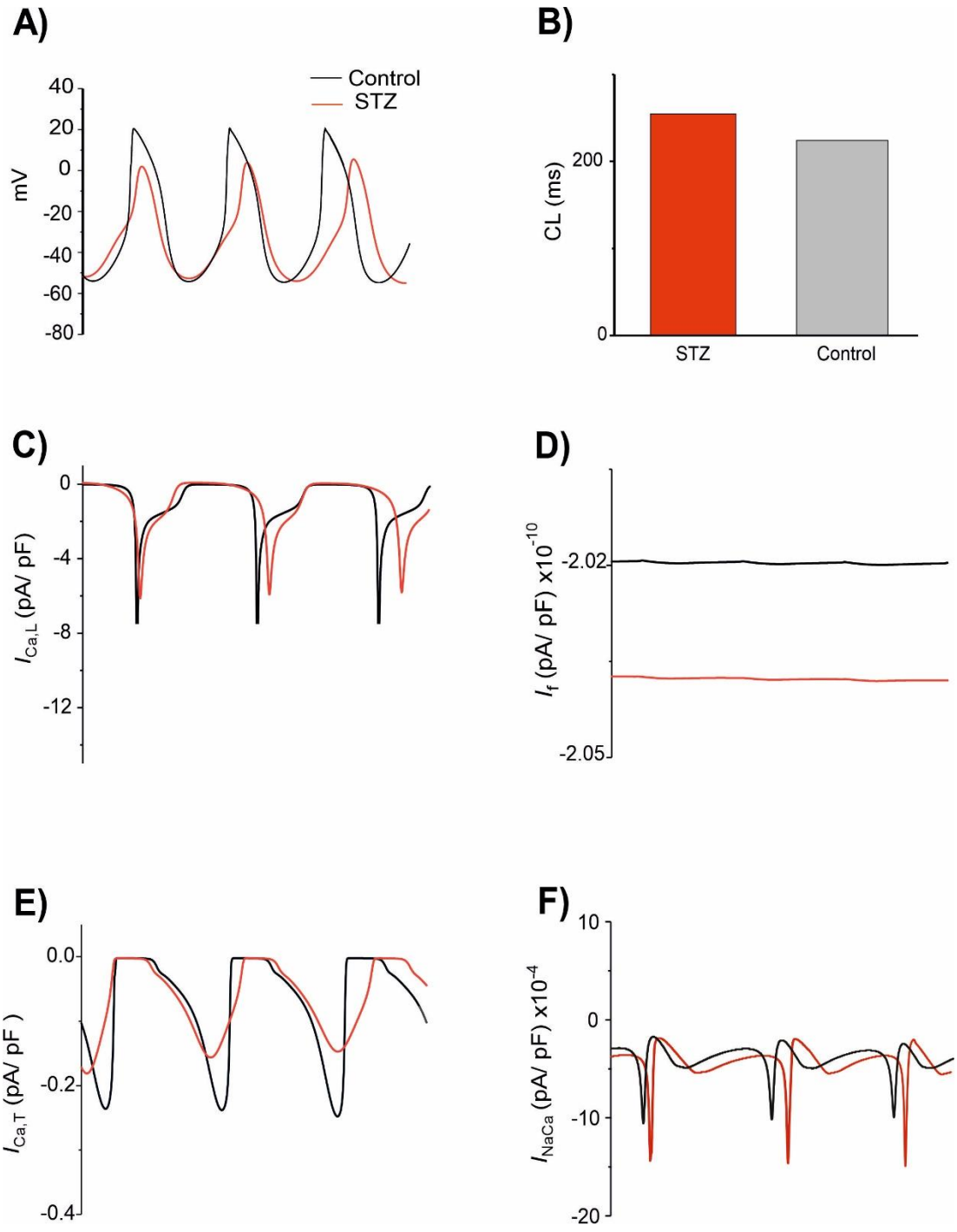

Figure 6.7. Functional effects of the remodelling of ionic channels currents on pacemaking APs in diabetes (red line) compared with control conditions (black line) in models of central SAN. (A) AP profiles; (B) the computed CL of the APs for both control and STZ conditions; the main remodelled ionic currents involved: (C) $I_{Ca,L}$, (D) I_f, (E) $I_{Ca,T}$, and (F) $I_{NaCa.}$

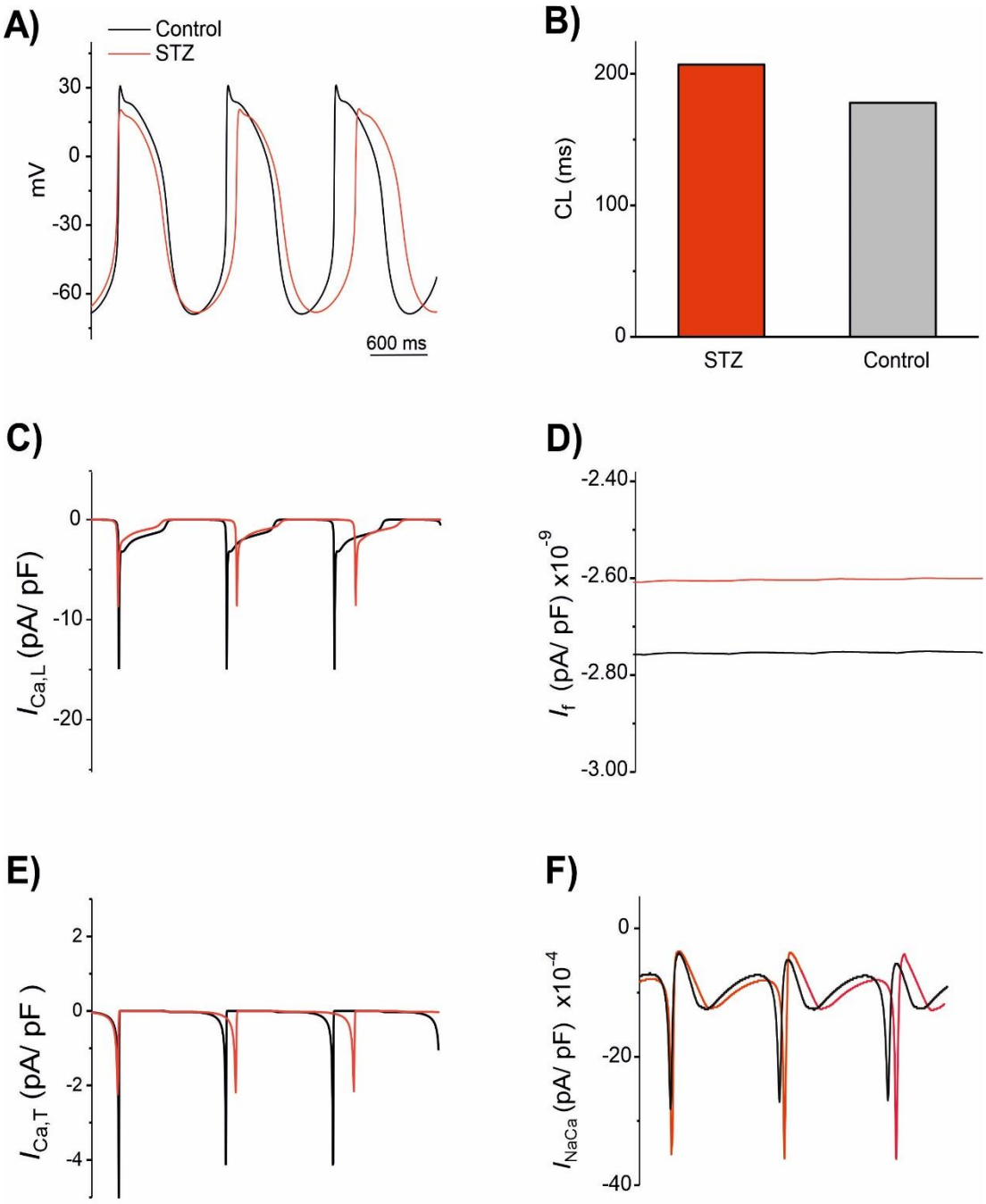

Figure 6.8. Functional effects of the remodelling of ionic channels currents on pacemaking APs in diabetes (red line) compared with control conditions (black line) in models of peripheral SAN. (A) AP profiles, (B) the computed CL of the APs for both control and STZ conditions. The main remodelled ionic currents involved: (C) $I_{Ca,L}$, (D) I_f, (E) $I_{Ca,T}$, and (F) I_{NaCa}.

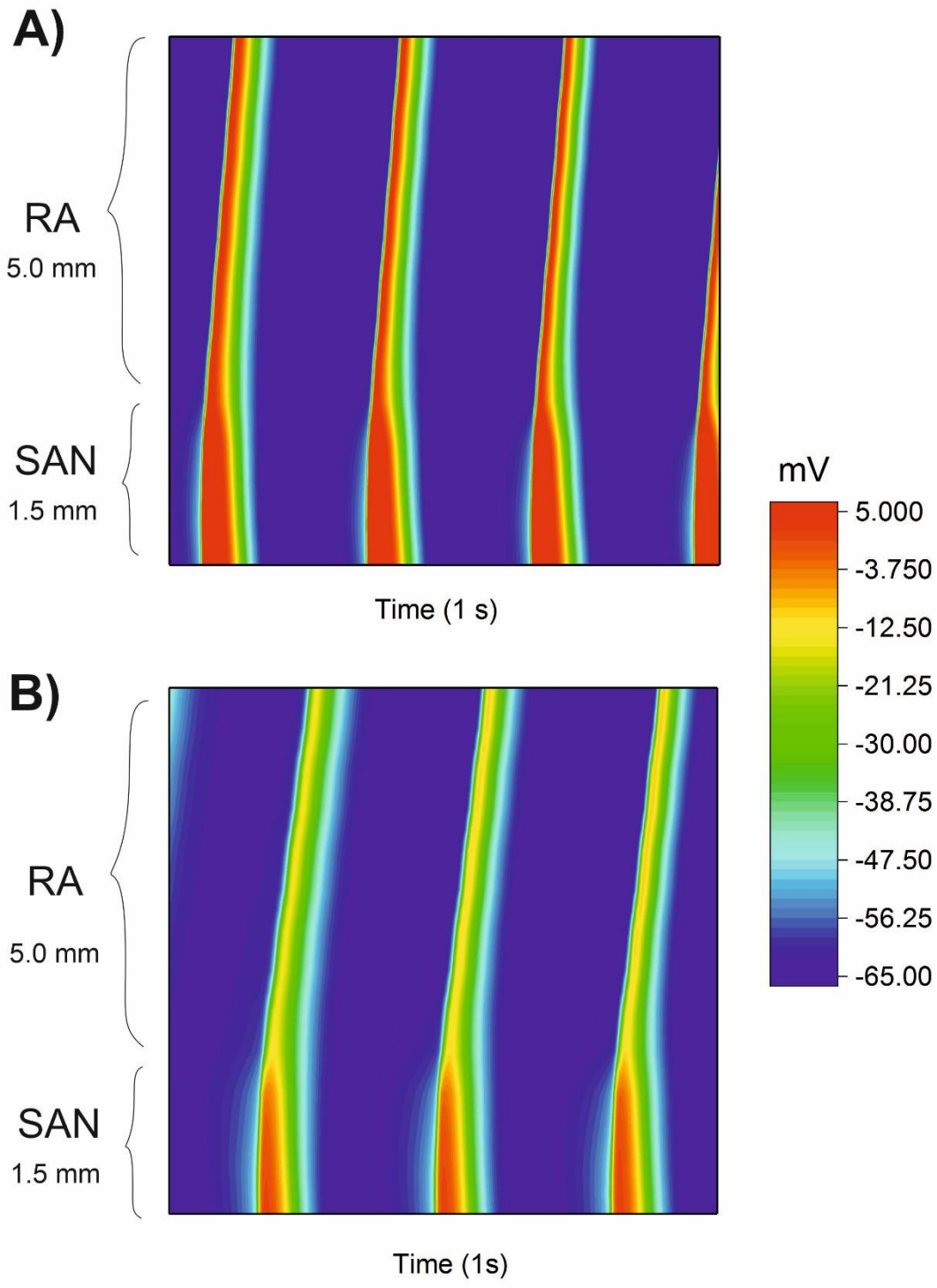

Figure 6.9. The action potentials computed using the 1D model of the intact SAN in (A) control, and (B) STZ-induced diabetic rat.

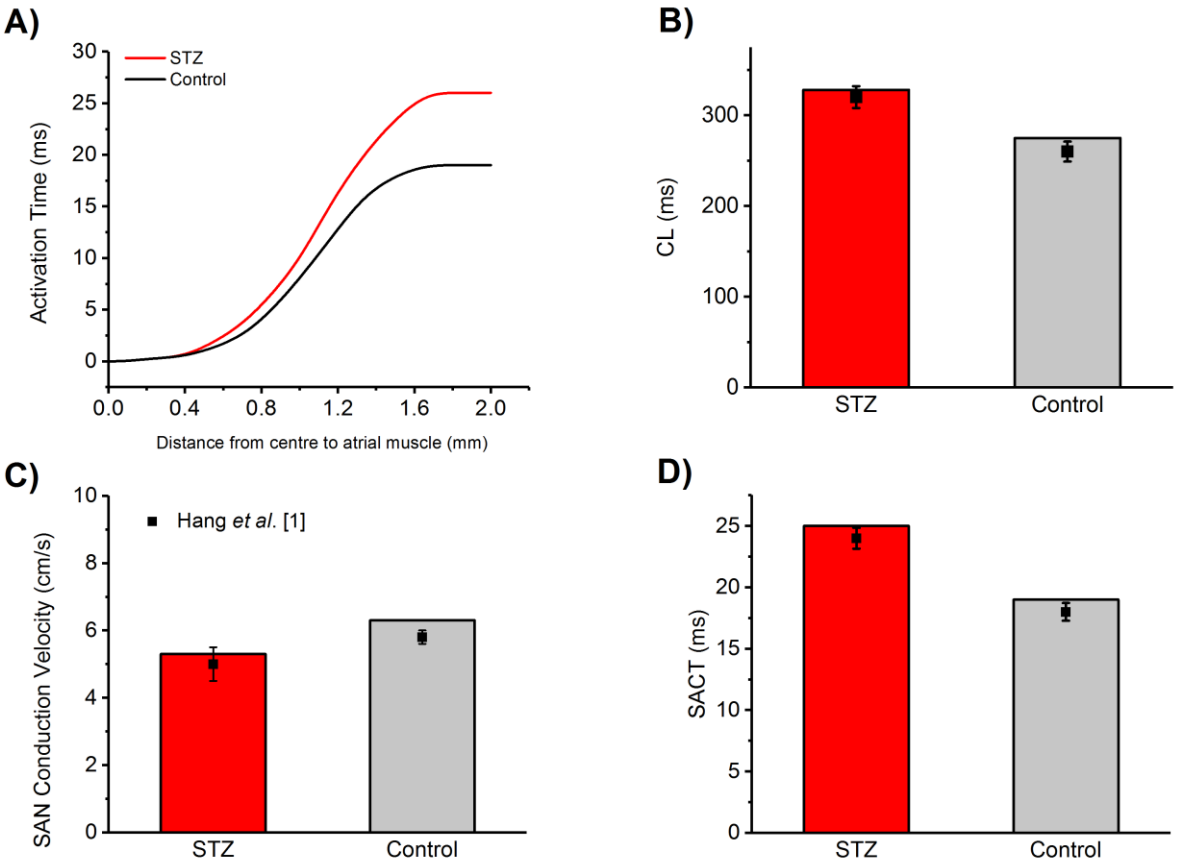

Figure 6.10. The computed activation activities of SAN in a STZ-induced diabetic rat and a control. (A) The activation time curves using the 1D model of the intact SAN in control (red line) and STZ-induced diabetic rat (black line). (B) Comparison of SAN CL, (C) SAN conduction velocity, and (D)SAN conduction time between the two groups. All data were comparable with the experimental record from SAN tissue by Huang *et al.* [7]

6.4 Discussion

Sinus bradycardia, a phenotype of sick node dysfunction (SND) can be associated with diabetes mellitus (DM). Recent experimental studies have focused on characterisation of the electrical remodelling of membrane-ion channels of SAN cells in STZ-induced type 1 DM rats.[1] This remodelling has been linked to abnormal cardiac activities that are characterised by the impaired initiation and conduction of cardiac electrical activity. However, it is still unclear how such changes at the cellular ion-channel level contribute to the mechanisms of this complex phenomenon, leading to depress the SAN's ability to pace and drive the surrounding atrium. For the work described in this chapter, we took inspiration from a computational approach to investigate this issue by developing a biophysically detailed mathematical model of action potentials for central and

peripheral rat SAN cells and incorporating them into a 1D string model of the rat SAN-right atrium.

6.4.1 Comparison with experimental data

The rat SAN model described in Chapter Five was further modified with taking into account the regional variation of cells in the SAN tissue. The peripheral model we built demonstrated faster pacemaking activity than the central SAN model, which has a similar behaviour of pacwmaking APs seen in rabbit peripheral cells. [24] Then, detailed electrophysiological formulations for the ion-channel currents in rat atrial cells were constructed in a single cell model. This was applied to rat atrial cells during postnatal development based on experimental data available from literature.[26,28,29] Both biophysically detailed SAN (centre and periphery) and adult right atrial cell models were used to construct a 1D rat SAN-right atrium model. The anisotropy of tissue capacitance, conductance properties and heterogeneity of AP characteristics were also considered in this model. The structure of the string model was based on rescaling the geometric data of the string rabbit SAN from Zhang *et al.* [24] Therefore, the one-dimensional model was a reasonable approximation of the intact rat SAN (see method section). The 1D model displayed similar behaviour to that of the intact rat SAN in terms of action potential profiles and the activation sequence of the SAN-atrium: the action potential was first initiated in the centre of the SAN, then transmitted to the atrium across the peripheral cells. [28] This 1D model also successfully reproduced the electrical conduction activities, including the activation time and conduction velocity of the SAN tissue under control conditions. All these data were also consistent with experimental observations from rat SAN tissue as shown in result section.

6.4.2 Ion channel deficiencies and SND in type 1 diabetic rats

In this section, findings are analysed at single-cell and tissue levels and tissue level as following:

At a single-cell level: our study has indicated that the integral effects of particular ionic channel deficiencies ($I_{Ca,L}$, $I_{Ca,T}$, I_f, and I_{NaCa}) as well as reduction of the C_m slows down pacemaker activity in both central and peripheral SAN cells. The partial blocking of the $I_{Ca,T}$ current led to an increase in the CL and affected dV/dt_{max}. In addition, the reduction of the $I_{Ca,L}$ was associated with a decreased AP amplitude and abbreviated $APD_{50,}$ both

accelerated the repolarisation process but produced an incomplete repolarisation as a consequence of reduced AP amplitude and abbreviated APD_{50}, and consequently, an elevated MDP was produced, leading to a reduced depolarisation current in the DD phase (such as I_{NaCa}). This slowed down in the time course between the MPD and the take-off potential, leading to an increased time interval between two successive pacemaking APs and resulting in bradycardia and a depressed heart rate. However, the simulated results showed that partial blocking of the I_f current (by 30%) did not produce an increase of the CL and had no effect on $dV/dt_{max.}$ This could be due to the modelling of the I_f in the rat SAN as native current, and the contribution of individual HCN channels were not considered in the rat SAN model.

At the intact SAN–atrium tissue level: ion channel remodelling ($I_{Ca,L}$, $I_{Ca,T}$, I_f and I_{NaCa}) as well as C_m of SAN in the STZ-induced diabetic condition slowed down the pacemaking rate. This effect was greater than that observed in the isolated central and peripheral cells. The integral effect of the remodelled ion channels produced an increase in the CL of 10.9% and 11.3% for the central and peripheral cell models, respectively, but increased the CL in the intact SAN–atrium tissue by approximately 17.8%. This great impact at the tissue level is attributed to the electrotonic interactions between the SAN and the right atrium via a cell-to-cell electrical coupling which causes an electrical load from the atrium to the SAN, this electrical load inhibited the SAN pacemaking ability to intiate the propagation and impaired the AP conduction.[32]In addition, the deficiency in the ion channels produced a lower MDP and a weaker pacemaking activity (low DDR and dV/dt_{max}) for both central region of SAN and boundary region between the SAN and the atrium (peripheral cells of the SAN). Therefore, the effect of ion-channel deficiency together with the inhibition from the atrium on impairment of pacemaking activity is accentuated as fewer ion channels become available to counterbalance the suppressive effect of neighbouring atrial cells. [34, 36]

6.5 Limitations of the models

The newly developed model has some limitations. The first is that the results obtained from the rat peripheral SAN model could not be validated against the experimental records. This is mainly due to a lack of available experimental data on APs or ion channels in rat peripheral cells of the SAN. Our rat peripheral SAN model was built

theoretically, based on a ratio calculated using the rabbit data available from Zhang *et al.* [24] The electrophysiological properties of the AP characteristics and different ion-channel currents will be improved if experimental data become available.

Another limitation related to the updated rat atrial cells model. [25] The age-related changes of the ion channels were investigated. Some of the available data were obtained from cultured cells for specific ion channels [26, 28, 29]. However, results would be improved if the other ion channels, such as the sodium and potassium channels, were also evaluated during ageing development. Although the electrophysiology of the remodelled ion channels in atria during age development has been investigated in different species such as rabbit and dogs,[37,38] we aimed to restrict our simulation to experimental data available for the rat.

The third limitation of this study was that, the 1D structure of the string model of the rat SAN-atrium tissue used in the study was reconstructed based on rescaling the geometry of the 1D rabbit model due to limitation of experimental data. [24] Although the 1D model is a computationally efficient approach that can be used to explore the behaviour of an intact SAN, it is an approximation of the intact SAN, and in the future a more realistic 2D or 3D model is required. Nevertheless, without consideration of realistic geometry, the model produced many characteristics of the rat SAN tissue such as conduction time and velocity in a manner that was quantitatively comparable with experimental data.

6.6 Conclusion

In this study, we have developed a new detailed 1D mathematical model of rat SAN–atrium tissue. The 1D SAN-atrium model successfully reproduced the initiation and propagation of rhythmic APs, with activation times and conduction velocities that were consistent with experimental observation. This new model could be a very useful tool to study certain conditions of the SAN, such as genetic defects or arrhythmias. The 1D model also has been used to investigate the effect of electrical remodelling in STZ-induced diabetes on spontaneous activity of APs and conduction across the SAN-atrium. The simulation results show that the reduced expression of the ion-channel currents associated with STZ-induced diabetes in rats can be linked to weakened pacemaking activity of the SAN.

References

1. Zhang Y, Wang Y, Yanni J, Qureshi MA, Logantha SJRJ, Kassab S, *et al.* Electrical Conduction System Remodeling in Streptozotocin-Induced Diabetes Mellitus Rat Heart. Front Physiol [Internet]. 2019 Jul 8;10. Available from: https://www.frontiersin.org/article/10.3389/fphys.2019.00826/full

2. Gami AS, Witt BJ, Howard DE, Erwin PJ, Gami LA, Somers VK, *et al.* Metabolic Syndrome and Risk of Incident Cardiovascular Events and Death. J Am Coll Cardiol [Internet]. 2007 Jan 30 [cited 2019 Oct 28];49(4):403–14. Available from: http://www.ncbi.nlm.nih.gov/pubmed/17258085

3. Veglio M, Chinaglia A, Cavallo Perin P. The clinical utility of QT interval assessment in diabetes. Diabetes Nutr Metab [Internet]. 2000 Dec [cited 2019 Oct 28];13(6):356–65. Available from: http://www.ncbi.nlm.nih.gov/pubmed/11232762

4. Linnemann B, Janka H. Prolonged QTc Interval and Elevated Heart Rate Identify the Type 2 Diabetic Patient at High Risk for Cardiovascular Death. The Bremen Diabetes Study. Exp Clin Endocrinol Diabetes [Internet]. 2003 Jul 7 [cited 2019 Oct 28];111(04):215–22. Available from: http://www.ncbi.nlm.nih.gov/pubmed/12845560

5. Rubler S, Reicher-Reiss H, Pulini M. Diabetes mellitus and impaired atrioventricular conduction. N Y State J Med [Internet]. 1975 Dec [cited 2019 Oct 29];75(14):2517–21. Available from: http://www.ncbi.nlm.nih.gov/pubmed/1059942

6. Hicks KK, Seifen E, Stimers JR, Kennedy RH. Effects of streptozotocin-induced diabetes on heart rate, blood pressure and cardiac autonomic nervous control. J Auton Nerv Syst [Internet]. 1998 Mar 3 [cited 2019 Oct 28];69(1):21–30. Available from: http://www.ncbi.nlm.nih.gov/pubmed/9672120

7. Huang X, Zhong N, Zhang H, Ma A, Yuan Z, Guo N. Reduced expression of HCN channels in the sinoatrial node of streptozotocin-induced diabetic rats. Can J Physiol Pharmacol [Internet]. 2017 May [cited 2019 Nov 4];95(5):586–94. Available from: http://www.nrcresearchpress.com/doi/10.1139/cjpp-2016-0418

8. Lei M, Goddard C, Liu J, et al. Sinus node dysfunction following targeted disruption of the murine cardiac sodium channel gene Scn5a. J Physiol. 2005;567(Pt 2):387–400. doi:10.1113/jphysiol.2005.083188

9. Verkerk A. O, Wilders R, Coronel R, Ravesloot J,Verheijck, E. E. Ionic Remodeling of Sinoatrial Node Cells by Heart Failure. Circulation. 2003;108:760-766.

10. Kharche S, Yu J, Lei M, Zhang H. A mathematical model of action potentials of mouse sinoatrial node cells with molecular bases. Am J Physiol Heart Circ Physiol [Internet]. 2011 Sep [cited 2018 Dec 12];301(3):H945-63. Available from: http://www.ncbi.nlm.nih.gov/pubmed/21724866

11. Butters TD, Aslanidi O V., Inada S, Boyett MR, Hancox JC, Lei M, et al.

Mechanistic Links Between Na $^{+}$ Channel (SCN5A) Mutations and Impaired Cardiac Pacemaking in Sick Sinus Syndrome. Circ Res [Internet]. 2010 Jul 9 [cited 2019 Nov 4];107(1):126–37. Available from: https://www.ahajournals.org/doi/10.1161/CIRCRESAHA.110.219949

12. Butters TD, Aslanidi O V, Zhao J, Smaill B, Zhang H, Lip G, et al. A novel computational sheep atria model for the study of atrial fibrillation. Interface Focus [Internet]. 2013;3(2):20120067. Available from: http://www.ncbi.nlm.nih.gov/pubmed/24427521%5Cnhttp://www.pubmedcentral.nih.gov/articlerender.fcgi?artid=PMC3638473

13. Csepe TA, Zhao J, Hansen BJ, Li N, Sul L V, Lim P, et al. Human sinoatrial node structure: 3D microanatomy of sinoatrial conduction pathways. Prog Biophys Mol Biol [Internet]. 2016 Jan [cited 2019 Jan 22];120(1–3):164–78. Available from: http://www.ncbi.nlm.nih.gov/pubmed/26743207

14. Papadimitriou D, Xanthos T, Dontas I, Lelovas P, Perrea D. The use of mice and rats as animal models for cardiopulmonary resuscitation research. Vol. 42, Laboratory Animals. 2008. p. 265–76.

15. Leong X-F, Ng C-Y, Jaarin K. Animal Models in Cardiovascular Research: Hypertension and Atherosclerosis. Biomed Res Int [Internet]. 2015;2015:1–11. Available from: http://www.hindawi.com/journals/bmri/2015/528757/

16. Konopelski P, Ufnal M. Electrocardiography in rats: a comparison to human. Physiol Res [Internet]. 2016 Nov 23;65(5):717–25. Available from: http://www.ncbi.nlm.nih.gov/pubmed/27429108

17. Boixel C, Gonzalez W, Louedec L, Hatem SN. Mechanisms of L-Type Ca2+ Current Downregulation in Rat Atrial Myocytes During Heart Failure. Circ Res [Internet]. 2001;89(7):607–13. Available from: https://www.ahajournals.org/doi/10.1161/hh1901.096702

18. Dai H, Wang X, Yin S, Zhang Y, Han Y, Yang N, et al. Atrial Fibrillation Promotion in a Rat Model of Rheumatoid Arthritis. J Am Heart Assoc [Internet]. 2017;6(12). Available from: https://www.ahajournals.org/doi/10.1161/JAHA.117.007320

19. Ferdous Z, Qureshi MA, Jayaprakash P, Parekh K, John A, Oz M, et al. Different profile of mRNA expression in sinoatrial node from streptozotocin-induced diabetic rat. PLoS One. 2016 Apr 1;11(4).

20. Howarth FC, Al-Sharhan R, Al-Hammadi A, Qureshi MA. Effects of streptozotocin-induced diabetes on action potentials in the sinoatrial node compared with other regions of the rat heart. Mol Cell Biochem [Internet]. 2007 May 30 [cited 2019 Jul 24];300(1–2):39–46. Available from: http://link.springer.com/10.1007/s11010-006-9366-5

21. Yanni J, Tellez JO, Sutyagin P V., Boyett MR, Dobrzynski H. Structural remodelling of the sinoatrial node in obese old rats. J Mol Cell Cardiol. 2010;48((2010)):653–662.

22. Abed HS, Samuel CS, Lau DH, Kelly DJ, Royce SG, Alasady M, et al. Obesity results in progressive atrial structural and electrical remodeling: Implications

for atrial fibrillation. Hear Rhythm [Internet]. 2012 [cited 2019 Mar 12];112(S190). Available from: http://dx.doi.org/10.1016/j.hrthm.2012.08.043

23. Tao T, Paterson DJ, Smith NP. A model of cellular cardiac-neural coupling that captures the sympathetic control of sinoatrial node excitability in normotensive and hypertensive rats. Biophys J [Internet]. 2011;101(3):594–602. Available from: http://dx.doi.org/10.1016/j.bpj.2011.05.069

24. Zhang H, Holden A V, Kodama I, Honjo H, Lei M, Varghese T, et al. Mathematical models of action potentials in the periphery and center of the rabbit sinoatrial node. Am J Physiol Hear Circ Physiol. 2000;279(2000):H397–H421.

25. Majumder R, Jangsangthong W, Feola I, Ypey DL, Pijnappels DA, Panfilov A V. A Mathematical Model of Neonatal Rat Atrial Monolayers with Constitutively Active Acetylcholine-Mediated K + Current. PLoS Comput Biol [Internet]. 2016 [cited 2018 Oct 31];12(6). Available from: https://journals.plos.org/ploscompbiol/article/file?id=10.1371/journal.pcbi.1004946&type=printable

26. Leuranguer R, Monteil A, Bourinet E, Dayanithi G, Joe¨ J, Nargeot J. T-type calcium currents in rat cardiomyocytes during postnatal development: contribution to hormone secretion. 2000 [cited 2018 Nov 1];(279:):H2540–H2548,. Available from: http://www.ajpheart.org

27. Avila G, Medina IM, Jiménez E, Elizondo G, Aguilar CI. Transforming growth factor-β1 decreases cardiac muscle L-type Ca^{2+} current and charge movement by acting on the Ca_v 1.2 mRNA. Am J Physiol Circ Physiol [Internet]. 2007 Jan [cited 2019 Jul 17];292(1):H622–31. Available from: http://www.ncbi.nlm.nih.gov/pubmed/16980347

28. Hatch. Age-associated changes to calcium handling proteins across the whole heart being a thesis submitted for the Degree of Doctor of Philosophy in the University of Hull by BSc (Hons) December 2012 Abstract. 2012;(December).

29. Kaplan P, Jurkovicova D, Babusikova E, Hudecova S, Racay P, Sirova M, et al. Effect of aging on the expression of intracellular Ca2+ transport proteins in a rat heart. Mol Cell Biochem [Internet]. 2007 Jun 4 [cited 2018 Mar 12];301(1–2):219–26. Available from: http://www.ncbi.nlm.nih.gov/pubmed/17549608

30. Tellez JO, Ma¸czewski M, Yanni J, Sutyagin P, Mackiewicz U, Atkinson A, et al. Ageing-dependent remodelling of ion channel and Ca 2+ clock genes underlying sino-atrial node pacemaking. Exp Physiol Exp Physiol. 9611:1163–78.

31. Boyett MR, Honjo H, Kodama I. The sinoatrial node, a heterogeneous pacemaker structure. Cardiovasc Res [Internet]. 2000 [cited 2018 Mar 1];47:658–87. Available from: www.elsevier.com

32. Ming Lei, Henggui Zhang, Andrew A. Grace, Christopher L.-H. Huang, SCN5A and sinoatrial node pacemaker function, Cardiovascular Research, Volume 74, Issue 3, June 2007, Pages 356–365 .Available from: https://doi.org/10.1016/j.cardiores.2007.01.009

33. Mangoni ME& JL nargeot, I. Genesis and Regulation of the Heart Automaticity. Physiol Rev [Internet]. 2008 [cited 2019 Mar 7];88(3):919–82. Available from: www.prv.org

34. Boyett MR, Honjo H, Yamamoto M, Nikmaram MR, Niwa R, Kodama I. Regional differences in effects of 4-aminopyridine within the sinoatrial node. Hear Circ Physiol [Internet]. 1998 [cited 2019 Aug 2];44(H1158–H1168, 1998). Available from: https://physiology.org/doi/pdf/10.1152/ajpheart.1998.275.4.H1158

35. Huang X, Yang P, Yang Z, Zhang H, Ma A. Age-associated expression of HCN channel isoforms in rat sinoatrial node. Exp Biol Med [Internet]. 2016 Feb [cited 2018 Mar 14];241(3):331. Available from: http://www.ncbi.nlm.nih.gov/pubmed/26341471

36. Boyett M, Holden AV, Kodama I, Suzuki R, Zhang H. Atrial modulation of sinoatrial pacemaker rate. Chaos, Solitons & Fractals [Internet]. 1995 Mar 1 [cited 2019 Oct 28];5(3–4):425–38. Available from: https://www.sciencedirect.com/science/article/abs/pii/0960077993E00349

Chapter Seven - Biophysical Modelling of HCN-Channel Change on Pacemaker in a Rat Subsidiary Atrial Pacemaker (SAP)

Addendum: *The work presented in this chapter has been submitted and published in J Physiol (2018) 596(24) pp 6141–6155. I participated in this paper by the simulation study. The experimental part has been done by other co-authers as shown below. The text presented here has been reworded where possible.*

TBX18 over-expression enhances pacemaker function in a rat subsidiary atrial pacemaker model of sick sinus syndrome

M. Choudhury, N. Black, **A. Alghamdi**, A. D'Souza, R. Wang, J. Yanni, H. Dobrzynski, P.A. Kingston, H. Zhang, M.R. Boyett and G. M. Morris

Author contributions

- Obtained funding: G.M.M. and M.R.B.;
- *In vitro* studies: M.C. and G.M.M.;
- qPCR: A.D., H.D., J.Y. and M.C.;
- **Computer modelling**: **A.A**., R.W. and H.Z.;
- Data analysis: G.M.M., M.C. and N.B.;
- **Production of figures, manuscript writing**: G.M.M., M.C, N.B, and **A.A**.;
- Experimental design and proof-reading: all authors.

Overview of biopacemaking

The idea of 'biopacemaking' advanced after the emergence of new technology that can alter cells at a molecular level, allowing us to either build ectopic pacemaker tissue or repair damaged pacemaker tissues. Numerous groups have responded to the call to locate the best strategy. Multiple groups have taken up the challenge to find the best method to create a robust and reliable bio-pacemakers as physiological beat to create a robust and reliable bio-pacemakers, as physiological beating rates, are autonomously sensitive and can be distributed safely and persistently over time. The ideal bio-pacemaker would be able to recapitulate the complex nature of the SAN. Bio-pacemaker research is, however, still in its infant stages, with more to learn about the most successful gene targets, delivery methods, locations of delivery and safety. Many approaches have been tested so far, focusing on using genes transferring methods based on viral vectors or using cell-based therapies based on stem cells or engineered cells.

One of the first biopacemaking strategy was to upregulate the β2-receptor in the SAN using naked plasmid injection to incorporate the β2-receptor gene into pigs and mice hearts. This increased basal heart rate and sensitivity to sympathetic stimulation. Although naked plasmid injections are low in toxicity and are non-infectious, this strategy has drawbacks; it was relatively inefficient at transfecting cells and expressing the gene of interest; and over-stimulation of the β-adrenergic pathway may cause arrhythmias. Another strategy of gene therapy called recombinant adenoviruses (RAds), which have been used effectively for several decades. One of the first applications in biopacemaking was to reduce IK,1 by 50-90% revealed pacemaking activity but also prolonged APD, reduced the speed of repolarization and left a more positive MDP, which could lead to ventricular arrhythmias or sudden death.

The research interest shifted to overexpression of HCN channels to increase the pacemaker current, If, without prolonging APD in neonatal rat myocytes. The upregulated of HCN2 promoted a robust pacemaker activity. This was Followed by HCN2-expressing adenovirus injection into the left atria of dogs, to create a site of spontaneous activity. Use of HCN channels, including the chimeric HCN212 channel, provided proof of concept that biopacemaking can produce an ectopic pacemaker responsive to autonomic stimulation and If blocking drugs like ivabradine. However, HCN2 expressed alone in ventricular tissue was too slow whilst HCN212

overcompensated, resulting in episodic ventricular tachycardia that was responsive to autonomic stimulation and If blocking drugs like ivabradine.

Another strategy to enhance pacing from overexpression of HCN2 in combination with upregulated adenylyl cyclase (AC1). The RAds expressing HCN2 and AC1 were injected into the dogs' left bundle branch with induced complete heart block, either singularly or in combination. Dogs that received either AC1 alone or HCN2-AC1 combined showed a robust speed up of basal heart rate and reduced reliance on electronic backup pacing. The finding showed that AC1 alone provided the best results overall with normal beating rate, reduced overdrive suppression and improved autonomic sensitivity in comparison with HCN2 alone, where the combined HCN2-AC1 overshot to develop a ventricular tachycardia. Strategy involving AC1 have produced result closest to physiological parameters so far.

Transcription factors, which involved in early SAN development, are interesting goals in bio-pacemaking research, they have the ability to activate multiple pacemaker mechanisms. Tbx18 is one of the most successful of these targets that provide a more supportive substrate being already capable of pacemaking and sensitive to autonomic control. This technique is usually used in ex vivo as well as in vivo within 48 hours of transduction to re-programme morphology and function of ventricular myocytes into pacemaker cells. When ex vivo was injected with the virus called Tbx18-expressing adenovirus in isolated ventricular cells of the neonatal rat, the membrane clock was affected by with upregulation of HCN4, while the Ca^{2+} clock was affected by increasing the intracellular Ca2+ release from the SR. When vivo was infected in with the same virus in the ventricular cells of guinea pigs, an ectopic pacemaker developed at the site of injection within 2-4 days with comparable characteristics of spindle-shaped morphology and beating rate to isolated SAN cells. Another key transcription factor, involved in SAN development, is Tbx3, it directly overexpresses the atrial gene programme, using a lentiviral vector in NRVM monolayers, to indirectly promote the pacemaker gene programme, therefore, creates a spontaneous activity based on DD, conduction slowing. Although restoring a physiologically normal system using Tbx18 looks very promising for targeting the dysfunctional SAN itself or nearby SAP tissue, this method has some limitations. Reproducing the complexity of the SAN will not be straight forward and further work on Ca^{2+} clock components would still need

interesting. Adenoviruses can be used experimentally but only express the target gene transiently in episomal DNA and so would not provide a long-lasting effect. Moreover, Adeno-associated virus displays longer lasting expression, but it is unclear whether this expression is episomal or truly genomic, and it also has a smaller packaging capacity for inserting target genes.

Cell-based therapies is an alternative approach for delivering a bio-pacemaker to the heart using human embryonic stem cells or modified cell implantation. In this method pacemaker cells are engineered in vitro and then transplanted. The pacemaker cells develop into cardiac tissue using transcription factors, and then a sub-population of these cells are implanted into ventricle tissue to give a rise to pacemaker activity. This resultant cell shows that Na+ current rather than L-type Ca2+ current was responsible for the phase 0 upstroke, and interestingly, demonstrate a strong If and IK,1, with supporting ventricular contractions for up to three months. Cell-based therapies suffer from a few problems. There are ethical concerns on using human embryos with this strategy, there is a risk of cell death, cell migration or rejection. Stem cells may transform into the wrong cell type or cause malignancy. Long-term immunosuppression might also be an unwanted necessity if these cells trigger a host immune response.

With these advanced developments of biopacemakers, there are still several challenges needs to be overcome to compete with the electronic pacemaker. The ideal biopacemaker should provide a permanent, safe and reliable usage to be used as a substitute to electronic pacemaker. They would also need to be cost effective, responsive to changing physiologic demands, and suitable for clinical trials in humans, therefore, there are still many issues that need to be solved before any option can be put forward as a viable strategy for human translation.

7.1 Introduction

The heart beat relies on a natural pacemaker, the sinoatrial node (SAN), a complex system of tissue , to initiate a robust reliable heartbeat under various physiological conditions.[1] Sick sinus syndrome (SSS) or sinus node disease (SND) is one of the most prevalent bradyarrhythmias in humans, causing slow heart rates, it increases with ageing population .[2] Clinical observation of the condition may manifest through paroxysmal pauses, chronotropic incompetence and periodic sinus bradycardia. The

condition may present as physical exercise limitation, which is a leading indicator of a need for electronic pacemaker implantation.[3] While electronic pacemakers have been proven to alleviate the symptoms of SSS,[4] but it has some limitations of the technology, including the need for frequent battery changes and occasional unresponsiveness to autonomic modulation, not to mention the implant complication rate of up to 12.4%. The alternative is the concept of 'bio-pacemaking', which relies on use of knowledge of the molecular biology of the sinoatrial node (SAN), combined with gene therapy development, to recreate SAN-like cells pacemaker tissue, which has a similar function to the SAN tissue in any myocardium tissue of the heart. This technique converts cardiac muscle to a pacemaker through injection of engineered viruses into cardiac muscle. This helps to mimic an electronic pacemaker without the need for external electronic pacemaker implantation, although this system also can be sensitive to the autonomic nervous system. There is potential for sustainable treatment of SND arrhythmia by reverse engineering of molecular abnormalities in dysfunctional pacemaker tissue.[5]

Various studies have been conducted to establish the effect of over-expression in HCN channels at the myocardium as a bio-pacemaker strategy. Some successes have been registered.[5] Even so, other studies have revealed that HCN channels are 'context-dependent', meaning that they display different, non-SAN functions when expressed in ectopic tissue). Therefore, it can be difficult to find an appropriate physiological heart rate with this approach.[6,7] Robust pacemaking by the SAN relies on a complex interaction of numerous mechanisms to produce a pulse. These mechanisms include a mutually entrained membrane, Ca^{2+} 'clocks' in which the Na^{+}/Ca^{2+} exchanger (NCX) is considered an important component, and the complex anatomy of SAN ultrastructure.[1] Consequently, the embryonic transcription factors T-box 3 (TBX) and T-box 18 (TBX18) in human are often the prime targets for bio-pacemaking, given that they play a key role in SAN development and therefore have huge influence over cardiac-tissue phenotype.[8] Ectopic expression of TBX18 has been demonstrated in ventricular cells to re-programme the ventricular cardiomyocytes into SAN-like cells with the capacity to reduce the requirement for electronic ventricular pacing in the case of an atrioventricular block.[9] However, SSS patients may require atrial or dual-chamber pacing in order to prevent 'pacemaker syndrome' and maintain cardiac synchrony.[10,11]. Morris *et al.*[12] showed in 2013 that expression of HCN channels

could accelerate spontaneous pulses in subsidiary atrial pacemaker tissue (SAP) that was bradycardic. This implies it has potential in SSS, but there have been no conclusive findings on bio-pacemaker approaches that target areas other than HCN genes.

In these experiments, the inferior extension of the crista terminalis (CT) was used to target TBX18 expression. This area was chosen because the CT tissue contained cells with nodal phenotype. For instance, cells in the CT are smaller than the cells in working atrial myocytes. Moreover, the CT has high levels of collagen and expresses numerous HCN channels, as does the central SAN.[12] Additionally, CT is considered to be the functional extension of the SAN, as an extension of the SAN complex [13,14,15]. Consequently, the area functions as a pacemaker zone when the leading pacemaker shifts from the failed central SAN during SSS.[16,17] The tissue in this area exhibits spontaneous pacemaker activity, with similar APs to that in the SAN (the maximum depolarisation rate and maximum diastolic potential are low, diastolic depolarisation slope).[18,19,20]

The present study aims to investigate the viability of substitute non-HCN gene targets to support bio-pacemaker treatment of SSS (NCX, TBX3 and TBX18). The study also assesses whether the chosen gene meets the primary target of rate acceleration, and examines bio-pacemaker physiology to inform treatment efforts for a broad spectrum of SAN dysfunction, not just bradycardia.

7.2 Methods

7.2.1 Experimental methods

7.2.1.1 Ethical approval, tissue culture and classification of spontaneous pacing behaviour

In this study we used eight-week-old male Wistar-Hannover rats, with weights in the range 300-350g. They had free access to food and water. A Schedule 1 procedure (concussion and cervical dislocation) was used to euthanise animals humanely, in compliance with Home Office provisions laid out under the Animals Act 1986 pursuant to the licence held by the University of Manchester. The rats were not anaesthetised as this was unnecessary.

Isolation of the SAN tissue and preparation of the subsidiary atrial pacemaker tissue **(**SAP) tissue, has been explained in previous work by Morris *et al.* (2013).[12] The SAN tissue sample was prepared by dissection of the entire right atrium (RA), which was immersed in sterile Tyrode solution at 37°C, after which the SAN was isolated. The SAN was opened along the anterior superior vena cava and anterior atrial wall to maintain the integrity of the posterior intercaval area. Morris *et al.* (2013) [12] have previously described the procedure of separating the SAP tissue. The SAP tissue was isolated by dissecting the RA tissue horizontally at the level of the fossa ovalis and removing the superior section along with the atrioventricular node.[12] Tissue culturing was performed in Advanced Dulbecco's Modified Eagle's Medium/Ham's F-12 (DMEM/F12, Thermo Fisher Scientific, Waltham, MA, USA) enhanced with 10% foetal bovine serum (Thermo Fisher Scientific), and penicillin, 500 units/ml (Sigma-Aldrich, St Louis, MO, USA); streptomycin, 0.5 mg/ml (Sigma-Aldrich); l-glutamine, 2 mM (Sigma-Aldrich). The tissue culture was prepared in a centrifuging system that was custom-prepared to maintain the sterile solution at optimum temperature and pH (37°C and pH 7.4 respectively). Two 0.22mm stainless-steel electrodes were used to record bipolar extracellular potentials, with use of a Powerlab amplifier and filter system with Labchart software (AD Instruments, Sydney, Australia) at a trial rate of 10 kHz.

To measure the influence of the target gene on the rate of pacing, we recorded the average of the spontaneous pacing rate within 46- 48h of culturing. The initial 12h (i.e. before expected major transgene expression) was employed as a control period to guarantee that the arrangements of the SAP samples posted comparable initial rates. Studies have associated SSS with unstable pacing rate, which manifests in the form of sinus pauses and paroxysmal bradycardia. To measure pacemaker stability during the 46-48h period in culture, the standard deviation of RR intervals (SDRR) and root mean square of consecutive variations in RR intervals (RMSDD) were recorded. A Poincaré plot (RR[n] vs. RR[n+1]) was drawn up for each tissue sample. The SD1 of the Poincaré sections was calculated (SDs of points vertical to the line of identity of the Poincaré curve), and the plotted curves were categorised into those that showed ectopic activity and those that did not, based upon visual inspection.

The effect on the pacing rate was measured at presence of β-adrenergic stimulation by isoprenaline (ISO) at 0.05μM (Sigma-Aldrich), and of I_f blockade, using a 2 mM of

CsCl (Sigma-Aldrich). In a separate experiment, we delivered the overdrive pacing through a coaxial stimulator electrode (Harvard Apparatus, Holliston, MA, USA) while using 3x2 min pacing trains to deliver 75% of the spontaneous cycle length for each sample. With voltage amplitude of 1.5x and pacing pulse width was 2ms. To obtain the corrected recovery time (cRT), the deffrence between recovery time (timed from the last paced heart beat to the next spontaneous beat) and the spontaneous cycle length were calculated. Given that previous work had shown that untreated SAP tissue preparation was used for the control rate,[12] which is not affected by adenovirus-carrying non-functional ion-channel protein or by green fluorescent protein (GFP),

7.2.2 Recombinant adenoviruses

Prof. Godfrey Smith kindly provided this study with recombinant adenoviruses Ad-TBX18, Ad-TBX3 (ABM Good), and Ad-NCX1-GFP, which were then amplified by passage through a filter-based AdEasy virus purification kit (Agilent Technologies, Santa Clara, CA, USA). A calibrated syringe (Nanofil, WPI, Sarasota, FL, USA) was used to deliver 1–2 μl of pre-heated (37°C) adenovirus through a 35G needle into the superior cut section of the CT in the SAP samples, to inject $\sim 1 \times 10^7$ pfu.[12]

7.2.3 PCR

Biopsy samples measuring 2mm were obtained and snap frozen after 48h of tissue culturing from (1) SAN samples, at the section where the SAN was situated; (2) SAP samples, at the inferior CT target area; and (3) the adenovirus-injected SAP samples, at the area of injection. MirVana kit was used to obtain RNA, which was treated with Turbo DNase. The SuperScript VILO Master Mix Kit was used to reverse transcribe total RNA to cDNA, and RNA concentration was recorded using a Nanodrop spectrophotometer. SYBT Green fluorescent probe assays were used to perform quantitative polymerase chain reactions (qPCR) in 96-well plates. Each reaction was performed in triplicate. The ΔC_t method was used to calculate transcript expression levels; data shown in graphs represent ΔC_t values. To measure the ratio of the abundant mRNA between the gene of interest and a housekeeping gene, *18S*, for each reaction, the following calculation was applied: (reaction efficiency) $^{C\,t}$ for 18S/ (reaction efficiency)$^{C\,t}$ for target gene.

7.2.4 Biophysically detailed computer modelling

7.2.4.1 Model development

To investigate the effect of alterations the expression of the HCN channels on cardiac electrical activity in SAP and SAP-TBX18 conditions, a mathematical model, developed by Kharche *et al.* (2011) [21], was used for simulation in this study. This model described the electrophysiological behaviour of the mouse SAN cell by a differential equation, as shown in Eq (7.1). Here V_m is the membrane potential (in mV), t is the time (in s), C_m is the cell capacitance per unit surface area (in 28pF), and I_{tot} is the sum of all transmembrane ionic currents (in pA) given by the Eq (7.2):

$$\frac{dV_m}{dt} = -\frac{1}{C_m} I_{tot} \tag{7.1}$$

$$I_{tot} = (I_{Na1.1} + I_{Na1.5}\, I_{Ca,T3.1} + I_{Ca,L1.2} + I_{Ca,L1.3} + I_{Kr} + I_{Ks} + I_{st} + I_{sus} + I_{to} + I_f + I_{b,Na} + I_{NaCa}) \tag{7.2}$$

The main goal of our simulation was to investigate how the pacemaking AP morphology and its characteristics were affected by the changes in the abundance of HCN. As demonstrated above, in the Kharche model the pacemaking current I_f is characterised as a single current.[21] This was modified based on available experimental data for a whole-cell patch clamp, to incorporate the three cardiac HCN isoforms 1, 2 and 4 (see Table7.1 and Figure7.1).[22] The model was adapted to include an isoform-specific I_f, consisting of $I_{f,HCN1}$, $I_{f,HCN2}$, and $I_{f,HCN4}$, each of which took into account the channel permeability to Na^+ and K^+ ions. The newly updated I_f can be represented as:

$$I_{f,HCN1} = I_{fK,HCN1} + I_{fNa,HCN1} \tag{7.3}$$

$$I_{f,HCN2} = I_{fK,HCN2} + I_{fNa,HCN2} \tag{7.4}$$

$$I_{f,HCN4} = I_{fK,HCN4} + I_{fNa,HCN4} \tag{7.5}$$

$$I_f = I_{f,HCN1} + I_{f,HCN2} + I_{f,HCN4} \tag{7.6}$$

Zong *et al.* [22] reported that the biophysical properties of the individual HCN1, HCN2, and HCN4 isoforms, coding I_f channels, were distinct from each other. The activation midpoint ($V_{0.5}$) for individual isoforms was determined and was found to vary between

isoforms (Table 7.1 below). HCN1 exhibited a more positive $V_{0.5}$ than HCN2 and HCN4. Based on these experimental characteristics, the activation midpoints for all isoforms were incorporated into the mouse SAN model as: −91.2 mV for $I_{f,HCN4}$; −92.0 mV for $I_{f,HCN2}$; and −75.2 mV for $I_{f,HCN1}$ (see Figure 7.1A). The activation time constants for HCN channels were also modified in this model, according to the parameters outlined by experimental measurements taken from Herrmann *et al.* [23] (Figure 7.1B). These experimental results showed various voltage-dependent time kinetics for individual HCN-channel isoforms. Figures 7.1C and D summarise the activation-midpoint and time-constant values used in the simulation. The incorporated formulation parameters employed for I_f were used in the simulation and validated by quantitative comparison of the simulated I–V relationship with experimental data.[23-26] (Figure 7.2A). The relative contributions of HCN1, HCN2 and HCN4 to the total I_f were calculated in this model, dependent on the relative maximal conductance of each channel according to experimental mRNA data for $g_{f,HCN1}$: $g_{f,HCN2}$: $g_{f,HCN4}$ in the proportions 3:1:6., in which the largest proportion is attributed to $g_{f,HCN4}$ (Figure 7.2B).

Table 7.1 The electrophysiological properties of individual HCN-channel isoforms, from Zong *et al.* [22]

HCN isoform	$V_{0.5}$ (mV)	Slope factor *k*	Relative contribution of each HCN isoform to total I_f
HCN1	-75.0	11.2	3
HCN2	-92.2	10.5	1
HCN4	-91.0	15.5	6

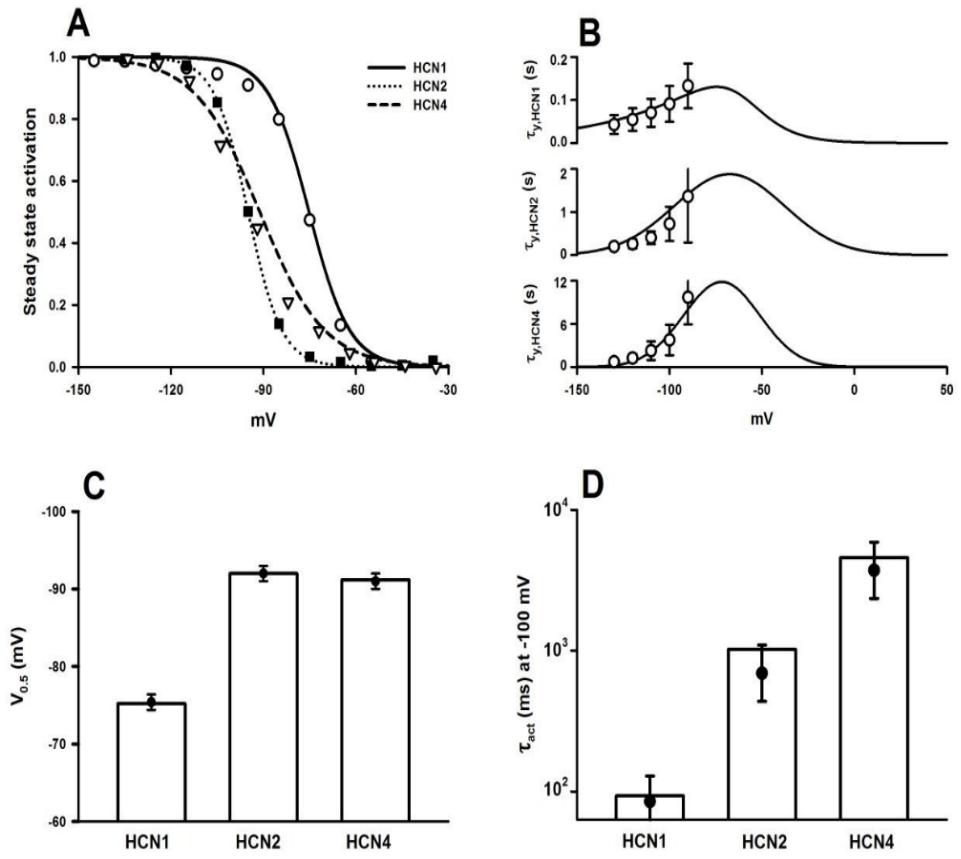

Figure 7.1. A summary of activation kinetics for three HCN isoforms. (A) Simulated steady state of the activation curve for different HCN channels; (solid, dotted, and dash lines), the data obtained for different HCN channels from Zong *et al.* [22] (open circles, triangles and filled squares); (B) Time constants curves for three isoform of HCN channels, taken from experimental data in Herrmann *et al.* [23]; (C) Bar charts illustrates the simulated activation midpoints of three HCN channels,plotted with the experimental data from Zong *et al.*[22] in error bars; (D) Bar charts show the time constants τ_{act} at -100 mV in simulation plotted with experimental data from Herrmann *et al.* [23], figure adapted from [26]

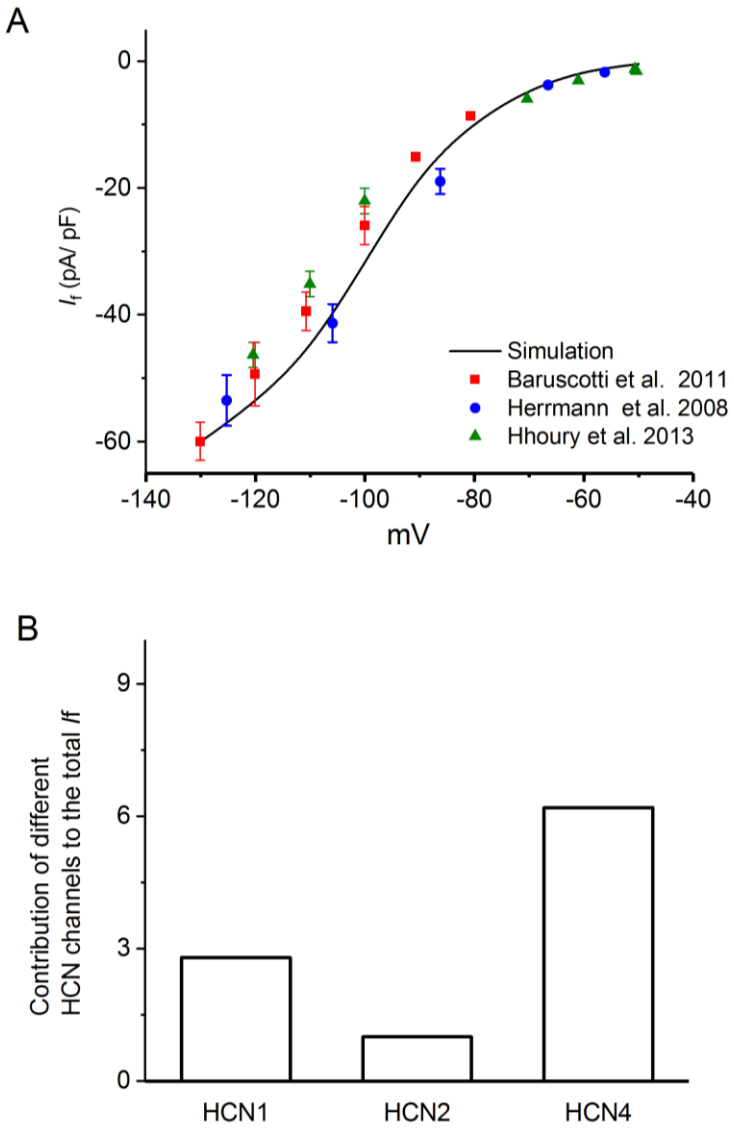

Figure 7.2 (A) I-V curve relationships for total I_f; solid line shows simulated current-voltage curve, while circles, squares, and triangles show experimental data from Baruscotti *et al* [27], Herrmann *et al.* [23], and El Khoury *et al.* [25] (B) The relative contribution of different HCN channels to the total I_f.

7.2.4.2 Modelling of the HCN-abandance in SAP and SAP-TBX18 conditions

The aim of the simulation was to assess the effect of predicted changes in I_f on the pacemaker-rate activities for each preparation (SAN, SAP and SAP-TBX18), based on measuring the abundances of HCN isoform in gene expression mRNA. During our experiments, we recorded the abundance of mRNA for all three HCN isoforms relative to the total I_f in normal SAN. The ratios of HCN1, HCN2 and HCN4 to the total HCN,

in normal SAN, were adjusted in the mouse SAN model based on our experimental findings, to the approximation of 0.6:1.4:8. Based on this ratio, HCN4 was still the main contributor to the total I_f, accounting for approximately 80% of the current. This was confirmed experimentally by previous research from Hoesl *et al.* [2] and Baruscotti *et al.* [4]. This method does not aim to generate definitive, biophysically detailed AP models, but it is a form of bioinformatics to explore the possible consequences of changes in transcript levels.

In order to simulate SAP and SAP-TBX18 conditions, the ratio of the gene expression of mRNA in each preparation relative to that in normal SAN was applied to the I_f in each case. This was represented as a blockage of total I_f in SAP and SAP-TBX18 of 76% and 45% respectively, and was applied by modification of the maximal conductance values for total I_f. The incorporated changes were validated by quantitative comparison of the characteristics of the simulated APs and I_f currents in both SAP and SAP-TBX18 conditions and of the APs in SAN. This is shown in the results section

7.3. Results

7.3.1 Impact of transgene expression on spontaneous pacemaker rate

Tissue samples were kept in culture for 48h and analysis of pre-determined beating heart rate was performed at between 46h and 48h, as shown in Figure 7.3. It was expected that direct expression of transgenes would show psychological effect on pacing within 24h[12], while it was predicted that the effect of transcription factors : TBX18 and TBX3 on pacing would be seen after at least 36h. [9] In the last 2h of culture, the un-injected SAP samples (n=14) were moderately bradycardic; SAP preparations showed a significantly slower rate (144.1 ± 8.6bpm, $P < 0.01$) when compared with that of the SAN preparations (n=15) (267.5 ± 13.6bpm, $P < 0.01$). The pacemaking record of the SAN, as seen in Figures 7.3A-E and F, showed a significantly faster rate across all points compared with that in SAP preparations.

Recombinant adenovirus was injected into SAP samples in the area close to the inferior projection of the CT that contained the bradycardic pacemaker tissue in position. [12] Figures 7.3 B shows that the beating rate of SAP-TBX18 from uninfected SAP tissue followed a divergent curve compared with those of SAN and SAP after 20h of culture, and the rate showed a significant statistic change by 44h. The results shown in Figure

7.3C- D indicate that the injection of SAP samples with Ad-TBX3 or Ad-NCX did not significantly affect the rate compared with untreated SAP, and during the control period(see Figure 7.3E), there were no significant changes in the rate for either SAP (225.2± 19.4 bpm) or SAP-TBX18 (247.8±15.7 bpm). Of all the treated SAP samples at the final analysis within 46h to 48 h (see Figure 7.3F) only the rate observed in SAP-TBX18 samples was significantly faster than that of the untreated SAP tissue (214.4 ± 14.4 vs. 144.1 ± 8.6 bpm, $P < 0.01$, Figure 7.3F). Thus, SAP-TBX18 preparations were selected for more detailed characterisation. qPCR was used to validate the expressions of TBX3 and TBX18 (Figures 7.3 G and H). There was a notable rise in mRNA abundance of the two gene targets when between treated and untreated preparations were compared. We also used confocal microscop to aquire a visual validation of NCX1 expression through bicistronic green fluorescent protein (GFP) expression. Solid signal was seen only in treated preparations (Data is not shown).

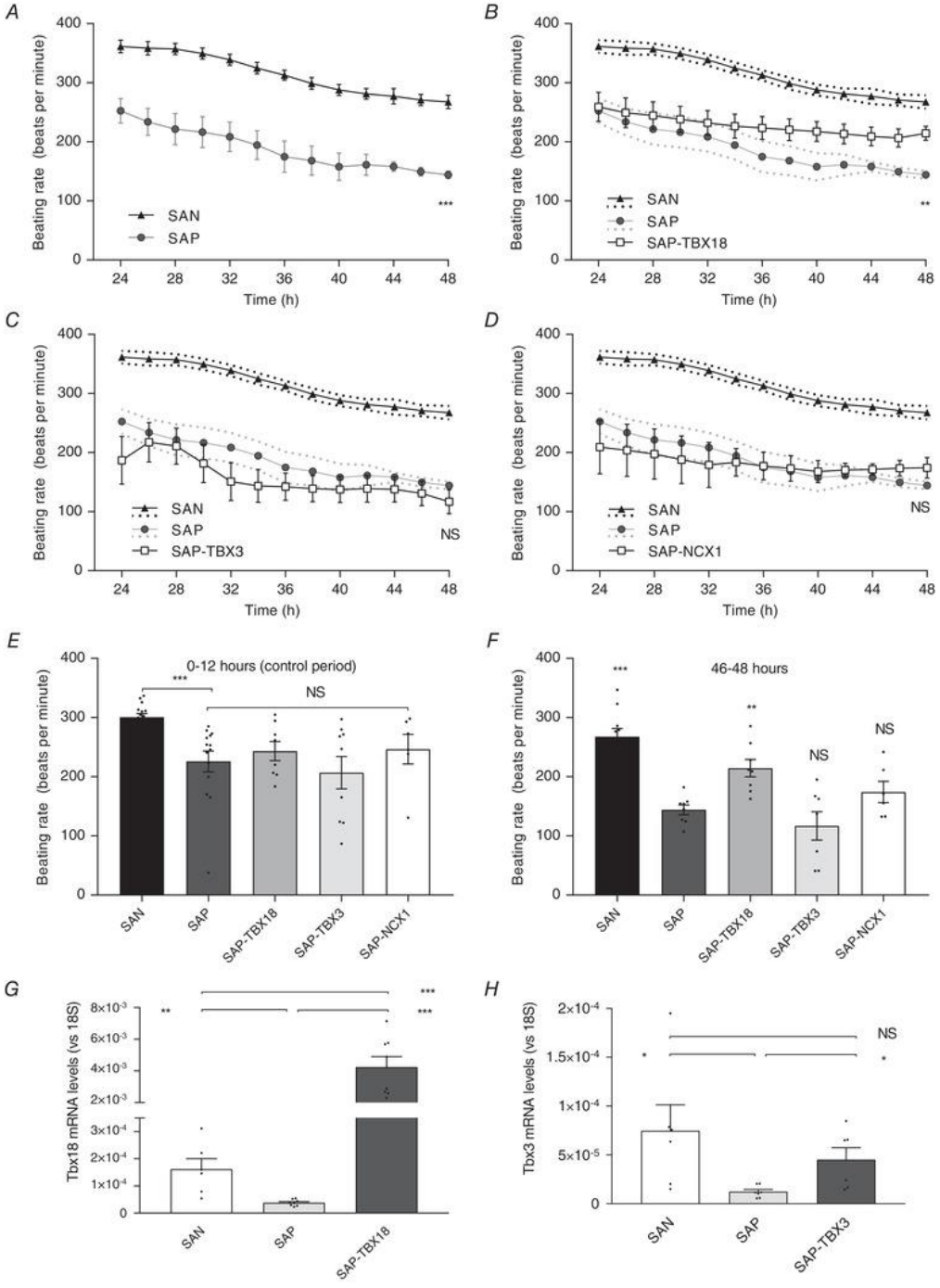

Figure 7.3 Increases of beating rates in SAN and SAP preparations resulting from adenovirus-mediated expression of TBX18, but not NCX or TBX3. (A) Uninfected SAP samples illustrate significantly slower beating rates than the SAN. (B) After 20h of culture, the beating rates of SAP-TBX18 samples diverged from those of uninfected SAP tissue and were significantly faster than those of the SAP at the final analysis as shown in panel (F). (C D) Injection of the SAP preparation with Ad-TBX3 or Ad-NCX1-GFP had no significant effect on the beating rate. (E) During the control period (0-12h) the beating rates were not significantly different. Statistical significance in panels A–D show the pre-specified comparison between beating rates in treated and untreated SAP during the final 2h. (E, F) Statistical significance comparison of the beating rates in untreated SAP preparations. (G, H)

The mRNA expressions of TBX18 and TBX3 through the qPCR method showed notable up-regulation in treated SAP preparations. Comparison results were conducted in SAN preparations. **Note:** n = 15 for SAN; n = 14 for SAP; n = 8 for SAP-TBX1; n = 9 for SAP-TBX3; n = 6 for SAP-NCX1; NS means not significant; $**P < 0.01$; $***P < 0.001$.

7.3.2. Impact of transgene expression on pacemaker stability

SSS displays bradycardia feature in addition to an instability of beating rate, which manifested as pauses and atrial arrhythmia.[14] Heart-rate variability (HRV) was used to analyse pacing behaviour between 46h and 48h to measure rate stability in: SAN (n=10); SAP-TBX18 (n=8); and SAP (n=14). It was found that, for these *ex vivo* experiments, low HRV, in the absence of autonomic input, indicated stable pacemaker activity. SAP-TBX18 showed improved parameters of rate stability when compared with untreated SAP: the standard deviation of beat-to-beat interval (SDRR) dropped from 39.3 ± 7.2ms in SAP to 6.9 ± 0.8ms in SAP-TBX18($P < 0.01$, Figure 7.4A), and root mean square of successive beat-to-beat intervals (RMSSD) dropped from 41.7 ± 8.2ms to 6.1 ± 1.2ms ($P < 0.01$, Figure 7.4B). The SD1 of the Poincaré plot dropped from 29.5 ± 5.8ms to 7.9 ± 2.0ms ($P < 0.01$, Figure7.4C). The Poincaré plots represented short RR intervals and pauses that appeared as outlying clusters in 25% of SAP-TBX18 and 57% of untreated SAP preparations (Figure 7.4D). Short RR coupling resulted in ectopic beats or may have represented early primary pacemaker firing. Note that preparation of an activation map was not possible to perform and confirm the origin of these beats, but changes in morphology was demonstrated from the SAN in the raw signal data. This can be seen in Figure 7.4Ea, which shows a different amplitude or axis, implying that they were likely to result from variant focus. Figures7.4E-G illustrate representative traces of stable and unstable rate characteristics, as well as representative Poincaréplots.

7.3.3. Impact of transgene expression on pacemaker physiology

The β-adrenergic receptiveness was assessed through use of isoprenaline (ISO) for each preparation. When compared with SAN samples, the SAP model showed reduced sensitivity (acceleration rate of 69.5% ± 12.6% in SAN vs. 27.8% ± 2.9% in SAP-TBX18, $P < 0.05$). For the SAP-TBX18 samples, the ISO reaction was restored

(acceleration rate of 121.3% ± 4.2% vs. rate in SAP of 27.8% ± 2.9%, $P < 0.001$). The typical SAN can display very little overdrive suspension in reaction to rapid pacing, whereas different pacemaker tissues as subsidiary Purkinje fibres may cause a prolongation of suppression in pacemaker activity after periods of overdrive pacing, as is the case with a disease of SAN. [28,29] The response of the tissue samples to overdrive pacing was analysed. The measured cRT of the SAP preparations was significantly longer than that of the normal SAN (124.6ms ± 10.1ms vs. 77.3ms ± 9.5ms, respectively, $P< 0.01$), whereas the TBX18 did not show any effect on the cRT in comparison with untreated SAP (140.0ms ± 23.1ms vs. 124.6ms ± 10.1ms, respectively, NS).

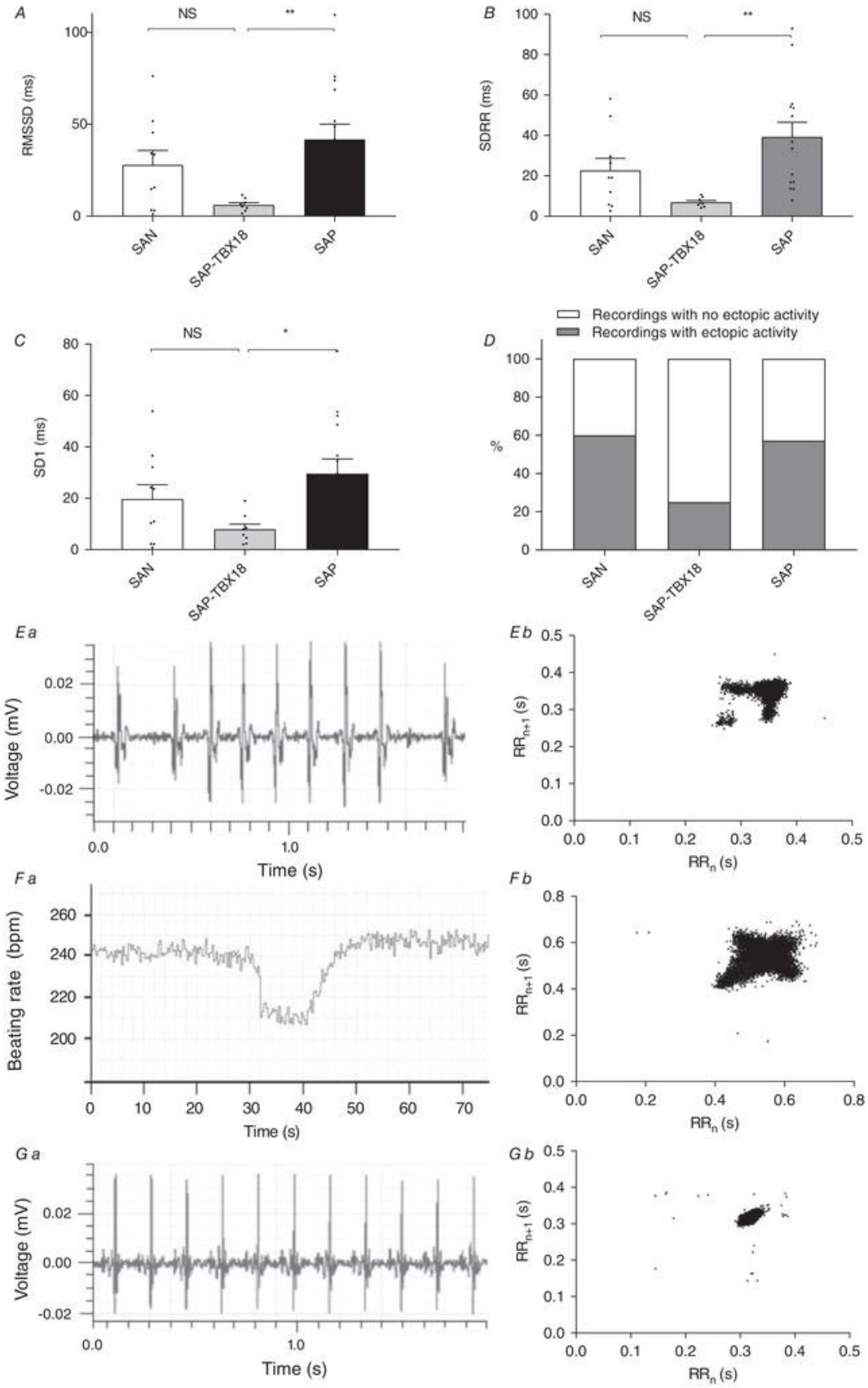

Figure 7.4 TBX18 enhances heart-rate stability in the SAP preparations. (A–C) Heart-rate stability improves in the SAP model due to TBX18 injection. (D) There is a significant improvement in all measures of heart-rate stability in SAP-TBX18

compared with those in untreated SAP. Poincaré plots post fewer clusters of pauses or widespread short-coupled RR intervals in SAP-TBX18 samples, although this data did not reach statistical significance. The premature beats recorded, as seen in *Eb,* show change in morphology that implies an ectopic focus of origin. (E) Examples of heart-rate behaviour in the SAN; (Ea) Example of measured extracellular potential from SAN preparation, showing the rate instability with sudden changes in RR intervals; (Eb) Sample Poincaré plot from SAN sample that depicts an unstable heart rate with high SD1 and outlying clusters that represent pauses and short RR intervals. (F) Example of SAP tissue that show unstable heart-rate behaviour; (Fa) RR plot from a SAP sample showing a beating rate instability with sudden heart-rate decelerations; (Fb) Poincaré plot from a SAP sample that shows unstable heart rate with high SD1 and without outlying clusters. (G) The measurement of heart-rate stability and behaviour in SAP-TBX18 preparations; (Ga) The recorded extracellular potential from a SAP-TBX18 sample that displays steady heart rate with slight variation in RR intervals; (Gb) Poincaré plot from a SAP-TBX18 sample showing a stable beating rate with low SD1 and no outlying clusters. n = 10 for SAN; n = 14 for SAP; n = 8 for SAP-TBX18; NS, not significant; $*P < 0.05$; $**P < 0.01$.

7.3.4. Impact of TBX18 on gene expression in the subsidiary pacemaker section,SAP

After 48h of culture we assessed mRNA levels using the reverse transcription RT-qPCR method (n = 8 replicates per condition). As demonstrated above, there was a notable positive chronotropic effect of TBX18 on the pacemaker activity of SAP tissue, and therefore, measurement of HCN channel expression was required in SAP samples to compare the measurement with that obtained from SAN preparations. HCN channels code for the hyperpolarisation-activated current, I_f, a vital pacemaker current. [1] The TBX18-treated SAP tissue displayed a switch of the dominant HCN isoform with a notable up-regulation of HCN2 from $1.0\times10^{-5}\pm2.2\times10^{-6}$ to $2.8\times10^{-5}\pm4.3\times10^{-6}$ (Figure 7.5A, $P<0.01$). There was a tendency towards up-regulation of HCN1, but this remained statistically insignificant (Figure 7.5B, $P = 0.076$). The HCN4 isoform displayed the largest abundance of HCN channels in SAN (Figure 7.5C, $P < 0.001$). Using abundance of HCN4 as the point of reference, the ratios of the HCN isoforms (HCN4/HCN1/HCN2 respectively) were: 1.00/0.07/0.17 for SAN; 1.00/0.97/2.07 for SAP; 1.00/3.30/11.50 for SAP-TBX18. Figures 7.5 D– F, $P < 0.001$, indicate ratios of isoform expression across the three groups by chi-squared.

The effect of TBX18 on expression on transcripts in the SAP was evaluated, as it is known to be vital for normal function of SAN. The ryanodine receptor, RYR2, is partly

responsible for pacemaking through the SAN Ca^{2+} clock. [1] Presence of TBX18 displayed a significant up-regulation of the RYR2 level, while TBX18 expression had no effect on levels of other SAN pacemaker clock components or of the connexins (gap junction proteins) Cx43 and Cx45 (Figure 7.6).

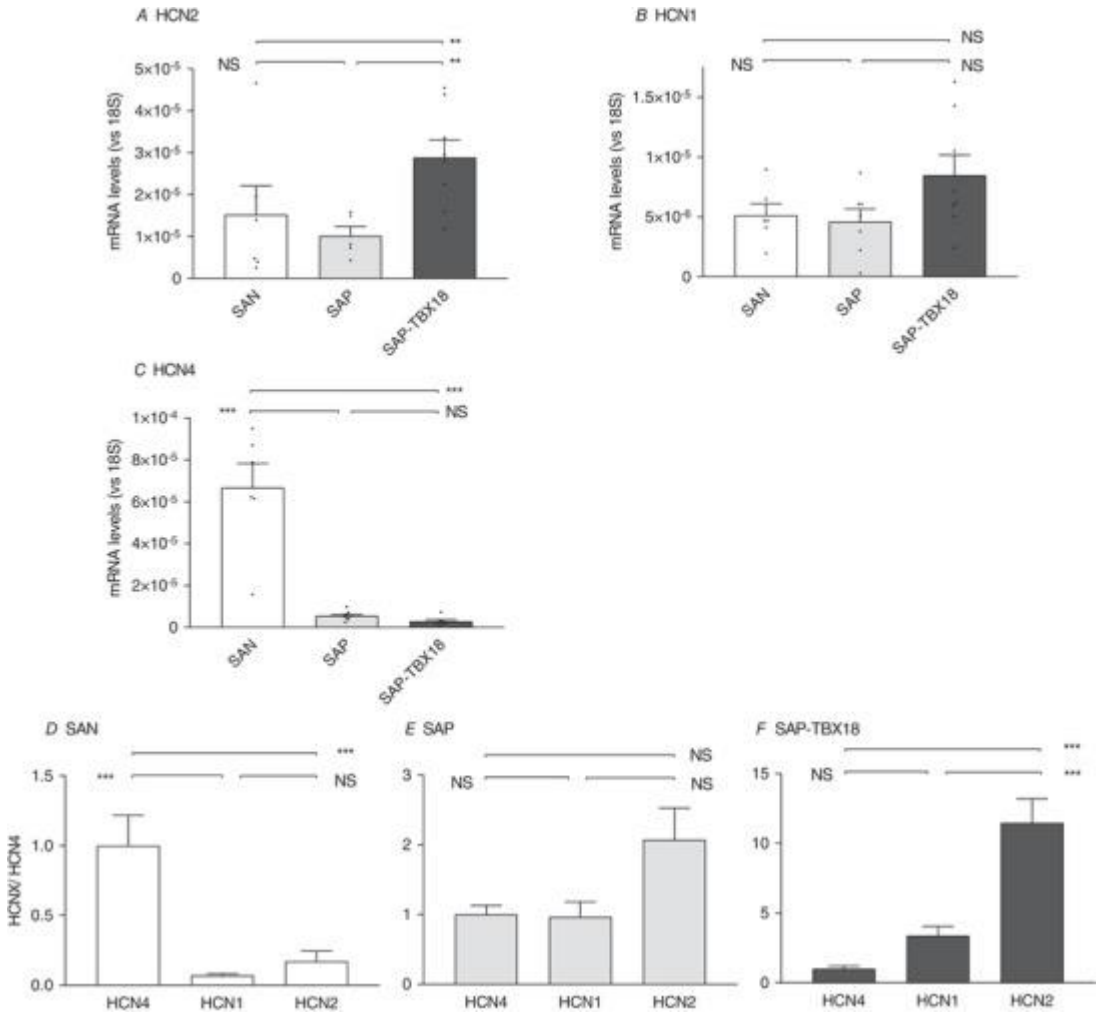

Figure 7.5 A comparison of HCN isoforms through measurement of mRNA levels**.** **(**A-C) Comparative abundances of HCN transcripts as recorded by qPCR in the SAN, SAP, and SAP-TBX18 preparations. (D-F) The calculated ratios of HCN channels in SAN, SAP and SAP-TBX18. Levels are displayed relative to HCN4, the most recurring isoform in the SAN. TBX18 results in a change in the relative mRNA level of the isoforms in the SAP sample with a significant up-regulation of HCN2 in comparison with the untreated SAP. SAP, n = 8; SAN, n = 8; SAP-TBX18, n = 8. NS, not significant. * $P < 0.05$; ** $P < 0.01$; ** $P < 0.001$. Individual data points are plotted as dots in bar graphs.

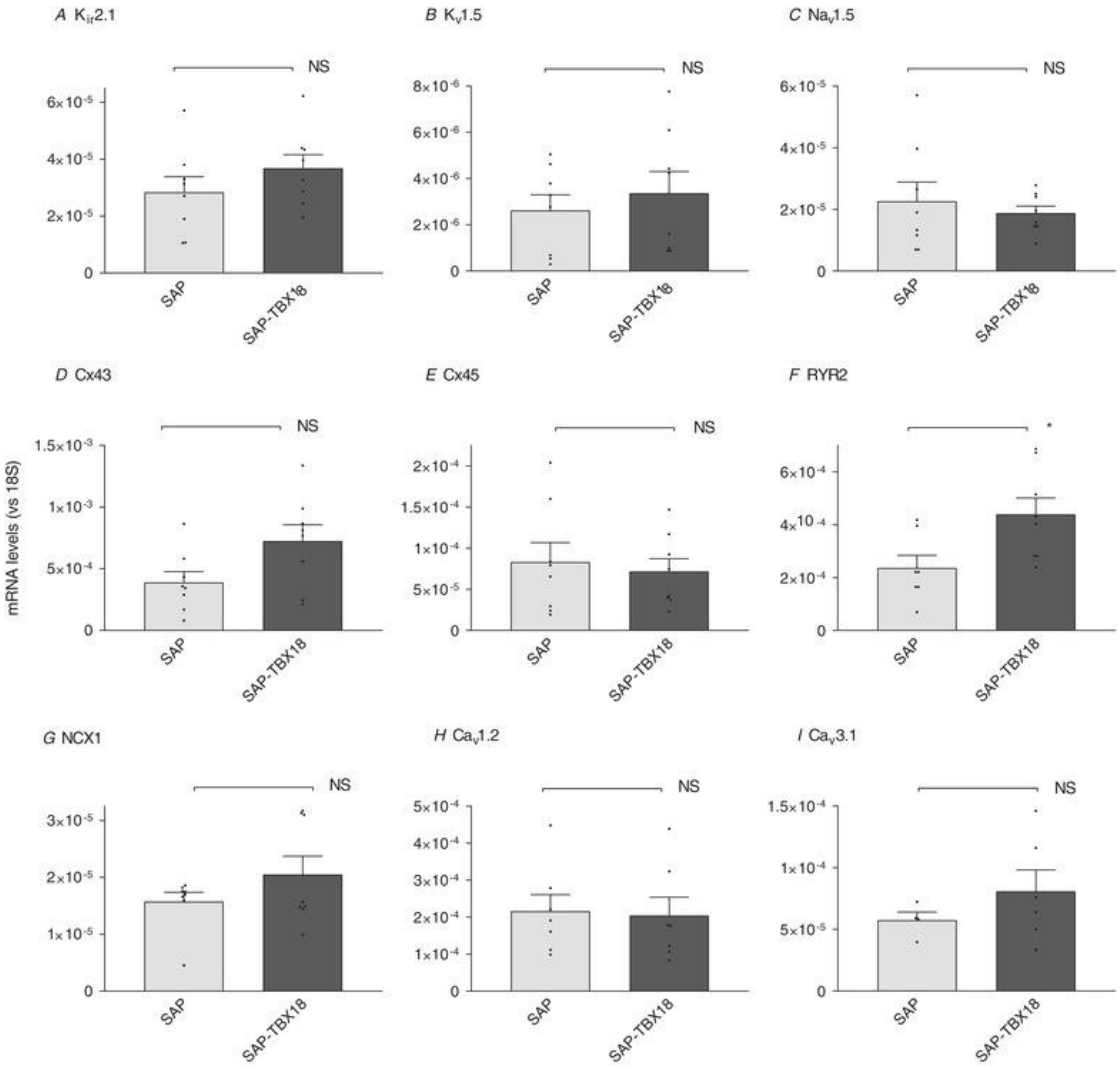

Figure 7.6 qPCR records of relative abundance of further ion channels that is related to the normal SAN, SAP and SAP-TBX18. Only RYR2 posted a notable rise in SAP-TBX18 compared with untreated SAP. The other measured genes remained largely unchanged. SAN, n = 8; SAP, n = 8; SAP-TBX18, n = 8. NS, not significant; * P<0.05.

7.3.5 Simulation of the effect of up-regulation of HCN channels on heart-beat rates

A detailed computer model of the SAN was used to assess whether changes in measured HCN mRNA abundances could be correlated with observed changes in the heart-beat rates, based on the assumption that the changes in mRNA were correlated with changes in protein and were directly attributable to the changes in I_f.

Our results confirmed that the raise of pacemaker rate that seen in SAP-TBX18 condition was primarily resulted from the observed up-regulation of HCN channels and therefore, increases in I_f. Figure 7.7 illustrates the simulated APs of SAN according to the measured HCN mRNA abundances. In the case of the SAP model, the simulated APs and I_f are represented in Figure 7.7Aa and compared with the SAN. The diastolic depolarisation rate (DD) in SAP was also smaller than that found in the SAN (0.17 V/s compared with 0.23 V/s). In the SAP preparation, the computed cycle length (CL) was grater by 16.5% compared to SAN, manifesting as a reduction in beat rate (265.3 bpm for SAP versus 306 bpm for SAN) (see Figure 7.9 and Table 7.2). Similarly, the simulated APs for SAP-TBX18 preparations in comparison with those of the SAN are shown in Figure 7.7Ba-b, with simulated I_f density. Simulating SAP-TBX18 condition has shown the DD slop has a greater value (0.2 V/s) compared with that in the SAP condition (0.17V/s). The computed CL value of the AP in the SAP-TBX18 preparations has smaller values (206.99ms) compared with SAP preparations(227.27ms), manifesting a restoring of the beating rate compared with that of the SAP (288bpm for SAP-TBX18 versus 264.8bpm for SAP).However, the simulated rate observed in the SAP-TBX18 was smaller than that seen in the SAN (308 bpm) (Figure 7.9 and Table 7.2).

We conducted a further simulation to include the effect of the increased RYR2 mRNA abundance found in the SAP-TBX18 model in addition to the increase in HCN abundances. The results showed a small effect on pacing, manifesting as an increase in the simulated beating rate to 298.5 bpm (Figures 7.9 and 7.10). These obtained data were qualitatively in agreement with the observed changes in beating rates shown in Figure 7.3. The SAN exhibited the fastest beating rate at 267.5±13.6 bpm, and the significant bradycardia of the SAP (144.1±8.6 bpm) was increased to 214.4±14.4 bpm by TBX18 expression. Note that this improved rate was still slower than the SAN rate.

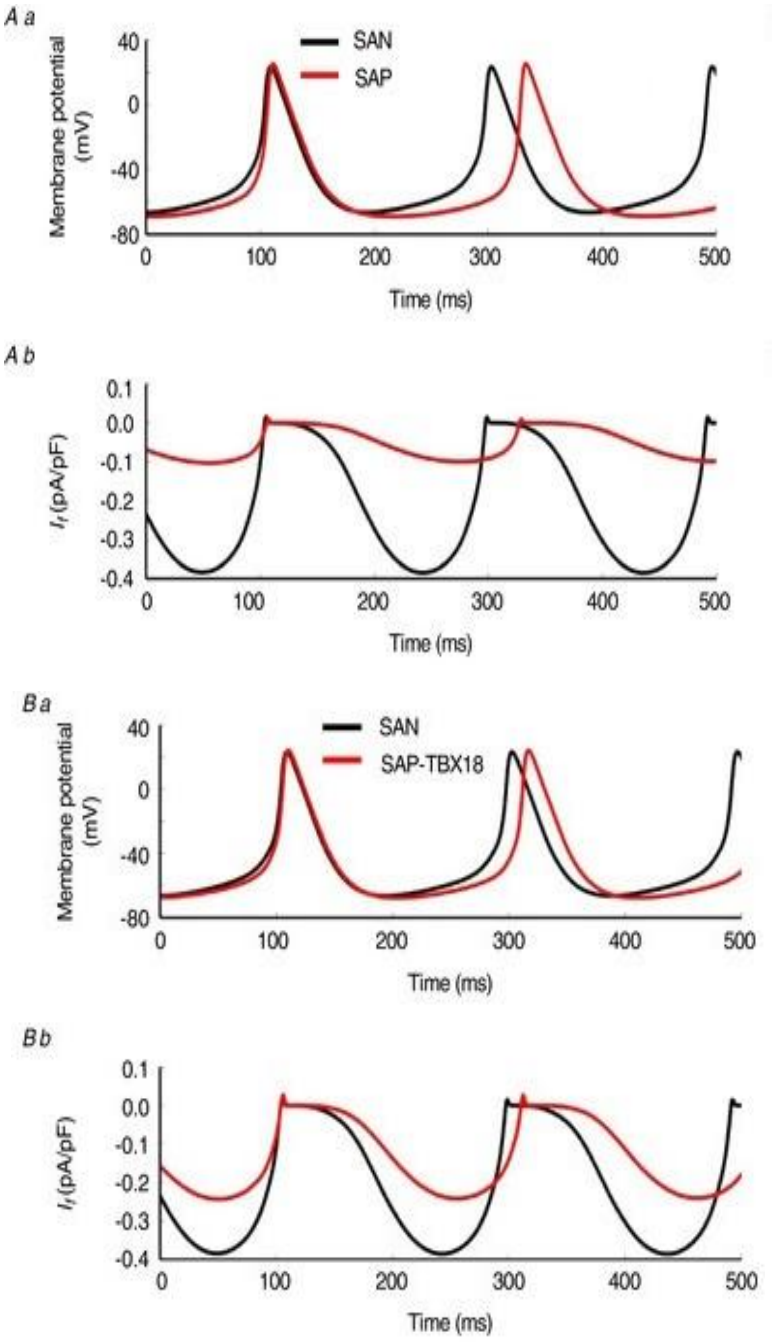

Figure 7.7 Simulation based on observed changed HCN mRNA abundances. Generated action potentials (Aa-Ba) and I_f (Ab-Bb) in SAP, and SAP-TBX18, respictvely. Simulation of the SAP and SAP-TBX18 were represented in (red lines) and compared with the SAN (black lines)

Table 7.2 Characteristics of simulated APs from SAN, SAP, and SAP-TBX18.

	SAN	SAP	SAP-TBX18
CL(ms)	194.32	227.27	206.99
MDP (mV)	-66.31	-68.7	-67.27
DD slop (V/s)	0.23	0.17	0.2
APD_{90} (ms)	56.45	61.42	58.29
TOP(Mv)	-46.65	-51.98	-49.85

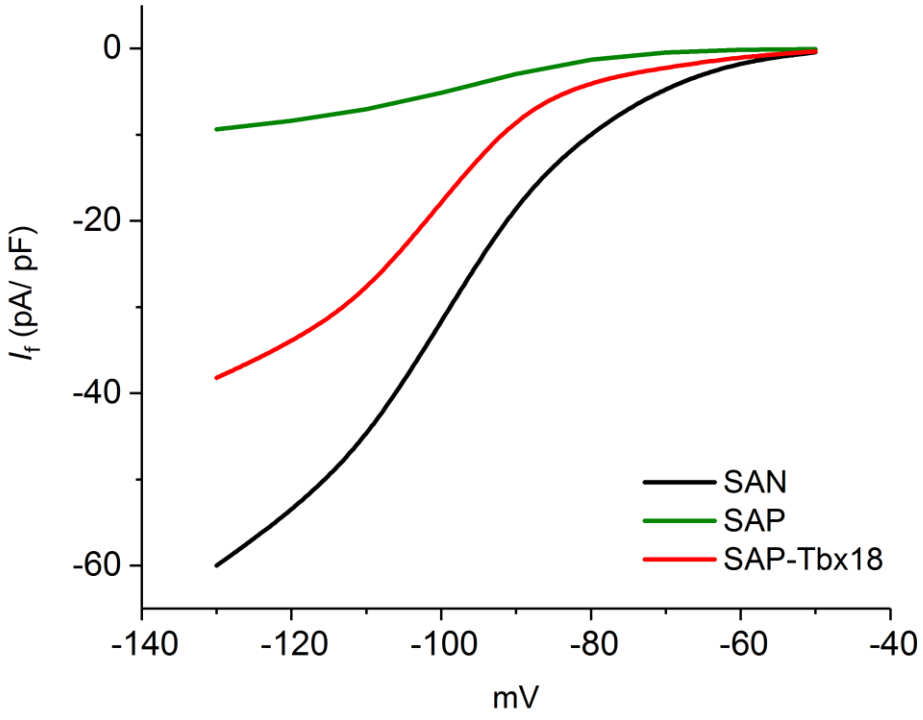

Figure 7.8 I–V relationship curves for I_f in normal SAN (black), SAP-TBX18 (red), and SAP (green).

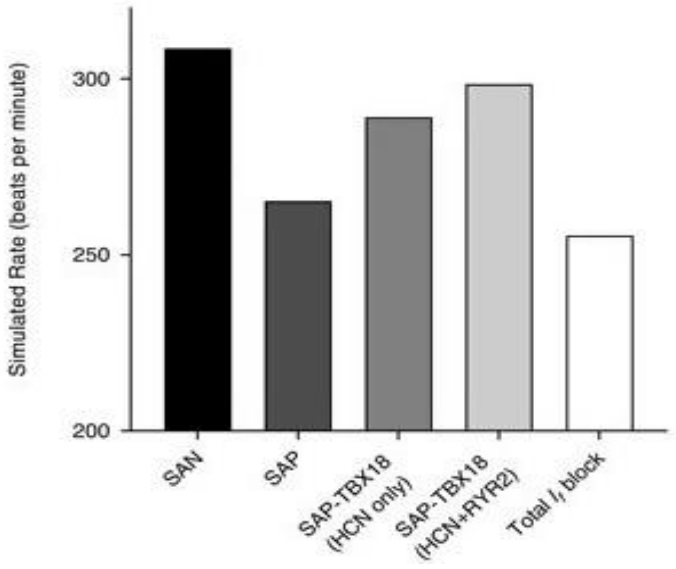

Figure 7.9 Simulated heartbeats are represented in different condition SAN; SAP; SAP-TBX18 (HCN only) in which the simulation shows only the alterations of HCN channels; and SAP-TBX18 (HCN+RYR2) in which the simulation shows the changes to HCN channel levels and RYR2 levels.

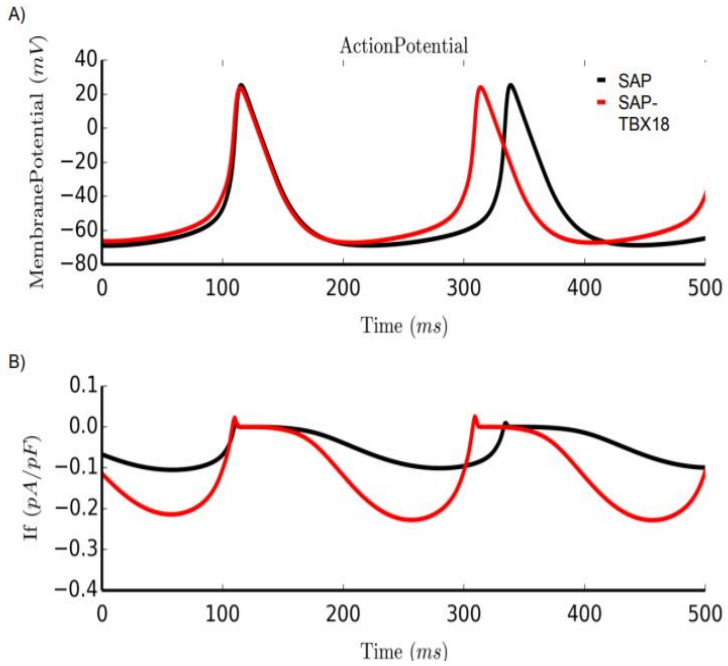

Figure 7.10 Simulated action potentials (A) and simulated I_f (B) for the SAP (black lines) and SAP-TBX18 (red), incorporating the measured abundances of RYR2 and HCN isoforms 1,2 and 4.

7.4. Discussion

7.4.1 Summary of main results

In this study three non-HCN-based strategies for bio-pacemaking in SSS were screend, using SAP from the inferior section of the sinoatrial node pacemaker complex. TBX3 and NCX1 failed to lead to the main goal of heart-rate acceleration. There is proof of concept with regard to the use of TBX18 over-expression as a bio-pacemaker treatment strategy for SSS. The Ad-TBX18 infected SAP demonstrated remarkable accelerated spontaneous pacing rate. Additionally, an improvement of heart-rate stability and heart-rate reaction to ISO was restored. These developments would be valuable in treating clinical SSS, which includes sinus pauses chronotropic incompetence, and bradycardia. The results were largely facilitated by TBX18 regulation of HCN2 and an overall increase in HCN-channel abundance; up-regulation of RYR2 was also witnessed. Biophysically computer simulation demonstrated that the observed effect on spontaneous pacing rates could be attributed to changes in HCN channel abundance. Up-regulation of RYR2 is has a small affect on the rate of acceleration.

7.4.2 Impact of TBX18 on gene expression in the SAP

Expression of TBX18 proved to be a reliable bio-pacemaker strategy; TBX18-induced improvement of the pacemaker function in the SAP sample was primarily triggered by an upregulation in the total abundance of HCN channels, mostly the HCN2 isoform, in addition to the up-regulation of RYR2. Contrary to predictions, there was no impact on expression levels of Cx43.

In ventricular myocytes, TBX18 expression has been shown to alter ventricular myocytes to SAN-like cells with spontaneous pacemaking activites, that is triggered by an up-regulation of HCN4 and of the Ca^{2+} clock. [9] Additionally, suppression of Cx43 expression has been found in neonatal mouse ventricular myocardium and porcine ventricular myocytes.[9,30] These differences can be attributed to species- or tissue-specific impacts of TBX18. One research group sucssefuly programmed the ventricular myocytes to pacemaker phenotype in rat, porcine and pig ventricular cardiomyocytes, [9,30] However, other studies have found only partial phenotypic oprogramming in mouse atrial myocardium. [31] TBX18 imposes a central SAN phenotype on TBX3-positive tissue during the developmental stages of the heart, and TBX18 knockout in

mouse present with severe hypoplasia of the central region of SAN 'head', but the SAN 'tail' follows normal development. [8,32] TBX3 and TBX18 expression are needed for complete, normal development of the SAN, which means that a lack of TBX3 in mature cardiomyocytes may hamper attempts to employ TBX18 as a bio-pacemaker in the functioning myocardium.

In SAP tissue, a high level of constitutive TBX3 expression may cause TBX18 to impose a more reliable pacemaker reprogram, with gene expression that varies from that observed when manifested in a functioning myocardium that is characterised by low levels of TBX3. [12] According to Hoogaars *et al.* (2004) [33], TBX3 is expressed even in the mature adult cardiac system. It functions by repression of differentiation of nodal tissue to functioning myocardium, and thus enables cells to acquire the pacemaker phenotype. Nevertheless, over-expression of TBX3 alone is not completely capable for programming cardiomyocytes into pacemaker cells, and over-expression of TBX3 is not enough to trigger an increase in HCN4 expression in mature mouse atria.[34] These findings suggest that the SAP pacemaker rate is unaffected by TBX3 expression, and attributes this to already high levels of TBX3 in the tissue.[12]

7.4.3 The biopacemaker effect

The impact of HCN2 on the spontaneous pacemaker rate of SAP tissue recorded in this study resonates with previous findings.[12] Morris and his colleagues have previously shown that up-regulation of HCN4 alone does not improve pacemaking, and only HCN212 or HCN2 have proved effective. These findings are intersting given that HCN4 is the main HCN isoform in the SAN and is expected to play a major role in the I_f in pacemaking APs under normal conditions. [35,36] Even so, the definitive role of HCN4 in determining the resting heart rate and accelerating it is not clear; patients who have been diagnosed with HCN4 mutations have been shown to exhibit a resting bradycardia but typical heart-rate reaction during physical excersise [37,38,39] Similar results have been seen in inducible HCN4 channels knockout mice, although severe generalised bradycardia did manifest in a cardiac-specific inducible HCN4 knockout. [23] The triggering of HCN4 in tissue outside the central SAN may be limited by the context dependence of HCN channels.[7]

The HCN2 and HCN1 isoforms may show more activity because HCN2 is under more

favourable activation kinetics compared with HCN4, and as noted by Biel *et al.*[40], HCN1 channel has a rapid activation time compared with the other isoforms. Additionally, HCN2 shows a higher cAMP sensitivity compared with the other cardiac isoforms. This may explain the enhanced ISO sensitivity observed in the SAP-TBX18 samples, and would demand careful investigation in a large animal model.

Biophysically detailed simulation here presented consistent results with the concept that the overall increase of HCN abundance, mostly through HCN2 isoform, can lead to increase the pacing rate of nodal tissue without having to raise HCN4 levels. Further evidence of this has been found in other bio-pacemaker groups, which have focused on the three isoforms that show more promising kinetics to generate physiologically relevant pacemaking. [41,7,42] There are theoretical advantages from using TBX18 over the use of HCN2 or HCN212 alone. It would be more likely to change several gene targets at the same time, including multiple HCN isoforms, along with Ca^{2+}-based processes, and thus would more reliably recapitulating the complex nature of the SAN. The present study supports this claim as it has displayed HCN2 and RYR2 up-regulation, a tendency for HCN1 up-regulation, and an alteration in HCN isoform ratio. Given that there was no direct comparison of TBX18 and expression of single HCN-ion channels in the SAP, interpretation to a large animal model or human would require systematic evaluation of both strategies.

7.4.4 Pacemaker stability

Heart-rate instability, in addition to a general bradycardia, is a notable feature of clinical SSS in the form of episodic severe bradycardia and pauses. Given that the SAP samples were *ex vivo*, it was possible to acquire the HRV through measuring the pacemaker stability over two hours, which represented approximately 24,000 beats. Over-expression of TBX18 significantly enhanced heart-rate stability in the SAP. This result resonates with a previous study of a cardiac-specific HCN2 knockout mouse, which revealed the presence of sinus pauses and rate instability, although no resting bradycardia was recorded. [40] In this study, heart-rate stability in a denervated preparation was assessed using HRV, but impacts of a probable reduction in HRV in a larg animal model would require more assessments.

When HRV was compared in the natural SAN and in the SAP, higher HRV was

expected to be observed in the SAP tissue, owing to the possibility of less steady pacemaking in the SAP tissue. There was a tendency for the SAP to display improved stability, but which was not statistically significant. The HRV in both the SAP and the SAN posted a large SD, which was probably symbolic of physiological heterogenty of the animals and the unpredictability of the pacemaker. The decrease in the SD would have demanded increasing the time for recording, but the tissue culturing for more than 48 hours presents a high risk of infection and tissue degeneration. The HRV displayed a tendency for reduction in the TBX18-treated SAP in comparison with the SAN, although not of statistical significance. While the reasons for this are not clear, the result may point to a more consistent population of pacemakers, meaning that unlike SAN-induced bio-pacemakers, which are complex and varied in ultrastructure, TBX18-induced pacemakers are more similar to each other. However, the variation in physiology may be relevant *in vivo* and thus would need further consideration in a big animal model.

7.4.5. Overdrive suppression

The uninfected SAP tissue displayed high overdrive suppression compared with SAN tissue, but SAP and SAP-TBX18 did not register any change in cRT. Overdrive suppression has been linked to both Ca^{2+} and Na^{+}-based mechanisms. [44,29,45] A study on canine Purkinje fibres found that brief trains of overdrive pacing resulted in reduced repression in low Ca^{2}-based solutions and greater repression in high Ca^{2+}-based solutions, while low Na^{+}-based solutions also resulted in a reduction in overdrive repression. Consequently, the Na^{+}/Ca^{2+} exchanger NCX might be involved. [46] Greater repression is also associated with higher intercellular levels of Ca^{2+}, increased K^{+} conductance and greater hyperpolarisation.

The cRT was altered in another experiment by ryanodine, which suggests greater overdrive repression in the context of 0.1μM ryanodine decrease of SR function. [47] Ad-TBX18 infection in the study did not cause any change in the K^{+}, Na^{+} channels and NCX, which referd to a lack of changes in the overdrive repression.

7.5 Limitations

This study was limited by the fact that SSS is a multifaceted disease that is hard to replicate *in vitro.* SAP tissue in the study reliably represented bradycardia, which is the

leading physiological pathology of SSS with instances of heart-rate unsteadiness. However, there is evidence to suggest that idiopathic SSS among humans may be attributed to a wider atrial myopathy that might account for the high incidence of atrial fibrillation in patients. [48] The genesis of idiopathic SSS is not entirely understood and there is a chance of structural alterations in and around the SAN, which would not be treated by localised expression of TBX18. This calls for assessment in large animal models before the same can be replicated in humans for trial.

The study was unable to quantify action potentials straight from the leading pacemaker region for comparison with modelling figures owing to the fragility of the tissue post culture. The study established that after 48 hours in culture, transfer of the tissue to different super-fusion solutions led to stalling of pacing activity both in virus-treated and control samples. Likewise, semi-quantitative display of changes in ion-channel protein through immunohistochemistry could not be performed given that the process was unreliable when using material extracted from cultured tissue. Consequently, the study had to rely on mRNA levels to measure changes in expression.

7.6 Translation to clinical application

Further considerations are needed to translate findings to clinical application. Like all experiments that utilise virally mediated gene expression, the major hurdle is steady, sustainable gene expression. Further experiments may be needed to realise a physiologically relevant heart rate using TBX18 over-expression in advanced animal models.

7.7 Conclusion

The study explains the first proof of concept for the use of TBX18 as a bio-pacemaker approach to treat SSS, a common heart disease responsible for high morbidity and mortality. It also offers the first comprehensive examination of the impact of a bio-pacemaker on heart-rate stability. This resonates with previously established electrophysiological attributes of the HCN2 channel and the detected phenotype of HCN2-deficient mice. Modelling the isoform-specific HCN channel electrophysiology demonstrates that observed changes in HCN abundance may explain the resultant changes in beating rates.

References

1. Monfredi O, Dobrzynski H, Mondal T, Boyett MR, Morris GM. The Anatomy and Physiology of the Sinoatrial Node-A Contemporary Review. Pacing Clin Electrophysiol [Internet]. 2010 Nov [cited 2019 Sep 15];33(11):1392–406. Available from: http://www.ncbi.nlm.nih.gov/pubmed/20946278

2. Jensen PN, Gronroos NN, Chen LY, Folsom AR, deFilippi C, Heckbert SR, *et al.* Incidence of and risk factors for sick sinus syndrome in the general population. J Am Coll Cardiol [Internet]. 2014 Aug 12 [cited 2019 Sep 15];64(6):531–8. Available from: http://www.ncbi.nlm.nih.gov/pubmed/25104519

3. Mond HG, Proclemer A. The 11th World Survey of Cardiac Pacing and Implantable Cardioverter-Defibrillators: Calendar Year 2009-A World Society of Arrhythmia's Project. Pacing Clin Electrophysiol [Internet]. 2011 Aug [cited 2019 Sep 15];34(8):1013–27. Available from: http://www.ncbi.nlm.nih.gov/pubmed/21707667

4. Brignole M, Auricchio A, Baron-Esquivias G, Bordachar P, Boriani G, Breithardt O-A, *et al.* 2013 ESC Guidelines on cardiac pacing and cardiac resynchronization therapy. Eur Heart J [Internet]. 2013 Aug 1 [cited 2019 Sep 15];34(29):2281–329. Available from: http://www.ncbi.nlm.nih.gov/pubmed/23801822

5. Rosen MR, Robinson RB, Brink PR, Cohen IS. The road to biological pacing. Nat Rev Cardiol [Internet]. 2011 Nov 16 [cited 2019 Sep 15];8(11):656–66. Available from: http://www.ncbi.nlm.nih.gov/pubmed/21844918

6. Siu C-W, Lieu DK, Li RA. HCN-Encoded Pacemaker Channels: From Physiology and Biophysics to Bioengineering. J Membr Biol [Internet]. 2006 Nov 8 [cited 2019 Sep 15];214(3):115–22. Available from: http://www.ncbi.nlm.nih.gov/pubmed/17558529

7. Qu J, Plotnikov AN, Danilo P, Shlapakova I, Cohen IS, Robinson RB, *et al.* Expression and function of a biological pacemaker in canine heart. Circulation [Internet]. 2003 Mar 4 [cited 2019 Sep 15];107(8):1106–9. Available from: http://www.ncbi.nlm.nih.gov/pubmed/12615786

8. Wiese C, Grieskamp T, Airik R, Mommersteeg MTM, Gardiwal A, de Gier-de Vries C, *et al.* Formation of the Sinus Node Head and Differentiation of Sinus Node Myocardium Are Independently Regulated by Tbx18 and Tbx3. Circ Res [Internet]. 2009 Feb 13 [cited 2019 Sep 15];104(3):388–97. Available from: http://www.ncbi.nlm.nih.gov/pubmed/19096026

9. Kapoor N, Liang W, Marbán E, Cho HC. Direct conversion of quiescent cardiomyocytes to pacemaker cells by expression of Tbx18. Nat Biotechnol [Internet]. 2013 Jan 16 [cited 2019 Sep 15];31(1):54–62. Available from: http://www.ncbi.nlm.nih.gov/pubmed/23242162

10. Sweeney MO, Hellkamp AS, Ellenbogen KA, Greenspon AJ, Freedman RA, Lee KL, *et al.* Adverse Effect of Ventricular Pacing on Heart Failure and Atrial Fibrillation Among Patients With Normal Baseline QRS Duration in a Clinical Trial of Pacemaker Therapy for Sinus Node Dysfunction. Circulation [Internet].

2003 Jun 17 [cited 2019 Sep 15];107(23):2932–7. Available from: https://www.ahajournals.org/doi/10.1161/01.CIR.0000072769.17295.B1

11. Link MS, Hellkamp AS, Estes NAM, Orav EJ, Ellenbogen KA, Ibrahim B, *et al.* High incidence of pacemaker syndrome in patients with sinus node dysfunction treated with ventricular-based pacing in the Mode Selection Trial (MOST). J Am Coll Cardiol [Internet]. 2004 Jun 2 [cited 2019 Sep 15];43(11):2066–71. Available from: http://www.ncbi.nlm.nih.gov/pubmed/15172414

12. Morris GM, D'Souza A, Dobrzynski H, Lei M, Choudhury M, Billeter R, *et al.* Characterization of a right atrial subsidiary pacemaker and acceleration of the pacing rate by HCN over-expression. Cardiovasc Res [Internet]. 2013 Oct 1 [cited 2019 Sep 15];100(1):160–9. Available from: http://www.ncbi.nlm.nih.gov/pubmed/23787003

13. Boineau JP, Canavan TE, Schuessler RB, Cain ME, Corr PB, Cox JL. Demonstration of a widely distributed atrial pacemaker complex in the human heart. Circulation [Internet]. 1988 Jun [cited 2019 Sep 15];77(6):1221–37. Available from: http://www.ncbi.nlm.nih.gov/pubmed/3370764

14. Morris GM, Kalman JM. Fibrosis, electrics and genetics. Perspectives in sinoatrial node disease. Circ J [Internet]. 2014 [cited 2019 Sep 15];78(6):1272–82. Available from: http://www.ncbi.nlm.nih.gov/pubmed/24837708

15. Stiles MK, Brooks AG, Roberts-Thomson KC, Kuklik P, John B, Young GD, *et al.* High-Density Mapping of the Sinus Node in Humans: Role of Preferential Pathways and the Effect of Remodeling. J Cardiovasc Electrophysiol [Internet]. 2010 May [cited 2019 Sep 15];21(5):532–9. Available from: http://www.ncbi.nlm.nih.gov/pubmed/19912447

16. Yanni J, Tellez JO, Sutyagin P V., Boyett MR, Dobrzynski H. Structural remodelling of the sinoatrial node in obese old rats. J Mol Cell Cardiol. 2010;

17. Joung B, Lin S-F, Chen Z, Antoun PS, Maruyama M, Han S, *et al.* Mechanisms of sinoatrial node dysfunction in a canine model of pacing-induced atrial fibrillation. Hear Rhythm [Internet]. 2010 Jan [cited 2019 Sep 15];7(1):88–95. Available from: http://www.ncbi.nlm.nih.gov/pubmed/19914141

18. Rubenstein DS, Lipsius SL. Mechanisms of automaticity in subsidiary pacemakers from cat right atrium. Circ Res [Internet]. 1989 Apr [cited 2019 Sep 15];64(4):648–57. Available from: http://www.ncbi.nlm.nih.gov/pubmed/2467760

19. Rubenstein DS, Fox LM, McNulty JA, Lipsius SL. Electrophysiology and ultrastructure of eustachian ridge from cat right atrium: a comparison with SA node. J Mol Cell Cardiol [Internet]. 1987 Oct [cited 2019 Sep 15];19(10):965–76. Available from: http://www.ncbi.nlm.nih.gov/pubmed/3437455

20. Rozanski GJ, Lipsius SL, Randall WC, Jones SB. Alterations in subsidiary pacemaker function after prolonged subsidiary pacemaker dominance in the canine right atrium. J Am Coll Cardiol [Internet]. 1984 Sep [cited 2019 Sep 15];4(3):535–42. Available from: http://www.ncbi.nlm.nih.gov/pubmed/6470333

21. Kharche S, Yu J, Lei M, Zhang H. A mathematical model of action potentials of mouse sinoatrial node cells with molecular bases. Am J Physiol Circ Physiol. 2011;301(3):H945–63.

22. Zong X, Krause S, Chen C-C, Krüger J, Gruner C, Cao-Ehlker X, *et al.* Regulation of Hyperpolarization-activated Cyclic Nucleotide-gated (HCN) Channel Activity by cCMP. J Biol Chem [Internet]. 2012 Aug 3 [cited 2019 Sep 15];287(32):26506–12. Available from: http://www.ncbi.nlm.nih.gov/pubmed/22715094

23. Herrmann S, Stieber J, Stöckl G, Hofmann F, Ludwig A. HCN4 provides a 'depolarization reserve' and is not required for heart rate acceleration in mice. EMBO J [Internet]. 2007 Oct 31 [cited 2019 Sep 15];26(21):4423–32. Available from: http://www.ncbi.nlm.nih.gov/pubmed/17914461

24. Baruscotti M, Bucchi A, Viscomi C, Mandelli G, Consalez G, Gnecchi-Rusconi T, *et al.* Deep bradycardia and heart block caused by inducible cardiac-specific knockout of the pacemaker channel gene Hcn4. Proc Natl Acad Sci U S A [Internet]. 2011 Jan 25 [cited 2019 Sep 16];108(4):1705–10. Available from: http://www.ncbi.nlm.nih.gov/pubmed/21220308

25. El Khoury N, Mathieu S, Marger L, Ross J, El Gebeily G, Ethier N, *et al.* Upregulation of the Hyperpolarization-Activated Current Increases Pacemaker Activity of the Sinoatrial Node and Heart Rate During Pregnancy in Mice. Circulation [Internet]. 2013 May 21 [cited 2019 Sep 15];127(20):2009–20. Available from: http://www.ncbi.nlm.nih.gov/pubmed/23609807

26. Wang R. Computational Investigation of the Mechanisms Underlying the Cardiac Pacemaker and its Dysfunction. 2015.

27. Chandler NJ, Greener ID, Tellez JO, Musa H, Molenaar P, Difrancesco D, *et al.* Molecular Architecture of the Human Sinus Node Insights Into the Function of the Cardiac Pacemaker. 2009 [cited 2019 Aug 13]; Available from: http://circ.ahajournals.org

28. Subcommittee to Assess Clinical Intracardiac Electrophysiologic Studies. Guidelines for Clinical Intracardiac Electrophysiologic Studies. A report of the American College of Cardiology/American Heart Association Task Force on Assessment of Diagnostic and Therapeutic Cardiovascular Procedures. Circulation [Internet]. 1989 Dec [cited 2019 Sep 16];80(6):1925–39. Available from: http://www.ncbi.nlm.nih.gov/pubmed/2688977

29. Boyett MR, Fedida D. Changes in the electrical activity of dog cardiac Purkinje fibres at high heart rates. J Physiol [Internet]. 1984 May 1 [cited 2019 Sep 15];350(1):361–91. Available from: http://www.ncbi.nlm.nih.gov/pubmed/6086897

30. Hu Y, Dawkins J, Cho H, … EM-S translational, 2014 undefined. Biological pacemaker created by minimally invasive somatic reprogramming in pigs with complete heart block. stm.sciencemag.org [Internet]. [cited 2019 Sep 15]; Available from: https://stm.sciencemag.org/content/6/245/245ra94.short

31. Greulich F, Trowe M-O, Leffler A, Stoetzer C, Farin HF, Kispert A. Misexpression of Tbx18 in cardiac chambers of fetal mice interferes with

chamber-specific developmental programs but does not induce a pacemaker-like gene signature. J Mol Cell Cardiol [Internet]. 2016 Aug [cited 2019 Sep 15];97:140–9. Available from: http://www.ncbi.nlm.nih.gov/pubmed/27180262

32. Christoffels VM, Mommersteeg MTM, Trowe M-O, Prall OWJ, de Gier-de Vries C, Soufan AT, *et al.* Formation of the Venous Pole of the Heart From an *Nkx2–5* –Negative Precursor Population Requires *Tbx18*. Circ Res [Internet]. 2006 Jun 23 [cited 2019 Sep 16];98(12):1555–63. Available from: http://www.ncbi.nlm.nih.gov/pubmed/16709898

33. HOOGAARS W, Tessari A, Moorman AFM, de Boer PAJ, Hagoort J, Soufan AT, *et al.* The transcriptional repressor Tbx3 delineates the developing central conduction system of the heart. Cardiovasc Res [Internet]. 2004 Jun 1 [cited 2019 Sep 15];62(3):489–99. Available from: http://www.ncbi.nlm.nih.gov/pubmed/15158141

34. Bakker ML, Boukens BJ, Mommersteeg MTM, Brons JF, Wakker V, Moorman AFM, *et al.* Transcription Factor Tbx3 Is Required for the Specification of the Atrioventricular Conduction System. Circ Res [Internet]. 2008 Jun 6 [cited 2019 Sep 15];102(11):1340–9. Available from: http://www.ncbi.nlm.nih.gov/pubmed/18467625

35. Milanesi R, Baruscotti M, Gnecchi-Ruscone T, DiFrancesco D. Familial Sinus Bradycardia Associated with a Mutation in the Cardiac Pacemaker Channel. N Engl J Med [Internet]. 2006 Jan 12 [cited 2019 Sep 15];354(2):151–7. Available from: http://www.ncbi.nlm.nih.gov/pubmed/16407510

36. Chandler NJ, Greener ID, Tellez JO, Inada S, Musa H, Molenaar P, *et al.* Molecular Architecture of the Human Sinus Node. Circulation [Internet]. 2009 Mar 31 [cited 2019 Sep 15];119(12):1562–75. Available from: http://www.ncbi.nlm.nih.gov/pubmed/19289639

37. Duhme N, Schweizer PA, Thomas D, Becker R, Schröter J, Barends TRM, *et al.* Altered HCN4 channel C-linker interaction is associated with familial tachycardia–bradycardia syndrome and atrial fibrillation. Eur Heart J [Internet]. 2013 Sep 14 [cited 2019 Sep 16];34(35):2768–75. Available from: http://www.ncbi.nlm.nih.gov/pubmed/23178648

38. Schweizer PA, Duhme N, Thomas D, Becker R, Zehelein J, Draguhn A, *et al.* cAMP Sensitivity of HCN Pacemaker Channels Determines Basal Heart Rate But Is Not Critical for Autonomic Rate Control. Circ Arrhythmia Electrophysiol [Internet]. 2010 Oct [cited 2019 Sep 15];3(5):542–52. Available from: https://www.ahajournals.org/doi/10.1161/CIRCEP.110.949768

39. Laish-Farkash A, Glikson M, Brass D, Marek-Yagel D, Pras E, Dascal N, *et al.* A Novel Mutation in the HCN4 Gene Causes Symptomatic Sinus Bradycardia in Moroccan Jews. J Cardiovasc Electrophysiol [Internet]. 2010 Dec [cited 2019 Sep 15];21(12):1365–72. Available from: http://www.ncbi.nlm.nih.gov/pubmed/20662977

40. Ludwig A, Budde T, Stieber J, Moosmang S, Wahl C, Holthoff K, *et al.* Absence epilepsy and sinus dysrhythmia in mice lacking the pacemaker channel HCN2. EMBO J [Internet]. 2003 Jan 15 [cited 2019 Sep 15];22(2):216–24. Available from:

http://www.ncbi.nlm.nih.gov/pubmed/12514127

41. Plotnikov AN, Sosunov EA, Qu J, Shlapakova IN, Anyukhovsky EP, Liu L, *et al.* Biological Pacemaker Implanted in Canine Left Bundle Branch Provides Ventricular Escape Rhythms That Have Physiologically Acceptable Rates. Circulation [Internet]. 2004 Feb 3 [cited 2019 Sep 15];109(4):506–12. Available from: http://www.ncbi.nlm.nih.gov/pubmed/14734518

42. Tse H-F, Xue T, Lau C-P, Siu C-W, Wang K, Zhang Q-Y, *et al.* Bioartificial Sinus Node Constructed via In Vivo Gene Transfer of an Engineered Pacemaker HCN Channel Reduces the Dependence on Electronic Pacemaker in a Sick-Sinus Syndrome Model. Circulation [Internet]. 2006 Sep 5 [cited 2019 Sep 15];114(10):1000–11. Available from: http://www.ncbi.nlm.nih.gov/pubmed/16923751

43. Bucchi A, Plotnikov AN, Shlapakova I, Danilo P, Kryukova Y, Qu J, *et al.* Wild-Type and Mutant HCN Channels in a Tandem Biological-Electronic Cardiac Pacemaker. Circulation [Internet]. 2006 Sep 5 [cited 2019 Sep 15];114(10):992–9. Available from: http://www.ncbi.nlm.nih.gov/pubmed/16923750

44. Watanabe EI, Honjo H, Boyett MR, Kodama I, Toyama J. Inactivation of the calcium current is involved in overdrive suppression of rabbit sinoatrial node cells. Am J Physiol Circ Physiol [Internet]. 1996 Nov 1 [cited 2019 Sep 15];271(5):H2097–107. Available from: http://www.ncbi.nlm.nih.gov/pubmed/8945930

45. Boyett MR, Honjo H, Kodama I. The sinoatrial node, a heterogeneous pacemaker structure. Cardiovasc Res [Internet]. 2000 Sep [cited 2019 Sep 15];47(4):658–87. Available from: http://www.ncbi.nlm.nih.gov/pubmed/10974216

46. Musso E, Vassalle M. The role of calcium in overdrive suppression of canine cardiac Purkinje fibers. Circ Res [Internet]. 1982 Aug [cited 2019 Sep 15];51(2):167–80. Available from: http://www.ncbi.nlm.nih.gov/pubmed/7094227

47. Bassani JW, Godoy CM, Bassani RA. Effect of ryanodine on sinus node recovery time determined in vitro. Brazilian J Med Biol Res = Rev Bras Pesqui medicas e Biol [Internet]. 1999 Aug [cited 2019 Sep 15];32(8):1039–43. Available from: http://www.ncbi.nlm.nih.gov/pubmed/10454767

48. Sanders P, Morton JB, Kistler PM, Spence SJ, Davidson NC, Hussin A, *et al.* Electrophysiological and Electroanatomic Characterization of the Atria in Sinus Node Disease. Circulation [Internet]. 2004 Mar 30 [cited 2019 Sep 15];109(12):1514–22. Available from: http://www.ncbi.nlm.nih.gov/pubmed/15007004

Chapter Eight - Discussion and Conclusions

8.1 Significance

The work described in this thesis focuses on the role of the age-related remodelling of ion channels on the electrical activities of the SAN, and the functional effect of these changes on the initiation of the pacemaking and condition activity of the heart. A family of biophysically detailed computer models offers a viable way to investigate how changes to ion-channel electrophysiology at cellular level can affect the electrical action potentials (APs) of the SAN at single-cell and tissue level. The research explained in this thesis utilised electrophysiological data from experiments in different species at cellular level to develop novel mathematical models of neonatal, aged and diabetic conditions. These data were subsequently incorporated into both anatomically and idealised detailed tissue geometries of the rabbit and rat SANs. This work provides novel insights into the understanding of the mechanisms that underlie initiation and sustenance of the electrical activities during ageing process and arrhythmias.

Before the findings of the thesis are discussed in more detail, it is necessary to briefly recapitulate the original work presented in each chapter. Firstly, in Chapter 4 a simulation study was described that investigated mechanistic insights into the reduced pacemaking rate of the rabbit SAN during postnatal development. This study was performed at single-cell and at tissue level using a 2D model of the SAN atrium based on biophysically detailed myocyte models. The details covered tissue heterogeneity, the anisotropy of tissue conductance properties and the complex geometry of the SAN. Use of this model to investigate the effects of ACh stimulation during age development of SAN-atrium tissue was also presented. Secondly, in Chapter 5 two case studies of sinus node dysfunction that arose from different pathways of electrical remodelling in ion channels in the ageing rat heart were described. In Chapter 6, we explained the development of a novel 1D rat SAN-atrium model, which could be used to model the electrophysiological behaviours of the rat SAN at tissue level. The model took into account both tissue heterogeneity and conduction anisotropy. This new model was used to investigate the electrical remodelling of channels that underlay sinus-node dysfunctions in diabetes induced by streptozotocin (STZ). Effects of this STZ diabetes

condition on impairment of the SAN's ability to pace and drive the propagation of APs to the atrium, as seen in sick sinus syndrome (SSS), were investigated. The last part of this thesis (Chapter7) described the utilisation of tissue from bradycardic rat subsidiary atrial pacemaker (SAP) to evaluate alternative gene targets: the $Na^{+/}Ca^{2+}$ exchanger NCX1, and the transcription factors TBX3 and TBX18 known to be involved in SAN embryonic development. This study was composed of experimental and modelling parts. In the modelling part, based on incorporation of isoform-specific HCN-channel electrophysiology, we used a mouse SAN model to investigate the effect of the measured changes in HCN abundance in SAP and SAP-TBX18 preparations on the beating rates. This final chapter summarises some major conclusions and presents a possible future development that may be useful in the subject.

8.2 Major conclusions

8.2.1 The mechanism underlying heart rate and pacemaker activity decline in rabbit SAN during postnatal development.

Marked age-related differences have been observed in morphology and characteristics of APs of neonatal and adult SAN cells. These may be attributable to different sets of ion-channel interactions during the different ages.[1] However, the underlying mechanism(s) of these interactions have yet to be elucidated. The objective of the study explained in Chapter 4 was to determine by biophysical modelling approaches the mechanisms underlying different pacemaking APs and heart rates between neonatal and adult SAN cells of the rabbit heart.

A mathematical model of neonatal rabbit SAN cells was developed in the work for this thesis by modifying the current densities and/or kinetics of ion channels and transporters in a SAN adult-cell model[2] based on available experimental data obtained from neonatal SAN cells. [3,5-12] Then, the same data used in the single-cell models were incorporated into a multi-cellular, two-dimensional model of the intact SAN atrium [13,14] to investigate the functional impact of ion channels altered during maturation on pacemaking electrical activities and their conduction at the tissue level. Effects of a neurotransmitter, acetylcholine, on the pacemaking activities in neonatal cells were investigated and compared with those in the adult at single-cell and tissue level.[15]

Our results show that different mechanisms can cause the slowdown of APs in rabbit SAN at single cells:1) alteration of the activation midpoint in I_{Na}, with a drop in conductance; 2) the shift of the activation and inactivation midpoint in $I_{Ca,L}$ with a reduction in L-type current densities; 3) the age-related change of the activation midpoint in I_f and the decrease in conductances as observed by Yang *et al.*[11]: and 4) the decrease of the gene expression in each of I_{Ks}, I_{Kr} and $I_{NaCa,}$ as found in Allah *et al.*[11] All these remodels of ion-channel properties between neonatal and adult SAN cells can explain the differences in their pacemaking APs and the heart rate. These findings provide mechanistic insight into the understanding of the reduced pacemaking rate of the rabbit SAN during postnatal development. These results were validated with experimental data.

In the 2D model of the intact SAN atrium, it was shown that cellular changes during postnatal development impaired pacemaking activities by increasing the activation time and reducing the conduction velocity across the SAN, and this finding was also seen in experimental observations.[10] Also, the neonatal SAN model, which incorporated the fast beating rates of a neonate, showed a greater sensitivity to parasympathetic modulation in response to vagal-nerve stimulation by acetylcholine (ACh) than those in the adults. For the neonate condition the simulation results at cellular level conclude that there is a critical concentration value of ACh at [ACh] > 8×10^{-8} M. At this concentration the spontaneous activity of the SAN is terminated in the central-cell model but not in the peripheral-cell model. This regional difference in sensitivity to ACh is thought to play a key role in pacemaker shift.[16] At tissue level, our results show that below the critical concentration of ACh, there is a slowing down of the spontaneous activity of the SAN and AP conduction across the SAN-atrium, but the central cells remain capable of pacing and behave as the leading pacemaker, thus, there is no pacemaker shift. However, when the ACh concentration is raised above 8×10^{-8}M, the spontaneous activity of the central SAN ceases, while the peripheral cells still act as pacemakers, and this results in a shift of the leading pacemaker from the central to the peripheral SAN cells.

The adult condition shows similar complex behaviour but with less sensitivity to the ACh concentration; the critical value of the ACh concentration was found to be above 15×10^{-8} M.[15] The high sensitivity of the leading pacemaker shift from the centre to the edge of the SAN periphery in the neonate condition may cause unstable pacemaking,

leading to possible sinus arrest or conduction exit block. These results provide novel insights into the understanding of the cellular mechanisms that underlie the differences in the cardiac pacemaking activities of the neonatal and adult SAN.

8.2.2 Age-related effects of ion-channel current changes in the rat SAN

The function of the SAN, the pacemaker of the heart, declines with age, and this results in increased incidence of SAN dysfunction (SND) in older adults. The study explained in Chapter 5 assessed potential ionic mechanisms underlying age-associated SND. This was performed through the characterisation of age-associated changes to ion-channel and Ca^{2+}-handling proteins by using the rat model as a reference to human ageing. Two group studies identified complex and various changes in some membrane-ion channels in aged rat SND. The first group was known as Ageing Study-1. It indicated considerable changes of gene expression in the SAN with up-regulation of mRNA in the ion channels Cav1.2, Cav1.3, KvLQT1 and Kv4.2, and in the Ca^{2+}-handling proteins, SERCA2a; and with down-regulation of Kv1.5, NCX, and HCN1, and the Ca^{2+} clock gene, RYR2. The second group, known as Ageing Study-2, suggested a significantly different pathway of some ion channels in these aged SAN cells, including down regulation of Cav1.2, Cav1.3 and HCN4, and the Ca^{2+} clock gene RYR2, and an increase of NCX and SERCA. Both data sets shared similar behaviour (down-regulation) for specific ion channels such as HCN4, and RYR2, while both data sets identified contradictory changes (either up-regulation or down-regulation) for some membrane-ion channels such as Cav1.2, NCX, and SERCA2a in aged-rat SND.

The aim of this work was to test a hypothesis that SND might arise from different ionic and molecular mechanistic pathways. To test this hypothesis, a mathematical model of the electrical AP of rat SAN myocytes [17] was modified to simulate the functional impacts of age-induced changes on membrane-ion channels and intracellular Ca^{2+} handling as observed in Ageing Study-1 [18] and Ageing Study-2. [8, 12,19] The role and relative importance of individual remodelled ion channel in the two datasets were also evaluated in three case studies.

Our results show that: 1) the age-induced changes in these sarcolemmal-ion currents and Ca^{2+} handling, based on either Ageing Study-1 or Ageing Study-2, can be accounted for by producing bradycardic effects as manifested by a marked reduction in the heart

rate that matched experimental observations; 2) although the SND arises from the integrated action of all remodelled ion channels in both studies, changes to I_{CaL} play the most important influence role although other remodelled channels and Ca^{2+} handling contribute to the heart-rate reduction in the older adult; 3) remodelled $I_{Ca,L}$, either up-regulated or down-regulated during the ageing, leads to a similar bradycardia effect, suggesting that age-related SND can be caused by different ionic pathways.

8.2.3 Development of one-dimensional rat SAN-atrium model

As part of this study, we developed a novel electrophysiologically and anatomically detailed 1D mathematical model of rat SAN atrium, which provides a good reproduction of the electrophysiological behaviours of the SAN at the tissue level. Our model was constructed on the basis of a biophysically detailed myocyte model which brought flexibility to the model; moreover, the tissue conduction anisotropy and heterogeneity were considered in our model. The geometry of the 1D constructed model was adapted from Zhang *et al.*[2], which included central, peripheral SAN, and right atrium, rescaled to consider the differences between the species. Diffusion values were fitted to produce a comparable total activation time and conduction velocities in the SAN-atrium tissue with those measured experimentally under controlled conditions.[12] The newly developed 1D model of the rat SAN atrium successfully produced similar propagation and condition activities to experimental observations in the rat SAN. A case study on cardiac pacemaking dysfunction associated with ion-channel remodelling in STZ-induced diabetic rat was presented.[20]

8.2.4 The mechanism of SND associated with ion-channel remodelling in STZ rat

Our simulations suggest that the integral effect of deficiencies in $I_{Ca,L}$, $I_{Ca,T}$, I_f and I_{NaCa} observed in the STZ-induced diabetic rat can result in abnormal activities in cardiac pacemaking and electrical conduction, that manifest as sinus bradycardia.[20] The underlying SND associated with ion-channel remodelling during the STZ condition in the diabetic rat share common typical behaviours of pacemaking activities with SSS, which result from genetic defects in HCN4 channel associated with this familial genetic defect as revealed in previous studies.[21-24]

With STZ-induced ion-channel remodelling, both the central and peripheral SAN cells are impaired. This weakens the SAN and increase the conduction time and reduces the CV, leading to slowdown of the pacemaking rates. The depressive effect of the electrotonic interaction between the SAN and the atrium becomes more prominent when the integral effects of remodelled $I_{Ca,L}$, $I_{Ca,T}$, I_f and I_{NaCa} are considered, and this increases the electrical load from the atrium to the SAN such that both the SAN pacemaking ability and the AP conduction are impaired. Similar effects are seen with HCN mutation despite the lack of effect of I_f reduction on the excitability of the atrial cells since atrial cells do not have I_f channels. The depressive effect of the atrium results from the weaker SAN due to a decreased I_f.

Other ionic-channel mutations, such as a defective SCN5A gene that encodes for a pore-forming α-subunit of the fast Na^+ channel, show impairment effects in the AP conduction of the SAN as well as the heart rate.[13,25] In this case, the pacemaking ability of peripheral-SAN cells is impaired more than that of central SAN cells that initiate and control the heart rate. The mutant I_{Na} reduces the atrial cell excitability, and increases the electrical load from the atrium to the SAN, thus impairing propagation of APs.[13]

8.2.5 The effect of HCN-channel change on pacemaker function in a rat SAP and SAP-TBX18 overexpression

Biopacemaking is a gene therapy approach that could become a viable alternative therapy to the electronic pacemaker that is required for SND patients. The aim of biopacemaking is to repair dysfunctional pacemaker tissue through restoration of the pacemaker activity, using the experimental manipulation of gene expression and inverse engineering of molecular abnormalities that occur in SND.

Various experiments have widely used the over-expression of the HCN pacemaker ion channel with some success.[26] In Chapter 7, the use of bradycardic rat SAP tissue was described to evaluate the effect of alternative gene targets on pacemaking rate and heart-rate stability as well as the restoration of isoprenaline response. These targets included the Na^+/Ca^{2+} exchanger NCX1, and the transcription factors TBX3 and TBX18 known to be involved in SAN embryonic development. Moreover, the chapter included a description of a simulation, based on incorporation of isoform-specific HCN channel electrophysiology. In the work described in Chapter 7, biophysically detailed computer

modelling was used to investigate the effect of the measured changes in HCN abundance in SAP and SAP-TBX18 preparations on observed changes in cardiac electrical activity. Results from experiment found that TBX3 and NCX1were not effective in accelerating the rate in SAP tissue. The findings from computer modelling showed that the alternation of the measured HCN abundance could explain the observed changes in beating rates. This suggests that gene therapy that targets TBX18 may have the potential to restore pacemaker function in human SSS and thereby avoid the need for electronic pacemakers.

8.3 Future work

The work presented in this thesis suggests multiple opportunities for future investigations, the most important of which are discussed here.

The computational modelling described in Chapter 4 provided a novel model for neonatal rabbit SAN cells at single-cell and multicellular 2D tissue level. The model has been well validated and can be further used to study the key mechanisms responsible for the fast heart rate in neonatal hearts**, w**hich may have value for the understanding and treatment of cardiac rhythm disorders in immature hearts. However, further 3D anatomical models that consider tissue anisotropy, heterogeneity and spatial structure might be more useful to investigate the initiation and conduction of APs in control or under vegal nerve condition (e.g., the phenomenon of the shift in leading pacemaking site). Moreover, the model of tissue geometry used in the neonatal case here was similar to that of the adult. It has been reported that during the growth of the rabbit, the heart weight and tissue size increase in the central and peripheral SAN and/or atrial tissue, suggesting that the AP conduction distance may increase with development.[11] Further research is therefore required to determine the tissue geometry in intact SAN-atrial tissue in neonate rabbits.

In Chapter 5, the mechanism that underlies the age-related SAN dysfunction is elucidated. Our results suggest that, while the integral action of all remodelled ion channels and Ca^{2+} handling, the remodelled $I_{Ca,L}$, either via a gain or loss of function, contributes primarily to age-related bradycardia. Therefore, ageing-related bradycardia can be linked to different remodelling "pathways", which may affect clinical treatment strategies. However, it has been reported that the incidence of sudden cardiac death takes place after a sudden loss of consciousness around one hour after the start of acute

symptoms.[27] This often happens during the night as the heart rate slows dramatically and the parasympathetic nervous system plays an important role.[27] It is estimated that about 30% of sudden cardiac deaths occur at night time.[28] This problem can affect people of any age, but is a particular issue among the healthy elderly and among well-trained athletes. Our computer simulation results show how the electrical APs and the heart rate are reduced in healthy aged animals. An interesting extension would be to simulate the effects of the neurotransmitter acetylcholine on the pacemaking activities for bradycardia-related dysfunction under condition of high vagal stimulation.

In the work described in Chapter 6, the mechanisms underlying SND that arise from STZ-induced diabetes in the rat were investigated at both the cellular and the 1D tissue levels. The costructed 1D model of the rat SAN atrium provided a good reproduction of the experimental observations and offered a useful tool for the study of cardiac primary pacemaker in healthy and dysfunction conditions.[12,21] However, it was an approximation of idealised intact SAN, and in the future a more realistic geometry tissue would be required. In order to explore the location of the leading pacemaker site and the effects of STZ-induced diabetes on SND during diabetes in whole organ level, and possible treatment through investigation of drug action, a 2D or 3D tissue modelling study ,based on realistic geometry, could be extended. This concluse that our 1D rat SAN model forms an important step toward our final goal to develop a forms an important step toward our final goal to develop a biophysically and anatomically detailed 3D model.

References

1. Larson ED, St JR, Sumner WA, Bannister RA, Proenza C. Depressed pacemaker activity of sinoatrial node myocytes contributes to the age-dependent decline in maximum heart rate. 2013;

2. Zhang H, Holden A V, Kodama I, Honjo H, Lei M, Varghese T, *et al.* Mathematical models of action potentials in the periphery and center of the rabbit sinoatrial node. Am J Physiol Hear Circ Physiol. 2000;279(2000):H397–H421.

3. Mangoni ME, DiFrancesco D, Robinson RB. A TTX-sensitive inward sodium current contributes to spontaneous activity in newborn rabbit sino-atrial node cells. J Physiol [Internet]. 1996 Apr 1 [cited 2018 Jan 30];492 (Pt 1(Pt 1):21–30. Available from: http://www.ncbi.nlm.nih.gov/pubmed/8730579

4. Baruscotti M, Robinson RB. Electrophysiology and pacemaker function of the developing sinoatrial node. Am J Physiol Hear Circ Physiol [Internet]. 2007 [cited

2017 Dec 26];293:2613–23. Available from: http://www.physiology.org/doi/pdf/10.1152/ajpheart.00750.2007

5. Baruscotti M, Difrancesco D, Robinson RB, Generali B. Single-channel properties of the sinoatrial node Na + current in the newborn rabbit. Eur J Physiol 2001; 442:192–196

6. Yang ZF, Sun Y, Li CZ, Wang HW, Wang XJ, Zheng YQ, *et al.* Reduced sinoatrial cAMP content plays a role in postnatal heart rate slowing in the rabbit. Clin Exp Pharmacol Physiol. 2006;33((8)):757–62.

7. Accili EA, Robinson RB, DiFrancesco D. Properties and modulation of If in newborn versus adult cardiac SA node. Am J Physiol Circ Physiol [Internet]. 1997 Mar [cited 2017 Dec 26];272(3):H1549–52. Available from: http://www.physiology.org/doi/10.1152/ajpheart.1997.272.3.H1549

8. Jones SA, Boyett MR, Lancaster MK. Declining into failure: The age-dependent loss of the L-type calcium channel within the sinoatrial node. Circulation. 2007;115(10):1183–90.

9. Protas LE V, Difrancesco D, Robinson RB, Difrancesco D, Rob- RB. L-type but not T-type calcium current changes during postnatal development in rabbit sinoatrial node. Am J Physiol Hear Circ Physiol. 2017;10032:1252–9.

10. Jones SA, Lancaster MK, Boyett MR. Ageing-related changes of connexins and conduction within the sinoatrial node. J Physiol [Internet]. 2004 Oct [cited 2017 Jul 26];560(2):429–37. Available from: http://doi.wiley.com/10.1113/jphysiol.2004.072108

11. Allah EA, Tellez JO, Yanni J, Nelson T, Monfredi O, Boyett MR, *et al.* Changes in the expression of ion channels, connexins and Ca2+-handling proteins in the sino-atrial node during postnatal development. Exp Physiol. 2011;96(4):426–38.

12. Huang X, Yang P, Yang Z, Zhang H, Ma A. Age-associated expression of HCN channel isoforms in rat sinoatrial node. Exp Biol Med [Internet]. 2016 Feb [cited 2018 Mar 14];241(3):331. Available from: http://www.ncbi.nlm.nih.gov/pubmed/26341471

13. Butters TD, Aslanidi O V., Inada S, Boyett MR, Hancox JC, Lei M, *et al.* Mechanistic links between Na+ channel (SCN5A) mutations and impaired cardiac pacemaking in sick sinus syndrome. Circ Res. 2010;107(1):126–37.

14. Bai X, Wang K, Yuan Y, Li Q, Dobrzynski H, Boyett MR, *et al.* simulation study Mechanism underlying impaired cardiac pacemaking rhythm during ischemia : A simulation study. American Institute of Physics; 2017;093934.

15. Zhang H, Holden A V., Nnobel D, BoyettT MR. Analysis of the Chronotropic Effect of Acetylcholine on Sinoatrial Node Cells. J Cardiovasc Electrophysiol [Internet]. 2002 May 1 [cited 2018 Feb 5];13(5):465–74. Available from: http://doi.wiley.com/10.1046/j.1540-8167.2002.00465.x

16. Zhang H, Butters T, Adeniran I, Higham J, Holden A V., Boyett MR, *et al.* Modeling the chronotropic effect of isoprenaline on rabbit sinoatrial node. Frontiers in Physiology. 2012 vol: 3 pp: 241

17. Tao T, Paterson DJ, Smith NP. A model of cellular cardiac-neural coupling that captures the sympathetic control of sinoatrial node excitability in normotensive and hypertensive rats. Biophys J [Internet]. 2011;101(3):594–602. Available from: http://dx.doi.org/10.1016/j.bpj.2011.05.069

18. Tellez JO, Ma¸czewski M, Yanni J, Sutyagin P, Mackiewicz U, Atkinson A, *et al.*

Ageing-dependent remodelling of ion channel and Ca 2+ clock genes underlying sino-atrial node pacemaking. Exp Physiol Exp Physiol. 9611:1163–78.

19. Hatch. Age-associated changes to calcium handling proteins across the whole heart . 2012. Doctor of Philosophy

20. Zhang Y, Wang Y, Yanni J, Qureshi MA, Logantha SJRJ, Kassab S, *et al.* Electrical Conduction System Remodeling in Streptozotocin-Induced Diabetes Mellitus Rat Heart. Front Physiol [Internet]. 2019 Jul 8;10:862. Available from: https://www.frontiersin.org/article/10.3389/fphys.2019.00826/full

21. Zhang. X. Simulation of Cardiac Pacemaker Dysfunction Arising from Genetic Mutations. 2011. Doctor of Philosophy

22. Monfredi O, Boyett MR. Sick sinus syndrome and atrial fibrillation in older persons — A view from the sinoatrial nodal myocyte. J Mol Cell Cardiol [Internet]. 2015 Jun [cited 2019 Nov 13];83:88–100. Available from: http://www.ncbi.nlm.nih.gov/pubmed/25668431

23. Baruscotti M, Barbuti A, Bucchi A. The cardiac pacemaker current. Journal of Molecular and Cellular Cardiology. Journal of Molecular and Cellular Cardiology 48 (2010) 55–64 Contents

24. Hao X, Zhang Y, Zhang X, Nirmalan M, Davies L, Konstantinou D, *et al.* TGF-1-mediated fibrosis and ion channel remodeling are key mechanisms in producing the sinus node dysfunction associated with SCN5A deficiency and aging. Circ Arrhythmia Electrophysiol [Internet]. 2011 Jun 1 [cited 2018 Mar 27];4(3):397–406. Available from: http://www.ncbi.nlm.nih.gov/pubmed/21493874

25. Lei, M., Zhang, H., Grace, A. A., & Huang, C. L. H. SCN5A and sinoatrial node pacemaker function. Cardiovascular Research. .2007: *74; 356–365*. 2007 Available from: https://doi.org/10.1016/j.cardiores.01.009

26. Rosen MR, Robinson RB, Brink PR, Cohen IS. The road to biological pacing. Nat Rev Cardiol [Internet]. 2011 Nov 16 [cited 2019 Nov 14];8(11):656–66. Available from: http://www.nature.com/articles/nrcardio.2011.120

27. Huikuri H V, Kessler KM, Terracall E, Castellanos A, Linnaluoto MK, Myerburg RJ. Reproducibility and circadian rhythm of heart rate variability in healthy subjects. Am J Cardiol [Internet]. 1990 Feb 1 [cited 2019 Nov 14];65(5):391–3. Available from: http://www.ncbi.nlm.nih.gov/pubmed/2301268

28. University of Manchester. Scientists reveal the mystery of sudden cardiac death [Internet]. ScienceDaily. [cited 2019 Nov 13]. Available from: www.sciencedaily.com/releases/2010/07/100706093235.htm

Appendix 1

Glossary

SAN	Sinoatrial node
CT	Crista terminalis
RA	Right atrium
PF	Purkinje fibre
SVC	Suoperior vena cava
IVC	Inferior vena cava
SND	Snioatrial node dysfunction
SSS	Sick sinus syndrome
ODE	Ordinary differential equation
ECG	Electrocardiogram
PDE	Partial differential equation
K^+	Potassium ion
Na^+	Sodium ion
Ca^{+2}	Calcium ion
R	Universal gas constant
t	Time
T	Absolute temperature in Kelvins (K)
F	Faraday constant
E_{Ks}	Reversal potential of IKs
E_{Na}	Reversal potential of Na+ ion
E_{Ca}	Reversal potential of Ca+ ion
AP	Action potential
V_m	Membrane potential
MDP	Maximum diastolic potential
RMP	Resting membrane potential

PA	Peak amaplitude
APD	AP duration
APD_{90}	AP duration at 90% repolarization
dV/dt_{max}	Maximum upstroke velocity of AP
TOP	Take off potential
C_m	Cell membrane capacitance
I-V	Current-voltage
$V_{0.5}$	Activayion or inactivation midpoint
$I_{Ca,L}$	L-type calcium current
$I_{Ca,T}$	T-type Ca2+ current
I_{CaP}	Sarcolemmal calcium pump current
I_f	Funny current
I_{ion}	Total ionic current
I_{Kr}	Rapid delayed rectifer potassium current
I_{Ks}	Slow delayed rectifer potassium current
I_{Na}	Fast sodium current
I_{NaCa}	Sodium-calcium exchanger current
I_{NaK}	Sodium-potassium pump current
I_{to}	Transient outward potassium current
I_{sus}	Sustained components of 4-AP-sensitive currents
SR	Sarcoplasmic reticulum
SERCA2a	Sarco(endo)plasmic reticulum Ca2≦-ATPase
RyR	Ryanodine receptor
Q_{10}	Functional change in a variable with a 10 K increase in temperature
mRNA	messenger ribonucleic acid
D	Diffusion coefficient
CV	Conduction velocit

Appendix 2

Rat SAN model parameters

Parameter	Value	Parameter	Value
F (C/mmol)	96.5	$K_{m,Nap}$ (mM)	14
R (J/mol-K0	8.314	$K_{m,Kp}$ (mM)	1.4
T (K)	310	kfTMM (mM^{-1}·ms)	2.277
$E_{Ca,L}$ (mV)	45	kbCM (ms-1)	0.542
$E_{Ca,T}$ (mV)	45	kbCQ (ms-1)	0.445
E_{Ks}(mV)	(RT/F)*ln([K]o+0.12*[Na]o) /([Na]i+0.12*[K]i)	kbTC (ms-1)	0.446
		kbTMC (ms-1)	0.00751
		kbTMM (ms-1)	0.751
E_K(mV)	(RT/F)*ln([K]o/[K]i)	kfCM (mM-1·ms -1)	227.7
E_{Na}(mV)	(RT/F)*ln([Na]o/[Na]i)	kfCQ (mM-1·ms -1)	0.534
E_{st}(mV)	18	kfTC (mM-1·ms -1)	88.8
$[Ca^{2+}]$o (mM)	2	V_{cell} (pl)	3.5
[CM]tot (mM)	0.045	V_i (pl)	0.46 Vcell - Vsub
[CQ]tot (mM)	10		
[K+]o (mM)	5.4	V_{rel} (pl)	0.0012 Vcell
[Mg+]i (mM)	2.5	V_{sub} (pl)	0.01 Vcell
[Na+]o (mM)	140	V_{up} (pl)	0.0116 Vcell
[TC]tot (mM)	0.031	τ_{tr} (ms)	60
[TMC]tot (mM)	0.062	τ_{diff_Ca} (ms)	0.04
P_{rel} (ms-1)	5	K_{up} (mM)	0.0006
P_{up} (mM/ms)	0.005	K_{rel} (mM)	0.0012

Rat SAN model Equations

SA node Sarcolemmal Ionic Current

L-type Ca^{2+} current

$$I_{Ca,L} = f\_PKA\_L \times g_{Ca,L} \times (V - E_{CaL}) \times d \times f \times fCa$$

$$\overline{d} = \frac{1}{1 + e^{-(V+12.1+V\_SHIFT\_L)/6}}$$

$$\tau_d = \frac{1}{\alpha_d + \beta_d}$$

$$\alpha_d = \frac{-0.02839 \times (V+35)}{e^{-(V+35)/2.5} - 1} - \frac{0.0849 \times V}{e^{-V/4.808} - 1}$$

$$\beta_d = \frac{0.0143 \times (V-5)}{e^{(V-5)/2.5} - 1}$$

$$\frac{dd}{dt} = \frac{\overline{d} - d}{\tau_d}$$

$$\overline{f} = \frac{1}{1 + e^{(V+30+V\_SHIFT\_L)/5}}$$

$$\tau_f = 44.3 + 257.1 \times e^{-\left(\frac{V+32.5}{13.9}\right)^2}$$

$$\frac{df}{dt} = \frac{\overline{f} - f}{\tau_f}$$

$$\alpha_{fCa} = Km_{fCa} \times \beta_{fCa}$$

$$\overline{f_{Ca}} = \frac{Km_{fCa}}{Km_{fCa} + [Ca]_{sub}}$$

$$\tau_{fCa} = \frac{\overline{fCa}}{\alpha_{fCa}}$$

$$\frac{df_{Ca}}{dt} = \frac{\overline{f_{Ca}} - f_{Ca}}{\tau_{fCa}}$$

T-type Ca^{2+} current

$$I_{Ca,T} = g_{Ca,T} \times (V - E_{CaT}) \times d \times f$$

$$\overline{d} = \frac{1}{1 + e^{-(V+26.3)/6}}$$

$$\tau_d = \frac{1}{1.068 \times e^{\frac{V+26.3}{30}} + 1.068 \times e^{\frac{-(V+26.3)}{30}}}$$

$$\frac{dd}{dt} = \frac{\overline{d} - d}{\tau_d}$$

$$\overline{f} = \frac{1}{1 + e^{(V+61.7)/5.6}}$$

$$\tau_f = \frac{1}{0.0153 \times e^{\frac{-(V+61.7)}{83.3}} + 0.015 \times e^{\frac{V+61.7}{15.38}}}$$

$$\frac{df}{dt} = \frac{\overline{f} - f}{\tau_f}$$

Rapid delayed rectifier K^+ current

$$I_{Kr} = g_{Kr} \times (V - E_K) \times (0.6 \times paF + 0.4 \times paS) \times piy$$

$$\overline{pa} = \frac{1}{1 + e^{-(V+24)/5}}$$

$$\tau_{paS} = \frac{1}{0.0042 \times e^{\frac{V-9}{17}} + 0.00015 \times e^{\frac{-(V-9)}{21.6}}}$$

$$\tau_{paF} = \frac{1}{0.0372 \times e^{\frac{V-9}{15.9}} + 0.00096 \times e^{\frac{-(V-9)}{22.5}}}$$

$$\frac{dpaS}{dt} = \frac{\overline{paS} - paS}{\tau_{paS}}$$

$$\frac{dpaF}{dt} = \frac{\overline{paF} - paF}{\tau_{paF}}$$

$$\overline{piy} = \frac{1}{1+e^{(V+9.6)/10.1}}$$

$$\tau_{piy} = 2$$

$$\frac{dpiy}{dt} = \frac{\overline{piy} - piy}{\tau_{piy}}$$

Slow delayed rectifier K^+ current

$$I_{Ks} = f\_Ks \times g_{Ks} \times (V - E_{Ks}) \times n^2$$

$$\bar{n} = \frac{\alpha_n}{\alpha_n + \beta_n}$$

$$\tau_n = \frac{1}{\alpha_n + \beta_n}$$

$$\alpha_n = \frac{0.014}{1+e^{-(V-40+SHIFT\_Ks)/45}}$$

$$\beta_n = 0.001 \times e^{\frac{-(V+SHIFT\_Ks)}{22}}$$

$$\frac{dn}{dt} = \frac{\bar{n} - n}{\tau_n}$$

Ca^{2+}-independent transient outward K^+ current

$$I_{to} = g_{to} rq(V - E_K)$$

$$\bar{r} = \frac{1}{1+e^{-(V-19.3)/15}}$$

$$\bar{q} = \frac{1}{1+e^{(V+49)/13}}$$

$$\tau_r = \frac{14.405}{1.037e^{0.09(V+30.61)} + 0.369e^{-0.12(V+23.84)}} + 2.7535$$

$$\tau_q = \frac{39.102}{0.57 \times e^{-0.08(V+44)} + 0.065 \times e^{0.1(V+45.93)}} + 6.06$$

$$\tau_{Sslow} = 3.7e^{-(V+70.0/30.0)^2} + 0.035$$

$$\frac{dr}{dt} = \frac{\bar{r} - r}{\tau_r}$$

$$\frac{dq}{dt} = \frac{\bar{q} - q}{\tau_q}$$

Steady-state outward K^+ current

$$I_{sus} = g_{sus} r (V - E_K)$$

$$\bar{r} = \frac{1}{1 + e^{-(V-19.3)/15}}$$

$$\tau_r = \frac{14.405}{1.037 e^{0.09(V+30.61)} + 0.369 e^{-0.12(V+23.84)}} + 2.7535$$

$$\frac{dr}{dt} = \frac{\bar{r} - r}{\tau_r}$$

Hyperpolarization-activated current

$$I_f = g_f \times (I_{fNa} + I_{fK})$$

$$I_{fNa} = g_{fNa} \times (V - E_{Na}) \times y^2$$

$$I_{fK} = g_K \times (V - E_K) \times y^2$$

$$\bar{y} = \frac{1}{1 + e^{(V+100-V\_shift)/13.5}}$$

$$\tau_y = \frac{0.7166529}{e^{-(V+425.5)/45.302} + e^{(V-73.08)/19.231}}$$

$$\frac{dy}{dt} = \frac{y_\infty - y}{\tau_y}$$

Sustained inward current

$$I_{st} = f\_PKA\_st \times g_{st} \times (V - E_{st}) \times qa \times qi$$

$$\overline{qa} = \frac{1}{1 + e^{-(V+57)/5}}$$

$$\tau_{qa} = \frac{1}{\alpha_{qa} + \beta_{qa}}$$

$$\alpha_{qa} = \frac{1}{0.15 \times e^{\frac{-V}{11}} + 0.2 \times e^{\frac{-V}{700}}}$$

$$\beta_{qa} = \frac{1}{16 \times e^{\frac{V}{8}} + 15 \times e^{\frac{V}{50}}}$$

$$\frac{dqa}{dt} = \frac{qa_{\infty} - qa}{\tau_{qa}}$$

$$\overline{qi} = \frac{\alpha_{qi}}{\alpha_{qi} + \beta_{qi}}$$

$$\tau_{qi} = \frac{1}{\alpha_{qi} + \beta_{qi}}$$

$$\alpha_{qi} = \frac{1}{3100 \times e^{\frac{V}{13}} + 700 \times e^{\frac{-V}{70}}}$$

$$\beta_{qi} = \frac{1}{95 \times e^{\frac{-V}{10}} + 50 \times e^{\frac{-V}{700}}} + \frac{0.000229}{1 + e^{\frac{-V}{5}}}$$

$$\frac{dqi}{dt} = \frac{qi_{\infty} - qi}{\tau_{qi}}$$

Background sodium current

$$I_{b,Na} = g_{b,Na}(V - E_{Na})$$

Muscarinic potassium channel current

$$I_{K\_Ach} = g_{K\_Ach} \times (Ki - Ko \times e^{\frac{-VF}{RT}})$$

Na^+-K^+ pump current

$$I_{NaK} = I_{NaK\_\max} \times (1 + (\frac{Km_{Kp}}{Ko})^{1.2})^{-1} \times (1 + (\frac{Km_{Nap}}{Nai})^{1.3})^{-1} \times (1 + e^{\frac{-(V - E_{Na} + 120)}{30}})^{-1}$$

Na^+-Ca^{2+} exchanger current

$$I_{NaCa} = k_{NaCa} \times \frac{[Na^+]_i^{\,3} \times [Ca^{2+}]_o \times e^{0.03743 V \gamma_{NaCa}} - [Na^+]_o^{\,3} \times [Ca^{2+}]_{sub} \times e^{0.03743 V (\gamma_{NaCa} - 1.0)}}{1.0 + d_{NaCa} \times ([Na^+]_i^{\,3} \times [Ca^{2+}]_o + [Na^+]_o^{\,3} \times [Ca^{2+}]_{sub})}$$

Intracellular Ca^{2+} Dynamics

$$J_{Ca,diff} = \frac{[Ca^{2+}]_{sub} - [Ca^{2+}]_i}{\tau_{diff\_Ca}}$$

$$J_{rel} = P_{rel} \times ([Ca^{2+}]_{rel} - [Ca^{2+}]_{sub}) \times \frac{[Ca^{2+}]_{sub}^{\ 2}}{[Ca^{2+}]_{sub}^{\ 2} + K_{rel}^{\ 2}}$$

$$J_{up} = P_{up} \times \frac{[Ca^{2+}]_i}{[Ca^{2+}]_i + K_{up}}$$

$$J_{tr} = \frac{[Ca^{2+}]_{up} - [Ca^{2+}]_{rel}}{\tau_{\_tr}}$$

Intracellular ion concentrations

$$\frac{d[Ca^{2+}]_i}{dt} = \frac{J_{Ca\_diff} \times V_{sub} - J_{up} \times V_{up} - I_{CaP}}{V_i}$$
$$-([CM]_{tot} \times f_{CMi\_rate} + [TC]_{tot} \times f_{TC\_rate} + [TMC]_{tot} \times f_{TMC\_rate})$$

$$\frac{d[Ca^{2+}]_{sub}}{dt} = \frac{-(I_{CaL} + I_{CaT} - 2.0I_{NaCa}) \times Cm/(2.0 \times F) + J_{rel} \times V_{rel}}{V_{sub}}$$
$$-(J_{Ca\_diff} + [CM]_{tot} \times f_{CMs\_rate})$$

$$\frac{d[Ca^{2+}]_{rel}}{dt} = J_{tr} - J_{rel} - [CQ]_{tot} \times f_{CQ\_rate}$$

$$\frac{d[Ca^{2+}]_{up}}{dt} = J_{up} - J_{tr} \times \frac{V_{rel}}{V_{up}}$$

$$\frac{d[Na^+]_i}{dt} = -(I_{st} + I_{b,Na} + 3I_{NaCa} + 3I_{NaK} + I_{f,Na}) \frac{Cm}{(V_i + V_{sub})F}$$

$$\frac{d[K^+]_i}{dt} = -(I_{Kr} + I_{sus} + I_{K\_Ach} + I_{to} + I_{Ks} + I_{f,K} - 2I_{NaK}) \frac{Cm}{(V_i + V_{sub})F}$$

Ca^{2+} buffering

$$\frac{df_{TC}}{dt} = Kf_{TC} \times [Ca^{2+}]_i \times (1 - f_{TC}) - Kb_{TC} \times f_{TC}$$

$$\frac{df_{TMC}}{dt} = Kf_{TMC} \times [Ca^{2+}]_i \times (1 - f_{TMC} - f_{TMM}) - Kb_{TMC} \times f_{TMC}$$

$$\frac{df_{TMM}}{dt} = Kf_{TMM} \times [Mg^{2+}]_i \times (1 - f_{TMC} - f_{TMM}) - Kb_{TMM} \times f_{TMM}$$

$$\frac{df_{CMi}}{dt} = Kf_{CM} \times [Ca^{2+}]_i \times (1 - f_{CMi}) - Kb_{CM} \times f_{CMi}$$

$$\frac{df_{CMs}}{dt} = Kf_{CM} \times [Ca^{2+}]_{sub} \times (1 - f_{CMs}) - Kb_{CM} \times f_{CMs}$$

$$\frac{df_{CQ}}{dt} = Kf_{CQ} \times [Ca^{2+}]_{rel} \times (1 - f_{CQ}) - Kb_{CQ} \times f_{CQ}$$

Appendix 3

Rat atrial model parameters:

Parameter	Value	Parameter	Value
F	96.9 C/mmol	G_{CaL}	4.8 x 10^{-5} dm^3/(F-ms)
R	8.314 J/mol-K	G_{CaT}	5.4 x 10^{-3} mS/µF
T	296 K	G_{Cab}	0.0008 mS/µF
C_m	1.0 µF/cm^2	G_{Nab}	0.000039 mS/µF
Q_{10}	1.8	G_{Kb}	10^{-6} mS/µF
$r_{nucleus}$	5.7934 µm	$G_{Na,310K}$	145 mS/µF
r_{SR}	6.0 µm	G_{Kur}	0.02 mS/µF
r_{SL}	10.5 µm	G_f	0.021 mS/µF
A_{cap}	1.3854 x 10^{-5} cm^2	G_{to}	0.00007 mS/µF
V_{SR}	0.0903 pL	k_{NCX}	6.804 x 10^{-17}pA/(pF.µM^4)
V_{NSR}	0.08127 pL	d_{NCX}	10^{-16} pA/(pF.µM^4)
V_{JSR}	0.00903 pL	γ	0.5
V_{myo}	3.94 pL	I_{NaK}	3.83916 pA/pF
$[Ca]_o$	1796 µM	K_{mNai}	186000 µM
$[Na]_o$	154578 µM	n_{NaK}	3.2
$[K]_o$	5400 µM	K_{mKo}	1500 µM
$[Na]_i$	13818.5982638 µM	τ_{fCa}	10 ms
$[K]_i$	130953.391484 µM	P_{NaK}	0.01833
G_{CaL}	4.8 x 10^{-5} dm^3/(F-ms)	v_1	0.01 ms^{-1}
G_{CaT}	5.4 x 10^{-3} mS/µF	V_{max}	0.9996 ms^{-1}
G_{Cab}	0.0008 mS/µF	K_{mf}	0.5 µM
G_{Nab}	0.000039 mS/µF	K_{mr}	3500.0 µM
G_{Kb}	10^{-6} mS/µF	H_f	2.0
$G_{Na,310K}$	145 mS/µF	H_r	2.0
G_{Kur}	0.02 mS/µF	k_{leak}	5 x 10^{-6} ms^{-1}
G_f	0.021 mS/µF	τ_{tr}	200 ms
G_{to}	0.00007 mS/µF	$TRPN$	35 µM
k_{NCX}	6.804 x 10^{-}	K_{mTRPN}	0.5 µM
d_{NCX}	^{17}pA/(pF.µM^4)	$CMDN$	50 µM
γ	10^{-16} pA/(pF.µM^4)	K_{mCMDN}	2.38 µM
k_a	0.5	$CSQN$	24750 µM
k_b	0.16	K_{mCSQN}	800 µM
	4	k_a	1

Rat atrial model equations:

Membrane potential:

$$\frac{\partial V}{\partial t} = \nabla \cdot (\mathcal{D}\nabla V) - \frac{I_{ion}+I_{stim}}{C_m},$$

$$I_{ion} = I_{CaL} + I_{CaT} + I_{NCX} + I_{Cab} + I_{Nab} + I_{NaK} + I_{Na} + I_f + I_{Ksus} + I_{K1} + I_{to} + I_{K,ACh},$$

Fast Na^+ current

$$E_{Na} = \frac{RT}{F} ln\left(\frac{[Na]_o}{[Na]_i}\right),$$

$$I_{Na} = 0.9 G_{Na} m^3 hj (V - E_{Na}),$$

$$\alpha_m = 0.32 \frac{(V+47.13)}{\left(1-e^{-0.1(V+47.13)}\right)},$$

$$\beta_m = 0.056 e^{\left(\frac{-V}{11}\right)},$$

If $V < -40m$

$$\alpha_h = 0.135 e^{\frac{-(V+70.0)}{6.8}}$$

$$\beta_h = 3.56 e^{0.079V} + 3.1 \times 10^5 e^{0.35V},$$

$$\alpha_j = 2.0(-1.2714 \times 10^5 e^{0.2444V} - 3.474 \times 10^{-5} e^{-0.04391V}) \left(\frac{V+37.78}{1+e^{0.311(V+79.23)}}\right)$$

$$\beta_j = 0.1212 \frac{e^{-0.01052V}}{1+e^{-0.1378(V+40.14)}},$$

otherwise

$$\alpha_h = 0.0$$

$$\beta_h = \frac{1.0}{0.13\left(1+e^{\left(-\frac{V+10.66}{11.1}\right)}\right)},$$

$$\alpha_j = 0.0,$$

$$\beta_j = \frac{0.3 e^{(-2.535 \times 10^{-7} V)}}{1.0+e^{-0.1(V+32.0)}},$$

$$m_\infty = \frac{1.0}{1.0+e^{\left(\frac{37.0+V}{-6.8}\right)}},$$

$$\tau_m = \frac{1.0}{\alpha_m+\beta_m}$$

$$h_\infty = \frac{1.0}{1.0+e^{\left(\frac{80.0+V}{0.2}\right)}},$$

If $V < -40mV$

$$\tau_h = \frac{0.06}{\alpha_h+\beta_h} + 1.5,$$

otherwise

$$\tau_h = \frac{0.75}{\alpha_h+\beta_h} + 0.15,$$

Calcium fluxes

$$J_{rel} = v_1 P_{o1}\left([Ca]_{JSR} - [Ca]_i\right),$$

$$J_{leak} = k_{leak}([Ca]_{NSR} - [Ca]_i),$$

$$J_{tr} = \left(\frac{[Ca]_{NSR} - [Ca]_{JSR}}{\tau_{tr}}\right),$$

$$\frac{dCa_{NSR}}{dt} = \frac{J_{up} - J_{leak} - J_{tr}}{V_{NSR}}$$

$$\frac{dCa_{JSR}}{dt} = \beta_{SR}\frac{-J_{rel} + J_{tr}}{V_{JSR}},$$

Free intracellular Ca^{2+}

$$\beta_{Cai} = \frac{1.0}{\left(1 + \frac{\overline{TRPN}K_{mTRPN}}{([Ca]_i + K_{mTRPN})^2} + \frac{\overline{CMDN}K_{mCMDN}}{([Ca]_i + K_{mCMDN})^2}\right)},$$

$$\frac{d[Ca]_i}{dt} = \beta_{Cai}\left(\frac{J_{CaSR} + J_{CaSL}}{V_{myo}}\right),$$

Ca^{2+} buffering

$$\beta_{SR} = \frac{1.0}{\left(1 + \frac{\overline{CSQN}K_{mCSQN}}{([Ca]_{JSR} + K_{mCSQN})^2}\right)},$$

Ryanodine receptor gating

$$K_{mRyR} = \frac{3.51}{1.0 + e^{\left(\frac{[Ca]_{JSR} - 530}{200}\right)}} + 0.25,$$

$$P_{C1} = 1 - P_{o1},$$

$$\frac{dP_{o1}}{dt} = k_a\left(\frac{[Ca]_i^N}{[Ca]_i^N + K_{mRyR}^N}\right)P_{C1} - k_b P_{o1},$$

SERCA

$$J_{up} = \frac{V_{max}\left(\frac{[Ca]_i}{K_{mf}}\right)^{H_f} - V_{max}\left(\frac{[Ca]_{NSR}}{K_{mr}}\right)^{H_r}}{1 + \left(\frac{[Ca]_i}{K_{mf}}\right)^{H_f} + \left(\frac{[Ca]_{NSR}}{K_{mr}}\right)^{H_r}},$$

$$J_{CaSR} = J_{rel} - J_{up} + J_{leak},$$

$$J_{CaSL} = (2I_{NCX} - I_{CaL} - I_{CaT} - I_{Cab})\frac{A_{cap}C_m}{2F \times 10^{-6}},$$

Temperature scaling in monolayer model:

$$h_{\infty,310K} = \frac{1.0}{1.0 + e^{\left(\frac{78.0 + V}{7.8}\right)}}$$

Furthermore, $\tau_{X,310K} = \frac{\tau_{X,296K}}{Q_{10}}$ for $X \in (m, h, j, d, f, fCa, ua, ui, Xs1, Xs2, Xr)$, and $G_{Na,310K} = 1.07G_{Na,296K}$.

$$f_\infty = \frac{1.0}{1+e^{\left(\frac{22+V}{6.1}\right)}},$$

$$\tau_f = 562.5e^{-\frac{(V+27.0)^2}{1000}} + \frac{10.0}{1+e^{(25-V)}} + 10.0,$$

$$a_{fCa} = \frac{1.0}{1+\left(\frac{[Ca]_i}{0.325}\right)^8},$$

$$b_{fCa} = \frac{0.1}{1+e^{\left(\frac{[Ca]_i-0.5}{0.1}\right)}},$$

$$c_{fCa} = \frac{0.2}{1+e^{\left(\frac{[Ca]_i-0.75}{0.8}\right)}},$$

$$fCa_\infty = \frac{a_{fCa}+b_{fCa}+c_{fCa}+0.23}{1.46},$$

$$k = \begin{pmatrix} 0, fCa_\infty > f_{Ca}, V > -60mV \\ 1, \quad otherwise \end{pmatrix},$$

$$\frac{dd}{dt} = \frac{d_\infty - d}{\tau_d},$$

$$\frac{df}{dt} = \frac{f_\infty - f}{\tau_f},$$

$$\frac{df_{Ca}}{dt} = k\frac{f_{Ca\infty} - f_{Ca}}{\tau_{fCa}},$$

T-type Ca^{2+} current

$$I_{CaT} = G_{CaT} bg(V - E_{Ca} + 106.5),$$

$$b_\infty = \frac{1.0}{1+e^{\left(-\frac{V+36}{6.1}\right)}},$$

$$\tau_b = 0.6 + \frac{5.4}{1+e^{0.03(V+100)}},$$

$$\tau_g = 1 + \frac{40.0}{1+e^{0.08(V+65)}},$$

$$\frac{db}{dt} = \frac{b_\infty - b}{\tau_b},$$

$$\frac{dg}{dt} = \frac{g_\infty - g}{\tau_g},$$

Na^+/Ca^{2+} exchanger current

$$I_{NCX} = k_{NCX}\frac{[Na]_i^3[Ca]_o e^{0.03743\gamma V} - [Na]_o^3[Ca]_i e^{0.03743(\gamma-1)V}}{1+d_{NCX}([Na]_o^3[Ca]_i + [Na]_i^3[Ca]_o)},$$

$$\tau_r = \frac{1000.0}{45.16e^{0.03577(V+50)}+98.9e^{-0.1(V+38.0)}},$$

$$\tau_s = 1000\left(0.35e^{-\left(\frac{V+70}{15}\right)^2} + 0.035\right) - 26.9,$$

$$\tau_{sslow} = 1000\left(3.7e^{-\left(\frac{V+70}{30}\right)^2} + 0.035\right) + 37.4,$$

$$\frac{dr}{dt} = \frac{r_\infty - r}{\tau_r},$$

$$\frac{ds}{dt} = \frac{s_\infty - s}{\tau_s},$$

$$\frac{ds_{slow}}{dt} = \frac{s_{slow\infty} - s_{slow}}{\tau_{sslow}},$$

Na^+/K^+ ATPase

$$\sigma = \frac{\left(e^{\left(\frac{[Na]_o}{67300}\right)} - 1\right)}{7},$$

$$f_{NaK} = \frac{1.0}{1+0.1245e^{\left(-\frac{0.1VF}{RT}\right)}+0.0365\sigma e^{\left(-\frac{VF}{RT}\right)}},$$

$$I_{NaK} = I_{NaK}\frac{f_{NaK}}{\left(1+\left(\frac{K_{mNai}}{[Na]_i}\right)^{n_{NaK}}\right)\left(1+\frac{K_{mKo}}{[K]_o}\right)},$$

Constitutively active K,ACh current

$$I_{KACh} = (0.296)\left(0.1 + \frac{0.18}{1.0+e^{\left(\frac{V+102.0}{10.0}\right)}}\right)(V - E_K - 10),$$

For SL membrane currents

L-type Ca^{2+} current

$$E_{Ca} = \frac{RT}{2F}ln\left(\frac{[Ca]_o}{[Ca]_i}\right),$$

$$I_{CaL} = 4G_{CaL}dff_{Ca}\frac{VF^2}{RT}\left(\frac{[Ca]_i e^{\left(\frac{2VF}{RT}\right)} - 0.341[Ca]_o}{e^{\left(\frac{2VF}{RT}\right)} - 1}\right),$$

$$d_\infty = \frac{1.0}{1+e^{\left(\frac{-1.8-V}{8.6}\right)}},$$

$$a_d = 0.25 + \frac{1.4}{1.0+e^{\left(\frac{-35-V}{13}\right)}},$$

$$b_d = \frac{1.4}{1+e^{\left(\frac{V+5}{5}\right)}},$$

$$c_d = \frac{1.0}{1+e^{\left(\frac{50-V}{20}\right)}},$$

$$\tau_d = a_d b_d + c_d + 10.0,$$

Slow delayed rectifier K^+ current

$$G_{Ks} = 0.0866\left(1 + \frac{0.6}{1+\left(\frac{0.000038}{[Ca]_i}\right)^{1.4}}\right),$$

$$I_{Ks} = G_{Ks}Xs_1Xs_2(V - E_{Ks}),$$

$$Xs_{1\infty} = \frac{1.0}{1+e^{\left(-\frac{V-10}{20}\right)}},$$

$$Xs_{2\infty} = Xs_{1\infty},$$

$$\tau_{Xs1} = \frac{1.0}{7.19\times10^{-5}\frac{(V+30)}{1-e^{-0.148(V+30)}}+1.31\times10^{-4}\frac{(V+30)}{e^{0.0687(V+10)}-1}},$$

$$\tau_{Xs2} = 4\tau_{Xs1},$$

$$\frac{dXs_1}{dt} = \frac{Xs_{1\infty}-Xs_1}{\tau_{Xs1}},$$

$$\frac{dXs_2}{dt} = \frac{Xs_{2\infty}-Xs_2}{\tau_{Xs2}},$$

Rapid delayed rectifier K^+ current

$$G_{Kr} = 0.0005228\sqrt{\left(\frac{[K]_o}{5.4}\right)},$$

$$I_{Kr} = G_{Kr}X_rR_r(V - E_K),$$

$$Xr_\infty = \frac{1.0}{1+e^{\left(-\frac{V+12.5}{10}\right)}},$$

$$\tau_{Xr} = \frac{1.0}{\frac{0.00138(V+14.2)}{1-e^{-0.123(V+14.2)}}+\frac{0.00061(V+38.9)}{e^{0.145(V+38.9)}-1}},$$

$$Rr_\infty = \frac{1.0}{1+e^{\left(\frac{V+9.0}{22.4}\right)}},$$

$$\frac{dXr}{dt} = \frac{Xr_\infty-Xr}{\tau_{Xr}},$$

Time-independent K^+ current

$$I_{K1} = 0.0489\left(\frac{K_o}{K_o+210}\right)\left(\frac{V-E_K-10}{1.0+e^{0.041(V-E_K-10)}}\right) + 0.01(V - E_K)$$

Transient outward K^+ current

$$I_{to} = G_tr(0.706s + 0.294s_{slow})(V - E_K),$$

$$r_\infty = \frac{1.0}{1+e^{\left(-\frac{V+3}{12}\right)}},$$

$$\tau_j = \frac{1.0}{\alpha_j + \beta_j},$$

$$j_\infty = h_\infty,$$

$$\frac{dm}{dt} = \frac{m_\infty - m}{\tau_m},$$

$$\frac{dh}{dt} = \frac{h_\infty - h}{\tau_h},$$

$$\frac{dj}{dt} = \frac{j_\infty - j}{\tau_j},$$

Hyperpolarization activated current

$$I_{fNa} = G_f y\big(0.2(V - E_{Na})\big),$$

$$I_{fK} = G_f y\big(0.8(V - E_K)\big),$$

$$I_f = I_{fNa} + I_{fK},$$

$$y_\infty = \frac{1.0}{1 + e^{\left(\frac{V + 78.65}{6.33}\right)}},$$

$$\tau_y = \frac{1000.0}{0.11885e^{\left(\frac{V+75}{28.37}\right)} + 0.56236e^{\left(\frac{V+75}{-14.19}\right)}},$$

$$\frac{dy}{dt} = \frac{y_\infty - y}{\tau_y},$$

Sustained outward K^+ current

$$I_{Ksus} = 0.001(I_{Kur} + I_{Ks} + I_{Kr}),$$

$$E_K = \frac{RT}{F} ln\left(\frac{[K]_o}{[K]_i}\right),$$

$$E_{Ks} = \frac{RT}{F} ln\left(\frac{[K]_o + P_{NaK}[Na]_o}{[K]_i + P_{NaK}[Na]_i}\right),$$

Ultra-rapid outward K^+ current

$$I_{Kur} = G_{Kur} u_a u_i (V - E_K),$$

$$u_{a\infty} = \frac{1.0}{1 + e^{\left(-\frac{V + 12.5}{25}\right)}},$$

$$\tau_{ua} = 0.493e^{-0.0629V} + 2.058,$$

$$u_{i\infty} = \frac{1.0}{1 + e^{\left(\frac{V - 100}{5.7}\right)}},$$

$$\tau_{ui} = 1200 - \frac{170.0}{1 + e^{\left(\frac{V + 45.2}{5.7}\right)}},$$

$$\frac{du_a}{dt} = \frac{u_{a\infty} - u_a}{\tau_{ua}},$$

$$\frac{du_i}{dt} = \frac{u_{i\infty} - u_i}{\tau_{ua}},$$